European Commission

JRC CONFERENCE AND WORKSHOP REPORTS

International Workshop on Numerical Modelling of NDA Instrumentation and Methods for Nuclear Safeguards

European Safeguards Research and Development Association

Hamid Tagziria, Ludovic Bourva, Peter Jansson

2018

ESARDA
European Safeguards Research & Development Association

NM-NDA-IMNS18

Wednesday 16th - Thursday 17th May 2018

LUX Congress
1 rue du fort Thungen
L-1499 Luxembourg

Dr. Ludovic Bourva, Workshop Chair
Dr. Peter Jansson, ESARDA NDA-WG Chaiman

Joint Research Centre

This publication is a Conference and Workshop report by the Joint Research Centre (JRC), the European Commission's science and knowledge service. It aims to provide evidence-based scientific support to the European policymaking process. The scientific output expressed does not imply a policy position of the European Commission. Neither the European Commission nor any person acting on behalf of the Commission is responsible for the use that might be made of this publication.

Contact information
Name: Hamid Tagziria
Address: Joint Research Centre, Via E. Fermi, 2749, 21027 Ispra VA, Italy
Email: Hamid.TAGZIRIA@ec.europa.eu
Tel.:

EU Science Hub
https://ec.europa.eu/jrc

JRC114178

PDF ISBN 978-92-79-98443-3 doi:10.2760/055930

Luxembourg: Publications Office of the European Union, 2018

How to cite this report: Tagziria, H., Bourva, L., Jansson, P.; International Workshop on Numerical Modelling of NDA Instruments and Methods for Nuclear Safeguards; Luxembourg: Publications Office of the European Union, 2018; ISBN 978-92-79-98443-3; doi:10.2760/055930; JRC114178.

European Safeguard Research
and Development Association

International Workshop on Numerical Modelling of NDA Instrumentation and Methods for Nuclear Safeguards

(NM-NDA-IMNS18)

Wednesday 16th — Thursday 17th May 2018

LUX Congress
1 rue du fort Thungen
L-1499 Luxembourg

Dr. Ludovic Bourva, Workshop Chair
Dr. Peter Jansson, ESARDA NDA-WG Chaiman

Table of Content

SESSION 3: Thursday 17th May 2018 – 8:30 – 12:00: Chair – Dr P. Jansson – (*University of Uppsala*)

Topic 1: Nuclear Spent Fuel Measurements

Topic 2: Nuclear Data and Post Processing

List of Participants

Dr ABBAS Kamel JRC Ispra Project Leader Via Fermi 21027 Ispra VA, Italy (0039)0332785673 kamel.abbas@ec.europa.eu

Dr ALMÁSI Isván Centre for Energy Research Senior Advisor 29-33 Konkoly Thege u. 1121 Budapest, Hungary (0036)30-9846553 almasi.istvan@energia.mta.hu

Dr ANCIUS Darius European Commission Safeguards Technology Officer 1, rue Henri Schnadt 2530 Luxembourg 4301-33442 darius.ancius@ec.europa.eu

Dr AULT Timothy National Nuclear Security Administration (USA, Contractor) NGFP Fellow (Pacific Northwest National Laboratory), 1000 Independence Ave., S.W. Washington, DC 20585, USA 202-586-0088 Timothy.ault@nnsa.doe.gov

Ms BALDIOLI Vittoria DSRL Radiometric Characterisation Specialist Dounreay Site KW14 7TZ Thurso UK (0044) 7845584658 Vittoria.baldioli@dounreay.com

Dr BARON Martin Bundesamt für Strahlenschutz (Federal Office for Radiation Protection) Scientific Adivsor Köpenicker Allee 120-130 10318 Berlin, Germany (0049)18333-4131 (0049)18333-4135 mbaron@bfs.de

Dr BELANGER-CHAMPAGNE Camille Helsinki Institute of Physics, University of Helsinki Postdoctoral researcher PO Box 64 00014 University of Helsinki, Finland (00) 358 40 138 7999 camille.belanger-champagne@gmail.com

Dr BORELLA Alessandro SCK•CEN Scientific officer Boeretang 200 2400 - Mol, Belgium (0032)485428785 aborella@sckcen.be

Mrs BORNHOEFT Marie Charlotte Fraunhofer INT Scientist Appelsgarten 2 53879 Euskirchen, Germany (0049)225118169 (0049)22511838169 marie.charlotte.bronhoeft@int.fraunhofer.de

Dr BOURVA Ludovic IAEA NDA system engineer PO Box 100 1400 Vienna, Austria (0043)12600-24543 l.bourva@iaea.org

Mr . BURR Tom IAEA/LANL A1333 Vienna International Centre A1220 Vienna, Austria (00) 43 2600 25675 tomburr7@gmail.com

Dr CALDEIRA BALKESTÅHL Li Uppsala University postdoc Ångströmlaboratoriet, Lägerhyddsvägen 1 75237 Uppsala, Sweden (0043)762372028 li.caldeira_balkestahl@physics.uu.se

Prof. CEDERWALL Bo KTH Royal Institute of Technology Head of Nuclear Physics Division Roslagstullsbacken 21 SE-10691, Sweden (00) 46737650580 cederwall@nuclear.kth.se

Mr CHARD Patrick Mirion Technologies Lower Dunbeath House, Forss Business Park KW14 7UZ Thurso UK (0044)1847808141 pchard@mirion.com

Prof.Dr CIZELJ Leon Jožef Stefan Institure Head of reactor Engineering Division Jamova cesta 39 1000 Ljubljana, Slovenia (00386)15885330 (00386)15885377 leon.cizelj@ijs.si

Prof. DENDOOVEN Peter Helsinki Institute of Physics, University of Helsinki Gustaf Hällströmin katu 2 00014 University of Helsinki, Finland (000) 358 41 495 7346 (00) 358 2 941 50522 peter.dendooven@helsinki.fi

Mr . ELTER Zsolt Uppsala University Postdoc researcher Ångströmlaboratoriet, Lägerhyddsvägen 1 75120 Uppsala, Sweden (0036)202997470 Zsolt.Elter@physics.uu.se

Dr FANCHINI Erica CAEN SyS s.r.l. Field application senior scientist Via Vetraia No 11 55049 Viareggio, Italy (0039)0584388398 (0039)0584388959 e.fanchini@caensys.com

Dr FINOCCHIARO Paolo INFN Laboratori Nazionali del Sud Head Technologist via S.Sofia 62 95123 Catania Italy (0039)095542284 finocchiaro@lns.infn.it

Mr FRIGERIO Adrien CEA-Valduc Engineer D101K 21580 Salives, France adrien.frigerio@cea.fr

Mr GEURKOV Gregor ORTEC/AMETEK Product Manager 801 S.Illlinois ave Oak Ridge, TN 37830 USA (001) 865 323 2195 gregor.geurkov@ametek.com

Dr HAYES Robert North Carolina State University/ Nuclear Engineering Department Associate Professor 2500 Stinson Dr 27695-7907 Raleigh, USA (001)919-515-2321 (001)919-515-5115 rbhayes@ncsu.edu

Mr . HILDINGSSON Lars Swedish Radiation Safety Authority (SSM) Senior specialist Solna Strandvag 96 17116 Stockholm, Sweden (0046)705685853 (0046)87994010 Lars.hildingsson@ssm.se

Dr HOLZLEITNER Ludwig JRC-Karlsruhe Scientific Officer Hermann-von-Helmholtz-Platz 1 76344 Eggenstein-Leopoldshafen, Germany (0049)7247 951 702 (0049)7247 951 99702 Ludwig.Holzleitner@ec.europa.eu

Mr. HONKAMAA Tapani STUK-Radiation and Nuclear Safety Authority Laippatie 4 00880 HELSINKI, Finland (00) 358405804804 (00) 358 9 75988400 Tapani.honkamaa@stuk.fi

Mr HUSZTI József Hungarian Academy of Sciences Centre for Energy Research (MTA EK), Nuclear Security Department Research scientist Konkoly-Thege M.29-33 1121 Budapest, Hungary (0036)13922222/3339 (0036)13922529 huszti.jozsef@energia.mta.hu

Dr JACOT-GUILLARMOD Roland Swiss Federal Office of Energy Safeguards Inspector Mühlestrasse 4 CH-3063 Ittigen (0041)58 462 69 20 (0049)58 462 00 78 Roland.jacot-guillarmod@bfe.admin.ch

Dr JANSSON Peter Uppsala University Researcher P.O. Box 516 SE-75120 Uppsala, Sweden (00) 46184715841 peter.jansson@physics.uu.se

Dr KAMAEV Oleg Canadian Nuclear Laboratories R&D Scientist 286 Plant Road K0J1J0, Chalk River, Canada 1 -613-584-3311 ext. 44636 oleg.kamaev@cnl.ca

Dr KÖBLE Theo Fraunhofer INT Leader of WG "Nuclear Security Policy and Detection Techniques" Appelsgarten 2 53879 Euskirchen, Germany (0049)2551 18271 (0049)2251 1838271 theo.koeble@int.fraunhofer.de

Dr LITICHEVSKYI Vladyslav Helsinki Institute of Physics, University of Helsinki Postdoctoral researcher Gustaf Hällströmin katu 2 00014 University of Helsinki, Finland (00) 358 401289887 vladyslav.litichevskyi@helsinki.fi

Mr MULLARKEY Paul Cavendish Nuclear Senior Physicist B14.1, Sellafield, Seascale CA20 1PG, Cumbria, UK 00 44 (0)19467 85226 Paul.mullarkey@cavendishnuclear.com

Mr NAOI Yosuke Japan Atomic Energy Agency Director Research Institute 765-1 Funaishikawa, Tokai-mura, Naka-gun Ibaraki-ken, 3191184, Japan (0081)29-282-1133 ex.803-40251 (0081)29 282 0155 naoi.yosuke@jaea.go.jp

Mr NOAM Omry IAEC Physicist/Researcher PO Box 7061 Tel Aviv, 61070, Israel (00972)523346327 omrynoam@gmail.com

Mr REICH Omer IAEC Physicist/Researcher POB 7061 61070 Tel Aviv, Israel (00972)524866525 Omer_re@walla.com

Mr. ROSSA Riccardo SCK•CEN Scientific collaborator Boeretang 200 2400 – Mol, Belgium (00) 32 1433 8035 rrossa@sckcen.be

Mrs ROUDIL Danièle CEA/EN Marcoule DMRC CETAMA president BP 17171 30207 Bagnols sur Cèze Cedex (0033)466796329 danielle.roudil@cea.fr

Mr RUYENS Jan JRC Geel Retieseweg 111 2440 Geel, Belgium (0032)14571976 jan.truyens@ec.europa.eu

Mr SATKOVIAK Lawrence Oak Ridge National Laboratory Non-proliferation Programs Director P:O: Box 2008, MS-6050 Oak Ridge, TN 37831-6050, USA (001)865 576 5650 (001)865-574 3900 satkowiaklj@ornl.gov

Dr SCHILLEBEECKX Peter EC-JRC Geel Scientific Officer Retieseweg 111 2440 Geel, Belgium (0032)14571475 peter.schillebeeckx@ec.europa.eu

Dr SCHUMANN Olaf Fraunhofer INT Scientist Appelsgarten 2 53879 Euskirchen (0049) 2251 18341 Olaf.schumann@int.fraunhofer.de

Dr SIMON Aliz IAEA Scientific Officer Vienna International Centre, PO Box 100 1400 Vienna, Austria (0043)2600-21706 aliz.simon@iaea.org

Dr TAGZIRIA Hamid JRC Ispra Senior Research Scientist Via E.Fermi 2749, TP 421 21021 Ispra, Italy (0039)033276324 Hamid.Tagziria@ec.europa.eu

Mrs TOMANIN Alice European Commission Euratom Inspector, Safeguards Technology Officer Rue Robert Stumper 10 2920 Luxembourg 4301-35320 alice.tomanin@ec.europa.eu

Dr TRAHAN Alexis Los Alamos National Laboratory Nuclear Engineer PO Box 1660 Los Alamos, NM 87544, USA (001)5056656248 Atrahan@lanl.gov

Mr VACCARO Stefano European Commission Euratom Inspector, Safeguards Technology Officer 1, rue Henri Schnadt 2920 Luxembourg 4301-31407 stefano.vaccaro@ec.europa.eu

Mrs WEBER Anne-Laure IRSN Laboratory Manager 31 av de la Division Leclerc 92326 Fontenay-aux-Roses, France (0033)158359864 (0032)142353100 anne-laure.weber@irsn.fr

Mr WHITE Timothy IAEA Expert PO Box 100 1400 Vienna, Austria (0043)12600-21918 (0043)26007 t.white@iaea.org

Mr WHITE Gareth Mirion Technologies B528, 10 Unit 1 Harwell OX11 0DF Oxford, UK (0044)1235838303 gwhite@mirion.com

Dr WORRALL Louise Oak Ridge National Laboratory R&D Scientist 1 Bethel Valley Road Oak Ridge, TN 37830 USA (001)8653130337 (001)8652412432 worralllg@ornl.gov

Mr YOO Hosik Korea Institute of Nuclear non-proliferation and Control Implementation of national safeguards activities, Vice President 1534 Yuseong-daero, Yuseong-gu 34054 Daejeon, Rep of Korea (0082)10 53132243 (0082)42 8618819 hsyoo@kinac.re.kr

Dr ZSIGRAI Jozsef JRC Karlsruhe Hermann-von-Helmholtz-Platz 1 76344 Eggenstein-Leopoldshafen, Germany Jozsef.zsigrai@ec.europa.eu

Modelling Passive Fast-Neutron Emission Tomography of Spent Nuclear Fuel

Paul A. Hausladen[1], Anagha S. Iyengar[1,2], Lorenzo Fabris[1], Jinan Yang[1], Jianwei Hu[1], Angela L. Lousteau[1]

[1]Oak Ridge National Laboratory
[2]Department of Energy Science and Engineering, University of Tennessee

Abstract:

For the past year Oak Ridge National Laboratory has been developing a passive fast-neutron emission tomography capability. Like the passive gamma emission tomography capability presently being evaluated by the International Atomic Energy Agency, the goal of this capability is to detect the removal or substitution of individual fuel pins in spent nuclear fuel assemblies for international safeguards applications, such as verifying the integrity of an assembly before transfer to difficult-to-access storage. The present imaging technique is based on neutron emissions originating primarily from curium-244, which is produced predominantly at the end of the exposure cycle. As a result, this technique may be sensitive not only to fuel pins that are removed or substituted after all irradiation, but also to fuel pins that are substituted and subsequently irradiated. At present, a laboratory prototype imager is under construction. The purpose of the prototype is to demonstrate an imaging capability sufficient to resolve individual fuel pins using commercially available boron straw detectors that can withstand the high gamma ray dose from a typical spent fuel assembly. To achieve both practical measurement durations and sufficient resolution to discern individual pins, the prototype imager employs a novel collimator design where the slits of a parallel-slit collimator are rearranged to distribute them around a ring surrounding the target fuel assembly. This presentation will report on simulations to understand the neutron signal-to-noise ratio and gamma dose rate as a function of the collimator design, the neutron detector's response to gamma rays as a function of dose rate, and image reconstruction challenges associated with this collimator design.

Keywords: fast neutron; spent fuel; tomography; repository; safeguards

1. Introduction

Oak Ridge National Laboratory (ORNL) is developing a new capability for passive fast-neutron emission tomography. Like the passive gamma emission tomography capability presently being evaluated by the International Atomic Energy Agency (IAEA) [1], the goal of this capability is to detect the removal or substitution of individual fuel pins in spent nuclear fuel assemblies for international safeguards applications, such as for verifying the integrity of assemblies before transfer to difficult-to-access storage. Traditional application of neutron measurements to spent fuel has been to quantify the ^{239}Pu content [2]. However, the plutonium content of spent fuel assemblies is insufficiently well-known from burnup codes to allow detection of the absence of a single rod from an assembly. In contrast, emission tomography works by using collimation to isolate activity along 'lines of response' through an object, such as a fuel assembly; by combining many collimated views through the assembly, the neutron emission from each fuel pin can be mathematically extracted. Then, pin positions with reconstructed activity that is inconsistent with the appropriate rate of neutron emission can be identified. This pin-by-pin accounting provides a robust check on the completeness of a fuel assembly against pin removals or substitutions.

Neutron-based tomography measurements have a number of potential advantages. First, neutron measurements may have better sensitivity for resolving individual pins towards the centre of larger fuel assemblies where the sensitivity of gamma emission tomography is limited by self-attenuation. Second, neutron measurements may be able to determine the fissile loading of each pin. In water, neutron

leakage from a fuel assembly can be approximately three times the value in air; these additional neutrons originate from thermal neutron–induced fission of fissile isotopes. Measuring a fuel assembly in water and in air may enable the induced fission component of each fuel pin to be isolated. Third, neutron measurements may be sensitive to assemblies containing fuel pins that were replaced after a single cycle in the reactor and subsequently irradiated in the core. This sensitivity is a consequence of the neutron signal originating primarily from the ingrowth of ^{244}Cm, which occurs predominantly at the end of the exposure cycle.

In previous work, ORNL demonstrated proof-of-concept emission-neutron computed tomography using fast fission neutrons that was capable of resolving individual pins of fresh plutonium mixed oxide fuel [3]. Unfortunately, this approach used high-resolution scintillation detectors that cannot withstand the overwhelming gamma-ray emissions from spent fuel. To address the challenges of spent fuel, a new parallel-slit ring collimator was devised [4]. This new design enables separation of collimator slits for more effective collimation and use of moderated, gamma blind detectors that can be used in relatively close proximity to the fuel for high efficiency. At present, a laboratory prototype imager is under construction whose purpose is to demonstrate sufficient capability to resolve individual fuel pins.

This paper documents the results of simulation studies to optimise the design of the prototype imager. In this regard, the 'optimal' imager minimise the time to resolve individual fuel pins. In practice, this means the optimal imager has the highest signal-to-noise ratio (SNR) for measurements of fuel assemblies while maintaining gamma dose rates that are tolerable to the detectors and reasonable overall size. For the optimization process, gamma dose rates and neutron responses were calculated for a survey of hundreds of collimator configurations whose parameters (such as collimator thickness and slit width) spanned the range of reasonable values.

This paper opens with a description of the parallel-slit ring collimator concept. Then, the neutron detectors and their response to high-dose gamma-ray fields are described to identify dose rates at which the detectors can operate. Then, the simulated response of a suite of imager designs to both gamma rays and neutrons is presented. Finally, using the response to neutrons, an estimated SNR is calculated for each configuration and the results presented as a function of gamma ray dose rate. The simulations find that the resolution limitations imposed by inter-detector scattering favour wider slits as allowed by dose rate limitations. Furthermore, tapered slits that are narrower in the steel layer and wider in the borated polyethylene layer enable the desirable combination of better gamma dose control and increased neutron efficiency.

2. The Parallel-Slit Ring Collimator

The novel parallel-slit ring collimator concept, first reported last year [4], enables development of a neutron imager that possesses sufficient resolution to identify individual fuel pins while also keeping the imager sufficiently compact, efficient, and radiation-resistant to be practical. The concept is based on parallel slits but achieves the required spacing between slits (and detector elements) by rotating the position of each slit through a known angle to achieve equal detector spacing around the outside of the collimator ring. In this way, correspondence to the parallel-slit collimator is maintained; that is, it isolates lines of response along the same chords across the central volume of the ring. This type of collimator is desirable for neutron imaging because it enables increased separation between collimator slits to effectively modulate neutrons and use of larger, moderated neutron detectors that are both efficient and largely insensitive to gamma rays. An imager employing this type of collimator can simultaneously sample a sufficient number of chords to eliminate the need for scanning at each projection angle.

An exemplar collimator design is shown in Figure 1. It consists of an annular collimator that fits around a spent fuel assembly. The inner diameter of 35.3 cm was chosen because it is sufficiently large to accommodate assembly widths up to 24 cm, and the range of outer diameters of the imager was chosen to fit within commercially available casks so that the size of the imager could be readily handled by a facility. The innermost 10 cm of the collimator is constructed of stainless steel (shown in green) for gamma ray shielding and structural integrity. Surrounding the stainless steel, there is a further 35 cm of collimator constructed from borated polyethylene (shown in yellow). The collimator has 100 slits in it, each terminating on a detector (shown in grey). The number of slits in the collimator (and therefore the number of detectors) was chosen so that there are sufficient lines of response to sample the gaps between fuel pins. Each detector is wedge-shaped in cross section and has an active length of 1 m; it

is composed of a high-density polyethylene moderator with 23 boron straws embedded in the moderator. Boron-straw detectors offer the advantage of achieving neutron efficiency in proportion to the volume of moderator but gamma sensitivity only in proportion to the relatively small gas volume used. Although the detectors detect neutrons at thermal energies, by incorporating boron in the collimator and placing a cadmium thermal-neutron filter between the collimator and detector, the imager responds primarily to fast neutrons. There is an additional 5 cm of borated polyethylene shielding on the outside of the detectors. Together, the width of the collimator slits and the thickness and materials of the collimator determine the resolution, efficiency, and gamma dose imparted to the detectors.

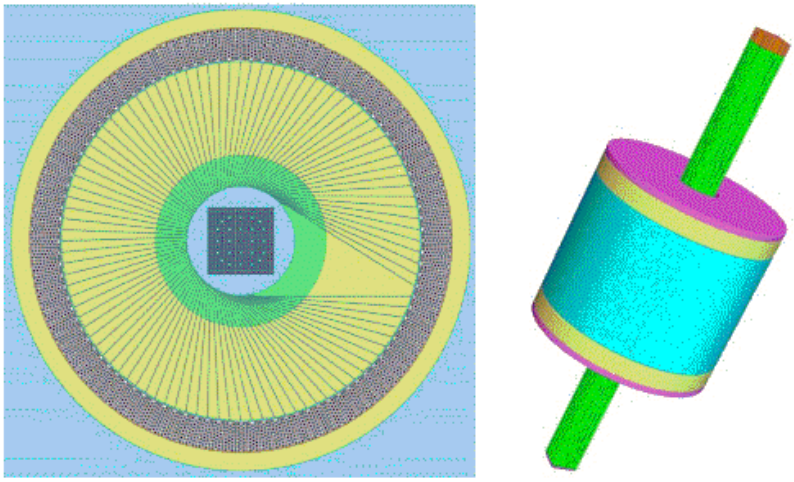

Figure 1: *Left*, 2-D view of the collimator: stainless steel (green), borated poly (yellow), and neutron detectors around. *Right*, 3-D configuration of the imager detectors around a typical fuel assembly (green) with stainless steel (pink) and borated polyethylene shielding (yellow) at the top and bottom of the imager to shield from the fuel that extends above and below the imager.

3. Survey of Collimator Designs

Simulations of gamma dose rates and neutron response were conducted over a range of collimator parameters to identify the optimal combination. In particular, sixteen different combinations of stainless steel and borated polyethylene thicknesses were simulated for each of 32 different slit widths for a total of 512 collimator configurations. These configurations included 9 parallel slits spanning 1–5 mm in 0.5mm intervals and 23 tapered slit combinations with inner dimensions of 1 mm, 2 mm, 2.5 mm, and 3 mm and outer dimensions that ranged from 0.5 mm more than the inner dimension to 5 mm in 0.5 mm intervals.

For the dose rate response, the dose rate was calculated for each detector for each configuration. Then, the aggregate of these simulations was used to understand the scaling of dose rate with collimator parameters. Simulations of gamma-induced pulse height spectra in the detectors suggest that the primary limitation of the detectors due to gamma irradiation is not pulse pileup but low-probability, high-amplitude interactions of single gamma rays. After comparison of calculated dose rates with results from prototype detector testing, configurations with dose rates that can be tolerated by the detectors were identified.

For the neutron response, an SNR was defined for evaluating the ability of a collimator to image a single fuel pin. The SNR considers both efficiency (counting statistics) and resolution. To calculate the SNR for a configuration, the neutron response to each detector has to be calculated on the millimetre length scale over the entire field of view (FOV) of the imager, roughly 100,000 points per projection angle. Simulating this number of points for hundreds of configurations is computationally prohibitive because simulation of a single point corresponds to roughly 1 hour on a single core. As a result, a fast way to estimate the response to all points in the FOV from the simulated response at a few points was devised.

Then, the SNR was calculated for all configurations, and collimator configurations with a favourable combination of SNR and dose rate were identified.

3.1. Gamma response

For the gamma dose calculations, the gamma source term for an exemplar spent fuel assembly was generated by the ORIGEN 2.2 isotope generation and depletion code. For these simulations, a 'worst case' fuel was assumed that has a burnup of 40 GWd/MTU and a cooling time of 1 year. The resultant emission rate of 4.03×10^{16} photons s^{-1} was appropriately apportioned among 24 (unequally sized) energy bins spanning 0–20 MeV. For the dose rate calculations, this gamma source was distributed evenly over the fuel elements of a 17 × 17 fuel assembly. Gamma transport was performed using the MCNP6 simulation code, and interactions within the P-10 fill gas of the detectors were tallied using the F6 tally. The value of the F6 tally (having units MeV g^{-1} $photon^{-1}$) was then converted to R h^{-1}.

The resultant simulated dose rates spanned the range from 60 R h^{-1} to 2,000 R h^{-1}, with lower values corresponding to thicker collimators and narrower slits. The scaling of dose rates with collimator parameters can be understood by plotting the dose rate per centimetre of steel as a function of the average collimator areal density (in g/cm^2). This plot is shown for the totality of simulations in Figure 2. Here, the dose rate drops exponentially with larger areal densities (that result from thicker collimators or narrower slits). The dose rates are shown per centimetre of stainless steel because for two collimators having different thicknesses of steel and the same areal density, the average density of the steel portion is reduced and gamma streaming is increased for the configuration with the thicker steel section by the relative thickness of steel.

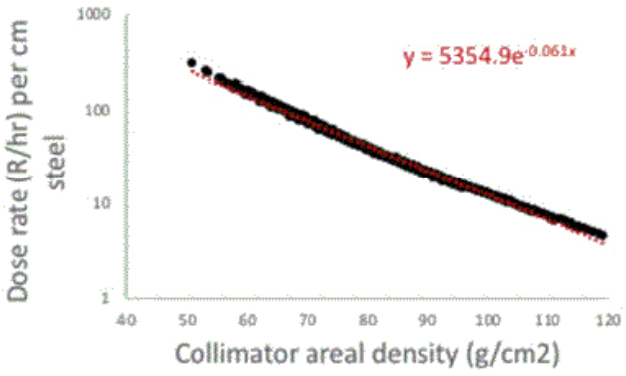

Figure 2: Gamma dose rates per centimetre stainless steel for all 512 cases as a function of the collimator areal density.

The calculated dose rates were compared to measurements of detector response at high dose rates performed at the ORNL RASCAL caesium irradiator facility with a prototype neutron detector that consisted of 23 straws. To emulate exposure to dose rates comparable to those originating from spent fuel, the detector was exposed to the highest possible dose rates available from the irradiator. At a distance of 78 cm from the irradiator opening, approximately 1/3 of the detector was illuminated with a dose rate of 432 R/h, equivalent to exposing 8 straws in their entirety to 432 R/h.

Gamma-induced counts in the neutron detectors originate from two sources: (1) pileup of many small pulses that bring the detector baseline over threshold and low probability and (2) high pulse height interactions of single gamma rays that deposit a substantial fraction of their energy. Pileup-induced counts can be eliminated by decreasing the signal collection time in the detector or instrumenting fewer straws per amplifier; the low probability, large pulses represent a fundamental limitation on detector sensitivity to gamma rays. To determine whether the present detectors are limited primarily from pileup or large single pulses, a high-statistics simulation of pulse heights due to irradiation of the detector by 662 keV gamma rays was performed using MCNP. Simulation of 1 second of irradiation in the configuration with a dose rate of 432 R h^{-1} is equivalent to 9.55×10^{10} 662-keV gamma rays. The resulting pulse height spectrum (together with a simulated neutron pulse height spectrum) was used to calculate the expected count rate as a function of energy. Using an empirical conversion of 300 mV/MeV, the simulated curves were plotted along with measured data for dose rates of 0 R h^{-1},

22 R h^{-1}, and 430 R h^{-1} (Figure 3). Here, the calculated count rates reproduce the measured count rates at 430 R h^{-1} but overpredict the count rates for a low threshold at 22 R h^{-1}. This discrepancy is most likely due to differences in the experimental and modelled spectra from the irradiator, where the former includes down-scattered energies from the collimator and attenuators. However, the simulations suggest that the detectors are either at or close to their fundamental limitation set by low-probability, large amplitude interactions of single gamma rays. As a result, only configurations having a maximum dose rate less than 500 R/h were considered for this application. Additionally, so that the detector pileup is comparable to the high dose rate measurements, the detectors will be instrumented with a preamplifier per row of eight straws.

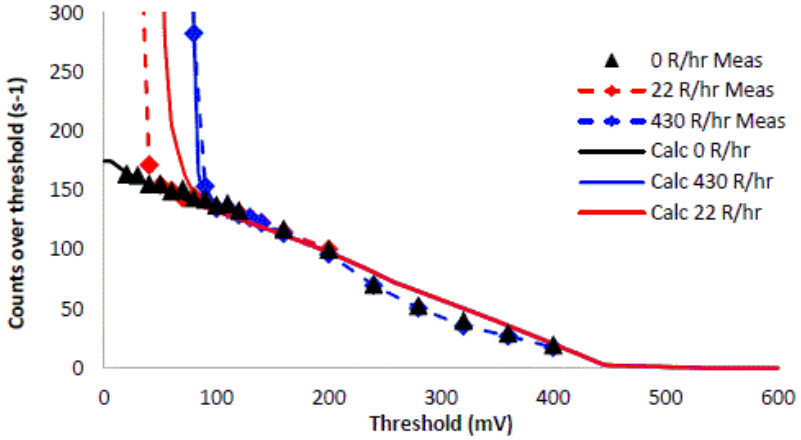

Figure 3: Measured and simulated counts per second as a function of detector threshold setting.

3.2. Neutron response

Ideally, each collimator configuration would be evaluated by simulating tomographic fast-neutron imaging measurements, performing image reconstruction on the simulated data, and evaluating the SNR in the reconstructed images. However, this approach would involve significant effort for each collimator configuration; instead, it is desirable to evaluate collimator configurations independent of reconstruction algorithms. For this purpose, a SNR is defined that captures the quality of data that feeds the image reconstruction. The best imager is the one that maximises sensitivity to a missing fuel pin. In general, to best reconstruct an image of the fuel pins, the activity associated with each fuel pin needs to be attributed to the pin itself rather than the inter-pin space. In this context, the 'signal' is defined as the magnitude of the difference between the calculated response to a single pin and the same level of activity attributed to the 'halo' surrounding that pin. An example of a pin and its corresponding halo is shown pictorially in Figure 4.

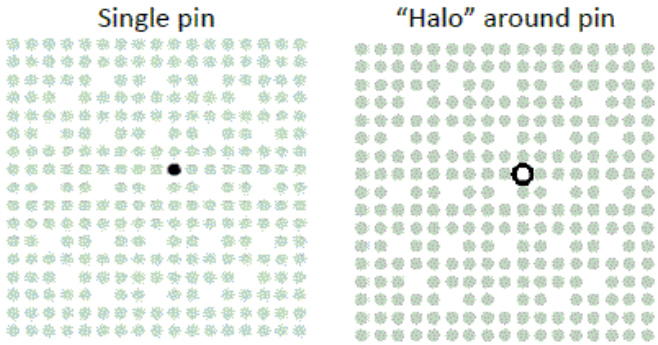

Figure 4: Image showing position of single pin versus the halo associated with that pin.

Likewise, the noise is given by the fluctuations in neutron counts for the full assembly (in the region of interest for the particular fuel pin). The SNR can then be written to compare this signal to the fluctuations in counts from the full assembly, given by Equation (1) below.

$$SNR = \sum \frac{|Response\ to\ pin - Response\ to\ halo|}{\sqrt{Response\ to\ assembly}} \quad (1)$$

To evaluate the SNR for each collimator configuration in the survey of configurations, the response of the collimator needed to be calculated on the millimetre length scale for the entire FOV for each projection angle. To evaluate this number of points, a way to quickly estimate the collimator response over the entire FOV from a few simulated points was devised. For this purpose, the response of a single slit can be thought of as having three components. The first component is the 'direct' response corresponding to neutrons that can travel down the slit unimpeded. The second component is the 'edge' response corresponding to neutrons that either transmit through or scatter within the walls of the slit. The third component is 'collimator penetration.' The relative intensities of the direct and collimator penetration components can be easily inferred from a few simulated points.

To investigate the edge response, a total of 676 simulations were performed where a ^{244}Cm line source was positioned at points along lines perpendicular to the centre line of a single slit collimator. The simulations were performed for slit widths between 1 mm and 5 mm in 0.5 mm increments and source distances of 5.04 cm, 10.08 cm, and 20.16 cm from the slit opening. After subtracting collimator penetration, the response across a single slit is predictable in terms of the projected slit width (Figure 5, right). For the purpose of SNR calculations, the edge response was estimated by a linear drop in response from the collimator edge to 1.8 times the projected slit width.

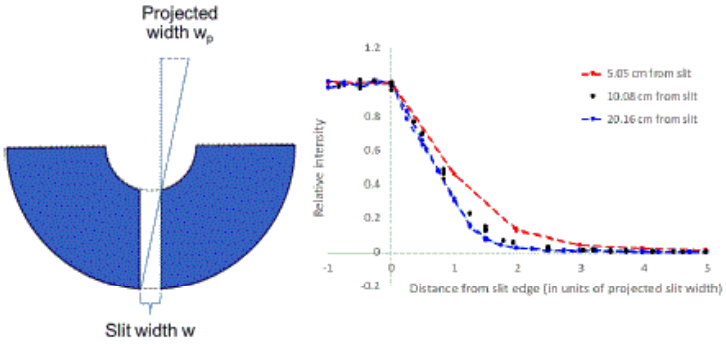

Figure 5: The scaled intensity for the sources at all three distances from the slit opening as a function of the projected width 'W_p'.

At this point, the response of the full FOV was estimated from a few simulated points. In particular, two points were simulated for each of the 512 collimator configurations. These points are shown on the left of Figure 6, with the red central point used to determine collimator penetration and the blue point closer to the slit opening used to determine the direct component. The corresponding collimator responses to sources positioned at each point are shown by the red and blue curves in the centre of Figure 6. Last of all, the estimated response over the full FOV for a single detector (detector 50) is shown on the right side of Figure 6. This response includes cross talk between the slits, where a neutron can travel down one slit but then scatter in the detectors and be detected in a neighbouring detector.

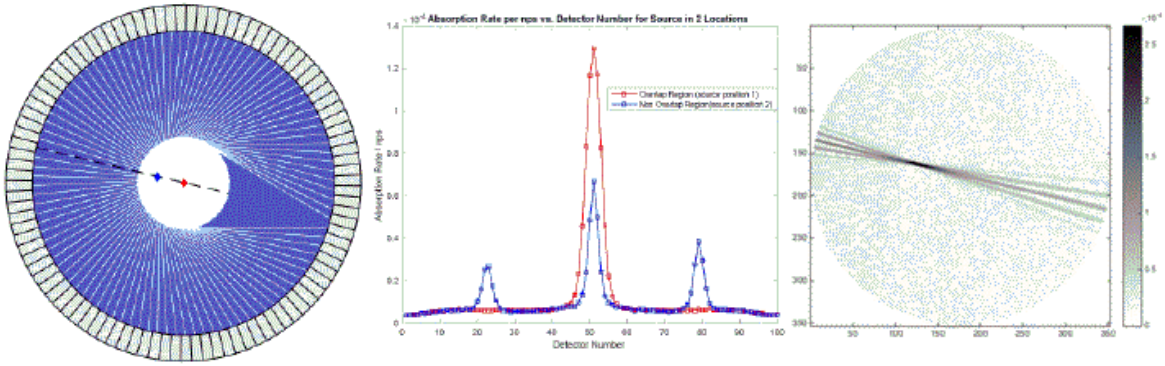

Figure 6: *Left*, diagram showing the positions of points used to characterise a collimator configuration. *Centre,* the corresponding responses to a ^{244}Cm line source positioned at these points for a collimator with 10 cm stainless steel, 30 cm borated poly, and 3-mm-wide parallel slits. *Right,* the estimated response over the full FOV.

The estimated response was calculated for each of the 512 collimator configurations and used to calculate the value of SNR. For the SNR calculation, the detector response was scaled by 1 million emitted neutrons per fuel pin per projection. For a fuel with 45 GWd/MTU burnup, this number of neutrons corresponds to a measurement time of approximately 3 seconds per projection or a total time of 5 minutes. Note that the SNR for the various configurations scales approximately like the geometric mean of the slit width (i.e., the square root of the product of the slit widths at the inner and outer collimator diameters) as can be seen in Figure 7.

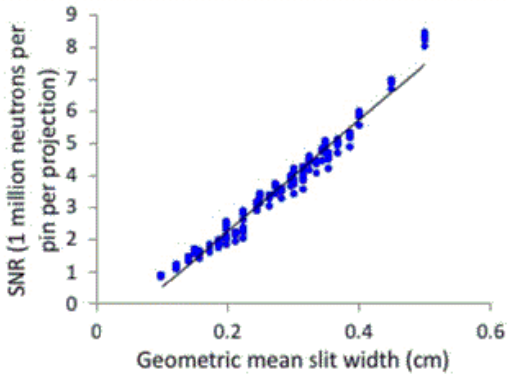

Figure 7: SNR for all 512 cases as a function of the slit geometric mean.

Over the range of slit widths considered, the SNR only increases. This is because the collimator resolution is limited primarily by inter-detector scattering, not slit width. Since the most favourable design is the one that has the highest SNR at a dose rate that is tolerable (less than 500 R h^{-1}), stainless steel improves collimator performance, not because it collimates neutrons effectively, but because it controls gamma dose rate and enables the use of wider, more efficient slits. Likewise, tapered slits are desirable because narrow slits in the steel region preserves the areal density of the collimator, whereas wider slits in the borated polyethylene region preserve efficiency. The SNR and dose rate for all collimator designs with a total thickness less than or equal to 45 cm are shown in Figure 8.

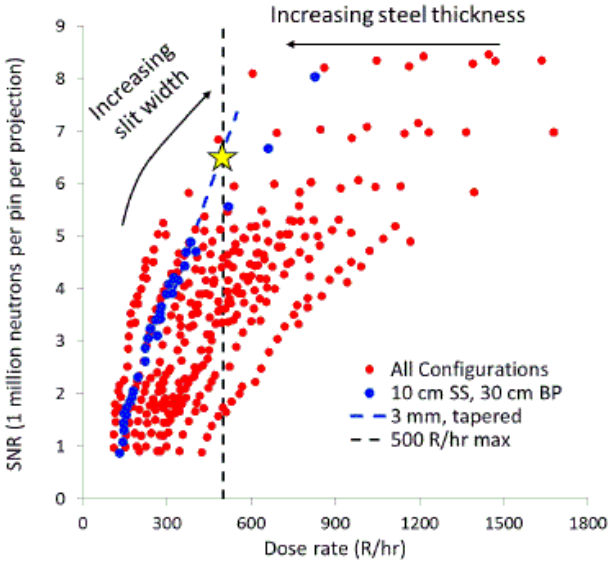

Figure 8: SNR as a function of the maximum gamma dose rate for each corresponding geometry. The optimal geometry (marked with yellow star) is shown along the 500 R/h line.

The position corresponding to a collimator having 10 cm of stainless steel and 30 cm of borated polyethylene, 3 mm slit width at the inner diameter, and 8 mm slit width at the outer diameter is marked with a star. This configuration gets close to the maximum value of SNR with a compact overall size. Note that the best collimator configuration for older, lower dose-rate fuels would have wider slits and perhaps less stainless steel.

4. Summary

Recently, ORNL devised the novel parallel-slit ring collimator concept to enable development of a neutron imager with sufficient resolution to identify individual fuel pins while also being sufficiently compact, efficient, and radiation-resistant to be practical. In the present work, a simulation study was performed to identify configurations of this imager concept that minimise the time to identify individual fuel pins. For evaluating different collimator configurations, an SNR was defined that depends on the ability of the collimator to attribute activity to the fuel pins rather than the inter-pin gap. Desirable configurations are those having a high SNR while maintaining a tolerable gamma ray dose rate in the detectors. The tolerable dose rate in the detectors is limited by the low-probability, large amplitude interactions of single gamma rays. The collimator resolution is effectively limited by inter-detector scattering, not slit width. Although steel poorly modulates neutrons, it effectively controls gamma dose so that wider, more efficient slits can be used. A collimator composed of a 10 cm stainless steel section and a 30 cm borated polyethylene section with tapered slits with a width of 3 mm at the inner collimator radius and 8 mm at the outer collimator radius produces a near-optimal value of SNR with a compact overall size.

5. Acknowledgements

This work is supported by the support of the U.S. Department of Energy, Office of Defense Nuclear Nonproliferation Research and Development in the National Nuclear Security Administration (NA-22). This research was also performed under appointment to the Nuclear Nonproliferation International Safeguards Fellowship Program sponsored by the National Nuclear Security Administration's Office of International Nuclear Safeguards (NA-241).

6. References

[1] Honkamaa, Tapani, et al.; *A Prototype for passive gamma emission tomography*; Symposium on International Safeguards: Linking Strategy, Implementation and People, Vienna, Austria; 2014.

[2] Humphrey, Marc A., et al.; *The Next Generation Safeguards Initiative's Spent Fuel Nondestructive Assay Project*; Journal of Nuclear Materials Management; Volume XI Number 3; Spring 2012; p 6–11.

[3] Hausladen, Paul, et al.; *Demonstration of Emitted-Neutron Computed Tomography to Quantify Nuclear Materials*; Report no. ORNL/TM-2011/357; Oak Ridge National Laboratory, 2011.

[4] Iyengar, Anagha, et al.; *Detection of Fuel Pin Diversion via Fast Neutron Emission Tomography*; JRC Conference and Workshop Reports; ESARDA 39th Annual Meeting; Dusseldorf, Germany; 2017; p 582–594.

Performance Evaluation Framework for the Passive Gamma Emission Tomography (PGET) System

Timothy White[1], Pauli Peura[1], Mikhail Mayorov[1], Alain Lebrun[1], Erin Miller[2], Vladimir Mozin[3], Nikhil Deshmukh[2], Rick Wittman[2], Andreas Musilek[4], Dieter Hainz[4]

[1]International Atomic Energy Agency, Vienna, Austria
[2]Pacific Northwest National Laboratory, Richland, WA, USA
[3]Lawrence Livermore National Laboratory, Livermore, CA, USA
[4]Atominstitut, Technical University of Vienna, Vienna, Austria

Abstract:

A Passive Emission Gamma Tomography (PGET) system has recently been authorized by the IAEA for verification of spent nuclear fuel assemblies (SFAs) and closed containers. The PGET system has demonstrated a capability to detect single missing or replaced pins in WWER-440, 17x17 PWR, and 10x10 BWR assemblies. Data processing and evaluation methods have been developed for the automated detection of anomalies that do not match declarations. These techniques have been tested on the data available from PGET field trials, but a larger sample size, including a larger variety of defects, is required in order to gain confidence in the detection limits and false-alarm rates of the instrument. To address the evaluation of system performance, a framework has been developed for the modeling and simulation of the PGET. The framework includes an MCNP-based simulation engine that allows the creation of assemblies with different pin-to-pin burnups from a single set of radiation transport runs and a transport model to estimate the scatter contribution, and an independent model of the detector response function. Simulations are benchmarked against PGET data collected of mockup fuel constructed from a set of ^{60}Co pins (10cm tall, 7mm diameter) assembled in square or hexagonal lattices. Pin activities are known, and a variety of missing pin geometries can be created, providing an opportunity to correlate simulated and actual data. Post validation, material parameters in the model are changed in order to simulate projection data from spent fuel assemblies and the simulation framework is used to create an ensemble of images for a scenario. A statistical analysis is performed to determine the detection probability and associated false alarm rate for that scenario. This process is first tested against the set of data collected in field trials of the PGET and is then be used to predict performance for untested cases.

Keywords: spent nuclear fuel, tomography, non-destructive assay, simulation, performance prediction

1. Passive gamma emission tomography system description

The Passive Gamma Emission Tomography (PGET) is a nondestructive assay system designed for the measurement of gamma-ray and neutron emissions from spent nuclear fuel. The system has been developed by numerous Member State Support Programs and the IAEA over the past decade [1]. The system is toroidal in shape, with an outer diameter of 95cm and an inner diameter (working area) of 33cm. The torus is 55cm tall. During operation, the torus is lowered into the fuel pond and placed either on an empty region of a fuel rack or on a stand-alone tripod on the floor of the pond. Spent fuel assemblies are retrieved from their location in the rack and lowered into the central hole in the PGET torus by the fuel-handling machine, held stationary for the duration of the measurement (typically 5 minutes) and then returned to the rack. The measurement torus is connected to a control unit (power supply, laptop computer) on the edge of the fuel pond by a single cable in a water-tight sleeve. The PGET system is shown in Figure 1.

The PGET performs three simultaneous measurements: gross neutron counting, medium resolution gamma-ray spectrometry, and two-dimensional gamma-ray emission tomography. In addition, the tomography data can be summed to obtain gross gamma-ray counts in predefined energy windows of interest. The neutron measurements are made with two tungsten shielded ^{10}B tubes coupled to counting electronics. Gamma-ray measurements are performed with 182 cadmium zinc telluride (CZT) detectors of dimensions 3.75mm x 3.75mm x 1.75mm. The detectors view the fuel through a pair of parallel-hole tungsten collimators. The collimator openings are 1.5mm wide by 100mm thick and are fan shaped in the vertical direction, tapering from 70mm at the fuel side to 5mm at the detector side. The output from each CZT crystal is connected to a four-channel discriminator enabling parallel acquisition of data from all detectors in four energy windows. Energy thresholds are user configurable, and are typically set to 400, 600, 700, and 1500keV. In addition, 14 of the CZT detectors can be multiplexed to a micro multi-channel analyzer for simultaneous spectral data acquisition.

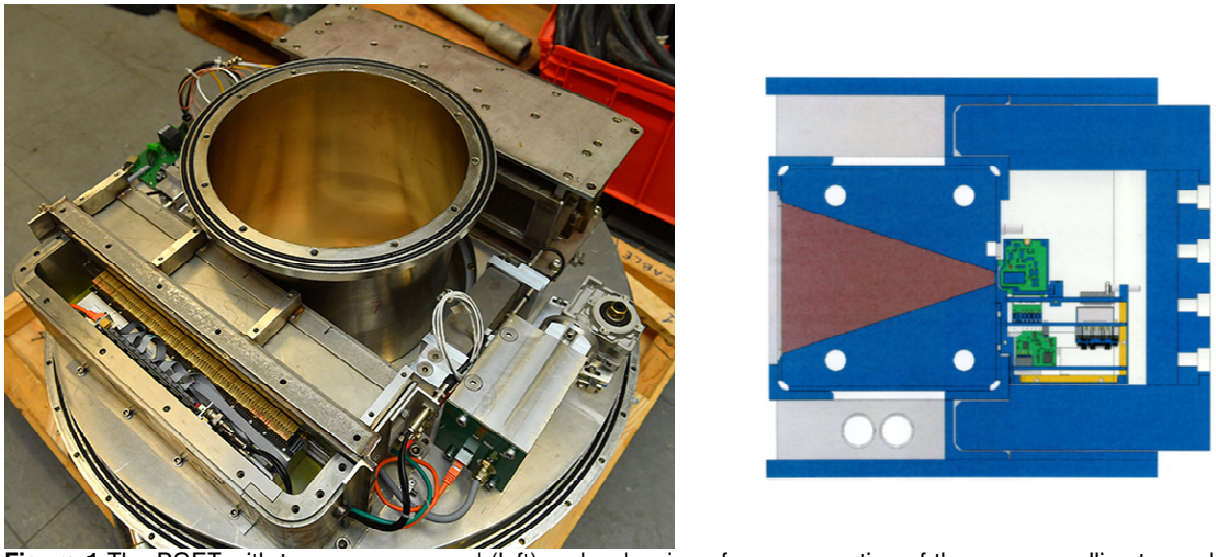

Figure 1 The PGET with top cover removed (left) and a drawing of a cross section of the gamma collimator and detector. The blue regions in the drawing represent tungsten shielding, and the triangular region is the collimator opening.

The gamma and neutron detectors are mounted on a rotating platform within the torus. During a measurement, the platform rotates slowly to collect parallel-beam projection data that create the sinograms to be reconstructed into a tomographic slice. Neutron counts and spectral data are summed as sinogram data are collected. A typical five minute long data collection uses a continuous motion of the rotation platform, with data read out at 800msec intervals to obtain a sinogram with 1-degree angular sampling. Data are reconstructed using the filtered backprojection algorithm [2] or an attenuation-corrected backprojection algorithm [3]. A data processing toolbox has been developed to pre-process the sinogram data, reconstruct, analyse the reconstructed image with respect to a declaration, and report the results.

The authorization of PGET as a Safeguards Instrument represents a significant advance of IAEA verification capabilities as the tomography capability allows the detection of as few as a single missing or replaced pin in a spent fuel assembly. Over 170 tomograms from 62 unique items have been collected during the testing phase of the PGET hardware and software. Single missing or replaced pins have been successfully detected in 17x17 PWR, 101x10 BWR, and WWER-440 fuel types. Testing has also demonstrated that pin-to-pin burnup variations and partially burnt pins due to placement of burnable poisons impact to the capability of detection of anomalies especially automated detection, as does the position of the anomaly within the assembly. Further testing of detection capability is desired, however testing opportunities at spent fuel ponds are infrequent and developing a set of well characterized assemblies with a variety of missing-pin variations is not feasible. Thus, in order to evaluate the tomographic capabilities of the PGET, a modelling and simulation capability to probe the detection limits must be developed. This paper will present a simulation framework for performance testing of tomography with PGET and the benchmarking approach to validating these simulations.

2. Evaluation framework

The framework for evaluating PGET performance has been adapted from earlier work that was used to compare the performance of different designs of a tomography system for inspection of spent nuclear fuel [4]. In this approach, ensembles of images are created and evaluated in order to generate receiver operating characteristic (ROC) curves. The ROC curve is a common approach to estimate a detection capability as a function of acceptable false-alarm rate as some decision metric is varied. The ensemble of images represent multiple measurements of an assembly with the same average burnup (BU) and cooling time (CT), but different pin-to-pin activities and incorporates counting statistics appropriate to the measurement time and detector response. In the earlier study, the goal was to optimize system design, and the variables included different collimator and detector combinations for parallel-beam emission tomography. In the present study, the geometry is fixed to that of the PGET device, and the only variables are fuel parameters and counting statistics.

Though the evaluation framework has many interwoven functions, the process can be conceptually aggregated into four major components:

- Description of the fuel assembly, including geometry (pin positions, fuel diameter, cladding, etc.) and gamma-emission information. Emission information may be calculated from declared information (initial enrichment, BU, and CT) or input as absolute activity. Pin-to-pin variations of activity must be included.
- Model of the PGET device and photon transport calculation. The Monte-Carlo N-Particle transport (MCNP6) code is used for photon transport. After a system model has been established MCNP input decks can be created automatically from a description of the data-collection parameters (angular sampling, integration time, etc.). The output data can be parsed into a set of energy-window sinograms of the full assembly, or a set of single-pin sinograms that can be independently scaled and then summed together to generate ensembles of data for the ROC analysis.
- Application of the detector-response function that is used to convert flux at the detector face (output from MCNP) to counts in predefined energy windows. Decoupling the detector response from the photon transport allows significant speed up in the simulation and provides the capability to investigate the effects of using different energy windows.
- Reconstruction and analysis of the data using the same GET software tools that are used with data from the instrument. The output from the toolbox – average reconstructed activity at each pin location – will be aggregated from each assembly in an ensemble to build histograms of the response.

The histograms of reconstructed activity can be considered to be estimates of probability density functions that will be used to generate the ROC curves. If the model is a faithful representation of the actual system, then a measured data point (reconstructed activities from an real spent fuel assembly) should, with some confidence, be drawn from these probability densities. The remainder of the paper will concentrate on the photon-transport component of the framework and the validation of simulation results.

3. Simulation approach

Projection data are modelled and simulated using MCNP6. The model includes the two tungsten gamma-ray collimators and the inner wall of the PGET torus, but does not include mechanical equipment (e.g., rotating platform) or the watertight enclosure. Fuel is modelled separately as solid uranium-oxide rods in zirconium-alloy cladding on a square or hexagonal grid, depending on the fuel type. The length of the pins is slightly longer than the height of the sensitive region of the PGET. The fuel can be placed in any lateral position and angular orientation in the PGET. The medium surrounding the fuel (between the fuel and the edge of the PGET) is water and the remaining space is modelled as air. A separate MCNP simulation is performed for each angular projection of the sinogram. Projection geometries are defined by rotating the PGET model about the stationary fuel. Photon histories are tabulated as F5 tallies at the front face of the gamma detectors, and a detector-response function is used to generate the spectral response and subsequent binning on the detector.

Convergence time for the simulations is dependent on the energy-bin structure of the F5 tally, specifically the size of the bins in the scatter region of the spectrum. For quicker results, narrow (1keV) energy bins are placed at the photopeak(s) of the isotope(s) that are being simulated, and photon histories are cut off when the photon's energy is reduced to just below the lowest energy peak. As this bin structure does not track photons that have undergone Compton scatter, they are referred to as 'direct-only' simulations, and the sinograms and reconstructions lack the low-amplitude signal and spatial blurring characteristic of the scatter signal in emission tomography. In order to better account for the scatter component, the photon-tracking cut-off can be reduced and an energy bin structure can be established in the region below the photopeaks; these are referred to as full-scatter-contribution (FSC) simulations.

There are two types of sinograms that can be extracted from either the direct-only or FSC simulation. A full-assembly sinogram includes the gamma contribution of all of the pins in the full assembly. In the case of an FSC simulation, this is a three-dimensional data set, where the third dimension is gamma-ray energy. These data can be used, for example, to gain insight on a specific measurement by including known pin-to-pin burnup variation. In addition to the full-assembly sinogram, a set of single-pin sinograms can be extracted from the tally. These sinograms represent the detector response to a single emitting pin, including all of the attenuation due to the other pins in the assembly and the surrounding water. The single-pin sinograms can then be scaled independently – to represent pin-to-pin activity (proportional to burnup) variations – and recombined to create a full-assembly sinogram. By repeating this process for appropriate random variations of pin-to-pin activity and noise, an ensemble of assemblies representing the same average burnup and cooling time can be created. This is the set of assemblies that is used for the prediction of system performance.

3.1 Simulation benchmarking

As a check on the fidelity of the scatter estimation in the MCNP simulation, a deterministic solution to the gamma-transport problem (RadSat, [5]) was calculated. The RadSat calculation uses the Attilla transport code to solve the Boltzman transport equation at all positions in space. An advantage of the RadSat approach is the capability to sample in energy on a finer grid than is sampled in the MCNP simulations, without convergence artifacts. Spatial and energy-bin data were compared between these approaches, with an emphasis in confirming that the wide energy bins used in the MCNP calculation that are used in order to ensure convergence in a reasonable time capture the scatter appropriately.

3.2 Atominstitut testbed

Laboratory space for testing and maintenance of PGET systems has been established at the Atominstitut at the Technical University of Vienna. Three hundred thirty ^{59}Co pins (7mm diameter, 100mm long) were placed in sealed aluminum tubes (10mm outside diameter, 1mm wall thickness) and irradiated in the TRIGA Mark IV reactor at the Atominstitut to produce a set of ^{60}Co pins that can be used to mock up spent fuel assemblies. These surrogate fuel pins have an activity of about 10MBq each and can be placed in baskets with a regular grid structure to simulate the distribution of activity in spent fuel assemblies. This provides a valuable capability to build, measure, and reconstruct tomographic data from a mockup assembly and then model the well-characterized object and simulate. If good agreement can be shown between the simulated and measured data, then confidence can be developed that, by only changing physical parameters in the model (e.g., pin size, density, isotopic composition), realistic simulations of spent-fuel assemblies can be generated.

4. Example results

In order to benchmark the simulation process, the mockup fuel assembly shown in Figure 2 has been constructed, measured, and simulated. The pins in each red, blue and grey coloured region of the assembly have mean activities of 10.3, 9.6, and 8.8MBq, respectively, with a narrow distribution about that mean as shown in the histogram of pin activities. For the measured data, the pins were chosen

randomly from each distribution; however in the modeled data, each pin was simulated with the mean

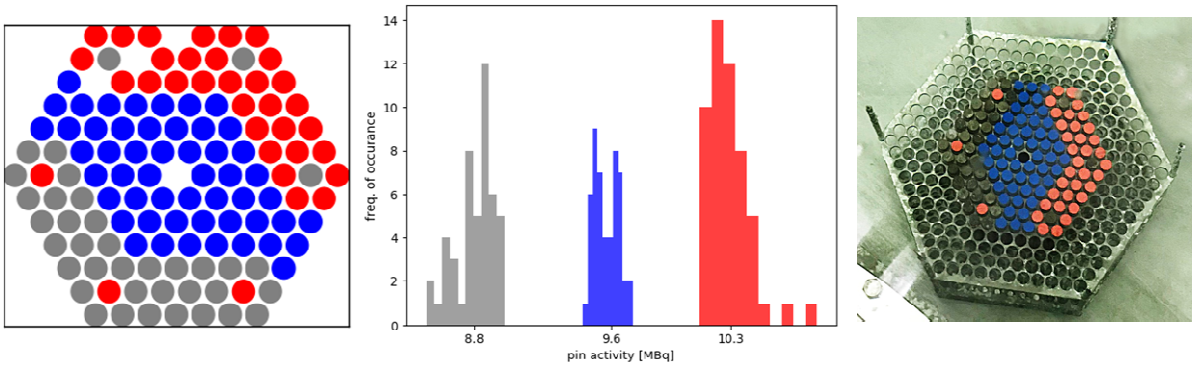

Figure 2 The WWER440 simulated assembly. The histogram plot shows the distribution of activity in pins of the physical assembly on the right. The simulated assembly used a single activity for each of the three regions.

activities. The simulated projections, when scaled to the activity in the pins and propagated through the detector response function and binned into PGET energy bins, were within a factor of 2 of the measured data, a better than expected match of the model with real data.

The calculated flux from the MCNP and RadSat simulations have been compared at the front of the collimator and at the detector. For the direct-only contribution, the two simulation approaches agree to within 5% for all detector pixels at all angles for the simulation providing confirmation of the propagation of primary photons through the assembly and water. A comparison of the FSC simulations front of the collimator demonstrates that the coarse energy-bin structure of the MCNP simulation closely compares to the fine energy bins in the RadSat version (Figure 3). This indicates that scatter in the object (fuel assembly and water) is being captured in the coarse energy bins of the MCNP simulation.

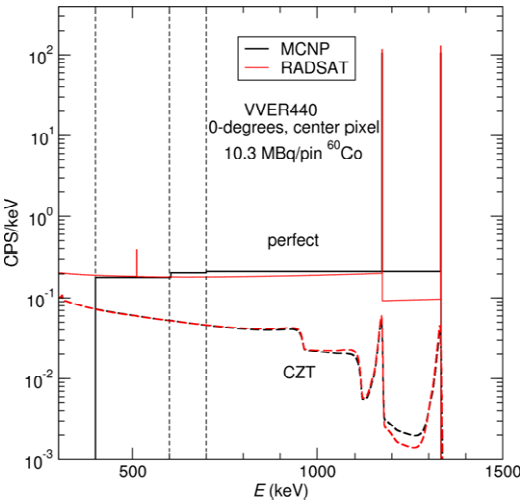

Figure 3 Comparison of the energy response of the MCNP and RadSat simulations. For the MCNP simulation, the photons were tallied into large energy bins corresponding to nominal PGET bins in addition to narrow bins at the photopeaks. The RadSat calculation used 10keV bins in the continuum.

In Figure the reconstructed images and the average reconstructed intensity from each pin from both the simulated and measured are compared. Two observations can be made from these data. The first is that at any radial distance greater than 40mm from the center of the assembly, it is possible to segregate pins whose activity differs by 15%[1]. This is a somewhat surprising result, as the PGET was designed to detect missing pins, not estimate pin-to-pin burnup activity. That the distribution of reconstructed activities from the simulated results is tighter than that of the real data is likely due to the distribution of activities that the simulated activities were drawn from. This can be investigated through further simulation.

These comparisons of reconstructed data provide encouragement that the simulated data reflects the system response, even as the projection data seems to underestimate the scatter. In order to complete this comparison, it is necessary to ask how well the simulated data can be used to perform the PGET task – detection of single missing pins – relative to the actual instrument. If it can be demonstrated that the simulated and real systems perform comparably on mockup fuel assemblies, then that provides confidence that when the model parameters are scaled from the mockup fuel values to real fuel values, the performance on real fuel can modeled. To test the ability on that task the two data sets are evaluated using the figure of merit (FOM) shown in Figure .

[1] At smaller radii, there are only 'blue' pins (mean activity of 9.6MBq).

For this FOM, the difference in the reconstructed activity at a pin location is subtracted for the values of each of the pins nearest neighbors, and these differences are plotted at the radial distance of the pin from the center of the assembly. Thus, if a pin has an activity similar to its neighborhood, then the FOM for that pin will be near zero, while brighter pins will have positive values and missing pins will have negative values. It is clear for these example data that with this FOM missing pins are clearly detectable, and the simulated results again track that of the measured data. However, this is for a single case. The evaluation framework will use the single-pin-sinogram data to generate an ensemble

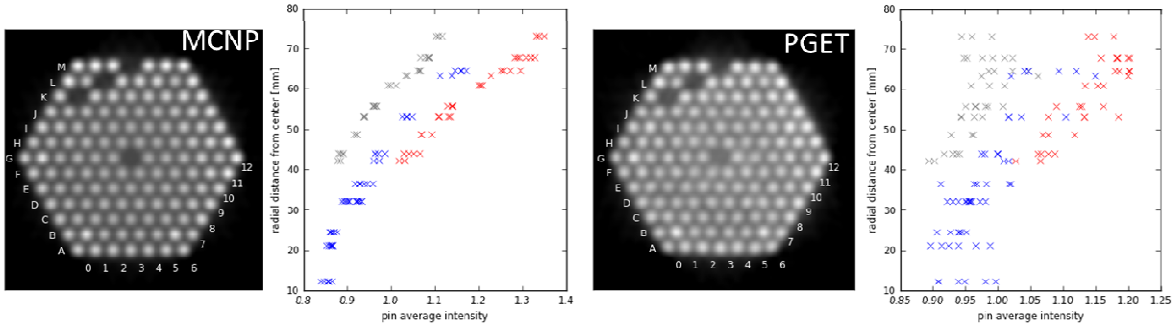

Figure 4 Reconstructed image and average pin activities from simulated data (left) and collected with the PGET.

of simulated sinograms, reconstruct these data, calculate the FOM for each, and then generate histograms (approximations to probability density functions) for the FOM. These data will be used develop ROC curves in order to evaluate the performance of the PGET.

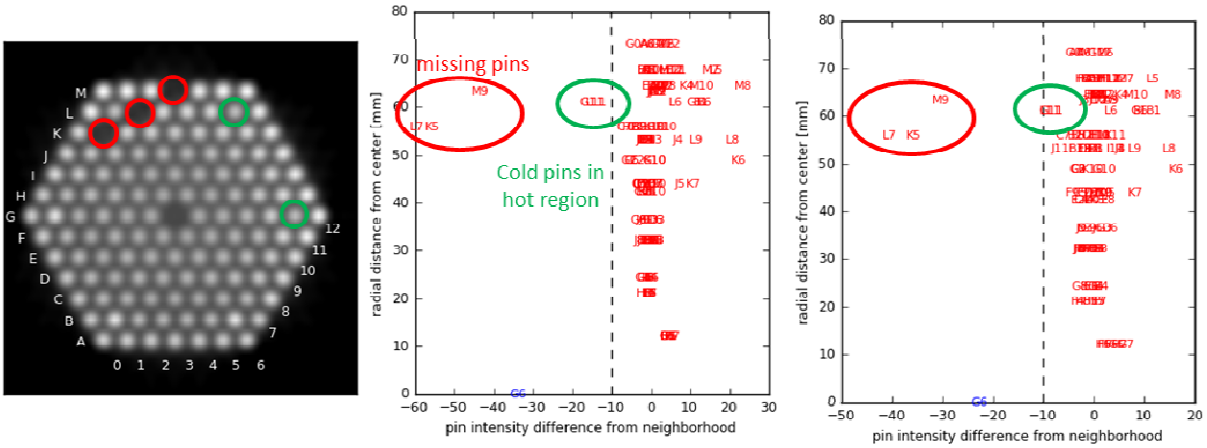

Figure 5 Reconstructed image of the mockup fuel assembly (left) and the figure of merit for the simulated data (middle) and mockup data. The letter-number annotation in the plots indicate the pin position in the image.

5. Conclusion

This work has described PGET, a newly authorized instrument for the verification of declarations of spent nuclear fuel. The PGET performs multiple simultaneous measurements of neutron and gamma emission, including emission tomographic measurements of the activity distribution in an assembly. A framework that will be used to estimate the performance of the tomographic system for the task of detecting missing fuel pins has been described. This framework depends on the ability to rapidly simulate emission tomography data, and it has been shown that the simulated data compares favorably with data measured on mockup fuel assemblies. Further modifications of the model are needed to ensure that the effects of scattered photons are adequately captured in the simulated data. Demonstrating that task performance on these mockup fuel assemblies can be captured in simulation provides confidence that by changing model parameters the performance on spent nuclear fuel assemblies can be estimated.

5. References

1. Honkamaa, T., Levai, F, Turunen, A, Berndt, R., Vaccaro, S., Schwalbach. P., *A prototype for passive gamma emission tomography*. Proceedings of the 2014 Symposium on International Safeguards, 189, 2014.
2. Kak, A.C., Slaney, M., *Principles of Computerized Tomographic Imaging*, IEEE Press, 1988.
3. Kunyansky, L. *A new SPECT reconstruction algorityhm based on the Novikov explicit inversion formula,* Inverse Problems 17 (2001) 293-306.
4. Smith, L.E, *et al., A Viability Study of Gamma Emission Tomography for Spent Fuel Verification: JNT 1955 Phase I Technical Report,* Pacific Northwest National Laboratory Report (25995) accessed 22 May 2018 at http://www.diva-portal.org/smash/record.jsf?pid=diva2%3A1040854&dswid=-594
5. L. E. Smith et al., *Coupling Deterministic and Monte Carlo Transport Methods for the Simulation of Gamma-Ray Spectroscopy Scenarios*, in IEEE Transactions on Nuclear Science, vol. 55, no. 5, pp. 2598-2606, Oct. 2008.

Geometry-based Variance Reduction in simulations of Passive Gamma Spectroscopy from Spent Nuclear Fuel

Zs. Elter, L. Caldeira Balkeståhl, S. Grape, C. Hellesen

Uppsala University, Division of Applied Nuclear Physics

Abstract:

This paper is intended to review the spent nuclear fuel gamma spectroscopy simulations used to create synthetic data in order to train multivariate analysis models. In such applications a vast amount of simulations are needed, hence the reduction of computing time is crucial.

In the study, the passive gamma measurement station at the Swedish Central Interim Storage Facility for Spent Nuclear Fuel, Clab, was considered. The station was modeled first with MCNPX and the gamma transport between a 17x17 PWR spent fuel assembly, ie. the source, and a high purity Germanium detector was simulated. Later, the station was modeled with an in-house point-kernel code named FEIGN. The concentrations of the gamma-ray emitting isotopes for the gamma transport computations were computed with the Serpent2 code.

Since the fuel pins are made of UO2, they are strong attenuators of gamma rays. The setup is also heavily collimated, considering the 1.5m long collimator between the detector and the source, which makes analog simulations very time-consuming. This paper reviews two solutions of the gamma transport simulations: one related to the coupled application of the point-detector and pulse-height tallies with MCNPX, and one based on a simple point-kernel model implemented in python. Since the second methodology provides the faster way of simulating the detector response, the result section of the paper focuses on this solution.

Keywords: passive gamma spectroscopy; spent nuclear fuel; simulation; monte carlo; point-kernel

1. Introduction

Several countries, including Sweden are planning to place irradiated nuclear fuel in geological repositories for final disposal. The spent fuel will be verified for safety and nuclear safeguards purposes before being placed in copper canisters which are lowered into the geological storage. The verification usually requires the application of non-destructive methods to verify operator declarations such as the BIC variables (burnup, initial enrichment, and cooling time), which characterize the fuel assembly to first order for nuclear safeguards [1]. The verification of spent fuel also needs to cover the detection of defects, ie. missing or replaced rods, being present in the spent fuel assembly.

Our on-going work addresses the possibility of applying passive gamma spectroscopy as a non-destructive method to verify the integrity of spent fuel [2]. Namely, we investigate through simulations whether the diversion of certain parts of a spent fuel assembly can be detected from the change in the recorded gamma spectra. Passive gamma spectroscopy was proved to be a fast and robust tool to extract the BIC variables of spent fuel and is used commonly to verify spent fuel [3-5], hence it is important to investigate whether the recorded spectra could provide further information even on the integrity of the assembly. For this work multivariate data analysis (MVA) techniques are applied to identify patterns in the spectra and to detect the defects from the changes in the spectra. The training of MVA methods (eg. classifiers) is based on synthetic data, so a vast amount of simulations of passive gamma spectra, ie. observations or samples are needed, thus the computational time of these samples is crucial.

Current paper focuses on the synthetic data generation. It tries to provide a tutorial on how to simulate passive gamma spectra of spent nuclear fuel assemblies in an efficient and reliable way, thus some parts of the text are rather informal.

First, in Sec. 2. the passive gamma measurement station is described, which was modeled in the simulations, and the challenges of simulating such station with Monte-Carlo methods is summarized. Then, Sec. 3. details the simulation methodology based on MCNPX computations, and the methodology based on an in-house point-kernel implementation, which calculates the geometric efficiency of the setup. Sec. 4. gives examples of the computed geometrical efficiency of the station for different defect scenarios.

2. Considered gamma measurement station

The modeled gamma measurement station is located at the Swedish central interim storage facility for spent nuclear fuel (Clab). A vertical and a horizontal cut of the modeled geometry is shown in Figs. 1A-B. The spent fuel is placed in a pool vertically. The distance between the center of the assembly and the wall of the pool is around 0.5 m. There is a cylindrical hole on the wall, perpendicularly facing the assembly, where an iron collimator is hosted, which allows a collimated gamma ray beam to reach a neighboring room where different detectors and data acquisition systems are installed. The vertical width of the collimator's slit is 5 mm, and the horizontal width is 23.4 cm on the pool side (Fig. 1D), and 8.2 cm on the detector side. The length of the collimator is 1.2 m, and the distance from the center of the assembly to the end of the collimator is 2.46 m.

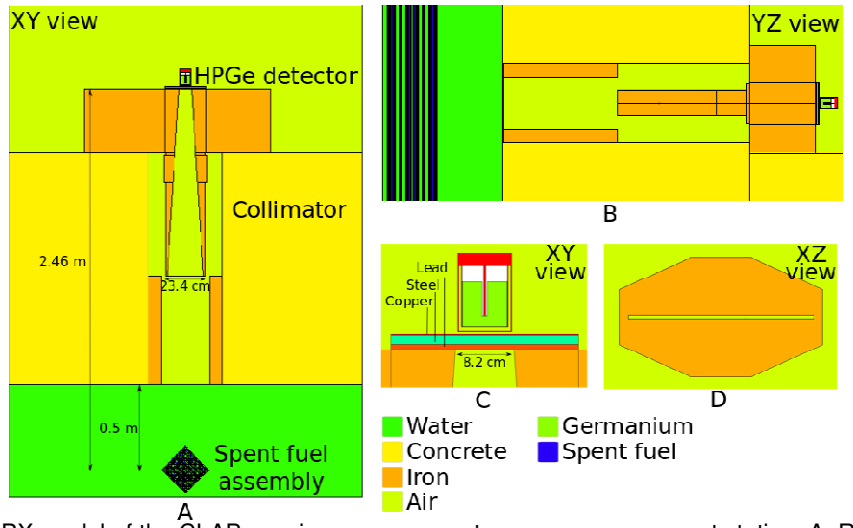

Figure 1: MCNPX model of the CLAB passive gamma spectroscopy measurement station: A: Radial (wrt. fuel) view of the station, B: Axial (wrt. fuel) view of the station C: the HPGe detector and the absorbers placed between the collimator and the detector D: Front view of the collimator from the spent fuel side

The detector was modeled as a high purity germanium crystal (61.5 mm in diameter) with its housing. Between the collimator and the detector three absorber sheets are positioned: 8 mm lead, 12 mm stainless steel and 1 mm copper (Fig. 1C). Further details of the gamma station may be found in [5].

In the simulations the fuel was considered as a PWR fuel assembly with UO_2 pellets and Zirconium cladding. The geometric properties of the assembly are summarized in Table 1. The assembly contains 264 fuel rods and 25 guide tubes. The guide tubes do not contain any absorber rods, although in reality the absorber rods may be present in the spent fuel assembly. In some of the simulations the fuel was considered to contain several dummy rods instead of fuel rods as detailed in Sec. 4.

	Pellet radius (cm)	Clad inner radius (cm)	Clad outer radius (cm)	Pitch (cm)	Matrix size
PWR	0.41	0.42	0.48	1.26	17x17

Table 1: Properties of modeled PWR fuel.

2.1. Challenges when simulating with Monte Carlo methods

The fuel pins made of UO_2 in cladding are strong attenuators of gamma rays. Therefore, during passive gamma spectroscopy mainly the outer rods of the assembly are contributing to the signal. Nevertheless, the defect identification can be based on the fact that the attenuation of gamma rays within the fuel assembly varies strongly with the energy of the gamma ray. Therefore, one expects that by replacing different parts of an assembly with non-radioactive, but strong attenuating materials, one may observe a different change in the passive gamma spectra for lower and higher energy gamma peaks compared to the spectra of an unperturbed assembly with the same BIC values.

Thus, simulating the geometry means that we have to sample all the source pins and several gamma energies. In the following the main constrains are listed, which make Monte Carlo simulations difficult:

- In an intact fuel assembly 264 fuel pins are present, which all need to be sampled (ie. one needs at least 264 random numbers to see at least one history originated from each pin)
- The spent fuel contains several gamma-emitting isotopes (in [2] the most important 12 isotopes are listed), which requires sampling more than 20 energy lines of the source.
- A gamma ray traveling from the pins directly to the detector needs to cross on average 3.2 cm of UO_2 and 46.3 cm of water, which results in only around 1% of the particles reaching the detector from the source (for 1.365 keV gamma photons). The problem thus can be considered as a deep penetration problem.
- The source is isotropic, however the gamma rays need to pass through a slit in a long collimator. After estimating the geometrical probability of a gamma ray reaching the detector ($A_{slit}/4\pi r^2$, where A_{slit} is the area of the slit on the detector side and r is the distance between the source and the detector), it is seen that 1 out of 100k particles will reach the detector.
- The passive gamma spectrum is usually averaged over the four corners of the assembly to account for asymmetries in the fuel.
- Additionally, when measurements or Monte Carlo simulations are performed, appropriate binning needs to be applied when recording the spectrum.

After summing up these constrains, it is seen that around 10^{11} source particles are needed to tally at least one gamma ray originated from each pin at each interesting gamma energy. In a measurement this may not be a problem, since as an example, in a spent fuel with BU=50 MWd/kgU and CT=15 y, the Eu-154 activity is around 10^9 Bq/cm^3, thus a measurement of few minutes can provide relatively good statistics on the gamma peaks.

3. Applied methodologies

When simulating passive gamma spectroscopy measurements, in fact the full-energy peak efficiency is determined which is the ratio of the number of counts in the full-energy peak at a given energy E, by the number of photons with energy E emitted by the source. The full-energy peak efficiency depends on the geometrical conditions and on the detector characteristics

$$\varepsilon_P(E) = \varepsilon_G(E) \cdot \varepsilon_I(E) \quad (1)$$

where $\varepsilon_P(E)$ is the full-energy peak efficiency, $\varepsilon_G(E)$ is the geometric efficiency related to the setup and $\varepsilon_I(E)$ is the intrinsic efficiency of the detector.

In case an analog Monte Carlo simulation of the gamma transport is done between the fuel assembly and the detector (as shown in Fig. 1), the full-energy peak efficiency is evaluated directly. However, due to the large amount of particle histories needed to simulate the gamma spectrum, using analog Monte Carlo method is clearly not affordable. Current section is dedicated to review two methods which were used to overcome the difficulties when simulating the spectra. One with the application of MCNPX and one with the implementation of a point-kernel model. In both methods the problem is split into two parts: the determination of geometric efficiency and the intrinsic efficiency. Possible fuel defects affect the geometric efficiency; thus its determination is the main task.

For the aim of the current paper, the determination of the source term is not important, the exact details can be found in [2] and are similarly done as in [3]. As a short summary, Serpent2 is used to compute the fuel inventory for various BU, CT and IE values, then the gamma emitting isotopes interesting for our study are extracted with python and the gamma emission spectrum is calculated based on the half-lives of the isotopes and the emission intensities of their gamma peaks (a table of these isotopes and peaks can be found both in [2,3]).

3.1. Old methodology with MCNPX

During the first phase of our research, the gamma transport between the spent fuel source and the detector was solved with MCNPX. The gamma source term, the material composition of the source and the density of the source material were taken from the Serpent2 computations.

As mentioned before, due to the low-efficiency transport geometry of the problem, the application of variance reduction methods is necessary. First, the possibility of truncating the geometry was investigated: it was shown that only a few cm axial part of the assembly contributes to the detector signal. Although, a real measured spectrum is an average taken over the axial length of the assembly, in the current work the material composition was considered uniform over the assembly, therefore the truncation does not bias the results. Also in the horizontal dimensions the geometry was truncated to a reasonable level.

Then, the gamma transport calculation was split into two parts: first, a point-detector (F5 in the MCNP jargon) tally was used to estimate the energy resolved photon flux at the location of the detector, and then a subsequent pulse-height (F8 in the MCNP jargon) tally computation was used to estimate the detector response. The first step is intended to evaluate the geometric efficiency of the system and the second step is intended to evaluate the intrinsic efficiency of the detector, as introduced in Eq. (1). The F5 tally provides a semi-deterministic solution of the transport problem. The history of the gamma ray is tracked with Monte Carlo, however at each interaction of the particle the contribution to a point detector is calculated analytically. In the second step, the source was considered as a surface source placed on the absorber sheets (with an area of the slit facing the detector and with a narrow emission angle) and the energy distribution was defined according to the results of the point-detector calculation. The same Monte Carlo solution for similar a transport problem can be found in [6].

In reality, the fuel assembly is rotated during passive gamma measurements and the recorded spectrum is an average taken over the four corners. Clearly, in order to achieve the same with simulations, one would need four subsequent computations taken over the four corners. Thus, as a further variance reduction, the collimator and the detector parts of the geometry shown in Fig. 1 were repeated (with the LIKE BUT option of MCNPX) in order to place one detector setup facing each corner in the same input. Then the flux measured by the four point detectors were averaged. It was shown, that this results in the same flux as averaging four subsequent runs, while the fuel is rotated. However, since the stochastic part of the computation needs to be carried out only once, 25% of the computing time is saved.

A great advantage of this methodology is the possibility of simulating the whole spectrum including both the peaks and the Compton continuum. An example of the computed passive gamma spectrum is given in Fig. 2.

Nevertheless, the F5 tally has an inherent flaw, which spoils the application of the above detailed methodology. Namely, the choice for the radius of the sphere of exclusion of the detector, which eliminates the $1/R^2$ singularity, is not trivial. For collisions within this sphere, the contributions to the detector become volume averages [7]. As the MCNP manual also highlights, this sphere "must not encompass more than one material" and "it should be about 1/8 to 1/2 mean free path of average energy particles at the sphere and zero in void" [8]. The detector point in this problem is located in air (the room next to the pool), close to strongly scattering media (ie. the collimator and the absorbers). Should air be considered as void and the radius be set to zero, or should the radius be set to 1/8 mean free path, which will necessarily encompass other materials? The problem arises from the fact, that single particle histories, which directly reach the detector region (and as shown in Sec. 2. this happens for few tens of particles out of a billion), contribute to the detector with a large weight resulting in arbitrary peaks with high statistical error in the spectrum. When increasing the radius of the exclusion sphere, these peaks disappear, however the real peaks related to the source energy lines

get smaller as well. Unfortunately, since low statistical errors cannot be achieved with analog simulations, it is impossible to verify whether the point detector results are reliable. The question of how to set the radius of the exclusion sphere is a frequently reoccurring subject in the mcnp-forum, and the users are often cautioned not to rely on point detector tallies for penetration problems [9].

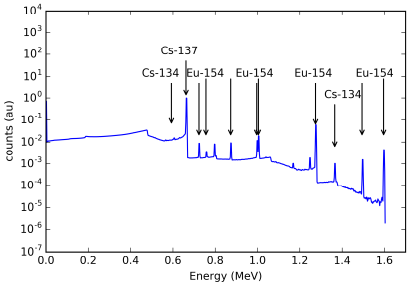

Figure 2: Example of the simulated spectrum for BU=45 MWd/kgU and CT=15y (with some prominent lines highlighted).

3.2. New methodology with point-kernel solution

When we train the MVA models, we want to include only the peak counts as features to represent the spectrum, thus computing the whole spectrum may be unnecessary and inefficient considering the computational time spent on particle histories which contribute only to the Compton background. One would expect that any particle which does not directly travel towards the detector, but scatters during its path will contribute to the background.

This reasoning suggests that computing the uncollided F5 tally (ie. the contribution of photons directly from the source to the detector) is satisfactory in the current problem. MCNPX can print this direct part of the point detector flux separately. However, one could argue that in relatively simple geometries, using MCNPX to compute an uncollided point detector tally is shooting sparrows with a cannon. The MCNPX calculations could be further accelerated by dismissing parts of the physics (without collision events, only the uncollided flux gets simulated). Then the sphere of exclusion does not play a role, since source particles cannot reach the detector region. Nevertheless, that would be an odd way to use a Monte Carlo based tool for deterministic computations.

Therefore, an "uncollided F5 tally" was implemented in python to estimate the geometric efficiency of fuel assemblies in 2D (ie. in collimated cases). The working title of the code is FEIGN (implying that the program pretends to be a transport code, however it is not). The user defines the geometry of the source, which needs to be a rectangular lattice and the positions in the lattice can be filled with coaxial cylinder elements (eg. fuel pins, cladding). The user also defines the material compositions of these cells and the detector points where the efficiency needs to be evaluated.

The program iterates through each source pin, calculates the slope and the intercept of the line drawn between the center of the given pin and the detector, and then iterates through all the positions between the source pin and the detector and determines the distances traveled in various materials by the photon by evaluating the intersections of the lines and the circles (eg. pins and cladding). An example of the working principle is illustrated in Fig. 3 for a simplified, 4x4 fuel assembly, which contains only fuel pins without cladding in water.

When the distances traveled in various materials are calculated, the attenuation law is applied to determine the proportion of photons reaching the detector point from the assembly. The total attenuation coefficients are taken from the XCOM database [10].

The main approximation of the method is that the energy-dependent build-up factor is not calculated. However, as argued above, photons which undergo collisions between the source and the detector are contributing only to the Compton continuum, therefore are not interesting for the calculation of the full peak efficiency.

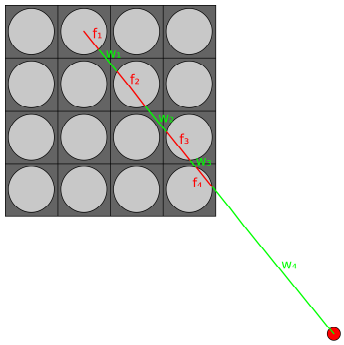

Figure 3: Working principle of FEIGN: example of a 4x4 assembly, where only fuel pins surrounded by water are present. The gamma ray emitted from the pin travels $f_1+f_2+f_3+f_4$ distance in fuel and $w_1+w_2+w_3+w_4$ distance in water before reaching the detector point.

The results of the code were compared with MCNPX results for simple geometries, and good agreement was found even in absolute values. Current paper does not intend to provide a complete time benchmark of the two methodologies, we just highlight that a FEIGN computation for a given assembly configuration takes couple of seconds on an average laptop, whereas MCNPX F5 tally computations take couple of hours on our cluster with 64 computing nodes. The complete details of FEIGN and its verification is planned to be published later.

4. Results

To demonstrate the output of the software, four fuel assembly configurations were chosen to calculate the geometric efficiency for. The selected configurations are shown in Fig. 4 and referred later as "Orig" (an intact, 17x17 fuel), "Exter", "Inter" and "Random" (assemblies with defects, where 80 rods were replaced with steel dummies in the periphery, in the central parts and in random positions, respectively). In all cases, four detector points were placed 55 cm away from the center of the fuel assemblies, facing each corner, and the following results are averages seen by these detector points.

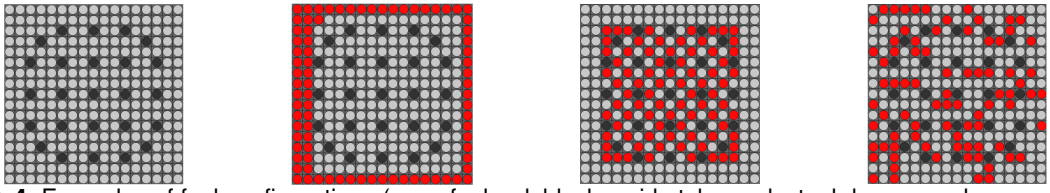

Figure 4: Examples of fuel configurations (grey: fuel rod, black: guide tube, red: steel dummy replacement rod). From left to right: "Orig" - intact fuel, "Exter" - 80 peripheral rods replaced, "Inter" - 80 central rods replaced, "Random" - 80 randomly selected rods replaced.

Fig. 5 shows the calculated geometric efficiency curves for the four configurations. The results show that in case the peripheral parts are removed, much less high energy photons can reach the detector, whereas in case the internal parts are removed, more photons can reach the detector at high energies than in the "Orig" configuration. Although, physically there is no point of normalizing the curve, normalization highlights how replacement of different parts affects the low and the high energy parts differently as shown in the right side of Fig. 5. It can be seen that in the "Exter" case the low energy photons, which tend to contribute to the detector mostly from the peripheral pins, are relatively shielded more than in the other cases.

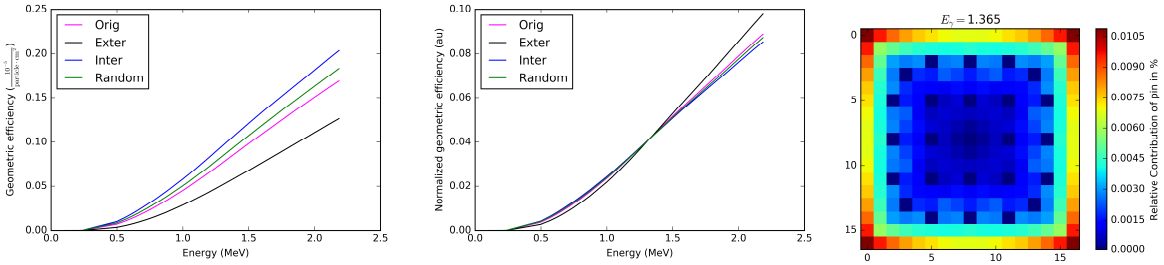

Figure 5: Left: The calculated geometric efficiency curves Middle: Normalized geometric efficiency curves. Right: pin-wise relative contribution to the detector signal

The code also allows for the quick evaluation of the pin-wise detector contributions, which may be useful for tomography studies to calculate pin-wise weights for reconstructing the tomographic images. An example is given in the right side of Fig. 5 for 1.365 MeV photons.

Finally, to create a synthetic dataset of gamma signatures, one needs to multiply the gamma emission spectrum (determined eg. from Serpent2 inventory calculations) with the geometric efficiency calculated by FEIGN, and then with an intrinsic efficiency curve of the detector, which may be determined with measurements, or with a separate Monte Carlo simulation.

5. Conclusions

Current work addressed the methodology of simulating passive gamma spectra of spent fuel recorded with a HPGe detector. The aim is to create a dataset in order to train MVA models which can identify defects in the fuel assemblies. The features in the models are the peaks in the gamma spectrum. First, the main simulational constrains of passive gamma measurement setups are summarized, it is shown that only an extremely small proportion of source photons are hitting the detector because the fuel rods are strong attenuators and a long collimator is placed between the source and the detector. Thus analog Monte Carlo simulations are not affordable.

Two methods were reviewed to create the synthetic data, one is based on the next-event generator or F5 tally of MCNPX and one involves the implementation of a point-kernel method. It is shown, that when the gamma transport is solved with Monte Carlo methods, the full spectrum can be simulated. Nevertheless, it is argued that for the MVA models one is only interested in the peak area, thus simulating the complete spectrum is not necessary and expensive.

Thus, the computer program FEIGN was created, which estimates the energy-dependent geometric efficiency of rectangular fuel assemblies. Some examples of the calculated geometric efficiency are given in this paper. With the aid of the software, the user can quickly transform the gamma emission spectra obtained with a fuel inventory code into passive gamma peaks, which can be then analyzed with MVA.

Although, some comparison between FEIGN and MCNPX has been done, we have not carried out any experimental verification yet. The calculated efficiency curves need to be compared to measured data in the near future.

5. Acknowledgements

The work was funded by the Swedish Radiation Safety Authority (SSM), grant number SSM2015-4125.

6. References

[1] A. Bolind, *Annals of Nuclear Energy,* 66, p31, 2014
[2] Zs. Elter et al.: Partial defect identification in PWR spent fuel using Passive Gamma Spectroscopy, *PHYSOR 2018 conference proceedings, 2018*
[3] C. Hellesen et al., *Annals of Nuclear Energy*, 110, p886, 2017
[4] C. Orton et al., *Nuclear Instruments and Methods in Physics Research Section A*, 629, p209, 2011
[5] S. Vaccaro et al., *Nuclear Instruments and Methods in Physics Research Section A*, 833, p208, 2016
[6] S. Jacobsson Svärd et al., *ESARDA BULLETIN*, n55, p10, 2017
[7] T. Goorley: Using MCNP5 for medical physics applications, LA-UR-05-2755
[8] MCNP6 user's manual version 1.0 edited by D. Pelowitz, 2013
[9] Letter from T. Booth in the mcnp-forum, subject "Improving point detector statistics", 2018. May 8.
[10] XCOM: Photon Cross Section Database, https://physics.nist.gov/PhysRefData/Xcom/html/xcom1.html, accessed: 2018 April.

Solid state Silicon + ^{6}LiF thermal neutron detectors: Geant4 simulations versus real data

Paolo Finocchiaro[1], Sergio Lo Meo[2], Stefano Caruso[3], Luigi Cosentino[1]

[1] INFN Laboratori Nazionali del Sud, Catania, Italy
[2] ENEA, Research Centre "Ezio Clementel", Bologna, Italy
[3] NAGRA, National Cooperative for the Disposal of Radioactive Waste, Wettingen, Switzerland

Abstract:

The lack and the increasing cost of ^{3}He have triggered in the last years a worldwide R&D program seeking new techniques for neutron detection. We have proved that commercial solid state silicon detectors, coupled with neutron converter layers containing ^{6}Li, can represent a viable solution for several applications. In order to better understand the detailed operation, the response and the efficiency of such detectors, a series of dedicated Geant4 simulations was performed and compared with real data collected in different configurations. The results show a remarkable agreement between data and simulations, indicating that the behavior of the detector is fully understood.

Keywords: solid state neutron detectors; simulation

1. Introduction

For many applications a realistic alternative is needed to ^{3}He-based neutron detectors which so far have been the most widely used systems, as they are almost insensitive to radiation other than thermal neutrons. Research and development on alternative thermal neutron detection technologies and methods are nowadays needed as a possible replacement of ^{3}He-based ones [1]. Commercial solid state silicon detectors, coupled with neutron converter layers containing ^{6}Li, have been proved to represent a viable solution for several applications as present in literature [2]-[8]. In order to better understand the detailed operation and the response and efficiency of such detectors, a series of dedicated GEANT4 [9] simulations were performed and compared with real data collected in a few different configurations [10]. The use of a fully depleted silicon detector, in combination with a ^{6}LiF neutron converter film, can be successfully exploited to detect thermal neutrons. The neutron conversion mechanism is based on the reaction

$$^{6}Li + n \rightarrow {}^{3}H\ (2.73\ \ MeV) + \alpha\ (2.05\ \ MeV)$$

which is the only possible decay channel following the neutron capture in ^{6}Li, and is free of gamma rays. The energy spectrum measured by the silicon detector in such a configuration has a characteristic shape, and allows to discriminate the capture reaction products from the low-energy background due to possible noise and gamma rays. Such a neutron detection technique, named SiLiF, was thoroughly studied by means of simulations and its response was compared to experimental data taken with a thermalized AmBe neutron source, with neutron beams, and in a certified thermal neutron field.

2. The detector setup

The considered solid state detectors were 3 cm x 3 cm double side silicon pads, assembled in a few different configurations. The reference configuration consists of a silicon pad coupled with a "*thin*" single layer of ^{6}LiF converter (1.6 μm thickness). Then we considered a silicon pad coupled with a "*thick*" single layer of ^{6}LiF converter (16 μm thickness), or with two "*thick*" layers of ^{6}LiF converter (2 x 16 μm thickness) one on each face of the detector. Finally, a stack of two identical samples of the

latter (2 silicon detectors and 4 x 16μm ^{6}LiF) was also considered. The ^{6}LiF, enriched in ^{6}Li at 95%, was deposited onto a 0.6 mm carbon fiber substrate and placed at 1 mm distance from the silicon surface. We remark that the thermal neutron inelastic and capture cross sections on carbon and fluorine are five orders of magnitude lower than on ^{6}Li. All of these mentioned configurations were reproduced in the simulation code GEANT4 v10.3, and Monte Carlo simulations were performed in two thermal neutrons irradiation schemes: *flood* i.e. with a uniform thermal neutron beam perpendicular to the detector face, and *isotropic*, i.e. with a uniform thermal neutron flux emitted from a spherical shell surrounding the detector. The corresponding experimental spectra were measured with an AmBe neutron source inside a big moderator (≈ 1 m^3 volume) thus mimicking the isotropic irradiation, and with a neutron beam at the INES [11] facility at Rutherford Appleton Laboratory, Didcot, UK, mimicking the flood irradiation. In addition spectra were also measured in a certified thermal neutron field ([12], [13]) at Physikalisch-Technische Bundesanstalt, Braunschweig, Germany.

3. The ^{6}LiF converter thickness

As mentioned above two thicknesses were considered, namely 1.6 μm ("*thin*") and 16 μm ("*thick*"). The *thin* layer was chosen as a reference, as the corresponding spectrum has a very characteristic shape which allows an easy identification of the triton and alpha structures with their endpoints, as shown in Fig. 1 left where we reported the simulation of the separate contributions and the total one in *flood* irradiation mode. In Fig. 1 right we compared an experimental spectrum measured with an AmBe source with two simulations respectively in *flood* and *isotropic* mode. The two simulations were normalized to the same number of neutrons impinging on the converter, the measured spectrum was normalized to the simulated ones in order to have the same number of counts in the triton peak. The agreement between the three spectra is remarkable, apart from the low energy region (up to ≈ 1.5 MeV) where the real data have a strong contribution from the high enery gamma rays produced by the AmBe source. The fraction of tritons below the alpha endpoint is only 3.1%, therefore a detector in this configuration could be reasonably used as a reference for the efficiency calibration of other detectors, using the triton peak area as a benchmark.

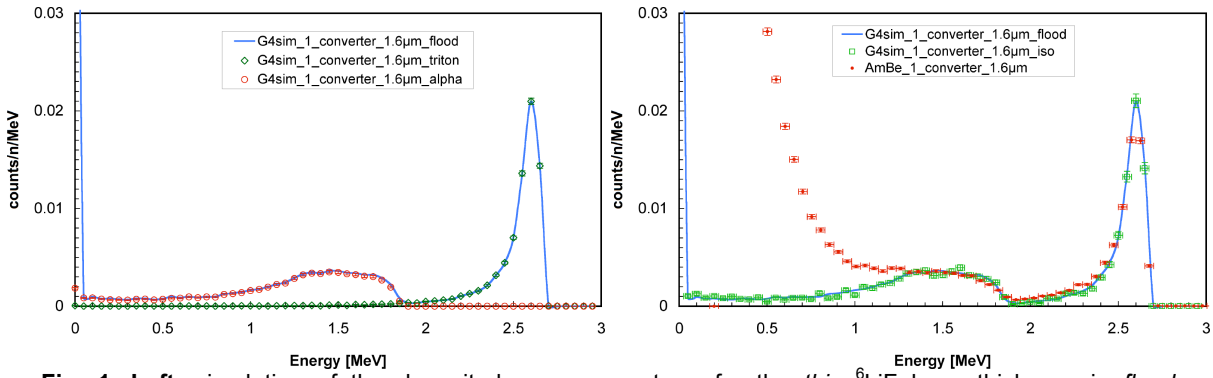

Fig. 1. Left: simulation of the deposited energy spectrum for the *thin* ^{6}LiF layer thickness in *flood* irradiation mode. The separate contributions from tritons and alphas are shown. **Right**: same spectrum for the *flood* and *isotropic* simulations, compared with an experimental result obtained with a thermalized AmBe neutron source.

The *thick* layer was chosen as 16 μm after simulating several different thickness values ranging from 8 to 16 μm. In Fig. 2 left we show the corresponding deposited energy spectra, where the 16 μm layer allows an easy identification of the alpha endpoint, quite useful for the energy calibration along with the triton endpoint. Moreover, the alpha range in ^{6}LiF is about 32 μm in straight line, therefore 16 μm sounded a reasonable half-range thickness value. On top of this, in Fig. 2 right we reported the simulated detection efficiency as a function of the converter thickness, that starts to saturate around 15-16 μm. As we will show in the following, the suggested gamma/n discrimination threshold is around 1.5 MeV, and the spectrum shape at 16 μm thickness is rather flat down to such a threshold value. Last but not least, LiF layers thicker than 16 μm tend to be rather delicate and are more easily detached from the carbon fiber substrate.
From the simulation we calculated the distribution of the z-direction cosine for tritons and alphas, in the *thin* and *thick* converter cases. The resulting plots (Fig. 3 left and right respectively) provide a clear

explanation of the different angular acceptance for tritons and alphas, obviously worse in the *thick* case. This is another reason for not using still thicker converters.

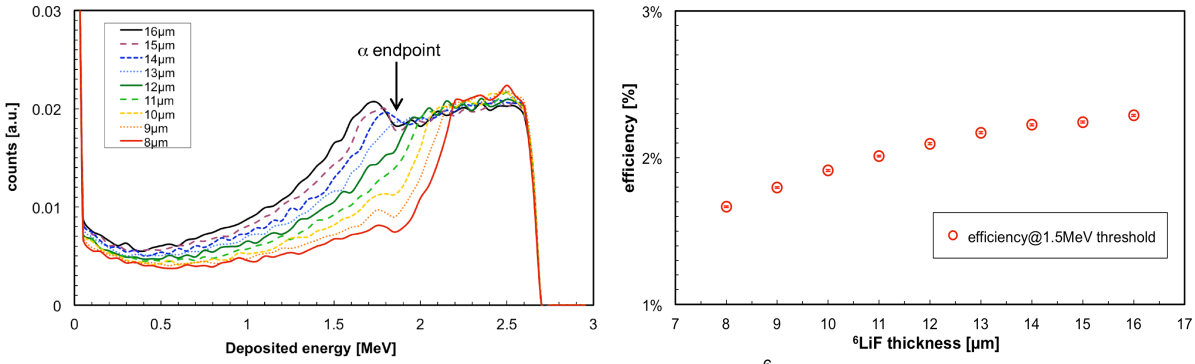

Fig. 2. Left: simulation of the deposited energy spectrum for several ^{6}LiF layer thickness values. The alpha endpoint for the 16 μm *thick* layer is shown. **Right**: the simulated detection efficiency, with a 1.5 MeV threshold, as a function of the converter thickness.

From the simulation we calculated the distribution of the z-direction cosine for tritons and alphas, in the *thin* and *thick* converter cases. The resulting plots (Fig. 3) provide a clear explanation of the different angular acceptance for tritons and alphas, obviously worse in the *thick* case. This is another reason for not using still thicker converters.

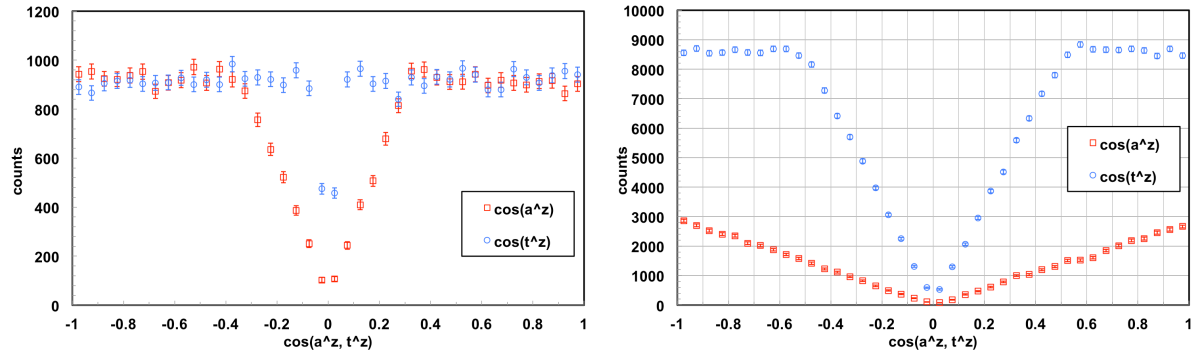

Fig. 3. Left: distribution of the z-direction cosines for alphas and tritons exiting the *thin* converter. The heavier (and less energetic) alpha particles are constrained in a smaller forward angular region than tritons. Alphas start to be suppressed above ≈ 70° [cos(a^z) ≈ 0.35], tritons above ≈ 86° [cos(t^z) ≈ 0.075]. **Right**: the same for the *thick* converter. The alpha particles are strongly suppressed, tritons start to be suppressed above ≈ 60° [cos(t^z) ≈ ±0.5)].

4. The sandwich SiLiF detector

The sandwich configuration examined in this case has a 16 μm thick converter on each face of the silicon detector. In the flood irradiation scheme simulation the back face reported ≈ 8% less counts, as expected due to the neutron beam attenuation while crossing the first converter (the attenuation in the silicon detector is much lower, as the reaction cross section for thermal neutrons in silicon is several orders of magnitude smaller than in ^{6}Li; the same applies to carbon and fluorine).

Fig. 4 shows the simulated energy spectrum on the silicon detector for the flood and isotropic irradiation schemes in the sandwich configuration, compared with two experimental results obtained respectively with a thermalized AmBe neutron source and with a thermal neutron beam at the INES facility. The energy calibration of the experimental spectra was done using the alpha and the triton endpoints. The gamma ray contribution with the AmBe source is much higher and extends to higher energy than with the neutron beam data, as expected. The experimental spectra were normalized to the simulated ones at the alpha endpoint value. We also simulated and measured a double-sandwich stack, basically obtaining the same spectra (not shown) and a correspondingly increased detection efficiency.

Measurements were also done at PTB in a certified thermal neutron field with Maxwellian distribution, where 98.4 % of neutrons have energies below the cadmium cut-off energy and the thermal neutron

flux at the reference position is 68.3±1.9 neutrons/cm^2/s with a uniform field size of at least 10 x 10 cm^2. Spectra were taken with and without a cadmium plate shield, and the flat ratio above 1.5 MeV, shown in Fig. 5, further justifies its choice as safe threshold value for the gamma/n discrimination. A *thin* (SiLiF1.6) and a a double-sandwich stacked *thick* (SiLiF64) detectors were tested in the certified field, and their measured and simulated detection efficiency values are listed in Table 1. The statistical uncertainty was negligible, therefore only the systematic one is given which derives from the uncertainty in the energy calibration.

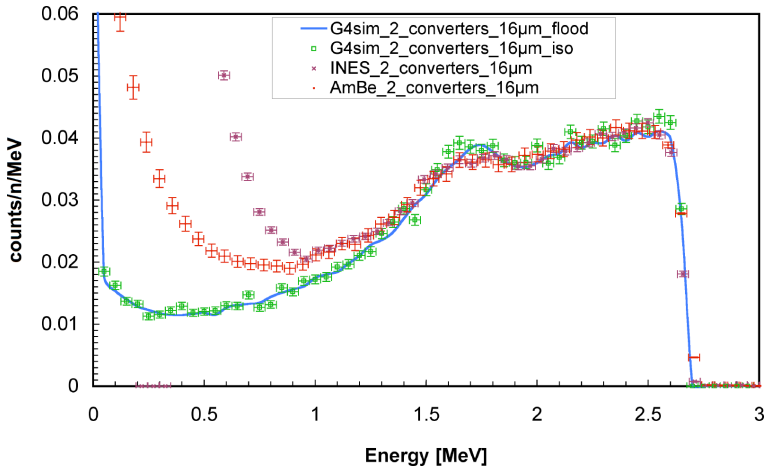

Fig. 4: The energy spectrum on the silicon detector for the flood and isotropic simulations in the sandwich configuration compared with two experimental results obtained respectively with a thermalized AmBe neutron source and with a thermal neutron beam at the INES facility.

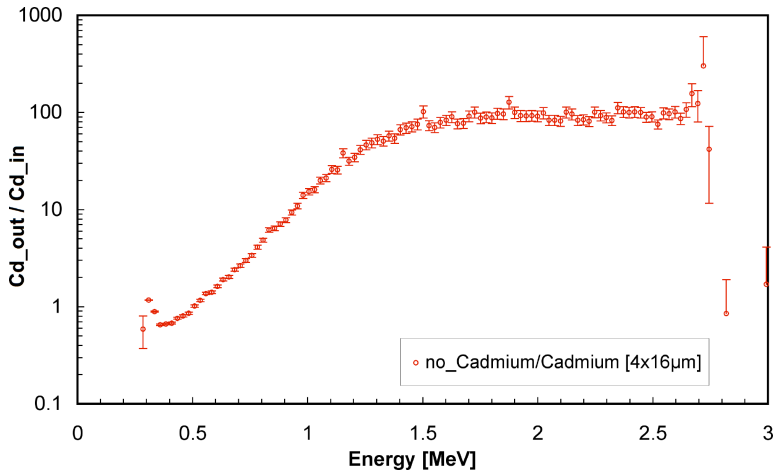

Fig. 5: Ratio between the spectra with and without a cadmium plate, that justifies the choice of 1.5 MeV as gamma/n discrimination threshold.

detector	simulated efficiency	measured efficiency
SiLiF1.6 thin 1.6 µm	0.48 %	0.50 ± 0.02 (syst) %
SiLiF64 double sandwich 16 µm	8.25 %	7.95 ± 0.35 (syst) %

Table 1: Simulated and measured detection efficiency

5. Gamma/neutron discrimination

Several simulations were performed with impinging monoenergetic gamma rays, obtaining the deposited energy spectra on the silicon detector which allowed to calculate the gamma sensitivity of

the detector as a function of the detection threshold (i.e. detection probability per incident gamma). As the minimum threshold investigated was 1 MeV, the sensitivity for gamma rays of 0.5 and 1.0 MeV resulted < 10^{-6} (that is, no counts in the 10^6 events simulated). This simulation allowed to calculate the gamma/neutron contamination probability for equal fluxes (i.e. the ratio of the gamma sensitivity to the neutron efficiency) as a function of the detection threshold for several gamma ray energies, which is shown in Fig. 6.

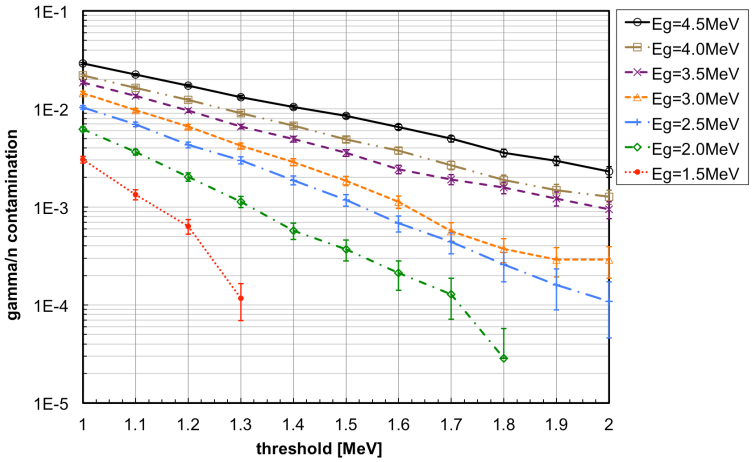

Fig. 6: The gamma/neutron contamination probability for several gamma ray energies and thermal neutrons (i.e. the ratio of the gamma sensitivity to the neutron efficiency) as a function of the detection threshold.

We also evaluated the background contribution due to secondary particles, mainly produced in the converter, in the carbon fiber substrate and in the detector itself. Table 2 lists the number of electrons, gamma rays and protons+ions, excluding alphas and tritons, hitting the silicon detector per incident neutron. The probability that they have energy E >1.5 MeV is quite small and this, combined with the tiny probabilty to release all of their energy in the silicon, results in a contamination probability ≈ 10^{-7}.

e-		gamma		protons+ions	
all	E > 1.5MeV	all	E > 1.5MeV	all	E > 1.5MeV
$8.4 \cdot 10^{-4}$	$1.1 \cdot 10^{-5}$	$1.2 \cdot 10^{-3}$	$1.0 \cdot 10^{-3}$	$7 \cdot 10^{-6}$	0

Table 2: Number of secondary particles hitting the silicon per incident neutron (excluding alphas and tritons)

The double sandwich detector was then tested, inside a polyethylene box moderator, with a weak AmBe neutron source (≈ 8.7 n/s on the detector). Immediately afterwards it was tested with a ^{22}Na source (total of $4 \cdot 10^5$ gamma/s on the detector, ≈ $1.33 \cdot 10^5$ of 1.27 MeV and ≈ $2.66 \cdot 10^5$ of 0.51MeV). The corresponding spectra, rescaled to one neutron and one gamma impinging on the detector, are shown in Fig. 7. The ratio between the integrals above 1.5 MeV provides a gamma/n value discrimination ≈ 10^{-7}.

6. Conclusion

The SiLiF detection technique is now rather consolidated, it proved to be straightforward and consistent with the result of GEANT4 simulations, and the gamma/n discrimination looks quite satisfactory. In order to investigate the possibility of using these detectors for nuclear material monitoring, in particular for spent nuclear fuel surveillance during storage and/or transport, Monte Carlo simulations based on a simplified spent fuel cask setup are currently being performed. The simulation results will be compared with real data from an experimental campaign to be held in 2018 in a real spent fuel storage site, where we plan to test and further characterize a few detector samples by placing them around spent fuel casks.

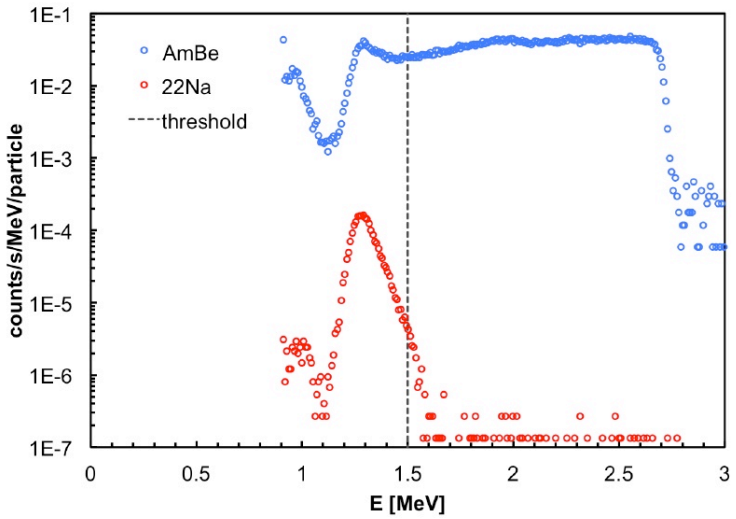

Fig. 7: Deposited energy spectra for neutrons and gamma rays normalized to unit flux.

7. Acknowledgements

We thank C. Marchetta and A. Massara for their constant assistance in the preparation of the ^{6}LiF converters. We are grateful to R. Nolte and D. Radeck for the opportunity to test the detectors at PTB, and to A. Pappalardo and C. Vasi for the test at INES. Last but not least, we are indebted with M. Ripani who is constantly supporting this work within the framework of the INFN-E strategic project.

8. References

[1] D.Henzlova et al., “Current Status of 3He Alternative Technologies for Nuclear Safeguards”, NNSA USDOE and EURATOM, LA-UR-15-21201.

[2] P. Finocchiaro, Nucl. Phys. News v.24, n.3, (2014) 34

[3] P.Finocchiaro, in *Radioactive Waste: Sources, Types and Management*, Nova Science Publishers, (2011)

[4] A. Pappalardo, M. Barbagallo, L. Cosentino, C. Marchetta, A. Musumarra, C. Scirè, S. Scirè, G. Vecchio, P. Finocchiaro, Nucl. Instrum. Methods Phys. Res. A810 (2016) 6.

[5] D. S. McGregor, M. D. Hammig, Y. H. Yang, H. K. Gersch, and R. T. Klann, Nucl. Instrum. Methods Phys. Res. A500 (2003) 272.

[6] M. Barbagallo, L. Cosentino, V. Forcina, C. Marchetta, A. Pappalardo, P. Peerani, C. Scirè, S. Scirè, M. Schillaci, S. Vaccaro, G. Vecchio, P. Finocchiaro, Rev. Sci. Instrum. 84, (2013) 033503.

[7] L.Cosentino, A. Musumarra, M. Barbagallo, N. Colonna, L. Damone, A. Pappalardo, M. Piscopo, P. Finocchiaro, Rev. Sci. Instrum. 86 (2015) 073509.

[8] A.Pappalardo, C. Vasi, P. Finocchiaro, Results in Physics 6 (2016) 12.

[9] S.Agostinelli et al., Nucl. Instrum. Methods Phys. Res. A506 (2003) 250.

[10] S. Lo Meo, L. Cosentino, A. Mazzone, P. Bartolomei, P. Finocchiaro, Nucl. Instr. Meth. A866 (2017) 48.

[11] S. Imberti et al., Meas. Sci. Technol. 19 (2008) 034003.

[12] M. Luszik-Bhadra, M. Reginatto, H.Wershofen, B.Wiegel, and A. Zimbal, Radiation Protection Dosimetry (2014), Vol. 161, No. 1–4, pp. 352–356.

[13] P. Finocchiaro et al., Nucl. Instrum. Methods Phys. Res. A 885 (2018) 86.

A Semi-empirical Approach to Validating Results from a Fast-neutron Coincidence Collar

Jonathan Beaumont[1], Mikhail Milovidov[2], Mikhail Mayorov[1]

1 International Atomic Energy Agency, Vienna International Centre,
PO Box 100, 1400 Vienna, Austria

2 Scientific Engineering Center Nuclear Physics Research,
2nd Murinsky Ave 28, Saint Petersburg, Russia

E-mail: j.beaumont@iaea.org

Abstract:

The IAEA has developed the fast neutron coincidence collar (FNCL), for the verification of non-irradiated low-enrichment uranium fuel assemblies using fast-neutron coincidence counting. The instrument uses liquid scintillation detectors to detect fast neutrons without the need for neutron moderation, allowing the coincidence gate to be reduced by three orders of magnitude. This results in large reductions in acquisition time for fast-mode measurements and minimal dependence on burnable neutron poisons. Speed, precision and accuracy of verification measurements are subsequently improved. A major drawback of liquid scintillators is that they have high sensitivity to gamma rays, and therefore require many layers of electronic processing to filter events. Computer modelling of FNCL is therefore beyond the scope of Monte Carlo simulation packages, such as MCNP, alone and other steps must be taken to validate coincidence measurements.
Experimental data collected by the FNCL also has its limitations. When measuring any neutron source it is not possible to measure neutrons in isolation; the data will be contaminated with gamma-ray detections, and pile-up events of both radiation types and combinations. Similarly, gamma-ray data will always have some contributions from neutron events. The data is also influenced by other factors such as drift and noise. It is therefore difficult to measure the response of the system to neutrons in isolation from the effects of misclassified gamma rays and other mentioned effects.
To bridge this gap, sample stream generator software (SSG) was developed to emulate binary data recorded by the FNCL system. The data stream is semi-empirical in nature, requiring inputs from experimental data, MCNP data and user defined parameters. These data were then injected into the FNCL digital processing to characterise the filters, verify their functionality and used to determine the system performance under ideal conditions. A full description of this software and the performance testing is provided.

Keywords: Monte Carlo; Modelling; Liquid scintillators; Neutron coincidence counting;

1. Introduction

List mode is now commonly used in nuclear material assay with neutron detection; by associating each detected neutron event with a time stamp, additional analysis and re-analysis of data can be performed. The approach implemented for processing and analysis of the FNCL data is an enhancement of this method; for each event, in addition to a time stamp, the FNCL data acquisition system (DAQ) records a detector identifier (FNCL is a multi-detector system) and the entire digital waveform of the analogue pulse on the photomultiplier tube (PMT) anode. The motivation for this was twofold. First, to improve reliability of operations by having the ability to perform the off-line analysis of data with corrected processing parameters. In case of any technical issues, the ability to re-inject the raw data upon correcting the issue reduces the risk of not being able to deliver verification result. The second reason is convenience and the higher degree of flexibility to develop, test and implement the

software algorithms for raw data processing, required by the application of FNCL for fresh material verification, later described in the details.

In this approach, once the electric pulses appear on the PMT anode, they get immediately digitized and time stamped. Any further processing and analysis is based on handling an “electronic” image of the electric waveform, e.g. with a binary record. This opens an interesting and attractive possibility to create a “synthetic” artificial stream of events and to inject it into the FNCL processing and analysis module for testing its performance. Similar technology has been used for testing of the radionuclide identification algorithms [1].

The benefits of such an approach are clear: one can create the stream of events comprising only neutrons, which is impossible in reality, to test and optimize the performance of the pulse-shape discrimination algorithm. One can inject a stream of pile-up events that correspond to gamma-gamma, neutron-gamma, gamma-neutron and neutron-neutron pile-ups under the fully controlled scenario(s) to develop the pile-up rejection algorithm.

Also, since the FNCL detectors are sensitive to gamma rays, which make up the majority of the data, it is important to study its effect to understand and minimize any perturbations to the calibration of the instrument. However, the reasonable question is to what extent the synthetic data are comparable to the real one? The paper below describes aspects of this technology and compares the synthetic and measured results.

2. Description of FNCL

2.1. Hardware and software

The FNCL comprises three detector panels. Each panel contains four EJ-309 liquid scintillation detectors (each with 0.5L of scintillator) coupled with ET9821B PMTs provided by Scionix, Netherlands. The detectors are coupled to a data acquisition unit (DAQ) containing a PC, high voltage supplies and 500 MHz, 14-bit digitizers to record detector pulses. The FNCL records all data during verification measurements. Each detection comprises the detector address, time stamp and full waveform at the specified resolution. The data is stored in binary format on a PC hard drive and can be re-interrogated at a later date if required. The instrument has custom software for operation and for the filtering of neutron coincidence events. Energy filtering is performed according to the energy in keVee (keV electron equivalent energy). The FNCL is provided by CAEN S.p.A, Italy. Further detail on FNCL hardware is provided in [2, 3].

2.2. FNCL data and analysis algorithms

Radiation events detected by FNCL detectors are recorded in real-time using integrated digitizers in the FNCL DAQ. During acquisition, data is written to a binary file containing for each event 1) the time stamp accurate to 2 ns 2) the detector number or address 3) the waveform sampled over 256 ns in 128 samples at 14-bit resolution. Events are recorded at a rate of typically 300-500 kHz during fuel measurement providing a substantial data stream which is recorded and digitally analysed on-the-fly by DAQ software.

Data is filtered using a sequence of digital filters optimised for speed when processing data. Further detail on FNCL software and filters is provided in [2, 3]. The filters are listed here in sequential order:

1. Pulse amplitude – this is the only filter present in the hardware, a threshold is set (typically 30 keVee) determined by pulse amplitude above which the digitizer will record and store the pulse and other information. The objective of this filter is to eliminate noise.
2. Coincidence – removes any events which are not coincident within the coincidence gate (typically 70 ns). The objective of this filter is to reduce data volume early in the process by eliminating non-coincident events.
3. Anti-cross-talk – removes any events which are likely to have been caused by a single radiation particle traveling from one detector to a neighbouring detector i.e., removes any events where adjacent detectors see coincidence within a short time gate (typically 14 ns). The objective of this filter is to remove false positives on coincident events.

4. Pulse integral – removes any events which have a light output below a threshold (typically 72 keVee) determined by baseline-subtracted pulse integral. The objective of this filter is to remove pulses at low energy where gamma-ray and neutron pulses are difficult to distinguish.
5. Pulse shape discrimination (PSD) – removes any events which have a PSD value in the gamma-ray region. The objective of this filter is to remove gamma-ray events.
6. Pile-up rejection – removes any pulses judged to be the result of two or more pulses overlapping using a peak search algorithm. The objective of this filter is to remove gamma-gamma pile-up which could be misinterpreted as neutron events.

The above filters can be modelled and applied to Monte Carlo data to some degree however stages 4, 5 and 6 require accurate modelling of the pulse shapes.

3. Description of sample stream generator (SSG)

The objective of SSG is to provide accurate modelling of neutron and gamma ray pulse shapes and data in the FNCL binary file format to facilitate testing and validation of the instrument and measurements.

3.1. Mathematical principles

The light output in the liquid scintillator EJ-309 [4] for the same detector type has been investigated and modelled [5]. The equations below describe the light output functions produced by detection of gamma rays (via electrons) and neutrons (via protons).

The light output for Compton electrons L_e as a function of electron energy is determined to be linearly proportional to a constant a and the electron energy E_e

$$L_e(E_e) = a \cdot E_e$$ a=2.6 photons/keV(e^-)

The light output for recoil protons L_p is more complex with a dependence on the proton energy E_p and several constants a (as above), b_0, b_1, and b_2.

$$L_p(E_p) = a \cdot \left(b_0 \cdot E_p + \frac{b_1 \cdot E_p}{1 + b_2 \cdot E_p} \cdot E_p \right)$$

$$b_0 = 0.082 \quad b_1 = 1.36 \times 10^{-4} \quad b_2 = 1.8 \times 10^{-4}$$

The number of electrons $\theta_{e,p}$ on the photocathode is then modelled. QE is the quantum efficiency of the photocathode with a value of around 30%.

$$\theta_{p,e}(E_{p,e}) = QE \cdot L_{p,e}$$

The light collection efficiency was estimated as 90% and the photocathode-dynode coupling was estimated as 75%.

The light resolution functions also documented in [5] were also applied.

3.2. Input parameters

Due to the semi-empirical nature of SSG, some inputs are required from real data and simulated data.

3.2.1. Neutron and gamma-ray waveforms

The neutron and gamma-ray waveforms are the fundamental constituents of the SSG. These were obtained experimentally from measurement of a Cs-137 source (3.39 MBq on date of measurement) and a Cf-252 source (222 kBq on date of measurement). The FNCL was calibrated using the 662 keV line in Cs-137 (observed as a Compton edge at 478 keVee) providing a linear energy calibration. Data was recorded with each source placed in the FNCL cavity.

A subsample of gamma rays was obtained by selecting gamma rays in the 200-300 keVee region. This region was chosen due to the fact that pulses have low statistical noise and this region also allows good PSD. A subsample of neutrons was obtained by applying the coincidence and PSD filters and selecting from the same 200-300 keVee region.

Each subsample was then reduced using a χ^2 test to eliminate any pile-up or unusually shaped events to find several thousand pulses. These pulses were then normalized and averaged to find typical pulse shapes for gamma and neutrons shown in Figure 1. The longer tail of the neutron pulse due to the delayed fluorescence component is apparent.

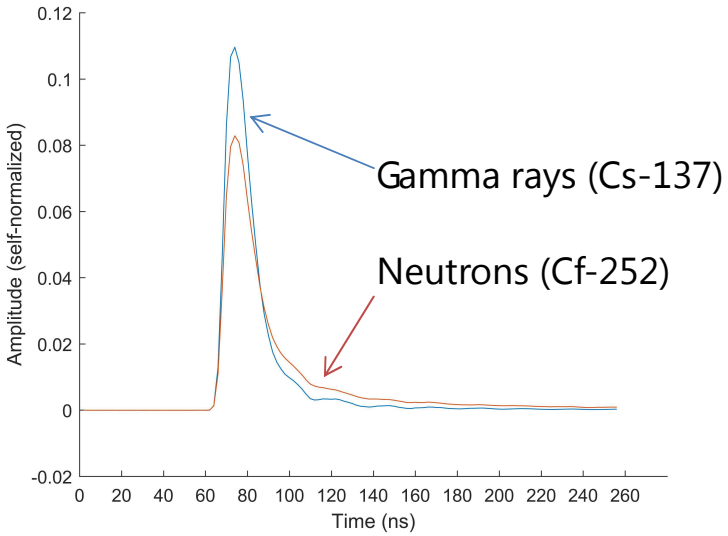

Figure 1. Waveform of neutron and gamma rays captured by the FNCL.

3.2.2. Energy spectra

The FNCL was calibrated in energy using baseline-subtracted pulse integrals, normalized to the Compton edge of Cs-137. Energy spectra were collected in the same way for ambient background, Cs-137 and Cf-252 using the aforementioned sources. The spectra were collected with no filters applied and with the pulse amplitude filter set very low to include low energy events (around 10 keVee). The objective was to include these smaller pulses in pile-up events at later stages. The energy spectra are shown in Figure 2.

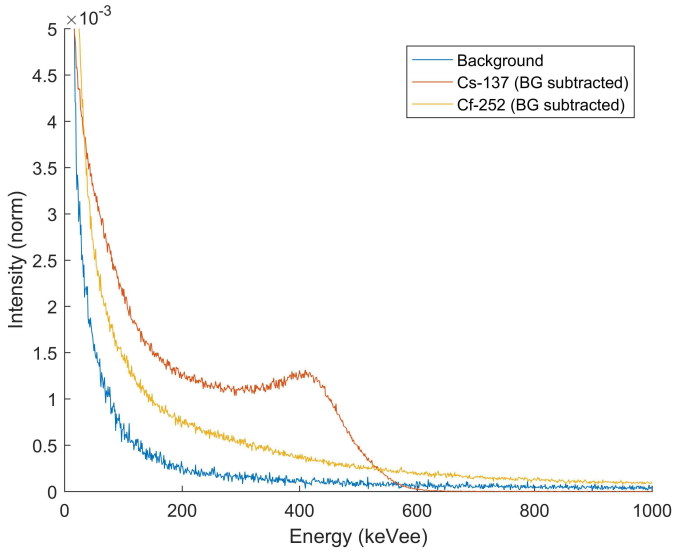

Figure 2. Pulse-integral spectra of background, Cs-137 and Cf-252.

3.3. Light pulse generation

3.3.1. Statistically generated events – spectrum seeded

Uncorrelated events such as background or passive gamma from an FFA also contribute to the experimental data pulses and will influence the data with occasional pile-ups or misclassifications. Therefore it is important to account for these events. Due to the high rate, modelling in MCNPX-Polimi the passive gamma from FFA measurements produces around 200 GB data output files and takes considerable computer time to produce and process. To account for these in a more practical approach, the pulse-integral spectra of the events was recorded, along with the detection rate, and used to seed light pulses. These could then be combined with Monte Carlo fission data before the generation of output pulses to allow the most realistic simulation of the synthetic data.

The time stamps of such events were modelled using a statistical approach with the spacing between the events Δt calculated using the detection rate on a single detector R and a random number ζ.

$$\Delta t = -ln(\zeta)R^{-1}$$

The light pulse energy was then sampled from the appropriate pulse-integral spectrum, and the process was repeated for all detectors to provide a list containing the pulse type (gamma ray or neutron), time stamp (ns), light pulse energy, and a marker identifying the event as generated from this method (spectrum seeded). This data is referred to as the light output sequence.

3.3.2. Monte Carlo generated events – MCNPX-Polimi seeded

The FNCL instrument has been modelled and benchmarked using MCNPX-Polimi and SimPLiS [6-8]. In this work the software filters were modelled within the analysis code and were applied to determine the singles and doubles rates, the FNCL data was not fully generated.

The output from Polimi was converted into light pulses using the described mathematical principles in section 2.1. The light pulses were then compiled in the light output sequence. This comprised the pulse type (gamma ray or neutron), time stamp (ns), light pulse energy, and a marker to identify the event as generated from this method (MCNPX-Polimi seeded).

3.3.3. Custom specified events

Custom events such as singles, doubles, triples, quads, neutron-gamma pile-up with specified pile-up distributions, and combinations of these can be specified in the light pulse stream to generate data for testing purposes. The light pulses were then compiled in the light output sequence. This comprised the pulse type (gamma ray or neutron) time stamp (ns), light pulse energy, and a marker identifying the event as generated from this method (custom seeded).

3.4. FNCL data generation

The light output sequence was compiled (from any combinations of the methods described in section 2.3) for each detector and was sorted into chronological order. A trigger level was specified, emulating the pulse amplitude filter in the FNCL hardware. When passing through the light output sequence, any pulse found above this level triggered a 256 ns recording of this pulse and any surrounding pulses in direct emulation of the FNCL digitizers. The digitizer trigger pre-delay of 36 ns and dead-time between recordings of 22 ns was also applied.

Each pulse was then generated using the appropriate neutron or gamma-ray waveforms (shown in Figure 1) with baseline noise and statistical noise applied. The resulting FNCL data waveforms and construction process are illustrated in Figure 3.

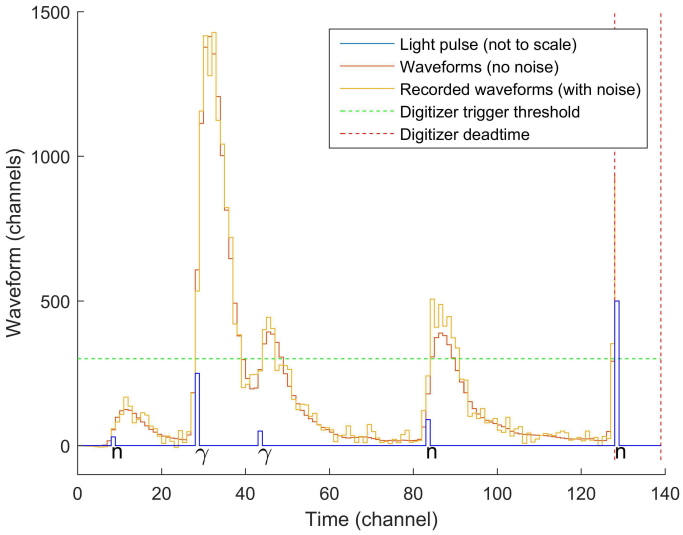

Figure 3. A synthetic FNCL digitized waveform comprising pile-up of three neutron and two gamma-ray events. The digitization is triggered by the first gamma ray which passes over the digitizer trigger threshold initiating the recording of the detector output over a 256 ns (128 channel) period. The first neutron is also recorded despite not triggering the digitization, similarly the neutron pulse in channel 129 is not fully recorded but contributes to the waveform as per the real data acquisition method.

4. Validation of SSG with gamma-ray and neutron sources

4.1. Validation of Cs-137 data

The gamma-ray generation was validated using the mentioned Cs-137 source on a single detector. A recording of 300 MB of data from FNCL detectors, with no filters applied, was used for comparison. The equivalent data was generated using the MCNPX-Polimi seeded and spectrum seeded approaches. The data were then analysed to find the pulse-integral distributions and PSD distributions shown in Figure 4 and demonstrate a good match.

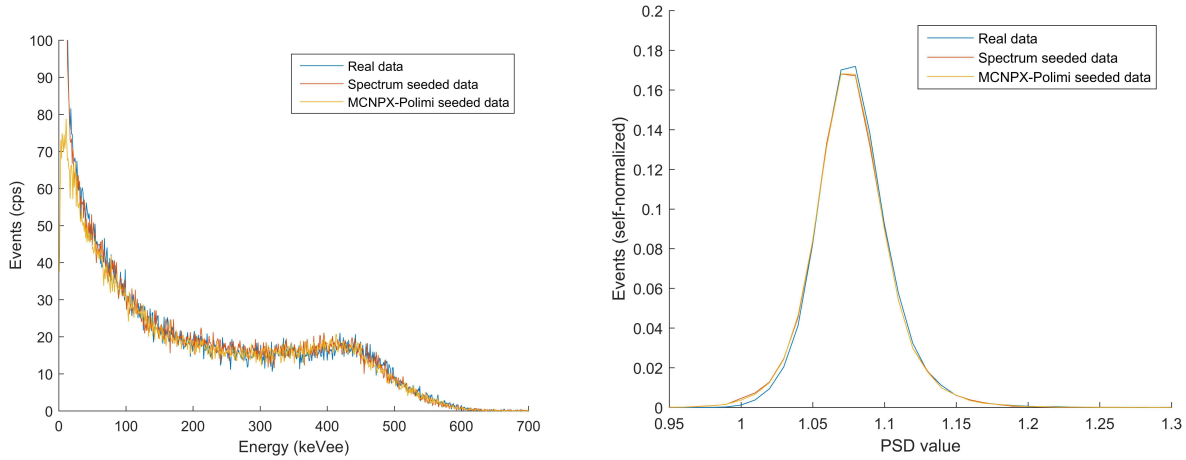

Figure 4. Real and synthesised Cs-137 data analysed to find the pulse-integral spectra (left) and PSD distributions above 72 keVee (right).

4.2. Validation of Cf-252 data

A recording of 2 GB (around 5 minutes of data) from a Cf-252 source was synthesised and used to validate neutron and gamma-ray data in combination. MCNPX-polimi seeded data was used to model

all fission events released from the source. Given the age of the source (around 10 years) the source was modelled using SCALE to provide an estimate of the transuranic material composition other than Cf-252 (mainly Cf-250). This was also included as a separate MCNPX-polimi seeded simulation data. Additional gamma rays from fission products in the source were seeded from the pulse-integral spectrum of Cf-252 shown in Figure 2. Example neutron and gamma-ray pulses are shown in Figure 5 comparing synthetic and real data.

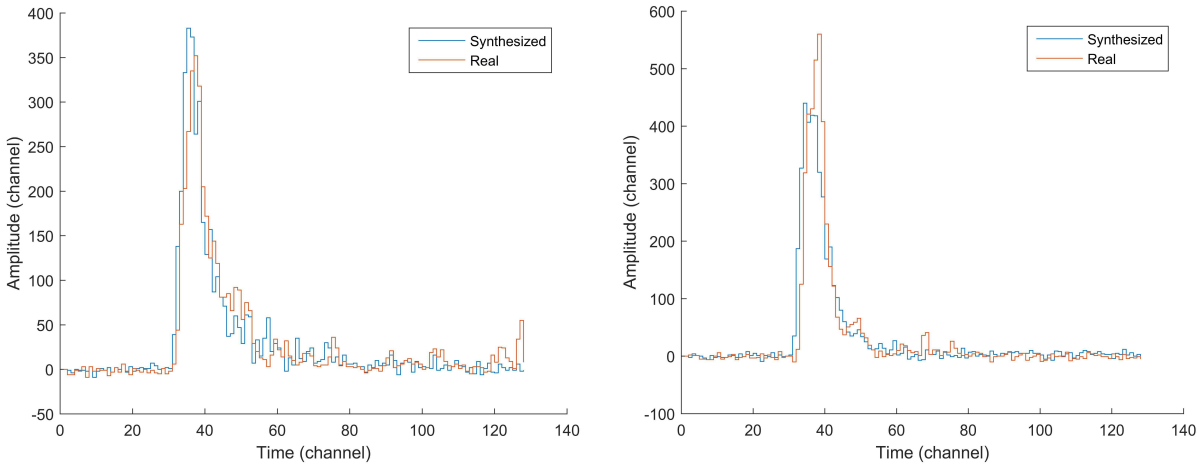

Figure 5. Comparison of real and synthetic data pulses for neutrons (left) and gamma rays (right) at 72 keVee

The most critical region of the data is the 72 to 200 keVee region where neutrons and gamma rays have the largest overlap and therefore the chance of misclassification is highest. The PSD distributions from three segments in this region were compared for simulated and real data and are illustrated in Figure 6. A good agreement is seen.

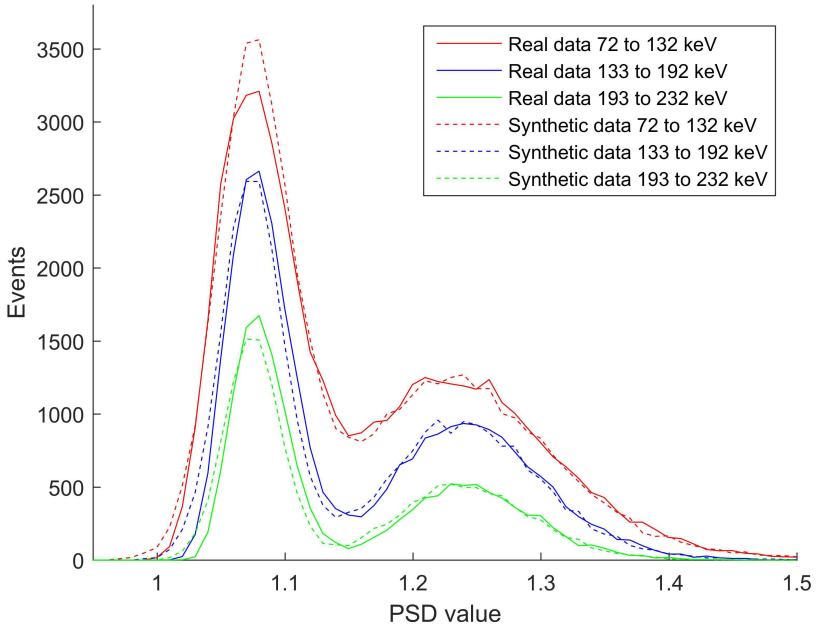

Figure 6. Real and synthesised Cf-252 data analysed to find the PSD distributions in segments above 72 keVee.

The full PSD plots of the real and synthetic data are shown in Figure 7 illustrating good agreement between the distributions, particularly in the low energy region where PSD distributions overlap. A summary of the two data sets, analysed with relevant methods, are shown in Table 1.

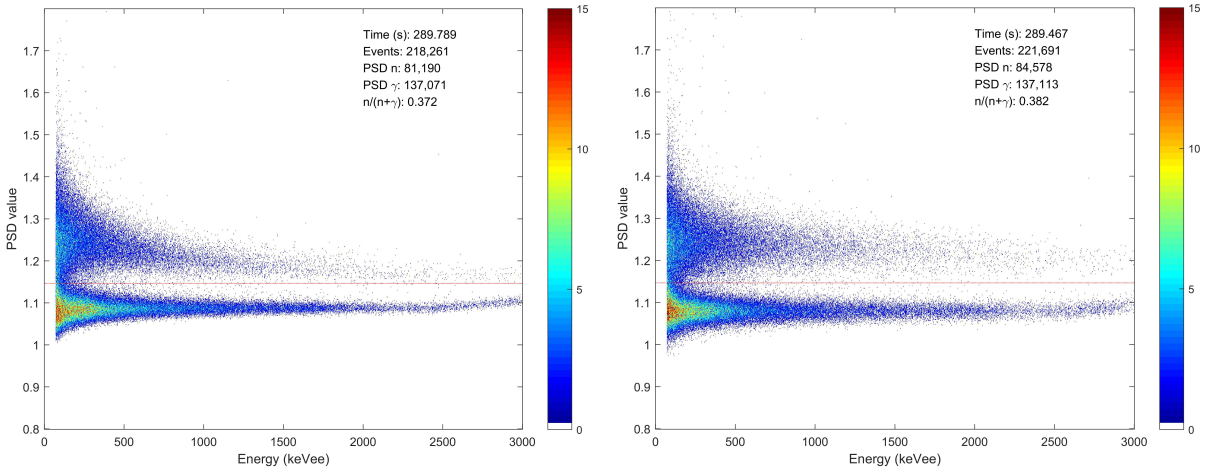

Figure 7. PSD plots of real (left) and synthetic (right) Cf-252 data on a single detector.

Table 1. Comparison of real and synthetic data of a Cf-252 source measured by the FNCL

Parameter	Real data	Synthetic data
Measurement time (s)	289.8	289.5
Events	219,204	221,691
Neutron events	81,190	84,578
Gamma-ray events	137,071	137,113
n/(n+γ)	0.372	0.382

5. Conclusions

The close matching of synthetic data with real data as presented demonstrates that digitized neutron and gamma-ray detections from EJ-309 detectors can be accurately modelled using the methods described. Synthetic data can therefore be manufactured for the FNCL instrument (or any other liquid scintillator system) and can be applied to probe the system for optimization or investigative purposes. The user has the ability to study the system under idealised or realistic conditions using inputs from simulations, recorded spectra, or user defined events. This allows realistic synthesis of measurement data under chosen conditions (backgrounds, passive gamma-ray fields, neutron fields etc.). The accurate emulation of the waveforms provides a useful tool for assessing pulse-shape discrimination and pile-up rejection filters, which are critical to the FNCL performance.

Given the high gamma-ray sensitivity of the instrument it is important to understand and quantify perturbations from gamma-ray events. For example, this software was used to optimize the pile-up rejection filter: to maximise neutron sensitivity whilst maintaining a low systematic uncertainty due to misclassified gamma-ray pile-up events. This ensures high accuracy of FNCL analysis when used in the field.

This software will also be used to investigate the effects of high gamma-ray fields or neutron fields on the instrument, ensuring that any effects are understood, quantified and corrected. This software will be used to continuously assess and investigate fast neutron detection systems used by the IAEA. In general, this semi-empirical approach can be used for optimisation of other NDA systems where the data processing is done in list mode.

6. References

[1] R.Arlt, K.Baird, J.Blackadar, C.Blessenger, D.Blumenthal, P.Chiaro, K.Frame, E.Mark, M.Mayorov, M.Milovidov, R.York, Semi-Empirical Approach for Performance Evaluation of Radionuclide Identifiers, 2009 IEEE Nuclear Science Symposium Conference Record, N16-6, p.990

[2] VeriFuel, a Liquid Scintillator-Based Fast Neutron Counter for Fresh Nuclear Fuel Measurements

Beaumont, J.S., Lee, T.H., Mayorov, M. et al. Proceedings of INMM 58th Annual Meeting, 2017
[3] Beaumont, J., Lee, T. H., Mayorov, M., Tintori, C., Rogo, F., Angelucci, B., Corbo, M., A fast-neutron coincidence collar using liquid scintillators for fresh fuel verification, J Radioanal Nucl Chem (2017) 314:803–812 DOI 10.1007/s10967-017-5412-x
[4] Eljen technology, ‘‘NEUTRON/GAMMA PSD EJ-301, EJ-309,’’ Eljen Technology. http://www.eljentechnology.com/products/liquid-scintillators/ej-301-ej-309. Accessed 30 May 2018
[5] Tomanin A, Paepen J, Schillebeeckx P, Wynants R, Nolte R, Lavietes A (2014) Characterization of a cubic EJ-309 liquid scintillator detector. Nucl Instrum Methods Phys Res Sect A 756:45–54
[6] Mckinney G, Durkee JS, Hendricks JS, James MR, Pelowitz DB (2011) MCNPX users manual, version 2.7. 0
[7] Padovani E, Pozzi SA, Clarke SD, Miller EC (2012) MCNPXPoliMi user’s manual, C00791 MNYCP, radiation safety information computational center, oak ridge national laboratory, vol 1
[8] Tomanin A, Peerani P, Maenhout G (2013) The SimPLiS code: a simulation post-processor for liquid scintillators

Use of neutron coincidence counters for the estimation of fissile content in irradiated material

R. Rossa[1], E. Boogers[1], A. Borella[1], S. Boden[1], W. Broeckx[1], L. Noynaert[1], K. van der Meer[1]

1) SCK•CEN, Belgian Nuclear Research Centre, Boeretang, 200, B2400 Mol, Belgium

Email: rrossa@sckcen.be

Abstract

Neutron coincidence counters based on ^{3}He proportional counters have been widely used for the detection of fissile material in applications such as nuclear safeguards, security, and decommissioning.

Recently, SCK•CEN purchased two used Canberra WM3400 neutron coincidence counters in the frame of the initial characterization process for the decommissioning of historical sodium loops. Several so-called In-Pile Sections (IPS) were irradiated in the BR2 reactor at SCK•CEN during 1970-1980's to study the rupture of fast reactor fuel in accidental conditions. The section of the IPS containing the original fuel pins was already removed from the SCK•CEN site for further R&D activities, but the residual fissile material in the remaining part, containing the loop components, needs to be quantified in order to determine the strategy for segmentation, conditioning and transportation.

This contribution focuses on the initial testing of the detectors to verify their correct operation. A Monte Carlo model of the detector was developed with the MCNPX-PoliMi code, and a comparison between experiments and simulation results have been conducted.

Measurements with a ^{252}Cf source were carried out and the point model equations were applied to calculate the detector efficiency and die-away time. The initial testing confirmed the operating conditions recommended by the manufacturer, although the Totals and Reals rates estimated with Monte Carlo simulations were approximately 6% and 18% larger than the measured values. In addition, a strong sensitivity to gamma-rays was observed in a series of experiments.

Keywords: neutron coincidence counting, Monte Carlo, safeguards, decommissioning

1. Introduction

The estimation of fissile content in irradiated material is important both for the nuclear material accountancy in the safeguards inspections and for its eventual segmentation, conditioning, and transportation (ADR, 2017). Among the non-destructive assays (NDA) available for measurement of nuclear material, neutron coincidence counters were developed from the 1970's (Ensslin, 1978), (Menlove, 1979) and are commonly used for the determination of fissile material for example in fresh fuel or in waste drums (Menlove, 1991).

Two coincidence counters were recently acquired by SCK•CEN for the estimation of fissile material in irradiated material that was part of R&D activities on sodium fast reactors. The so-called In-Pile Sections (IPS) were irradiated in the BR2 reactor at SCK•CEN during 1970-1980's to study the fuel

behavior in accidental conditions (Schleisiek, 1987). The section of the IPS containing the original fuel pins was already removed from the SCK•CEN site for further R&D activities, but the residual fissile material in the remaining part needs to be quantified.

This contribution describes the first steps in the testing of the coincidence counters and the development of the Monte Carlo model of the detector. The principles of coincidence counting and analytical formulations are included in Section 2, whereas Section 3 contains the description of the coincidence counter and the associated Monte Carlo model. Finally, the results from the measurements conducted with the counters are reported in Section 4 and compared with the results obtained from Monte Carlo simulations. The general conclusions and overview of future work are presented in Section 5.

2. Principles of coincidence counting

2.1. Rossi-alpha distribution

Neutrons are emitted from radioactive materials by (α,n) reactions, spontaneous fission, or induced fission. In the first case only one neutron is emitted per reaction, whereas usually more than one neutron is emitted in the fission process. Coincidence counters exploit this difference to estimate the presence of fissile material in the measured sample (Ensslin, 1991).

Starting from an arbitrary neutron detection, the distribution of the number of detected neutron events as a function of time is expressed by the Rossi-Alpha distribution in Formula (1). The height of the distribution (S) as a function of time t is the sum of a constant contribution (accidental events, A) and an exponential term due to the real coincidence events (R). The mean neutron lifetime in the detector is also called die-away time (τ) and is determined primarily by the detector geometry.

$$S(t) = A + R\, e^{-\frac{t}{\tau}} \qquad (1)$$

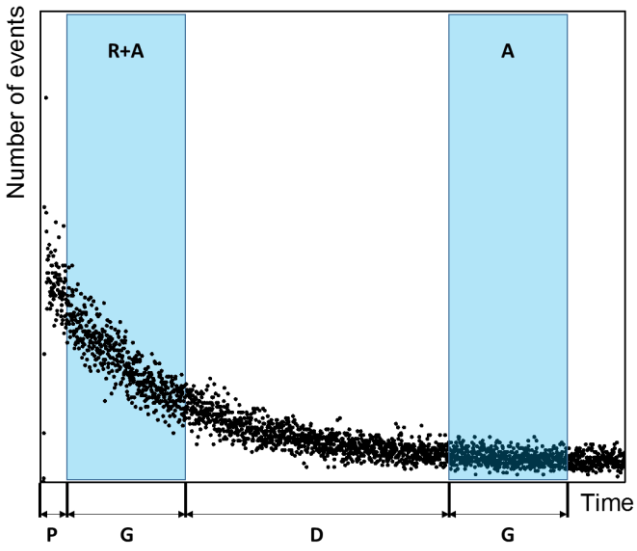

Figure 1: Rossi-alpha distribution of the detected neutron events as a function of time. P refers to the pre-delay, G to the gate, D to the long delay. The X-axis is not shown in scale for graphic reasons. The areas under the curve related to real coincidence events (R) and accidental events (A) are also depicted.

A Rossi-Alpha distribution for a ^{252}Cf source is shown in Figure 1 with the visualization of the real plus accidental (*R+A*) and accidental (*A*) events. In neutron coincidence counting, a short pre-delay (*P*) is introduced after the detection of the start event to neglect the effect of pulse pileup and electronic dead-times. Then a gate (*G*) is opened to count the sum of reals and accidental events (*R+A*), and finally after a long delay (*D*) a second gate is opened to record only the contribution from accidental events (*A*). For most application the pre-delay is in the order of a few μs (e.g. 4.5 μs), the gate width is between 32 and 64 μs, and the long delay around 1000 μs (Menlove, 1991).

2.2. Analytical formulations

2.2.1. Totals rate

The totals rate (T_R) detected by the instrument is proportional to the detector absolute efficiency (ε) and source strength (N_E) as shown in Formula (2).

$$T_R = \varepsilon \, N_E \qquad (2)$$

2.2.2. Accidentals rate

The rate of accidentals events (A_R) is related to the gate width and to the total events rate according to Formula (3). This Formula assumes a random distribution of the accidentals events, and under this assumption the uncertainty of the accidentals events is calculated as the square root of the accidental events.

$$A_R = G \, T_R^2 \propto \varepsilon^2 \, N_E^2 \qquad (3)$$

2.2.3. Reals rate

The reals rate (R_R) is related with Formula (4) to the difference between the *(R+A)* and the *(A)* scalers obtained from the shift register. In addition to the measurement time (*t*), the exponential terms in Formula (4) account for the pre-delay (*P*), the finite duration of the prompt gate (*G*), and delayed gate (*D+G*).

$$R_R = \frac{(R+A)\ scaler - (A)\ scaler}{e^{-P/\tau}\left[1 - e^{-(G/\tau)}\right]\left[1 - e^{-(D+G)/\tau}\right] t} \propto \varepsilon^2 N_E \qquad (4)$$

The uncertainty of the reals events was calculated with Formula (5), assuming that the scalers for the *(R+A)* and *(A)* events are uncorrelated and follow the Poisson distribution (Ensslin, 1991).

$$\sigma_R = \sqrt{(R+A) + A} \qquad (5)$$

2.2.4. Die-away time

The die-away time of the detector can be determined with Formula (6) (Ensslin, 1991) by measuring a neutron source with two different gate settings G_1 and G_2, where G_2 is twice G_1, and with Real scalers rates $R_{R,1}$ and $R_{R,2}$, respectively.

$$\tau = -\frac{G_1}{ln\left(R_{R,2}/R_{R,1} - 1\right)} \qquad (6)$$

2.2.5. Efficiency

The absolute efficiency (ε) of the detectors was calculated with two approaches in this contribution. First the efficiency was calculated with Formula (2) from the Totals rate. This value was compared to the one obtained by combining the Totals and Reals rates with the factorial moments according to Formula (7). Formula (7) was taken from (Pedersen et al., 2014) where a different formalism is introduced compared to (Ensslin, 1991). In (Pedersen et al., 2014) the neutron coincidence observable are expressed in terms of factorial moments of the neutron emission distribution; this distribution expresses the number of neutrons emitted in spontaneous fission events (Ensslin, 2007) and the first factorial moment represents the average number of neutrons emitted per fission event. The values of the factorial moments were found in (Croft, 1993).

$$\varepsilon = \frac{R_R}{T_R}\frac{\nu_{s(1)}}{\nu_{s(2)}} \qquad (7)$$

3. Monte Carlo model of the detectors

Two Canberra WM3400 neutron coincidence counters (Canberra, 2010) were recently purchased by SCK•CEN as second-hand equipment with two Canberra JSR-12 shift registers (Canberra, 2006) for data acquisition and analysis. Each detector was tested by the manufacturer before the first sale and the results of the testing are available in so-called Canberra checklist reports. Figure 2 shows a picture of one of the detectors during a measurement conducted at SCK•CEN with the ^{252}Cf source. Each detector has six ^{3}He tubes with 2.54 cm diameter and active length of 91 cm; the ^{3}He tubes are aligned in a single row and the ^{3}He tubes are embedded in polyethylene to ensure neutron moderation. The moderator is enclosed in an aluminum cover, and a 1-mm layer of Cd is applied to five sides of the moderator below the aluminum cover. Only the side facing the radioactive source is not covered by Cd. The ^{252}Cf source shown in Figure 2 had an activity of 1 µCi at the reference date (August 15, 2015) with a declared uncertainty on the activity of 15% (Eckert&Ziegler, 2012).

Figure 2: Picture of the Canberra WM3400 neutron coincidence counter and position of the ^{252}Cf source used in the testing.

A Monte Carlo model with the MCNPX code (Pelowitz, 2011) was developed from the technical characteristics of the detectors. Figure 3 shows the inner section of the model to highlight the position of the ^{3}He tubes within the polyethylene. The MCNPX-PoliMi V.2.0 code (Padovani et al., 2012) and the MPPost post-processor (Miller et al., 2012) were used for the data analysis to obtain the Rossi-Alpha and multiplicity distributions.

The MCNPX-PoliMi code requires to perform the Monte Carlo simulation in the so-called analog mode, in which each particle has a weight equal to 1. This is set by the following lines:

$$CUT{:}\,N \quad 2j \;\; 0 \;\; 0 \qquad (8.1)$$

$$PHYS{:}\,N \quad j \;\; 100 \;\; 3j \;\; -1 \qquad (8.2)$$

The source term in the MCNPX-PoliMi code was defined with the IPOL card as follows:

$$IPOL \quad +10 \;\; -2 \;\; 2 \;\; 1 \;\; 2j \;\; 6 \;\; 201 \;\; 202 \;\; 203 \;\; 204 \;\; 205 \;\; 206 \qquad (9)$$

The first term sets a ^{252}Cf spontaneous fission source with a Watt energy spectrum, the second term defines in case of induced fission an isotropic emission, the third term is used to correlate neutron and photon production, and the fourth term applies a photon emission delay in all fission events. Two other entries are set to default values (*2j*), and finally the six cells with the ^{3}He tubes are defined (*201, …, 206*).

The neutron flux tally (so-called F4 type) was calculated for each ^{3}He tube with the FM treatment (Pelowitz, 2011) to simulate the detector response taking into account the (n,p) reaction cross-section for ^{3}He and a ^{3}He pressure of 4 atm (Canberra, 2010). The (R+A) and (A) scalers were calculated with the MPPost post-processor from the output file of the Monte Carlo simulation and specifying a pre-delay time of 4.5 µs, a gate width of 64 µs, and a long delay of 1000 µs.

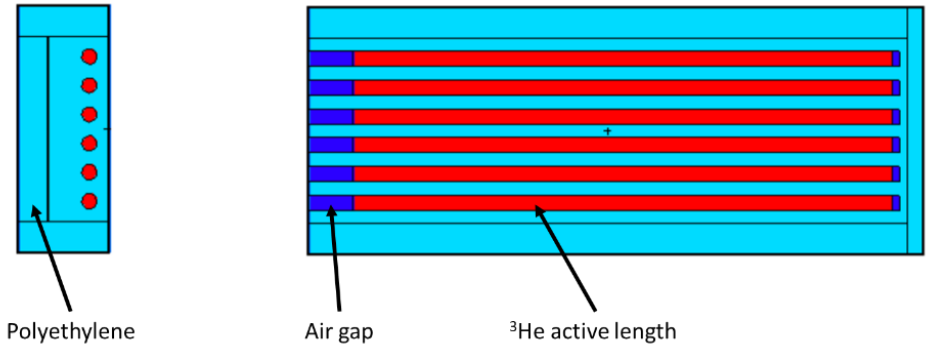

Figure 3: 2D-views of the Canberra WM3400 counter developed with the MCNPX Monte Carlo code.

4. Results

4.1. Optimal high-voltage

The totals rate was measured with the neutron source as the high-voltage was varied from 1560 V to 2000 V with steps of 20 V. Figure 2 shows the position of the neutron source on the slab counter.

For both detectors these measurements were carried out with the gate width set to 64 µs and the measurement time to 240 s. The background contribution to the measurements with high voltage lower than 1800 V was lower than 1% for both systems, and increased up to 15% for the measurement at 2000 V. The Canberra checklist reports the background measurement only for the recommended high voltage setting and for both systems was within 1%.

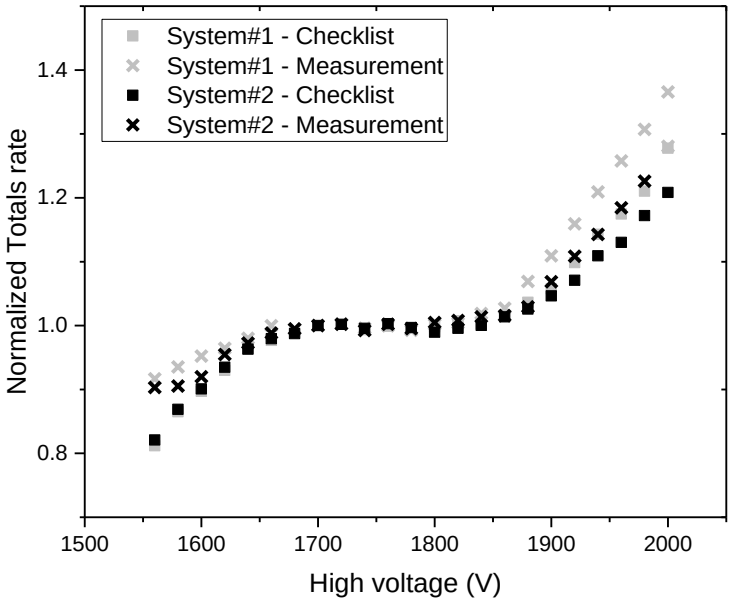

Figure 4: Totals rates obtained for different values of high voltage. Each series is normalized to the value obtained with the high voltage at 1700 V.

The totals rate were then normalized to the values obtained with the high voltage at 1700 V and plotted in Figure 4. For each system the normalized rates reported in the checklist and obtained in the measurements are shown. For each case a characteristic S-shaped curve was obtained, with a plateau ranging approximately between 1660 and 1800 V. The optimal high voltage value should be selected in the plateau region, and as close as possible as the low voltage end. Therefore, for both systems the optimal high voltage was set to 1700 V and this is in line with the results in the Canberra checklist.

4.2. Detector efficiency

The absolute efficiency (ε) was calculated for both systems first according to Formula (2), as the ratio between the totals rate (T_R) and the neutron emission rate of the ^{252}Cf source (N_E). The totals rate was taken from the measurement of the ^{252}Cf source placed in the central section of the detector with 1-hour measurement time and recommended values for high voltage (1700 V), pre-delay (4.5 µs), and gate width (64 µs). The neutron emission was estimated from the source certificate and from nuclear data from the JEFF-3.1 library (Koning et al., 2010). The calculated absolute efficiencies were 7.68 ± 1.15 % and 7.25 ± 1.09 % for System#1 and System#2, respectively. In addition, the efficiency was calculated also with Formula (7) leading to values of 7.22 ± 0.08 % and 6.72 ± 0.09 % for System#1 and System#2, respectively.

A Monte Carlo simulation was carried out with the source term in direct contact with the detector to replicate the geometry in Figure 2. The Totals rate and Reals rate calculated with the MPPost post-processor were respectively about 6% and 18% larger than the measured values. This difference can be due to variations in the detector design from the nominal values and will be investigated in future work. The calculated efficiency using the Totals rate and Reals rate from the Monte Carlo simulation was 7.69 ± 1.15 % using Formula (2), whereas by using Formula (7) was 7.39 ± 0.02 %.

The absolute efficiency reported in the Canberra checklist was 1.84% and 1.81% for System#1 and System#2, respectively. The absolute efficiency depends on the measurement setup, and since no

detailed information is available in the Canberra checklist, a comparison is not possible with the values from the experimental campaign at SCK•CEN.

4.3. Die-away time

The die-away time was calculated from the measurements of the ^{252}Cf source with increasing gate width. The die-away time (τ) for each system was calculated as a fit of the measured Reals scaler rate (R_S) as a function of the gate width (t). Starting from the Rossi-Alpha distribution in Formula (1), the curve used for the fit was:

$$R_S = R_0\left(1 - \exp(-{}^{t}/_{\tau})\right) \qquad (10)$$

The source position during the measurements is indicated in Figure 2. Both the values of the *(R+A)* and *(A)* scalers were recorded as a function of the gate width, and the reals scaler was calculated as the difference between the measured scalers. For all measurements the high voltage was kept at 1700 V and the measurement time was set to one hour. The uncertainty of the reals scaler rate was below 1% whereas for the accidentals scaler rate it was below 3%. In addition, the scalers rates were also calculated from the Monte Carlo simulation used for the estimation of the efficiency. The value of the gate width was set with the MPPost post-processing software.

The normalized values for the reals and accidentals scaler rate are shown in Figure 5 for System#2 and for the Monte Carlo simulations. Similar results were obtained for System#1 but they are not included for graphical reasons. The values from checklist, measurements, and simulations are reported. For each data series the values were normalized to the cases obtained with gate width of 250 µs. The fit obtained with Formula (10) resulted in die-away times of 57.0 ± 1.0 and 58.7 ± 1.2 µs for the measurements with System#1 and System#2, respectively. The fit reported in the checklist led to die-away times of 58.2 and 56.5 µs, respectively. The die-away time calculated with the results of the Monte Carlo simulation is of 55.5 ± 1.0 µs.

The die-away time was also estimated with Formula (6) and the results are shown in Tables 1-3 respectively for System#1, System#2, and the Monte Carlo simulation. By increasing the value of the gate width, the die-away times calculated with the two approaches agree within a few microseconds for both systems.

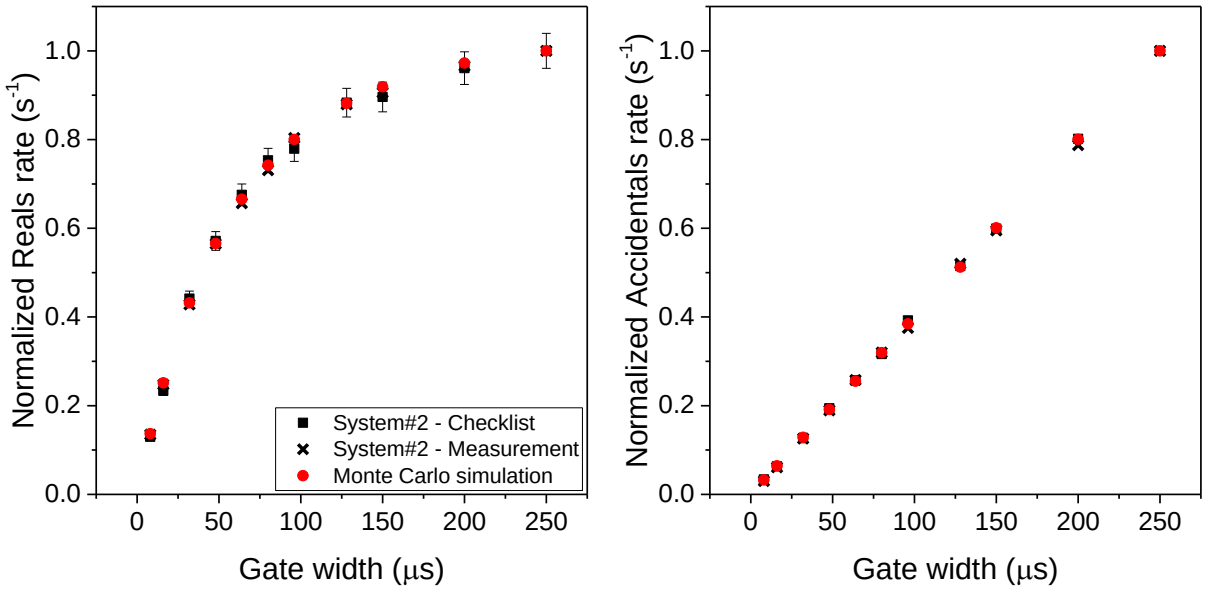

Figure 5: Reals scaler rate (left plot) and Accidentals scaler rate (right plot) obtained for different values of gate width. Each series is normalized to the value obtained for gate width of 250 μs. Similar results were obtained for System#1 but they are not included for graphical reasons.

Table 1: Analytical estimation of the die-away time from the Reals scaler rate. The values refer to System#1.

Gate width G_1 (μs)	Reals scaler rate R_1 (s^{-1})	Gate width G_2 (μs)	Reals scaler rate R_2 (s^{-1})	Die-away time τ (μs)
8	3.0	16	5.6	65.9 ± 15.3
16	5.6	32	9.7	49.0 ± 3.5
32	9.7	64	14.8	49.6 ± 1.8
48	12.5	96	17.7	55.2 ± 1.6
64	14.8	128	19.5	55.9 ± 1.4

Table 2: Analytical estimation of the die-away time from the Reals scaler rate. The values refer to System#2.

Gate width G_1 (μs)	Reals scaler rate R_1 (s^{-1})	Gate width G_2 (μs)	Reals scaler rate R_2 (s^{-1})	Die-away time τ (μs)
8	2.6	16	4.8	45.0 ± 7.9
16	4.8	32	8.4	50.7 ± 4.1
32	8.4	64	12.8	50.8 ± 2.0
48	11.0	96	15.7	55.7 ± 1.7
64	12.8	128	17.1	59.3 ± 1.6

Table 3: Analytical estimation of the die-away time from the Reals scaler rate. The values refer to the Monte Carlo simulation.

Gate width G_1 (μs)	Reals scaler rate R_1 (s^{-1})	Gate width G_2 (μs)	Reals scaler rate R_2 (s^{-1})	Die-away time τ (μs)
8	3.1	16	5.7	44.9 ± 3.7
16	5.7	32	9.8	48.5 ± 1.8
32	9.8	64	15.1	52.0 ± 1.0
48	12.9	96	18.2	54.6 ± 0.8
64	15.1	128	20.1	56.9 ± 0.7

4.4. Sensitivity to gamma-rays

A set of measurements were conducted at the Laboratory for Nuclear Calibration (LNK) of SCK•CEN using either a ^{137}Cs or ^{60}Co gamma-ray source. The source to be used depended on the desired dose rate of the measurement, and also the distance between source and detector was adjusted for each measurement to achieve the desired dose rate. The neutron detectors were exposed to gamma-ray dose rates from 10 μSv/h to 3 mSv/h. The same set of measurements were conducted also by using the gamma-ray sources with the ^{252}Cf neutron source used in the previous tests. The results of the measurements are shown in Figure 6.

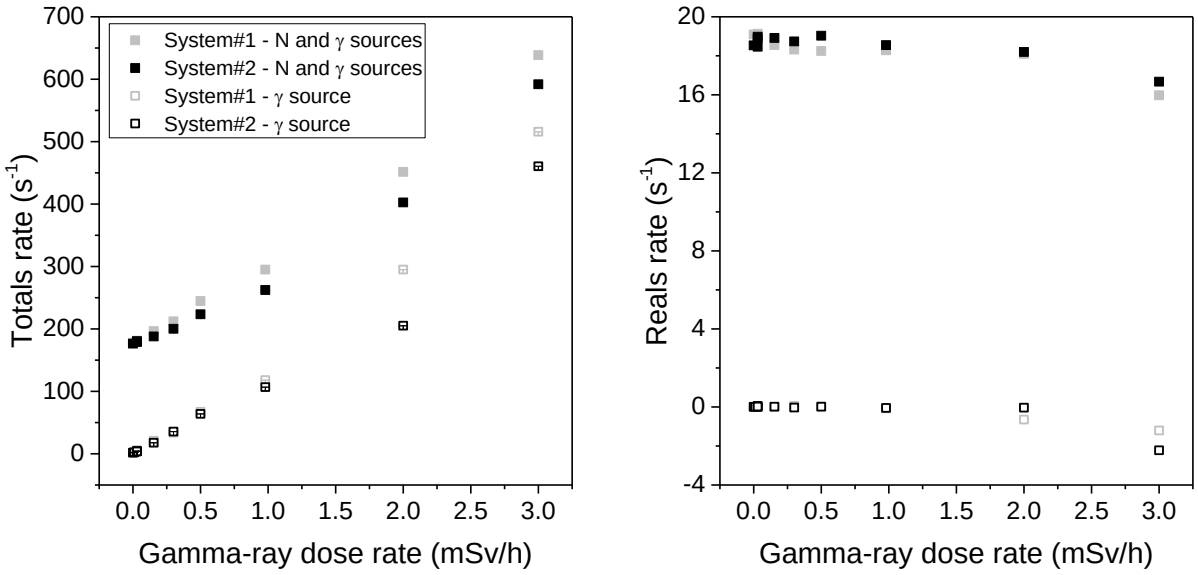

Figure 6: Totals rates (left) and Reals rates (right) measured as a function of the gamma-ray dose rate. Both the cases with and without the ^{252}Cf neutron source are shown.

It was found that the Totals rate increases with the gamma-ray dose rate already from 10 μSv/h, and this trend was observed with the gamma-ray source alone or in combination with the ^{252}Cf source. The Reals rate remains within 5% compared to the background value, but decreases of about 15% at a gamma-ray dose rate of 3 mSv/h. Similar results were obtained for both neutron coincidence counters.

During a separate measurement campaign, several measurements were conducted with strong ^{252}Cf and AmBe sources and the detector in the same configuration to check the long term stability and

repeatability of the measurements. The results obtained showed that the Totals rates were consistent between different measurements, but the Reals rate changed within a factor two. For some measurements the rate of the (R+A) scaler was larger than the rate of the (A) scaler, leading to negative values of the Reals rate. Considering the observed high sensitivity to gamma-rays and fluctuations in the measured Reals rate, a change in the electronic systems was decided to reduce these issues. This change is currently ongoing and new tests are foreseen in the future to verify the correct operation of the new electronic systems.

6. Conclusion and future work

Two used neutron coincidence counters were recently acquired for the measurement of irradiated material with the goal of quantifying the residual fissile material.

Initial testing was conducted to verify the correct operation of the detectors and to get experience in the measurement and data analysis with this detector type. The operating parameters such as high-voltage and gate width are consistent with the recommended values given by the manufacturer, and also the die-away time is within a few µs from the nominal value. The detector efficiency is higher than the value stated by the manufacturer but the measurement setup used by the manufacturer is not reported, therefore a direct comparison is not possible. However, the detectors showed a strong sensitivity to gamma-rays, as well as significant fluctuations in the Reals rate comparing measurements with the same setup. The similar behavior was observed for both detector units.

A Monte Carlo model of the detectors was also developed and the results of the simulations were compared to the measured data. The calculated totals rate and reals rate were respectively about 6% and 18% larger than the measured values. The resulting detector efficiency and die-away time computed with the Monte Carlo simulations are within 10% of the measured data.

The electronic system used in the coincidence counter is currently being updated to reduce the gamma-ray sensitivity and counting fluctuations. Future work includes a sensitivity study with Monte Carlo simulation on design parameters of the detectors, testing of the new electronic system, and finally the measurement of irradiated In-Pile Sections to quantify their residual fissile content.

References

ADR, 2017. “European Agreement concerning the International Carriage of Dangerous Goods by Road”. United Nations Economic Commission for Europe (UNECE).

Canberra, 2006. http://www.canberra.com/products/waste_safeguard_systems/pdf/JSR12-SS-C28919.pdf. Last accessed 05/03/2018.

Canberra, 2010. http://www.canberra.com/products/waste_safeguard_systems/pdf/WM3400-SS-0258.pdf. Last accessed 05/03/2018.

Croft S., et al., 1993. “Topics in neutron multiplicity counting at Harwell”. ESARDA international workshop on passive neutron coincidence counting.

Eckert & Ziegler, 2012. “Industrial Radiation Sources – Product information”.

Ensslin N., et al., 1978. “Neutron Coincidence Counters for Plutonium Measurements”. Nuclear Materials Management VII (2), 43-65 (1978).

Ensslin N., 1991. “Principles of neutron coincidence counters”. Passive nondestructive assay of nuclear materials (LA-UR-90-732).

Ensslin N., 2007. “Passive neutron multiplicity counting”. Passive nondestructive assay of nuclear materials – 2007 Addendum (LA-UR-07-1402).

Koning A. J., et al., 2010. "Status of the JEFF Nuclear Data Library". Proceedings of the International Conference on Nuclear Data for Science and Technology, 2010, pp.1057-1062.

Menlove H. O., 1979. “Description and Operation Manual for the Active Well Coincidence Counter”. Los Alamos Scientific Laboratory report (LA-7823-M).

Menlove H. O., 1991. “Neutron Coincidence Instruments and Applications”. Passive Nondestructive Assay of Nuclear Materials (LA-UR-90-732).

Miller E., et al., 2012. “MCNPX-PoliMi Post-Processor (MPPost) Manual”. Radiation Safety Information Computational Center, Oak Ridge National Laboratory.

Padovani E., et al., 2012. “MCNPX-PoliMi User’s Manual”. Radiation Safety Information Computational Center, Oak Ridge National Laboratory.

Pedersen B., et al., 2014. “Non-Destructive Assay – Passive Neutron”. Lecture of the 7FP GENTLE intersemester course on nuclear safeguards & security.

Pelowitz D., editor, 2011. “MCNPX user’s manual version 2.7.0”. Los Alamos National Laboratory LA-CP-11-00438.

Schleisiek K., et al., 1987. “MOL7C experiments on local fault propagation in irradiated LMFBR fuel subassemblies”. Nuclear Engineering and Design 100 (1987) 435-445.

MCNP6 simulation validation of fast neutron coincidence detection system for nuclear security and safeguards applications

Débora M. Trombetta[1], Bo Cederwall[1], Kåre Axell1[2]

[1]Department of Physics, KTH Royal Institute of Technology

[2]Swedish Radiation Safety Authority

Abstract

The use of interrogation techniques to evaluate materials concerning their nuclear content is fundamental in fields such as nuclear safeguards and security. Important requirements in techniques as nuclear isotopes detection, identification and mass measurements are low uncertainty and short measurement times. A non-destructive analysis (NDA) is the common choice, and passive techniques are preferred since the material cannot be irradiated in many cases due to safety or other constraints. Detection of fast neutrons has several potential advantages compared to systems based on thermal and epithermal neutron counters, the most important being the much shorter required coincidence time and the correspondingly reduced rate of background due to accidental coincidences. Organic scintillators are well suited for this purpose due to their fast timing and composition being based on carbon and hydrogen, fast neutrons having a large elastic scattering cross-section with hydrogen nuclei. This paper presents results of MCNP6 simulations of a neutron-neutron (nn) coincidence setup for characterization of special nuclear materials based on liquid organic scintillation detectors. The simulations are compared with measurements of a variety of different samples of ^{240}Pu material using the results from a previously published study using a setup consisting of 16 detectors of the same type.

Keywords: liquid scintillator detector; MCNP; NDA; nuclear safeguards; SNM.

1. Introduction

An essential element of nuclear safeguards and security measures involves the detection and identification of special nuclear materials (SNM). Thermal neutron well counters based on ^{3}He are the most common detectors used in domestic and international nuclear safeguards, and nuclear security systems, such as in radiation portal monitors (RPM) [1-2]. In 2011, the International Atomic Energy Agency (IAEA) addressed the question of a possible replacement for helium-3-based neutron detectors [3] due to the possible future shortage of helium-3. Since then, the development of alternative technologies has been intensified. A technology that has gained attention is the use of organic scintillators [4-7], which due to their fast timing and pulse shape discrimination capabilities enable efficient detection and identification of gamma rays and neutrons [8-9]. The use of this type of detectors may result in a higher sensitivity for detecting special nuclear materials, since fissioning systems are associated with the emission of both neutrons and "cascades" of gamma rays depopulating excited states in the fission products. Most of these gamma rays are "prompt", i.e. emanate from short-lived nuclear states, and their multiplicity distribution can be extended significantly beyond an average of 5-10 [10-12]. The use of particle coincidences has been extensively used in the prediction of nuclear materials mass, in particular for multiplying sources. However, the use of gamma-gamma correlations for this purpose has two main concerns. The first is related to their highly attenuation by the fissile material itself, which imposes a limitation in the size/quantity of the sample to be investigated. In this case, the information acquired is mainly limited to the surface region from the material that is studied in the case of large and dense samples. The second concern is and the strong background from decay gamma-rays that exists for large quantities of material, which can create an overwhelming rate of

accidental coincidences. Neutron-neutron coincidence techniques are therefore usually preferred [5,8,13,14,15,16,17] as they are also subject to low natural background rates, even though the spread in the correlation time for neutrons pairs is larger than for photons, due to the time-of-flight dependence on the neutron energy. Indeed, it has been shown [5] that a multidetector setup based on organic liquid scintillation detectors can be as efficient in detecting SNM as a high-end commercial system based on moderated He-3 counters [18].

The use of Monte Carlo simulations for such studies is very common, in particular using the MCNPX-PoliMi [5, 6, 19, 20,21,22] since it was developed specially for this propose. There is a significantly lower number of studies using GEANT4 in the literature [23, 24, 25] and a possible explanation for that is that the generic GEANT4 code is not well-suited for this type of simulations [24]. The version 6 of MCNP is released with new features [26], beyond the ones already present in the MCNP4 and MCNPX. The production of secondary gamma particles are done via a link to the LANL developed cascading gamma-ray multiplicity code. The spontaneous decay option that implemented in the MCNPX (2008) was extended in the version 6 to include spontaneous neutrons (PAR=SN). Also a new model for the correlated prompt secondary-particle production was adopted.

This paper presents MCNP6 simulations validation using data analysis results of a published paper by Dolan *et. al*. [5] to predict ^{240}Pu mass using correlations between the fast neutrons from plutonium dioxide samples. The validation of simulations using experimental results give confidence in the use of the proposed computational method and modeling tool for more complex geometries in future works.

2. Material and Methods

This section presents the two experimental setups used to benchmark the simulations, along with the computational modeling setup, physics model and post processing analysis method.

2.1 Experimental Setup

The experimental setup reported in Ref. [5] consisted of two concentric rings of eight EJ-309 detectors each, placed in a cylindrical geometry using an aluminum holding structure surrounding a cavity with a diameter of 34 cm. Each detector had a cylindrical shape with 7.62cm diameter and 7.62cm height (3”x3”x3”). A lead shield with a thickness of 1cm was placed around the samples to reduce the gamma-induced signals in the detectors. Two time-synchronized CAEN V1720, 12-bit, 250-MHz, 8-channel digitizer modules were used to record the detector signals. The paper reports a dynamic range of 650-6600 keV for the neutron energy deposited in the scintillators. Pulse shape analysis was employed in order to separate neutron-induced signals from the gamma-ray background.

In the original article the measurements of nn coincidences were reported and compared with results obtained using the MCNPX-PoliMi simulation code.

The experiment used four well-characterized encapsulated PuO_2-containing samples, from JRC (Join Research Center), Ispra. These samples have effective masses of $^{240}Pu_{eff}$ varying from 0.42g to 2.30 g, see Table 1. The Pu-240 effective mass ($^{240}Pu_{eff}$) is defined by including also the other even Pu isotopes that contribute with spontaneous fission neutrons, being proportional by their masses in the sample and their spontaneous fission yield and is given by the Eq. 1.

$$M(^{240}Pu_{eff}) = m(^{240}Pu) + 2.51m(^{238}Pu) + 1.67m(^{242}Pu) \quad (1)$$

Sample ID	1	2	3	4
Isotope	Unit (g)			
^{238}Pu	0.001	0.004	0.046	0.064
^{239}Pu	6.184	5.638	4.885	4.140
^{240}Pu	0.417	0.948	1.216	1.679
^{241}Pu	0.004	0.018	0.096	0.099
^{242}Pu	0.003	0.024	0.138	0.278
$^{240}Pu_{eff}$	0.42	1.00	1.56	2.30
Total mass	6.716	6.787	6.816	6.719

Table 1: Isotopic composition of the studied PuO_2 samples.

The pulse shape discrimination (PSD) technique was used to differentiate between neutron- and gamma-induced signals [27]. This technique is based on the difference between the shapes of the scintillation signal due to excitation by neutrons and gammas, through recoil protons and recoil electrons, respectively [26-27]. The tail and total pulse integrals are used for the PSD together with the ratio of these quantities according to Eq. 2.

$$R \equiv \frac{Tail\ integral}{Total\ integral} \tag{2}$$

2.3 Monte Carlo Simulations

Computational simulations were performed using the code Monte Carlo N-Particle, version 6 (MCNP6) [28].

The samples were modeled according to their composition and geometry information including the encapsulation used. In the computational environment they were modelled as a volumetric source with isotropic emission. The spontaneous fission (SF) source option was used to simulate the spontaneous fission yield from the Pu nuclides in the sample, and the FMULT card used with METHOD=5, which means that the LLNL (Lawrence Livermore National Laboratory) Fission Library was chosen. For spontaneous fission the Watt fission spectra parameters is used for the actinides nuclides ^{242}Pu, ^{240}Pu, ^{238}Pu – taking into account the multiplicity and energy of neutrons and gammas released. Induced fission is also considered - important due to the presence of ^{239}Pu in the samples. For induced fission, the energy spectra are chosen from parameters in the nuclear data table of the transport cross section.

The scintillator detector modeling was done based on manufacturer's detector information, which describes its characteristics and dimensions [31]. Fig.1 show the visualization of the computational modeled geometry from the experiment.

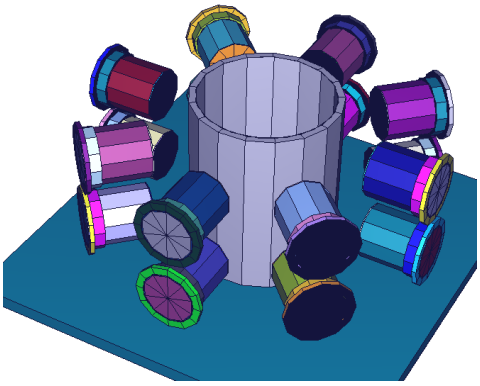

Fig. 1: MCNP6 modeling of experimental setup [5]. The sample was place at the center of the setup and surrounded by lead shielding.

In order to access the time correlations between the emitted neutrons from the fission events the card PTRAC was used in the MCNP6 simulations. PTRAC has already been used in the literature to simulate time correlations between neutrons [32 - 33]. This card generates an output file of user-filtered particle events, giving information on each interaction and movement of each particle in the system, such as: type of event (collision, capture, termination or a banked event); time of a given event: momentum; and particle energy after a given event. In the literature it was used with the option for coincidence neutron capture. In the literature it was used with the CAP option (neutron capture tally), that scores the number of captured neutrons in a specific combination of nuclides at the end of each history. In this paper the particle scattering events were tracked, and the time and energy released were accessed. Filters were applied for particle type and the area of interest, which was limited to the sensitive volume of the detectors.

A post processing code in MATLAB [34] was used to organize the PTRAC output file in a table, filter the events and perform the calculations of correlation time and energy deposition. The script identifies scattering events for neutrons generated in the same fission event in different detectors within a coincidence time window of 200ns. With detector count rates of around 1 kHz, no significant pileup of fission events was present. Therefore, no correction was applied to the simulation results to compensate for such effects.

3. Results - Simulation Validation

To validate the simulation, the rates of single neutrons and nn coincidences were compared with the experimental results.

3.1 Single neutron and nn coincidence count rates

The rate of single neutrons and nn coincidences were calculated with the MCNP6 code and are compared with the experimental results in Figs. 2. Similar coincidence windows of around 200 ns were used.

Fig 2 presents the neutron singles and nn doubles rates as a function of the $^{240}Pu_{eff}$ mass for the results of the data analysis for experimental setup [5] and the corresponding MCNPX PoliMi simulations taken

from Ref. [5] along with the MCNP6 simulations performed in the present work. The measurement and MCNP simulation points are in quite good agreement for both the single-neutron and nn coincidence count rates in this case. However, the MCNP6 simulation performed somewhat better than that using MCNP PoliMi for coincidence events. It is important to note that there are expected differences between the simulation and the experimental data due to certain experimental factors which are not taken into account by the simulation code. Examples of this are non-uniform light collection in the scintillators and misclassification of particles. As discussed in Ref. [5], these discrepancies between the experiment and the simulation could hence be explained by experimental limitations rather than the simulation physics.

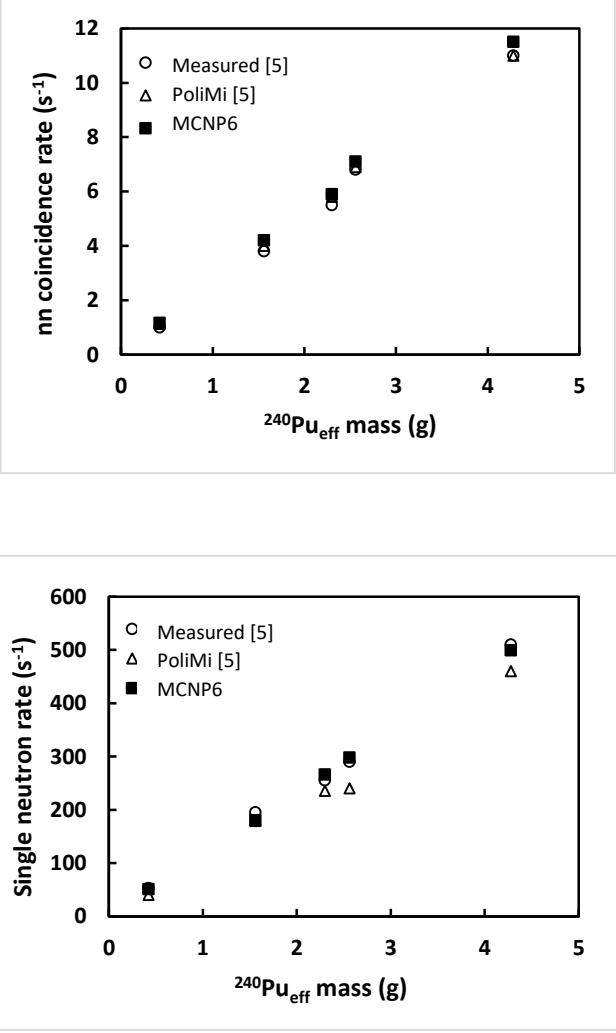

Fig.2: Single neutron and nn coincidence rates as function of $^{240}Pu_{eff}$ mass for experiment setup. The measurements and MCNPX PoliMi simulations were taken from Dolan *et al*. [5].

Table 2 presents the comparison between the experimental results and the MCNP6 simulations in numerical form.

The difference between measured and simulated nn coincidence rates were found to be between 11% and 4% for the experimental setup [5]. Differences of similar magnitude were reported in the comparison

with MCNP PoliMi simulations by Dolan *et at.* [5], with a maximum of 13% for the smaller sample, number 1. The single neutron rates presented smaller differences, ranging from 2% to 8%.

Sample ID	Measured/MCNP6	
	Single n	nn coincidences
1	1,03	0,89
3	1,08	0,90
4	0,95	0,93
2 +3	0,97	0,96
1+3+4	1,02	0,96

Table 2: Ratios of single neutron, nn rates obtained by the experiment [5], relative to values calculated using MCNP6.

3.2 Calibration Curves for mass prediction using nn coincidences

Calibration curves were fitted using the experimental data and simulations.

In Ref. [5] a R^2 value of 0.994 was reported for the linear fit, while the MCNP6 simulations with this setup present a linear fit with R^2 value of 0.998. The systematic error for the mass characterization technique was estimated using four out of the five data points to plot a new linear fit curve, and using the fifth measured point as an unknown – sample 3 was used for that purpose. The reported (slightly steeper) slope value for this new curve is 2.52 coincidences/g($^{240}Pu_{eff.}$)/s. The same procedure was done with the simulations and the calculated slope for the new calibration curve was 2.68 coincidences/g/s. The difference between the slopes calculated for the measurements [5] and the simulations with MCNP6 was 6%.

4. Conclusions

An alternative simulation approach that makes use of the MCNP version 6 and the PTRAC card for calculating particle coincidences rates on an event-by-event basis has been developed. It was validated to quantify small amounts (ranging from 0.5g to 1.5g) of ^{240}Pu in samples using measurements a reference the study performed by Dolan *et al*. [5]. In order to validate the simulations both the absolute rates for single neutrons and nn coincidences and the slope in the linear fits to these rates as a function of effective ^{240}Pu mass were considered.

The MCNP6 simulations for experimental setup from were in good agreement with the experimental results presented by Dolan *et al*. [5] - with a maximum difference of 11% for the nn coincidence rates. The agreement was slightly better than that of the MCNPX PoliMi simulations reported [5

The quality of neutrons multiplicity results relies on the PSD performance, and since this paper used as basis results from previous experiments, which means that no control of the data acquisition process or equipment performance were possible, a more detailed investigation on the ability of the methods applied in the simulation to reproduce correctly the real data acquisition could be done with a controlled experiment that makes use of better equipment and improved data analysis techniques. As pointed in

the reference paper by Dolan *et al*. “a key aspect to the success of such kind of system is the quality of the electronics, including fast and robust photo-multipliers tubes”.

Anyhow the present work proves that the MCNP6 is comparable to the MCNP-PoliMi code for the proposed problem when it makes use of the LLNL fission library and the PTRAC card even without using the CAP option for neutrons. This possibility opens tracks for future works that could include the study with other particles than neutrons.

References

1 - Ensslin, N., Harker, W.C., Krick, M.S., Langner, D.G., Pickrell, M.M., Stewart, J.E., Application guide to neutron multiplicity counting, Los Alamos Report LA-13422-M, (1998).

2- Manlove, H.O., Swansen, J.E., Nuclear Technology 71, 2, (1985).

3 - Pickrell, M.M., Lavietes, A.D., Gavron, V., Henzlova, D., Joyce, M. J., Kouzes, R. T., and Menlove, H.O., The IAEA Workshop on Requirements and Potential Technologies for Replacement of 3He Detectors in IAEA Safeguards Applications, Journal of Nuclear Material Management 41 (2), (2013).

4 - Robinson, S.M., Runkle, R.C., Newby, R.J., A comparison of performance between organic scintillation and moderated 3He-base detectors for fission neutron detection, Nuclear Instruments and Methods in Physics Research A 784, (2011).

5 - Dolan, J.L., Flaska, M., Poitrasson-Riviere, A., Enquvist, A., Peerani, P., Chichester, D.L., Pozzi, S.A., Plutonium measurements with a fast-neutron multiplicity counter for nuclear safeguards applications, Nuclear Instruments and Methods in Physics Reseacrh A 763 (2014).

6 - Paff, M.G., Monterial, M., Marleau, P., Kiff, S., Nowack, A., Clarke, S.D., Pozzi, S.A., Gamma/neutron time-correlation for special nuclear material detection – Active stimulation on highly enriched uranium, Annals of Nuclear Energy 72, (2014).

7 -Paff, M.G., Ruch, M.L., Riviere, A.P., Sagadevan, A., Clarke, S.D., Pozzi, S.A., Organic liquid scintillaton detection for on-the-fly neutron/gamma alarming and radionuclide identification in a pedestrian radiation portal monitor, Nuclear Instruments and Methods in Physics Research A 789 (2015).

8 - Kaplan, A.C., Flaska, M., Enqvist, A., Dolan, J.L., Pozzi, S.A., EJ-309 pulse shape discrimination performance with a high gamma-ray-to-neutron ration and low threshold, Nuclear Instruments and Methods Physic Research Sect. A 729, 463-468, (2013).

9 -Enqvist, A., Lawrence, C.C., Wieger, B.M., Pozzi, S.A., Massey, T.N., Neutron light output and resolution functions in EJ-309 liquid scintillaton detectors, , Nuclear Instruments and Methods Physic Research Sect. A 715, 79-86 (2013).

10 - Lemaire, S., Talou, P., Kawano, T., Chadwick, M.B., Madland, D.G., Phys. Rev. C 72 (2005) 014602.

11 - Hamilton, J.H., Ramayya, A.V., Zhu, S.J., Ter-Akopian, G.M., Oganessian, Yu.Ts., Cole, J.D., Rasmussen, J.O., Stoyer, M.A., Prog. Part. Nucl. Phys. 35 (1995) 635.

12 – Bleuel, D.L. *et al*, Nuclear Instruments and Methods in Physics Research A624 691 (2010).

13 - Shin, T.H., Fulvio, A. Di, Clarke, S.D., Chichester, D.L., and Pozzi, S.A., Fast-neutron multiplicity counter for the detection of diversion scenarios, Conference paper (2017).

14 - Sufen Li, Suizheng Qiu, Quanhu Zhang, Yonggang Huo, Hongtao Lin, Fast-neutron multiplicity analysis based on liquid scintillation}, Applied Radiation and Isotopes 110, 53 to 58 (2016).

15 - Chichester, D.L., Thompson, S.J., Kinlaw, M.T., Johnson, J.T., Dolan, J.L, Flaska, M., Pozzi, S.A., Statistical Estimation of the performance of a fast neutron multiplicity system for nuclear material accountancy, Nuclear Instruments and Methods in Physics Research A 784, 448 (2015).

16 - Chichester, D.L., Pozzi, S.A., Dolan, J.L., Kinlaw, M.T., Kaplan, A.C., Flaska, M., Enqvist, A., Johnson, J.T., Watson, S.M., MPAC fast neutron multiplicity system design concepts, INL/EXT-12-27619, Idaho National Laboratory (2012).

17 - A. Enquvist, M. Flaska, S. Pozzi, Measurement and simulation of neutron/gamma-ray cross-correlation functions from spontaneous fission, Nuclear Instruments and Methods in Physics Research A 595, 426-430 (2008).

18 – Industries, Neutron Safeguards Systems–CANBERRA, "Model JCC-31High Level Neutron Coincidence Counter", 2009.Available at ⟨http://www.canberra.com/products/waste_safeguard_systems/neutron-safeguards-systems.asp? Accordion1=2⟩

19 - Padovani, E., Pozzi, S.A., MCNP-PoliMi ver.1.0 user's manual, CESNEF-021125, Library of Nuclear Engineering Department, Politecnico di Milano, November (2002).

20 - Clarke, S.D., Flaska, M., Pozzi, S.A., Peerani, P., Neutron and gamma-ray cross-correlation measurements of plutonium oxide powder, Nuclear Instruments and Methods in Physics Research A 604, 618-623 (2009)

21 - Monterial, M., Marleau, P., Paff, M., Clarke S., and Pozzi, S.A., Multiplication and presence of shielding material from time-correlated pulse-height measurements of subcritical plutonium assemblies, ariv:1701.03848v1, physics.ins-det (2017).

22 - Miller, E.C., Dolan, J.L., Clarke, S.D., Pozzi, S.A., Tomanin, A., Peerani, P., Marleau, P., Mattingly, J.K., Time-correlated pulse-height measurements of low-multiplying nuclear materials, Nuclear Instruments and Methods in Physics Research A 729, 108-116 (2013).

23 - Allison, J., Amako, K., Apostolakis, J., Araujo, H., Arce Dubois, P., Asai, M., Barrand, G., Capra, R., S. Chauvie, R. Chytracek, G. Cirrone, G. Cooperman, G. Cosmo, G. Cuttone, G. Daquino, M. Donszelmann, M. Dressel, G. Folger, F. Foppiano, J. Generowicz, V. Grichine, S. Guatelli, P. Gumplinger, A. Heikkinen, I. Hrivnacova, A. Howard, S. Incerti, V. Ivanchenko, T. Johnson, F. Jones, T. Koi, R. Kokoulin, M. Kossov, H. Kurashige, V. Lara, S. Larsson, F. Lei, O. Link, F. Longo, M. Maire, A. Mantero, B. Mascialino, I. McLaren, P. Mendez Lorenzo, K. Minamimoto, K. Murakami, P. Nieminen, L. Pandola, S. Parlati, L. Peralta, J. Perl, A. Pfeiffer, M. Pia, A. Ribon, P. Rodrigues, G. Russo, S. Sadilov, G. Santin, T. Sasaki, D. Smith, N. Starkov, S. Tanaka, E. Tcherniaev, B. Tome, A. Trindade, P. Truscott, L. Urban, M. Verderi, A. Walkden, J. Wellisch, D. Williams, D. Wright, and H. Yoshida, "Geant4 developments and applications," IEEE Transactions on Nuclear Science, vol. 53, no. 1, pp. 270–278, (2006).

24 – Muller, J.M., and Mattingly, J., Neutron and gamma ray coincidence measurements of a high-multiplication, subcritical assembly of weapons-grade plutonium, 978-1-4673-9862-6/15 IEEE (2015).

25 –Naeem, S.F., Clarke, S.D., Pozzi, S.A., Validation od Geant4 and MCNPX-PoliMi simulations of fast neutron detection with the EJ-309 liquid scintillator, Nuclear Instruments and Methods in Physics Research A 714, (2013).

26 - LA-UR-14-28473 Approved for public release; distribution is unlimited. Title: MCNP 6.1.1 - New Features Demonstrated Author(s): Mckinney, Gregg Walter Brown, Forrest B. Hughes, Henry Grady III James, Michael R. Martz, Roger Lee McMath, Garrett Earl Wilcox, Trevorwas (2014).

27 –Knoll, G.F., Radiation Detection and Measurement (4th Ed.), Wiley, New York (2010)

28 - Brooks, F.D., Nuclear Instruments and Methods, 162, 477 (1979).

29 - Di Fulvio, A., Shin, T.H., Jordan, T., Sosa, C., Ruch, M.L., Clarke, S.D., Chichester, D.L. and Pozzi, S.A., Passive assay of plutonium metal plates using a fast-neutron multiplicity counter}, Nucl. Inst. Meth. In Phys. Research A 885, 92-101 (2017).

30 - MCNP6 Users Manual - Code Version 6.1.1beta, LA-CP-14-00745 (June 2014).

31 - Eljen Technology, Neutron/gamma PSD liquid Scintillator EJ-301, EJ-309, (n.d.) <*http://http://www.eljentechnology.com/products/liquid-scintillators/ej-301-ej-309*> (accessed 17 November 2017)

32 - Kaplan, A.C., Henzl, V., Menlove H.O., *et al*., Determination of spent nuclear fuel assembly multiplication with the differential die-away self-interrogation instrument, Nuclear Instruments and Methods in Physics Research A 757, 20-27 (2014).

33 -Evans, L.G., Schear, M.A., Hendricks, J.S., Swinhoe, M.T., Tobin, S.J., and Croft, S., A new MCNPX PTRAC coincidence capture file capability: a tool for neutron detector design, Conference Paper, Los Alamos National Laboratory (2011).

34 - MATLAB R2017a, The MathWorks, Inc., Natick, Massachusetts, United States

Simulation of a neutron multiplicity counter and comparison to validation experiments

Olaf Schumann, Theo Köble, Wolfram Berky, Monika Risse

Fraunhofer Institute for Technological Trend Analysis INT
Euskirchen, Germany

Abstract:

Neutron coincident counting is a useful tool, both to determine the nature of a neutron source and to extract parameters like the multiplicity, α-ratio and ultimately the mass. For the latter, well characterized detectors, like the Active Well Coincident Counter (AWCC), enable the measurement of uranium or plutonium content in the order of several grams.
The multiplicity analysis also can determine if an unknown neutron source emits fission neutrons and thus possibly contains special nuclear material. The Ortec Fission Meter is an instrument designed exactly for this purpose. It consists of a highly efficient moderated ^{3}He neutron detector and a Windows Mobile handheld computer with dedicated software. It is powered by batteries and intended for field use. In order to gain a deeper understanding of the measured data and to predict the dependence of the analysis on different parameters like additional shielding, Fraunhofer INT performed a Monte-Carlo simulation of the instrument. A MCNP simulation of the source assembly and the instrument results in the arrival times of the neutrons for one single source event. Further software modules allow the generation of a pulse train and perform the same analysis as the Fission Meter hard- and software. While the count rate of the simulation and a validation experiment were in agreement, the calculated Feynman-Variance showed a significant deviation. The main cause is presumably a small fraction of double pulsing from the discriminator. The inclusion of this effect in the post-processing results in a very good agreement of measured and simulated data.

Keywords: neutron multiplicity; MCNP simulation; validation experiment; double pulsing

1. Introduction

Neutron multiplicity counting is a useful tool, both to determine the nature of a neutron source and to extract parameters like the multiplicity, α-ratio and ultimately the mass [1]. A multitude of different instruments have been developed to characterize neutron sources and determine the mass of fissile isotopes in different containers, e.g. the Active Well Coincident Counter (AWCC) or the Plutonium Scrap Multiplicity Counter (PSMC) [2]. The technique has found applications for safeguard purposes, nuclear material holdup determination and waste characterization.
But it could also be employed to determine the nature of an unknown source for nuclear search and emergency response in a homeland security context. Here the focus lies on the detection of radioactive material that might be potentially used for a radioactive dispersal device or even an improvised nuclear device. A quick and reliable measurement under field conditions is an important characteristic for such a task. The Ortec Fission Meter, which was developed at the Lawrence Livermore National Laboratory, is an instrument which is applicable for such a measurement and is commercially available [3]. It is a highly efficient moderated ^{3}He neutron detector with integrated electronics for multiplicity counting and a Windows Mobile handheld computer for measurement control and data evaluation. The detector unit consists of two connected panels, each containing 15 ^{3}He-tubes. The tubes have an active length of 19 inch and are filled with 7.5 bar of ^{3}He. One side of each panel is covered by a thin HDPE-moderator. This side is designated the thick side, while the other one is called the thin side. The device is battery-powered and with approx. 27 kg weight it can be considered as portable. It is advertised as a “proof positive” identification device for fission neutron sources through multiplicity analysis and as heaving the highest sensitivity in a portable package. The Fission Meter determines simultaneously 512 multiplicity distributions with gate lengths von 1 µs up to

512 µs and the Rossi-α distribution. From the different multiplicities, a plot of the Feynman variance as function of the gate time is generated.
In order to get a better understanding of the measurement results obtained with the Fission Meter and to predict the outcome of hypothetical measured objects, we decided to perform a numerical modelling of the Fission Meter. As it is the case with every simulation, a validation of the obtained results with a real experiment is of uttermost importance. Only then one can have some confidence that the obtained results from a simulation have some value in examining the detector response to otherwise inaccessible objects. For this we measured a simple ^{252}Cf-source in a controlled geometry with the Fission Meter and tried to obtain simulation results which describe the measurements as well as possible.

2. Measurements and Numerical Modeling

Modeling and experimental measurement of a simple geometry was performed, in order to validate the ability of our modeling approach to predict the Fission Meter results for different measurement conditions. This will ultimately lead to a better understanding of the influence which different measurement conditions, such as additional moderating material, have on the result. These influences can be hard to control in an experimental measurement, but are easier to handle in a numerical simulation.

2.1. Experimental results to model

The experimental results we want to obtain are the count rate, the multiplicity distribution, and the Feynman variance. The multiplicity distribution is a histogram, whose n-th bin gives the number of times M_n, when within a specific time interval Δ, the gate time, exactly n neutrons are counted. If for instance within the gate time 4 neutrons are counted, the value of M_4 is increased by one. When repeating this process many times, the multiplicity distribution is obtained. The sum of all entries from the histogram is the total number of measurement cycles. Multiplied by the gate time this gives the measurement time. The number of neutrons measured can be obtained by the fact that M_1 times exactly 1 neutron was measured, M_2 times 2 neutrons were measured, etc. The number of measurement cycles C and the number of registered neutrons N can be obtained by:

$$C = \sum M_n \qquad N = \sum n \cdot M_n \tag{1}$$

These relations can be generalized by the moments of the distribution

$$\mathcal{M}_i = \frac{1}{i!}\sum_{n=i}^{\infty} \binom{n}{i} M_n \tag{2}$$

If the source were to emit neutrons in a purely random fashion, the distribution would be a Poisson distribution. The defining property of this distribution is that its standard variance equals the mean value. The deviation of the obtained distribution from the Poisson distribution and thus the deviation of the source from a purely random and uncorrelated one can be quantified by the variance to mean ratio. This is the well-known Feynman variance Y_{2f}, which can be expressed in terms of the moments as follows:

$$Y_{2f} = \frac{\mathcal{M}_2}{\mathcal{M}_1} - \frac{1}{2}\frac{\mathcal{M}_1}{\mathcal{M}_0} \tag{3}$$

The Fission Meter determines simultaneously 512 multiplicity distributions with gate length from 1 µs up to 512 µs and generates a plot of the Feynman Variance Y_{2f} as function of the gate time. From a point kinetic reactor model, Feynman has derived [4] the theoretical dependence of this function as:

$$Y_{2f}(T) = R_{2f} \cdot \left(1 - \frac{1 - e^{-\lambda T}}{\lambda T}\right) \tag{4}$$

Where λ is the inverse of the neutron lifetime; the mean time it takes from the creation of a neutron to its detection. The time from creation of an individual neutron to its detection itself is exponentially distributed. The neutron life time determines the shape of the curve. If it is small, the curve starts much steeper and reaches the limit earlier. If the neutron life time is large, the curve is shallow and reaches its limit later. The value R_{2f} is the limiting value, towards which the curve will eventually tend.

2.2. Experimental Setup

Experimental data have been recorded in a laboratory used for neutron irradiation experiments by a neutron generator. In this lab, we could ensure that the walls and the ceiling had a distance of a minimum of 2 m to the Fission Meter and the source in order to reduce the backscattering of the neutrons. Concerning the floor, the Fission Meter was positioned above a pit that is covered with open mesh flooring covered by a thin plywood layer, so that the concrete floor also was 2 m below the Fission Meter. The walls and the roof consist of concrete with a thickness of 1 m to 2 m. A ^{252}Cf-source with approx. 240 kBq was used in these experiments and placed in different distances from the center of the Fission Meter.

Figure 1: Picture of the experimental setup used in the measurements. The Fission Meter is placed on an open mesh flooring which is covered by plywood. It is used in its closed configuration and the white moderator side is facing outwards. The source is placed on the edge of a scissor lift and positioned in the center of the Fission Meter. All walls, ceiling and the concrete floor under the open mesh flooring are more than 2 m away from the source and the detector in order to reduce scattering.

The Fission Meter was used in its closed configuration, that is, the two panels were folded together with both their thick side facing outwards. The background count rate with the Fission Meter without any source was quite low, in the order of 0.8 cps. During the measurements, the Fission Meters position was fixed and the source was positioned at different distances from the front surface. The results of the measurements are given in table 1, an overview of the setup is shown in figure 1. As common with neutron measurements, the data show no clear $1/r^2$ dependence on the distance but vary more like 1/r. This effect is likely due to the backscattering from the room. The count rate for all distances is well above the background rate of 0.8 cps.
The Feynman variance also shows a decrease with increasing distance but seems to saturate at a value of approximately 3.7 %. As it should be proportional to the efficiency of the detector, it is expected that is also shows a $1/r^2$ dependence, which was definitely not seen here.
These experimental data were the reference data that were attempted to reproduce with numerical methods described in the next section.

Distance (cm)	Time (s)	Count rate (cps)	Feynman Variance (%)		Neutron die away (µs)	
			exp.	sim.	exp.	sim.
5	8418	1012.55(35)	8.616(23)	4.998(31)	12.92(18)	27.76(12)
10	3177	715.95(47)	7.066(37)	3.475(25)	10.92(17)	27.04(11)
20	3933	408.48(32)	5.580(34)	1.851(18)	7.59(14)	27.86(12)
50	7307	139.33(14)	4.264(28)	0.546(10)	3.518(86)	29.76(18)
100	841	60.74(27)	3.72(10)	0.107(33)	3.40(11)	43.9(11)
200	2576	31.47(11)	3.768(72)	0.0562(47)	3.16(14)	43.05(41)

Table 1: Specifications of the measurements taken with the Fission Meter. Shown is the distance from the source to the surface of the Fission Meter, the acquired measurement time, the obtained count rate, the Feynman Variance, calculated from the longest gate time of 512 µs, and the neutron die away time. The latter two values are also given for the simulated results. The measurements at 5 cm and 50 cm were performed for more than 2 h in order to obtain good statistics for the multiplicity counting.

2.3. Numerical Modeling and Post-Processing

Numerical modeling was performed by using MCNPX Version 2.7.0 [5] and tailor made scripts for post-processing of the output. A MCNP geometry description of the Fission Meter was prepared based on data provided by Ortec on the geometry of the moderator assembly and by GE Energy / Reuter-Stokes for the used ^{3}He-tubes. The model includes the ^{3}He-tubes, the detailed moderator assembly and the outer aluminum case, while batteries, the electronic components and other components have been omitted.

In a first simulation, the response of a single ^{3}He-tube to thermal neutrons was determined. The tube is positioned with its axial axis in the z-direction. A monoenergetic thermal neutron beam with 25 meV and rectangular cross section is directed at the tube in x-direction. The cross section of the beam encompasses the complete tube assembly. The number of capture reactions of ^{3}He is recorded by a f8-tally with the "ft8 cap 2003" special treatment. Due to this, a variance reduction is not possible and was thus not employed. The density of the ^{3}He-gas is calculated without any quench gas from its nominal pressure of 7.5 bar and is equal to $9.25 \cdot 10^{-4}$ g/cm^{3}. The neutron flux per unit time is given by the number of histories normalized by the cross section of the simulated beam, the number of captures per unit time results from the f8-tally. This simulation yields a thermal neutron sensitivity of 88.90 cps/nv while manufacturer specification from the spec sheet is 71.81 cps/nv. The quotient of this value of 80.1% is interpreted as an intrinsic efficiency reduction where a neutron capture does not, for whatever reason, lead to a signal on the output of the tube. This effect is accounted for in the following simulations.

The second set of simulations is the calculation of the predicted count rate. Beside the Fission Meter, the room of the laboratory including the pit underneath the Fission Meter and the wooden layer on the open mesh flooring were modeled. All other items in the laboratory were neglected. The source was represented by a minute sphere filled with pure ^{252}Cf and the source definition was a spontaneous fission source (PAR=SF). The number of captured neutrons was again recorded by an f8-tally with capture treatment. This yielded finally the number of captures within the Fission Meter per source spontaneous fission. Combined with the intrinsic tube efficiency of 80.1% and the number of spontaneous fissions of the used ^{252}Cf-source, this could be converted to an absolute count rate. No other corrections have been made to the data.

The third and final set of simulations was done in order to generate the multiplicity distributions, as measured by the Fission Meter. The geometry description and general setup was the same as for the count rate determination. That is, the Fission Meter, the room and the plywood were modeled and all other items of the room were neglected. The source was likewise a spontaneous fission source, which emitted the neutrons for each history at a time of 0. All termination events within the ^{3}He-Volume of the Fission Meter were recorded to a binary PTRAC-file with the following MCNP input line:

```
PTRAC FILE bin WRITE all EVENT=ter FILTER=900,ICL
```

The PTRAC-file was then post-processed to give the multiplicity distribution. This was done by a set of python scripts. First the PTRAC-file was converted to a format[1], where for each history the arrival times of the neutrons in the detector are listed. From this file a pulse train was created by generating a sequence of exponentially distributed random variables. The sum of this sequence gives the points in time where a spontaneous fission occurs. For each fission event, one of the histories from the PTRAC-file was randomly selected. For each neutron in that history a Russian roulette is played with the intrinsic efficiency of the tube (80.1%) and if it survives, the arrival time is added to the time of the fission. As a neutron from a preceding fission event might arrive later than from the actual fission event, the times have to be sorted. We choose to do this on-line with a priority queue instead of generating all fission times first and then sorting a possible very large set of "almost sorted" neutron arrival times. With this process, the sorting efficiency is greater, as only few arrival times have to be present in the priority queue, as all neutron detection times smaller than the current fission time could be extracted from the queue. In addition a continuous and possibly endless stream of detection times can be generated in this way and feed to the analyzing algorithm. This allows collecting intermediate results and obtaining multiple evaluations with increasing "measurement time". This pulse train is then analyzed by a code that is equivalent to the procedure that has been published for the Fission Meter [6]. Finally the multiplicity distribution and Rossi-α data is saved in the same format as the experimental data from the Fission Meter.

[1] This was implemented with a HDF5-file containing one array of all arrival times, and one an index of which times belong to a which source event. Especially for large number of histories, it is much faster to read the HDF5-file compared to parsing the PTRAC file or to read a text based format.

3. Results

Figure 2 shows the results of the simulation of the count rate, compared to the experimental data. As explained in section 2, the results of the simulations were only scaled by the source intensity and the tube efficiency; no other corrections were made. The experimental data can be very well described by the simulation. Only at large distances the simulations tend to overestimate the count rate by approximately 20%. Nevertheless, this shows how well the detector is described by the numerical modeling.

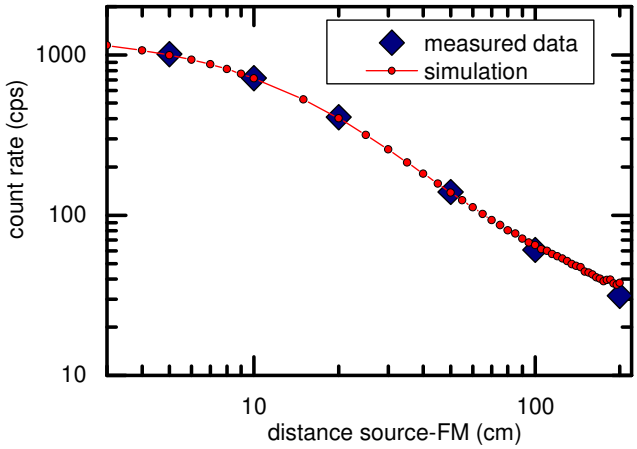

Figure 2: Comparison of the measured and simulated count rate dependence on the distance between source and Fission Meter. The simulation results were scaled by the tube efficiency and the actual neutron source strength. No other corrections were made. The agreement between experimental data and numerical results is very good.

Figure 3 shows the results of the measured and the simulated Feynman variances as function of the gate time. In contrast to the count rates, the agreement between these curves is poor. Neither the limiting value nor the shape is reproduced in the simulations. The values of Y_{2f} for long gate length are systematically about 3.7% larger for the experimental values than in the simulations, as seen in table 1. This is very prominent for the larger distances. While the simulation predicts a quite small overall value for Y_{2f} with a shape that conforms to that of formula 4 for the distances 100 cm and 200 cm, the experimental results show an abrupt increase to approx. 4% within the first few microseconds and can't be reasonably described by formula 4. This step like jump would result in a very short neutron die-away time of some few microseconds, which is quite unphysical.

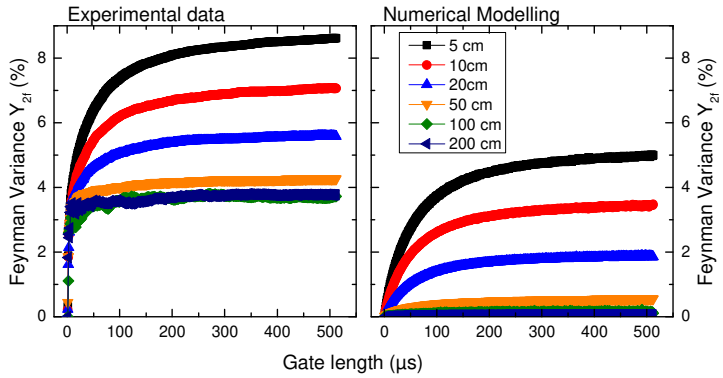

Figure 3: Comparison of the measured (left) and simulated (right) Feynman Variance for different distances. The experimental data could not be reproduced by the simulation.

Furthermore, the Feynman variance should show a linear dependence on the detector efficiency, which would result in a vanishing value for increasing distances, but that is not seen in the data. Thus there seems to be an additional "background" correlation in the data that has a characteristic time of at most a few microseconds, that seems to be independent on the distance, and that is absolutely not reproduced by the numerical modeling.

3.1 Double pulsing contribution

A hint for the cause of this effect comes from the Rossi-α measurement that is shown in figure 4. The plot shows a prominent sharp peak in the experimental data that occurs at a time difference of 1 µs. This peak is not reproduced at all in the simulated data. A peak structure in the Rossi-α data is described in the literature as due to double pulsing. Double pulsing could occur, if the charge signal on the input of the amplifier/discriminator circuit shows a dip, e.g. due to different charge collection times from the two charged ejectiles from the ^{3}He(n,p)t reaction. Other causes might be reflections on signal lines due to inadequate termination, wrong impedance or cable breaks.

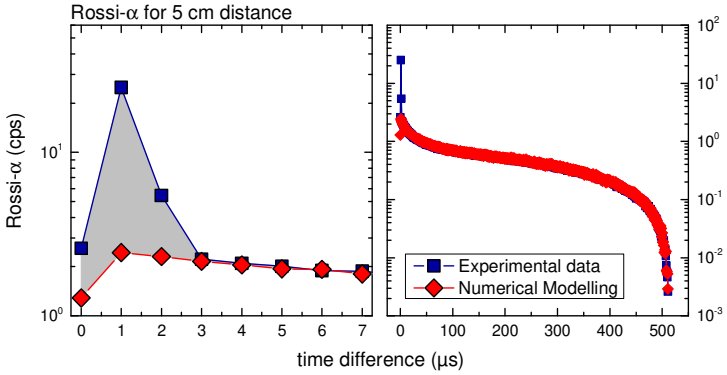

Figure 4: Rossi-α plot of the experimental and simulated data for a distance of 5 cm. The peak in the experimental data is not reproduced in the simulations. The left graph is a magnification of the right one.

The effect of double pulsing on the Feynman variance can be determined from its formulation in terms of the detection probabilities for a single source event. While formula 3 is valid for a multiplicity distribution from a counting experiment, where counts from different source events can overlap, it can be shown [7], that for a single source event, the Feynman variance has the form:

$$Y_{2f} = \frac{\sum_n n \cdot (n-1) \cdot p_n}{\sum_n n \cdot p_n} = \frac{\mathcal{M}_2}{\mathcal{M}_1} = \frac{p_2 + 3p_3 + 6p_4 + 10p_5 + \cdots}{p_1 + 2p_2 + 3p_3 + 4p_4 + \cdots} \tag{5}$$

Here, the p_n are the probabilities that n neutrons from a single spontaneous fission source event are detected within the time gate. This is a combination of the source multiplicity, the detection efficiency and a factor that relates the gate length to the neutron die away time. For arbitrarily long gate times, all neutrons from a single source event are counted in the same gate and Y_{2f} tends to R_{2f}.To take double pulsing into account, one introduces the probability δ that a single neutron generates two counts instead of only one. If n neutrons are detected, each one can result in a double pulse with a probability δ and n up to $2n$ counts might be registered. The exact number is given by a binomial distribution.
This allows the calculation of the the two moments $\mathcal{M}_1$ and $\mathcal{M}_2$ with the double pulsing included. For long gate times, it is ensured that all pulses are registered within the same gate and the resulting formula for R_{2f} is given by:

$$\hat{R}_{2f} = \frac{\widehat{\mathcal{M}}_2}{\widehat{\mathcal{M}}_1} = \frac{\mathcal{M}_2 \cdot (1+\delta)^2 + \mathcal{M}_1 \cdot \delta}{\mathcal{M}_1 \cdot (1+\delta)} = R_{2f} \cdot (1+\delta) + \frac{\delta}{1+\delta} \approx R_{2f} + \delta \tag{6}$$

As the two pulses of a double pulse might be registered in different gates, it is more challenging to determine an analytic expression for the time dependence of the Feynman variance with double pulsing for different gate length. Nevertheless, this result allows determining the double pulsing probability from the difference of the experimental and simulated Feynman variance data at large gate length. Interestingly, it is basically constant for all distances and has a value of $\delta = 3{,}7\%$.
An analysis of the height of the peak in the Rossi-α data with an analytical model [7] allows an independent determination of this value and yields consistent values. This also allows extracting the time difference between the two signals within a double pulse. A good agreement with the measured data could be reached by a normal distribution with a mean of 1.06 µs and a width of 0.3 µs, for all measured distances.
This is all information that is required to be included in the double pulsing in the post-processing of the simulated multiplicity data. For every neutron that is inserted into the pulse train, a second signal is inserted with a probability $\delta = 3.7\%$. The time difference between first and second signal is drawn from

a normal distribution with a mean of 1.06 µs and a width of 0.30 µs. The processing of this modified pulse train will then proceed as described above. The results of the Feynman variance calculation with double pulsing included is shown in figure 5.

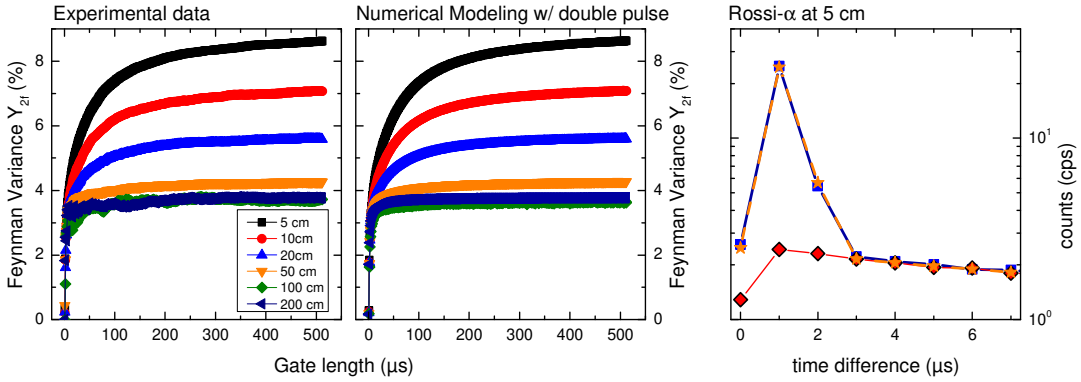

Figure 5: Comparison of the measured (left) and simulated (middle) Feynman Variance for different distances. In contrast to figure 3, the experimental data could be reproduced very well by incorporating a double pulsing of 3.7% in the post-processing of the simulation data. On the right, the beginning of the Rossi-α for 5 cm is shown in analogy to figure 4. With the inclusion of double pulsing, the peak could be reproduced very well.

These graphs are based on the same MCNP-simulation results as those in figure 3, but include the effect of a double pulsing probability of 3.7%. This results in a very good agreement between numerical modelling and experimental data. The shape of the Feynman Variance and the limiting value R_{2f} matches very well for all distances. Also the peak in the Rossi-α data could be replicated with this approach.

4. Discussion

The findings from section 3 show that the detailed numerical modeling yields results that are in very good agreement with the experimental data. The count rate is easily reproduced to a few percent without any artificial scaling of the data. Only the efficiency of the neutron tube needs to be scaled, so that the simulation results from MCNP are equal to the manufacturer stated value. One contribution of this scaling is the unknown composition of the quenching gas as this is considered proprietary information. Instead, the gas was simulated as pure ^{3}He with the nominal pressure. This definitely leads to an overestimation of the sensitivity, which results in the need of the scaling.
For the multiplicity distribution and especially the Feynman variance, the numerical method has to be refined. The experimental data can be reproduced very accurately, when double pulsing is taken into account. This allows replicating the shape and absolute value of the Feynman variance and, at the same time, the peak in the Rossi-α data. The inclusion of double pulsing can be done entirely in the post-processing of the MCNP PTRAC date. Thus the most time consuming step, the Monte Carlo simulation of the detector response, is independent of this step.
The amount of double pulsing of 3.7% in the Fission Meter used in this investigation seems to be quite high. Measurements with a second Fission Meter indicate a much lower value in the order of 0.5%. This might point to a hardware problem of the Fission Meter used in this work, such as a defective preamp, a bad or faulty connection, or HV issues. This will be investigated in more detail in the future.
Nevertheless, the measurement data for unknown configurations of fissile material can be simulated with our approach. This can be done for an ideal Fission Meter that shows no double pulsing at all, and in addition the effect of double pulsing can be included. This work shows also that a small amount of double pulsing can have quite some influence on the evaluation of multiplicity data. Especially, the resulting Feynman variance values are larger, and the change of the shape of the Feynman curve results in fitted neutron die away times that are much smaller than their real values. Sometimes, the die away times can get unphysically small. In the case of the Fission Meter, the neutron die away time serves as an indication of additional moderator, which is thus hindered by the double pulsing.

5. Acknowledgements

This work was partly funded by the German Federal Ministry for the Environment, Nature Conservation and Nuclear Safety under contract number 3616R01683. The author would like to thank AMETEK/Ortec for providing an engineering drawing of the moderation assembly and GE Electric for providing an engineering drawing and technical information on the used ^{3}He-tubes.

6. References

[1] Reilly D., Ensslin N., Smith H., Kreiner S.; *Passive Nondestructive Assay of Nuclear Materials*; United States Nuclear Regulatory Commission, 1991

[2] Ensslin N., Harker W.C., Krick M.S, Langner D.G., Pickrell M.M., Stewart J.E.; *Application Guide to Neutron Multiplicity Counting;* Los Alamos National Laboratory; 1998; LA-13422-M

[3] Ortec; *Fission Meter Portable Neutron Source Identification System User's Manual;* Rev. B; 2007

[4] Walston S.; *The Idiot's Guide to the Statistical Theory of Fission Chains;* 2009; Lawrence Livermore National Laboratory; LLNL-TR-414245

[5] D.B. Pelowitz, Ed.; *MCNPX Users Manual Version 2.7.0;* 2011; LA-CP-11-00438

[6] Rowland M.S., Alvarez R.A.; *Real-Time Multi-Mode Neutron Multiplicity Counter;* 2013, US Patent 8,384,004 B1

[7] Schumann O., not yet published

Monte Carlo simulations for the determination of the ^{235}U enrichment with the infinite thickness methodology

A. Borella[1], R. Rossa[1]

1) SCK•CEN, Nuclear Science and Technology unit,
Boeretang 200, B-2400 Mol, Belgium

Email: aborella@sckcen.be

Abstract:

One of the ways to determine the ^{235}U enrichment with non-destructive assay is by using the so-called enrichment meter. This method measures the enrichment from the observed intensity of 186 keV gamma line and relies on the fact that, if the sample under investigation is large enough, the amount of 186 keV quanta emerging of the sample does not depend on the physical form of the sample material. Hence, the name of infinite thickness.

According to this method, a gamma ray detector is equipped with shielding and collimation and guidelines to determine the geometry configuration to ensure that the infinite thickness conditions are met are given in the KfK report 3752 [1].

In this work, we evaluate with Monte Carlo simulations the infinite thickness conditions for a reference case of a U_3O_8 sample with a collimator of 3 cm diameter and 1 cm thickness; in addition, we investigate the impact of parameters such as the density, chemical form, non-heterogeneity of the sample on the calculated number of 186 keV gamma-rays emerging from the sample.

Keywords: Infinite thickness; Uranium enrichment; Monte Carlo; modelling

1. Introduction

The KfK report 3752 [1] is a document that describes the basics of the ^{235}U enrichment assay technique with the so-called “enrichment meter” principle and discusses aspects related to systematic errors associated to the measurements. The main features of the Certified Reference Material EC-NRM-171/NBS-SRM-969 are also discussed.

The determination of the ^{235}U enrichment relies on the detection of the 186 keV gamma-ray. The number of detected quanta is proportional to the ^{235}U content of a sample, the emission probability and the total detection efficiency. The total detection efficiency depends also on the sample characteristics; given the finite thickness of the sample and the large self-attenuation at 186 keV, a correction to account for the photon attenuation in the sample material is necessary. This task is however difficult, since it requires knowledge such as size and density about the sample being measured that are not always known.

These problems can be overcome by carrying out measurements in conditions such that the sample is (quasi) “infinitely thick”. In an “infinitely thick” sample the gamma radiation coming from layers beyond a certain thickness are self-absorbed in the sample itself and do not escape the surface of the sample being assayed. This means that the number of 186 keV quanta emerging from the sample does not depend on the sample thickness. If the infinite thickness condition is met, the enrichment is proportional to the measured 186 keV gamma-rays count rate provided that the enrichment is uniform throughout the sample and the measurements are carried out in a counting geometry where detector and collimator are fixed [1].

Ref. [1] describes the use of reference material EC-NRM-171/NBS-SRM-969 to determine the proportionality constant. In addition, it gives quantitative guidance to define the collimator height and diameter such that the infinite thickness condition can be met in all directions when measuring with a sufficiently large detector. Ref. [1] also goes to great length to discuss the impact of other factors such as sample matrix materials and container walls.

It can be proven that, assuming a 1-dimensional geometry, the number of 186 keV photons *G* per unit area emerging an infinite thick sample can be expressed as:

$$G = \frac{ln2}{T_{1/2}} P_{186} \frac{\beta}{\sigma_U} E \qquad (1)$$

Where $T_{1/2}$ is the half-life of ^{235}U, P_{186} emission probability of the 186 keV gamma ray, σ_U the photon attenuation cross section for Uranium in cm^2, *E* the enrichment in atom percent. The factor β is matrix correction factor defined as

$$\beta = \frac{1}{\left(1+\frac{\sum_{i\neq U} N_i \sigma_i}{N_U \sigma_U}\right)} = \frac{1}{\left(1+\frac{\sum_{i\neq U} \rho_i \mu_i}{\rho_U \mu_U}\right)} \qquad (2)$$

and represents a correction factor for the fact the stoichiometry of the sample may contain elements *i* other than uranium. As indicated, β can be expressed both in terms of particle density *N* and attenuation cross section σ or density ρ and the mass attenuation coefficient μ. Equation (1) is valid if the sample is spatially homogenous in terms of enrichment and matrix composition. The equation remains valid also for other geometries [1] and local variation in the density do not affect *G* provided that the two above mentioned conditions are met.

Eventually the observed count rate is proportional to *G* taking into account other effects such as the intrinsic detector efficiency, solid angle and the presence of attenuators between sample and detector. A fixed detector-collimator setup is therefore needed to guarantee that the proportionality is kept throughout the measurements.

We have developed a model of one the measurement conditions suggested in [1] and carried out Monte Carlo simulations to determine the impact on the number of 186 keV quanta emerging from the sample due to quantities such as sample density, matrix material and sample size. In addition, the biases due to non-spatial uniformity of the and positioning on the sample are also studied. The results are presented in this paper.

2. Model

2.1. Reference case

Based on the design information available in [1] we built a model of a sample resembling reference sample EC-NRM-171/NBS-SRM-969 in the MCNP6 code version 6.1 [2]. The modelled sample consisted of U_3O_8 encapsulated in an 2 mm thick cylindrical aluminium container. The dimensions were larger than the actual reference sample to allow an easier investigation of the impact of radius and sample thickness. In addition, we also modelled a lead collimator on top of which the reference sample was positioned. The collimator height and diameter were arbitrarily set to 1 cm and 3 cm, respectively. The modelled geometry is shown in Fig. 1. A 1 mm distance between the collimator and the aluminium container bottom sample is also present to account for the recessed bottom form of the samples.

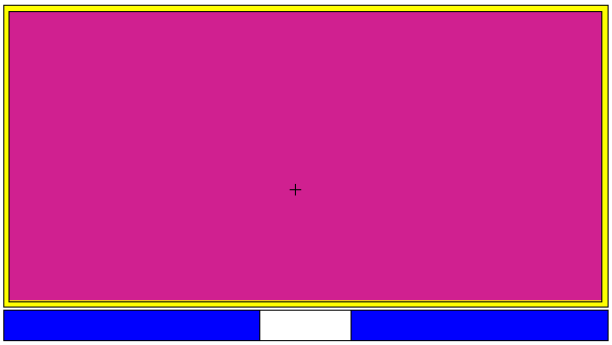

Figure 1: Geometry as modelled in MCNP6.

A source term represented by photons of 185.7 keV was uniformly distributed in the volume of the U_3O_8. The number of 185.7 keV photons emerging from the bottom of the collimator cavity was tallied. Only the elemental composition of the materials were modelled and only photons were transported in the simulations. It is important the notice that the enrichment does not affect the photon transport in the sample but only the number of emitted quanta as also proven by Eq. 1; the MCNP calculations are normalized per source quanta and therefore one has to multiply by the number of ^{235}U atoms and P_{186} to calculate the number of emerging photons. No detector was included in the simulations, but as explained above, for a given detector, the number of full energy counts is proportional to the number 185.7 keV photons emerging from the bottom of the collimator. The statistical uncertainty on the tally ranged between 0.01 and 0.05%.

In the reference case, we considered reference U_3O_8 as filling material with a density of 2.50 g/cm^3, and a 5 cm emission along Z, radius 5 cm. Such a radius is large enough that the infinite thickness conditions are not affected by the sample diameter. According to [1], for the given geometry and attenuator, when U_3O_8 reference sample with a density of 2.50 g/cm^3 is used in combination with a 1 cm height and 3 cm diameter collimator, the minimum sample amount that allows to collect 99.9% of gamma-ray is 165 g, with a corresponding sample thickness of 2.08 cm and radius of 3.17 cm. As stressed by [1] pg. 32, there can be more combinations of radius and thickness allowing a 99.9% sample thickness but with a larger mass of material.

2.2. Nuclear data

Ref. [1] quotes a value for the linear attenuation coefficient of 1.268 cm^2/g for U_3O_8 with an uncertainty of approximatively 5%. This number enters in the equations used to determine the infinitely thick conditions and one can expect different result when this quantity is changed. Ref. [1] neglects the effect of coherent scattering and explicitly indicates that the attenuation to be used is the “total narrow-beam cross section minus coherent cross section”.

In our work, we also investigated what values are used in the default library of MCNP6.1. In addition, we also verified the linear attenuation coefficient as given by the XCOM code of NIST [3] where the attenuation coefficients are given with and without coherent scattering. The effect of coherent scattering are accounted for by MCNP.

An overview of the linear attenuation coefficients given by Ref. [1], MCNP6 and Ref. [3] is given in Table 3 as well as the share of coherent scattering (% CS). There is a difference of about 1% on Uranium where also the impact of coherent scattering is higher.

Chemical species	Ref. [1]	MCNP6.1	XCOM		% CS
H	0.248	0.250	0.249		0.0
N	0.125	0.125	0.125		1.1
O	0.125	0.125	0.125		1.4

F	0.119	0.118	0.119		1.8
U	1.473	1.463	1.462		5.0
U_3O_8	1.268	1.259	1.259		5.0
UO_2	1.313	1.304	1.304		5.0
UF_4	1.145	1.137	1.137		4.9
UF_6	1.034	1.027	1.027		4.9
Uranyl Nitrate $UO_2(NO_3)2\times6H_2O$	0.767	0.762	0.762		4.7

Table 1: Overview of linear attenuation coefficients in cm^2/g and share of coherent scattering cross section (% CS).

2.1. Variations from the reference case

Several design variations were carried out to investigate their impact on the number of 185.7 keV photons emerging from the bottom of the collimator cavity. More specifically we have investigated the following sample related quantities:

- density of U_3O_8
- thickness
- chemical form of different U compounds
- radius
- non uniformity

The goal of these design variations was also to verify how they affect the emerging number of photons when for example the infinite thickness conditions are not met.

3. Results

3.1. Density variation

In the conditions of the reference case, the thickness of the sample is well beyond the value of the recommended thickness in [1]. We determined the number of emerging photons for different values of the sample density while keeping unchanged the other sample characteristics.
The results are shown in Fig. 2 and reveal that the expected number of emerging photons is not affected by the sample density for values starting from 1.25 g/cm^3. For values of the sample density of 1.0 g/cm^3 we observe a small decrease in the number of emerging photons. In ref. [1], an approximate minimum sample height for uniform U_3O_8 samples is given. For a density of 1.0 g/cm^3 the thickness value is 5.45 cm which is above the considered sample thickness.

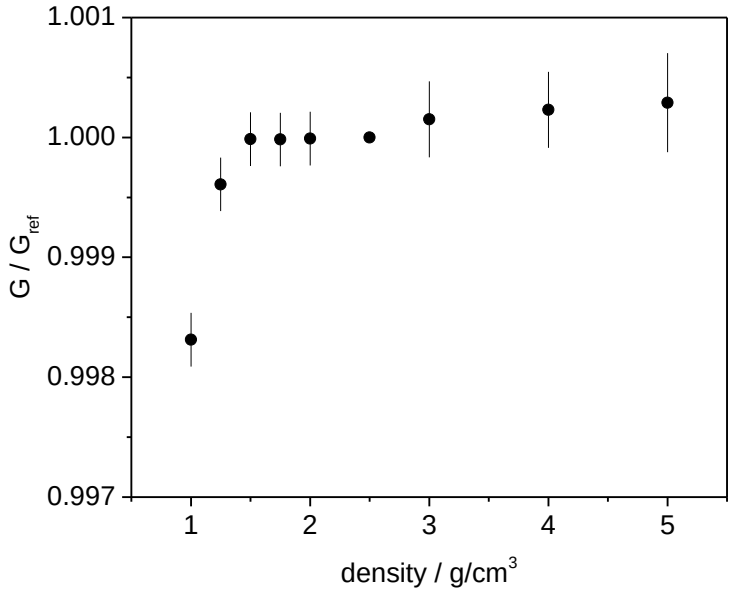

Figure 2: Number of emerging photons G as a function of the sample density compared to the reference case.

3.2. Chemical form

As explained in Eq. 1, the stoichiometry of the sample has impact on the number of emerging quanta through the factor β. A difference in the emerging number of photons is to be expected even if the dimension of the sample are always such that the infinite thickness condition is always met for all the chemical forms. This factor can be estimated from basic nuclear data as done in Ref. [1].
These coefficients beta were calculated for different chemical compounds and compared with the one given in Ref. [1]. The uncertainty was about 0.0006. The density of the material was 2.5 g/cm^3 for all the cases. The results agree well except for the Uranyl Nitrate case where a difference of about 1% can be seen. Since there are no major differences nuclear data for H, N, O the difference can be due the different linear attenuation coefficient for U.

Sample	This work	Ref. [1]
U_3O_8	0.9846	0.9849
UO_2	0.9888	0.9886
U	1.0000	1.0000
UF_4	0.9748	0.9750
UF_6	0.9623	0.9630
Uranyl Nitrate $UO_2(NO_3)2\times6H_2O$	0.9004	0.9098

Table 2: Emerging photons G as a function of the sample stoichiometry compared to the U case.

3.3. Sample thickness and radius

According to [1], a sample thickness of 2.08 cm and radius of 3.17 cm allows to collect 99.9% of the emitted quanta. We verified that 99.87$\pm$0.02 % of the emerging photons are tallied with those values of thickness and radius.

The number of emerging photons as function of the sample thickness for a radius of 5 cm was also determined. The results are given in Fig. 3. The data reveal an exponential trend which is consistent with the exponential attenuation of gamma radiation.

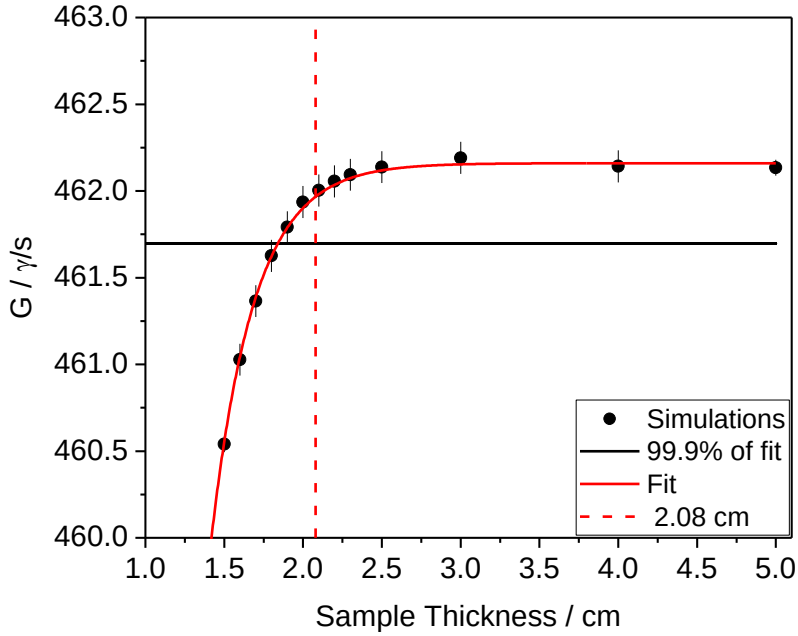

Figure 3: Number of emerging photons G as a function of the sample thickness.

A fit of the data revealed that that 99.9 % thickness is reached at approximately 1.84 cm. A direct comparison of these data with the data of [1] is not possible since the minimum sample thickness depends on the sample radius. Having a different radius may therefore result in a different value of the 99.9% sample thickness.

The number of emerging photons as function of the sample radius for a thickness of 5 cm was also determined. The results are given in Fig. 4. Also in this case, we observed that the count rate exhibits an exponential behaviour and the infinite thickness conditions are well met for the recommended value of 3.17 cm.

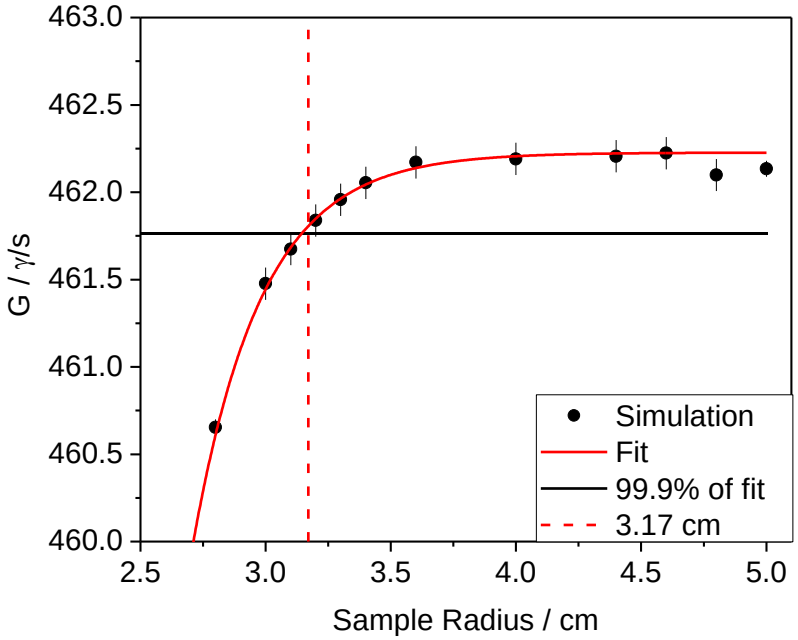

Figure 4: Number of emerging photons G as a function of the sample radius.

3.4. Sample non uniformity

We have investigated the impact of axial and radial non uniformity in the gamma source corresponding to variation in ^{235}U density and therefore in enrichment on the expected emerging number of photons.

3.4.1. Radial non uniformity

For a uniform cylindrical sample the number of photons emitted by a shell of radius *r* and thickness *dr* is proportional to the product *rdr* and therefore the radial probability function is described by a linear function [2]. We carried out simulations with a radial probability density function (pdf) for the source term in the form of

$$p = Ar^a$$

between a radius 0 and 5 cm;
Given that *p* must be normalized A is then

$$A = \frac{a+1}{R^{a+1}}$$

A value of *a* equal to 1 means a uniform uranium enrichment but the interpretation of other values of *a* is not straightforward. To help understanding the physical meaning of *a*, we calculated the corresponding ^{235}U enrichment as function of the radius that would generate such a pdf and it is shown in Fig. 5.

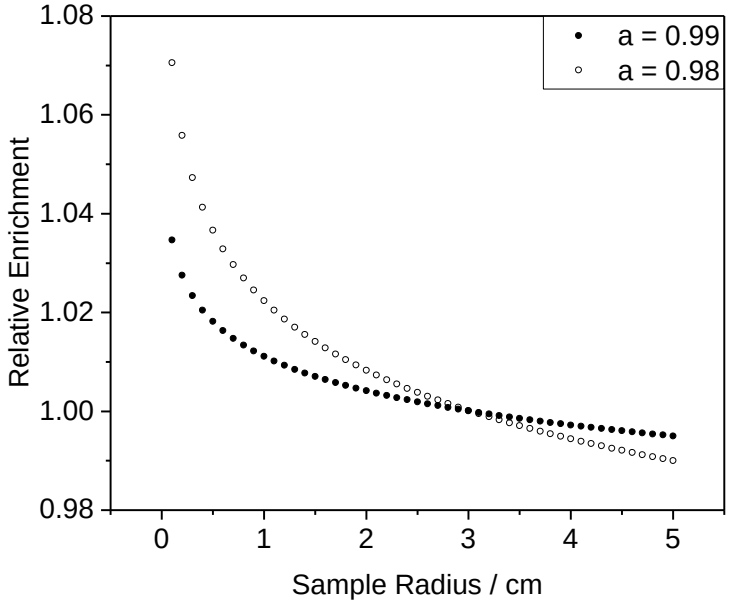

Figure 5: Relative enrichment as a function of the sample radius.

Values of *a* smaller than 1 correspond to cases where the enrichment is higher at the centre of the cylinder while for values of *a* larger than 1 the enrichment is larger at the edges of the cylinder.
The enrichment changes in a non-linear way as a function of the radius; it can be proven that at 5 cm it it deviates by *(a-1)/2* compared to the uniform case. So *a=0.99* corresponds to a change of the enrichment of 0.5% at 5 cm radius.

The obtained results are given in Table 3. The uncertainty is less than 0.001.

a	G/G_{ref}
0.98	1.022
0.99	1.011
1.01	0.990
1.02	0.980

Table 3: Emerging photons G as a function of the *a* parameter.

3.4.2. Axial non uniformity

We considered some arbitrary scenarios where the axial distribution of 186 keV gamma-rays was not uniform. The considered cases are step functions [4] defined in 96 steps along the 5 cm sample thickness. The values of the functions are as follow:

A. increasing by 11%

B. decreasing by 10%
C. with alternating steps equal to 1 and 0
D. with alternating steps equal to 1 and 0.95
E. with alternating steps equal to 1 and 0.9

Case	G/G_{ref}
A	0.953
B	1.048
C	1.085
D	1.003
E	1.006

Table 4: Emerging photons G as a function for the considered cases compared to the reference case.

The uncertainty is less than 0.001.

4. Conclusion

In this paper, a short overview of the measurement of the uranium enrichment with the infinite thickness method was provided. Based on the findings and recommendations of Ref. [1], we developed a Monte Carlo model of a measurement geometry including collimator, attenuator and sample. The model allowed to estimate the number of emerging photons through the collimator. Several design variations were implemented compared to a reference scenario. Quantities that were changed included density of the sample, thickness, chemical form, radius and non-uniformity.

The model results allowed to study the impact of such parameters and were compared with the recommendations given by Ref. [1]. In general, the obtained results agree well with the recommendations given by Ref. [1].

8. References

[1] Matussek P., *Accurate Determination of ^{235}U Isotope Abundance by Gamma Spectrometry, A User's Manual for the Certified Reference Material, EC NRM 171/NBS SRM 969*, KfK Report 3752, 1984
[2] Goorley J.T., et al., *Initial MCNP6 Release Overview - MCNP6 version 1.0*, LA-UR-13-22934, 2013
[3] Berger M.J., Hubbell J.H., Seltzer S.M., Chang J., Coursey J.S., Sukumar R., Zucker D.S. and Olsen K., *XCOM: Photon Cross Section Database (version 1.5)*. [Online] Available: http://physics.nist.gov/xcom [2018, March 5]. National Institute of Standards and Technology, Gaithersburg, MD.
[4] https://en.wikipedia.org/wiki/Step_function

Comparison of the Response of Handheld Neutron Detectors: Measurements and Calculations.

Martin Baron, Joachim Gregor, Jürgen Kesten, Emily Alice Kröger

Bundesamt für Strahlenschutz, Köpenicker Allee 120-130, 10318 Berlin

Abstract:

Handheld neutron detectors are used for various applications, for instance the detection of nuclear material, workplace monitoring and the search for neutron sources. Most of these simple instruments are not able to measure and display dose rates, which are important for estimating threats and for radiation protection.
Comparative measurements were carried out in order to gain information about the neutron dose rate response factors for two handheld neutron detectors at different source-detector distances in a building. It was found that the neutron count rate and the dose rate do not correspond to the 1/r²-law: the neutron dose rate response factors strongly depend on the surrounding structures. Monte-Carlo-simulations were carried out in order to reproduce the experimental results and in order to gain more understanding of the influence of the surrounding structures. The deviations from the 1/r²-law result mainly from increased neutron flux due to reflection. Additionally the reflected and moderated neutrons change the energy spectrum of the local neutron radiation field, resulting in an increased or decreased neutron flux response depending on the thickness and composition of the moderator used for the neutron detector.

Keywords: handheld neutron detector; neutron flux response; MCNP

1. Introduction

Handheld neutron detectors are used to detect and localize neutron-emitting radioactive materials and help identify special nuclear materials (SNM) [1]. These instruments are designed for optimized sensitivity in neutron detection, while keeping volume and mass in a suitable range to allow for handheld operation. Most of them are not able to show neutron dose rates, since this would require a far more complex detector composition [2].
Measurements with two different handheld detectors and one neutron rem counter were carried out in order to gain information on neutron dose rate response factors in a building at different heights and source-detector distances.
Deviations from the 1/r²-law were found, as mentioned by, for example, Vega-Carrillo et al [3] and Scallan [4]. In order to investigate the influence of the scattering and moderation of the neutron radiation, MCNP6-calculations [5] were carried out. In this paper, the measured and the simulated results are compared and discussed. A table of neutron dose rate response factors for the two handheld neutron detectors for measurements inside a large building is developed, in order to assist initial radiation protection and activity estimates at the scene during a deployment.

2. Experimental

The two handheld detectors used for the measurements were the neutron search detector KSAR1U.06 and the neutron search probe FHT 752 EH. The Biorem FHT 752H was used as a neutron rem meter. The measurements were carried out along the center line throughout a hall with approximate dimensions of 18 m x 30 m x 5 m (see Figure 1). The front and rear walls consist of glass windows. The 32 cm-strong concrete floor is covered by 3 cm thick marble slabs. The ceiling and the walls are also concrete. At a distance of ~23 m and +/- ~7.5° from the position of the source are two concrete pillars, also covered with marble slabs. Source and detectors were both kept at three different heights: on the floor, 1 m and 1.85 m and at nine different distances from 30 cm to

28 m. A Cf-252 source (Cf2.N02 Eckert & Ziegler) with a neutron emission rate of $8.3 \cdot 10^5$ n/s was used for the experiments.

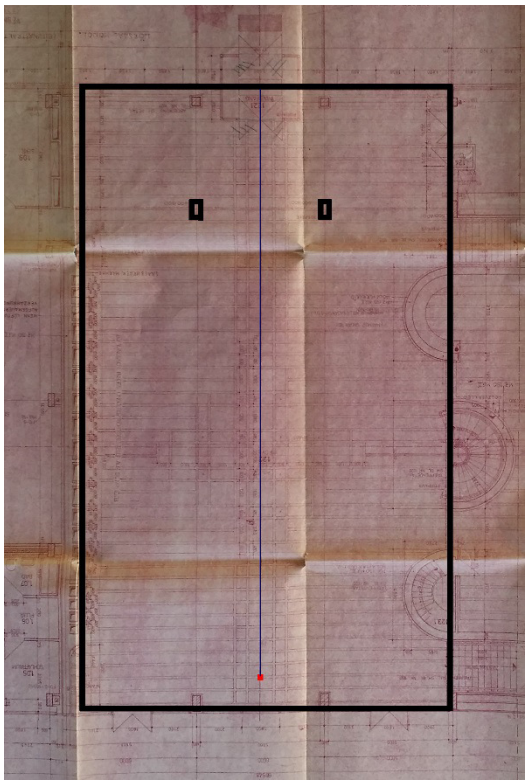

Figure 1: Plan of the hall where the measurements were carried out. The black lines mark the boundary of the hall and the pillars. The boundary on the right side is not strict due to stairways and open spaces. The red dot marks the location of the source. The measurement devices were located in a defined distance along the blue center line.

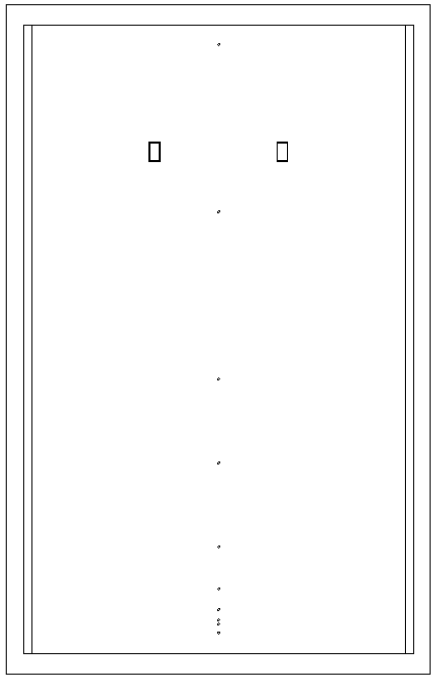

Figure 2: Model of the hall in MCNP. The outer most lines define the border of the simulation. The lowermost dot represents the location of the source. The other dots mark the position of the dose function (ICRP-21) modified F4-tallys.

3. Simulation details.

The MCNP-simulations were carried out using MCNP6 from the Los Alamos National Laboratory [5]. The code was run on Windows 7 computers with Intel processors, using single tasks and multitasking with Multitasking Preference Inventory (MPI). By using variance reduction via a superimposed weight window mesh and a sufficient number of particles, the relative error of the tally results was around or under 1%.
The KSAR1U.06 was simplified to three cylindrical He-3 tubes inside a cuboid moderator, neglecting housing and electronics. In the same way, the FHT 752 EH was modeled as one cylindrical He-3 tube in a cylindrical moderator. The Biorem was not modeled at all, due to missing information about the dimensions of the complex moderator inside.
For the source, a Watt fission spectrum for Cf-252 was used and its housing was modeled. The thermal neutron scattering model for the polyethylene moderator was used.
For the simulated dose rate, a dose function (ICRP-21) modified F4-tally was used. An F4-tally modified by FM-card to count the (n,p)-reactions of He-3 in the tubes was assumed to be the signal of the handheld detectors.
The material composition of the concrete was taken from PNNL-15870 Rev. 1 [6] material 97. In later simulations other material compositions for concrete were used in order to gain information about its influence.

4. Results

Due to the large variation in the source-detector distance, the count rates and the dose rates change over around four orders of magnitude (see Table 1, 2 and 3). In order to visualize the measurement data, the dose rates are divided by the calculated dose rate of a point source in vacuum and plotted in Figure 3a. The fluence response, R_Φ, of the handheld detectors, assuming the neutron flux of a point source in vacuum, is calculated and plotted in Figure 4a and 5a.

The theoretical neutron flux of a point source Φ at the distance r is:

$$\Phi = \frac{sourcestrength}{4\pi r^2} \qquad \text{(I)}$$

where the source strength is the neutron emission rate in neutrons per second. The fluence response is the quotient of measurement signal and neutron flux Φ.

$$R_\Phi = \frac{signal}{\Phi} \qquad \text{(II)}$$

The dose rate may be calculated from the neutron flux using the ambient dose equivalent coefficient 385 pSv·cm² for Cf-252 from [7].

$$ambient\ dose\ rate\left[\frac{nSv}{h}\right] = \Phi \cdot 0.385\ nSv \cdot cm^2 \cdot 3600\ s/h \qquad \text{(III)}$$

The graphs in Figure 3a, 4a and 5a show a deviation from the 1/r²-law for all measurement devices. The response of the FHT 752 EH varies significantly from the manufacturer's value (see Figure 5a). Measurements with four different detectors of that model show the same behavior. Helpful discussions with the manufacturer revealed that the data about the fluence response of the FHT 752 EH in the outdated manual was a rough estimate.

All handheld detectors, including the dose rate meter, show a similar behavior. In distances close to the source (within approximately 1 m) there is an increased signal for the measurement on the ground. The number of reflected neutrons is in the same order of magnitude as from direct neutron radiation. At elevated height, this is not the case. With increasing source-detector distance, the signal is greater than that expected from the 1/r²-law. While the direct radiation is decreasing with the source-detector distance, the fraction of reflected neutrons becomes more and more important. At distances larger than approximately 20 m, the signal from the reflected neutrons appears to fade. Due to the dimensions of the hall, there were no measurement points at longer distances possible. Calculations (see below) suggest that the effect is real and cannot be attributed to an effect of the pillars or the end of the hall.

Although the general trend of the signal is similar for all detectors, the size of the effect differs. For the FHT 752EH and the KSAR1U.06, the maximum response increase is by a factor of 10 or 8, respectively. For the dose rate meter, the ratio increases only by a factor below three. This result is likely caused by the differing effectiveness of the moderator around the detector tubes and, therefore, the differing response functions for the detectors (see Section 5).

In order to support and quantify the reasoning mentioned above, MCNP6 calculations were carried out. Figure 3b shows the ambient dose rate in the modeled hall at the location of the measurement devices divided by dose rate of a point source (see equation I, II and III). Here no detector is modelled, but the neutron flux F4-tally is modified by a built-in dose function. The graph reproduces the measurements in Figure 3a qualitatively. One reason for the divergence between the results displayed in Figure 3a and 3b might arise from the deviation in the response function of the dose rate meter compared to the built-in dose function from ICRP 21 applied to the simulated results. Another reason, especially applicable to the divergence at bigger distances, could be the simplification of the modeled hall (see Figure 2) and, additionally, the fact that the simulation completely neglects the humidity of the concrete walls. In the simulation the material composition of the concrete was taken from PNNL-15870 Rev. 1 [6] material 97. It has a mass fraction of hydrogen of 1%. Preliminary results from simulations using concrete compositions with a lower hydrogen content show a much better agreement to the measured data (not shown here). For the handheld neutron detectors KSAR1U.06 and FHT 752 EH, the simulated results (Figure 4b and 5b) correspond to the measurements. For all simulation results there is an underestimation of the signal, which suggests an oversimplification of the hall model as mentioned before. Taking to account the simplicity of the model, the agreement can be considered to be acceptable.

Source	on the floor		1 m height		1,85 m height	
Detector distance (cm)	dose rate (nSv/h)	uncertainty (%)	dose rate (nSv/h)	uncertainty (%)	dose rate (nSv/h)	uncertainty (%)
40	82150	1.06	63400	0.93	62750	0.93
60	38600	1.63	29500	1.43	26100	1.34
110	10100	2.81	9550	2.23	9020	2.17
210	2740	3.37	3230	3.66	2900	3.47
410	738	6.67	936	7.51	891	7.33
810	263	12.28	334	17.51	302	16.66
1210	135	14.34	167	13.82	155	15.38
2010	44	15.98	65	17.25	60	14.92
2810	21	16.71	27	9.51	26	21.15

Table 1: Measurement data of the Biorem FHT 752H

Source	on the floor		1 m height		1,85 m height	
Detector distance (cm)	meas. signal (cps)	uncertainty (%)	meas. signal (cps)	uncertainty (%)	meas. signal (cps)	uncertainty (%)
36	1578.00	0.32	1096.00	0.39	1060.00	0.39
56	678.00	0.50	483.00	0.59	455.00	0.61
106	175.00	0.80	162.00	0.83	140.00	0.88
206	50.30	1.05	59.00	1.19	49.70	1.29
406	17.20	1.79	21.80	1.59	21.10	1.62
806	8.08	2.01	8.72	1.94	9.64	1.85
1206	5.16	1.57	5.54	1.10	5.57	1.40
2006	2.26	2.15	2.49	1.05	2.50	1.16
2806	0.94	2.04	0.99	1.59	0.89	2.02

Table 2: Measurement data of the KSAR1U.06

Source	on the floor		1 m height		1,85 m height	
Detector distance (cm)	meas. signal (cps)	uncertainty (%)	meas. signal (cps)	uncertainty (%)	meas. signal (cps)	uncertainty (%)
34	385.50	0.46	231.00	0.60	198.50	0.65
54	131.50	0.80	107.00	0.88	83.70	1.00
104	33.70	1.57	35.80	1.53	28.20	1.72
204	10.60	1.98	13.40	1.76	11.46	1.91
404	4.31	2.78	5.21	2.53	5.05	2.57
804	2.09	3.99	2.34	3.77	2.43	3.70
1204	1.31	2.46	1.43	2.25	1.44	2.29
2004	0.58	4.38	0.66	2.14	0.64	2.35
2804	0.19	7.18	0.25	3.45	0.23	4.31

Table 3: Measurement data of the FHT 752 EH

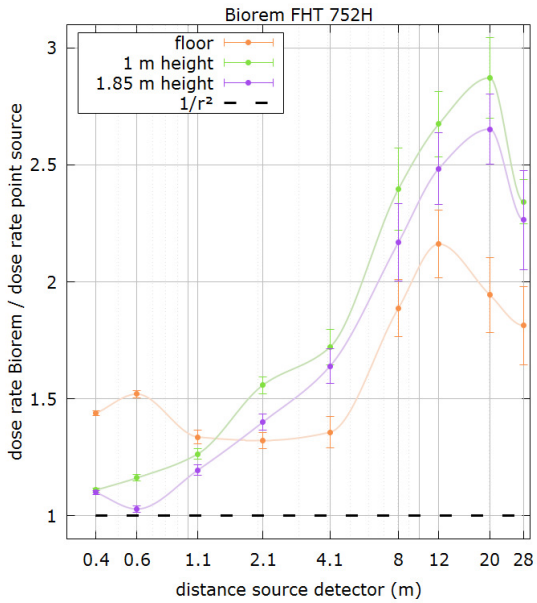

Figure 3a: Dose rate measured by Biorem FHT 752H divided by the calculated dose rate of a point source according to equation III at three different heights vs. source-detector center distance; the measured points are connected for guiding the eye only.

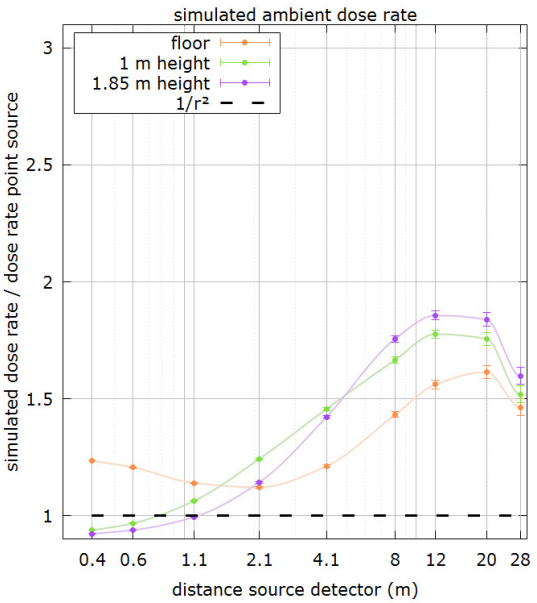

Figure 3b: Dose rate resulting from the MCNP calculation (F4-tally modified with the dose function from ICRP-21) at the positions of the measurement device Biorem FHT 752H divided by the dose rate of a point source according to equation III at three different heights vs. source-detector center distance; the points are connected for guiding the eye only.

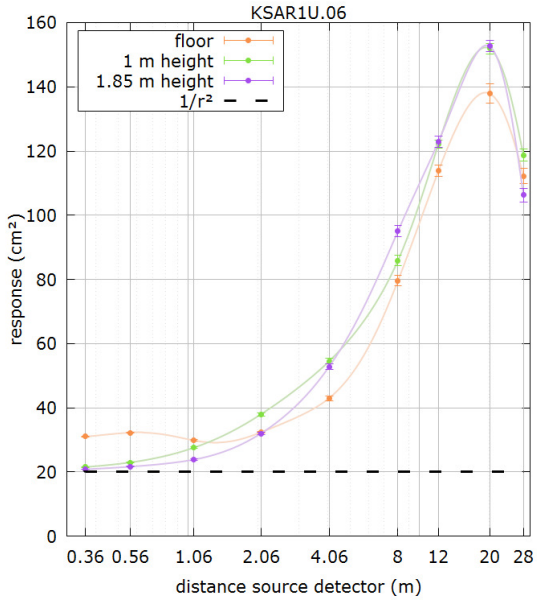

Figure 4a: The response according to equation II using the measurement signal of the neutron search detector KSAR1U.06; the measured points are connected for guiding the eye only. The dashed line at 20 cm² represents the manufacturer's data.

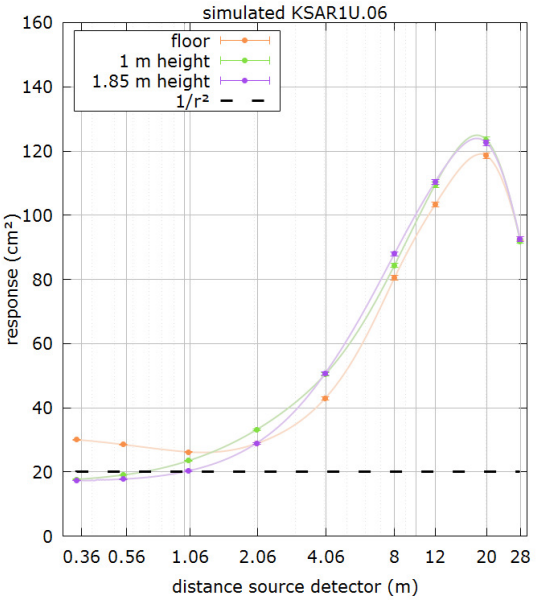

Figure 4b: The response according to equation II using the simulated signal of the neutron search detector KSAR1U.06; the points are connected for guiding the eye only. The dashed line at 20 cm² represents the manufacturer's data.

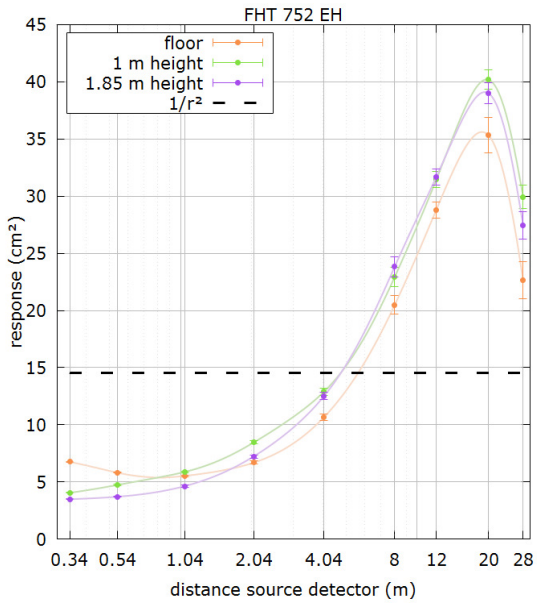

Figure 5a: The response according to equation II using the measurement signal of the neutron search probe FHT 752 EH; the measured points are connected for guiding the eye only. The dashed line at 14.55 cm² represents the manufacturer's data (10.5 ips/µSv/h for Cf-252).

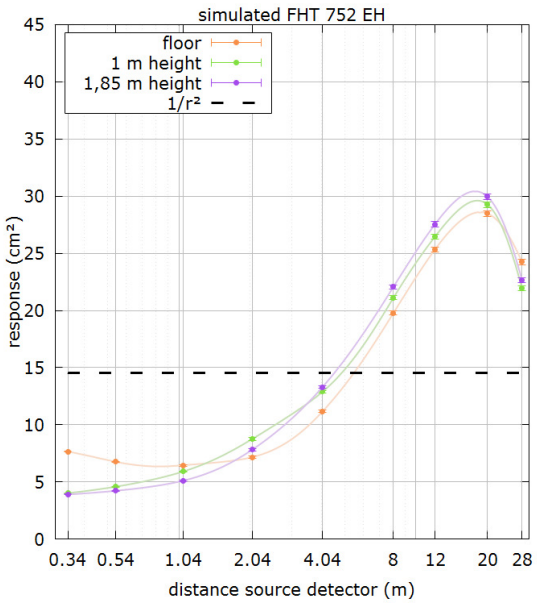

Figure 5b: The response according to equation II using the simulated signal of the neutron search probe FHT 752 EH; the points are connected for guiding the eye only. The dashed line at 14.55 cm² represents the manufacturer's data (10.5 ips/µSv/h for Cf-252).

5. Discussion

As suggested in Section 4, the dominating effect leading to the increased measured signal is an increased neutron flux compared to the neutron flux of a point source (see equation I). The quotient of the simulated neutron flux and the neutron flux of a point source (see equation I), shown in Figure 6 follows the same trend as shown in Figures 3a to 5b. The quotient rises at a distance of 20 m to a value of 5.9 at 1.85 m height. Figure 3c, 4c and 5c show the same quantity as in Figure 3b, 4b and 5b, respectively, but with the simulated neutron flux substituted for the neutron flux of a point source (see equation I). The graphs still do not show parallel lines, thus there are additional effects besides the increased neutron flux at longer distances compared to the point source. While for the KSAR1U.06 and FHT 752 EH there is still an increase in the response at larger distances, the dose rate decreases with increasing distance compared to the dose rate of a Cf-252 point source with the simulated flux.

The energy distribution of the neutron radiation gives an explanation for these results. In Figure 7, the simulated neutron energy spectrum is shown for the source and at a source-detector distance of 30 cm and 20 m within the model of the measurement location. The source spectrum is a Watt fission spectrum with its maximum at around 1 MeV. Close to the source, at 30 cm, thermalized neutrons already dominate the spectrum. The further away from the source, the fewer fast neutrons are present.

The response functions of the simulated measurement devices are plotted in Figure 8. The KSAR1U.06 and FHT 752 EH are both most sensitive for neutrons with a kinetic energy between approximately 1 eV and 2 keV, with a broad maximum around 10 eV. Therefore, the response increases at larger source-detector distances due to the enhanced portion of slow and intermediate neutrons. The Biorem FHT 752 H response function is designed to mimic the dose function. Its response function does not completely satisfy that goal as shown for a similar model in the technical note from CERN [8]. Its maximum in response is around 4 keV at significantly higher energy than for the other detectors. Thus, the response decreases along with the portion of fast and intermediate neutrons.

At distances longer than 20 m the decrease in measurement signal for all measurement devices is also seen in the simulations. Measurements at longer distances than 28 m were not possible, but in simulations with an increased room size the signal decreases even below the 1/r²-law estimate. This was also observed in the measurement at 70 m (result

0.1 cps, expected 0.4 cps, measuring thermal neutrons outdoors) carried out by A.J. Peurrung et al. [9]. At such distances from the source, most of the neutrons are already thermalized. Additional collisions do not significantly increase thermalization, but instead lead to the capture of thermalized neutrons by the surrounding material. Thus the count rate decreases.

The question could be raised as to whether these measurements and simulations are transferable to other structures. The marble slabs are a unique feature of the measurement location. In one simulation, the marble slabs were exchanged with ordinary concrete. As a result, the neutron flux changes only slightly. The dose rate is lowered by about 7 %, while the signal of the FHT 752 EH decreased by only 2 %. Variation of the material compositions of the simulated ordinary concrete leads to a change in the dose rate at 20 m of roughly about 25 %. The simulated signal of the handheld devices at this distance may even vary as much as 40 %. Preliminary results point to an important influence of the hydrogen content, similar to that seen for shielding [10]. By changing the hydrogen content one may fit the simulation to the measured data. The aim of this investigation was to implement a rather simple model of the hall not to carry out data fitting. Other simulations (not shown here) reveal that the influence of the concrete pillars is nearly negligible. Despite the marble slabs, the hall is an ordinary concrete hall. Measurements in concrete halls with similar dimensions should reveal similar results. As is already known, the dimensions have an important influence. The closer the walls, the stronger the influence of reflected neutrons.

Additionally to the detailed analysis of the influence of the material composition of the concrete, the influence of the human body that holds the device also has to be considered in future experiments and calculations. Also, other commonly used and more up-to-date devices need to be examined. The goal would be to model scenarios that are important to security and civil protection authorities.

As a result of this investigation, a table (Table 4) with conversion factors was developed for initial estimates during a deployment using the KSAR1U.06 and FHT 752 EH. These factors are only valid to Cf-252 sources. Moderated sources or (α,n)-sources need to be investigated in future experiments.

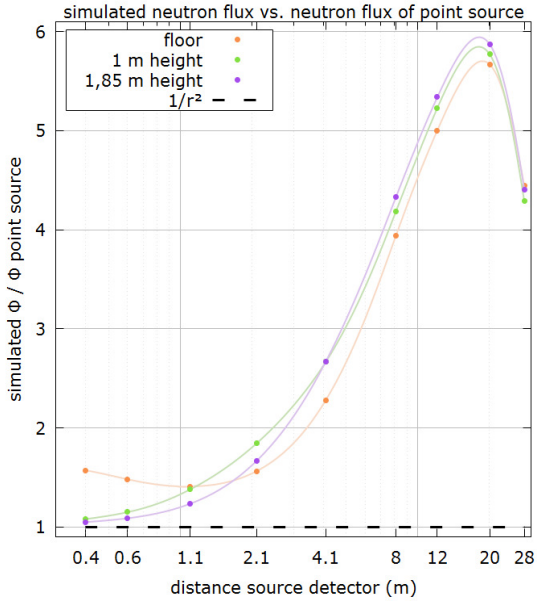

Figure 6: Simulated neutron flux vs. the neutron flux of a point source according to equation I at the positions of the measurement devices; the points are connected for guiding the eye only.

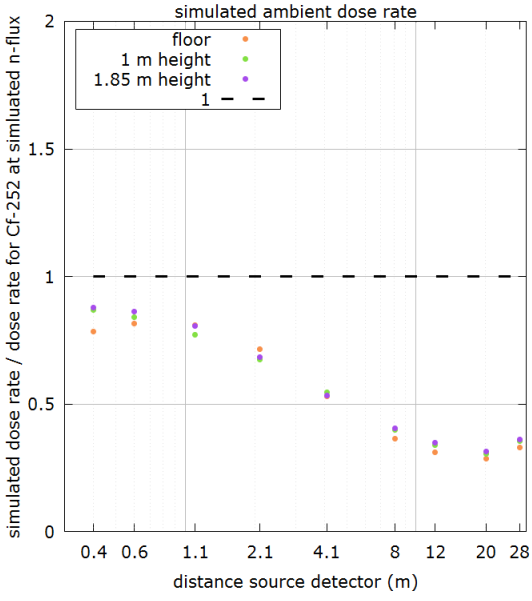

Figure 3c: Dose rate resulting from the MCNP calculation (F4-tally modified with the dose function from ICRP-21) at the positions of the measurement device Biorem FHT 752H divided by the dose rate calculated via the ambient dose equivalent coefficient 385 pSv·cm² for Cf-252 by using the simulated neutron flux.

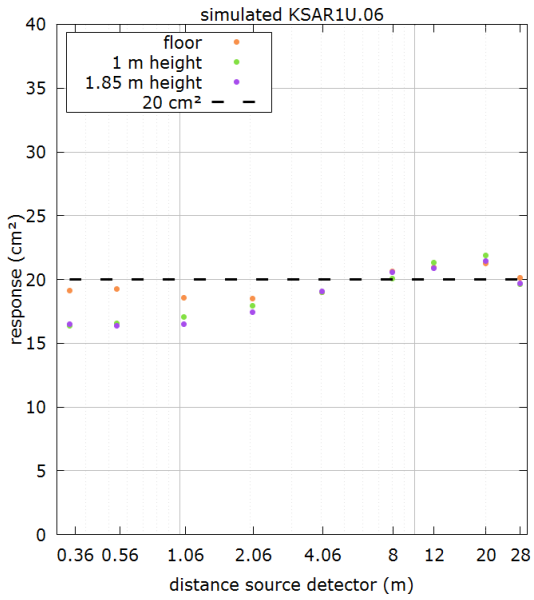

Figure 4c: Simulated signal of the neutron search detector KSAR1U.06 divided by the simulated neutron flux. The dashed line at 20 cm² represents the manufacturer's data.

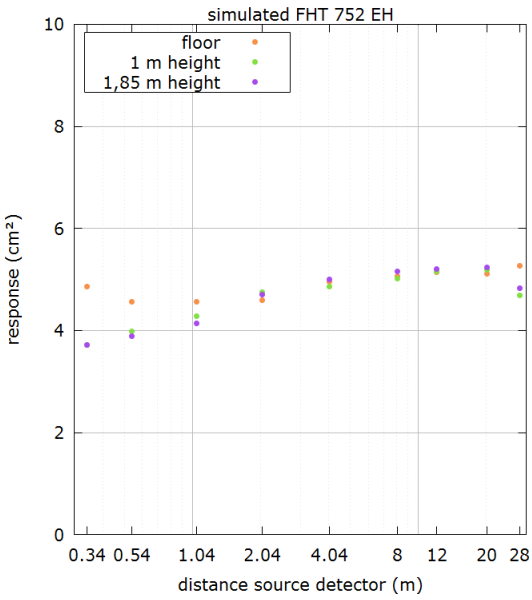

Figure 5c: Simulated signal of the neutron search probe FHT 752 EH divided by the simulated neutron flux. The manufacturer's data is not shown (14.55 cm²).

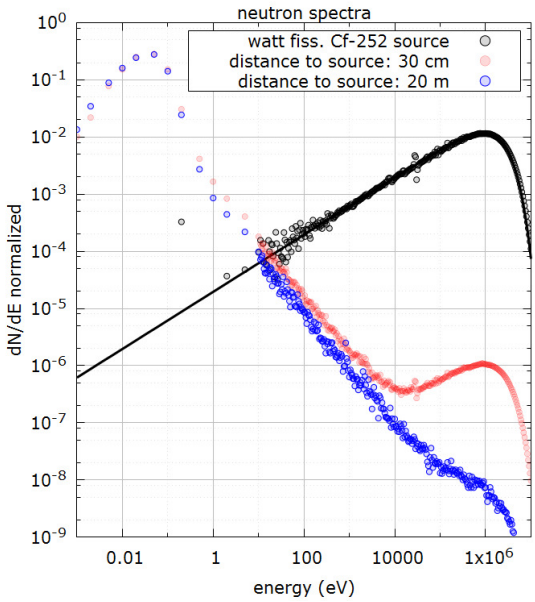

Figure 7: Simulated neutron energy spectra of the neutron radiation from the source (black) and at 30 cm from the source (red) and at 20 m from the source (blue). The black line represents the Watt fission spectrum for Cf-252. The spectra are normalized to an integral of one.

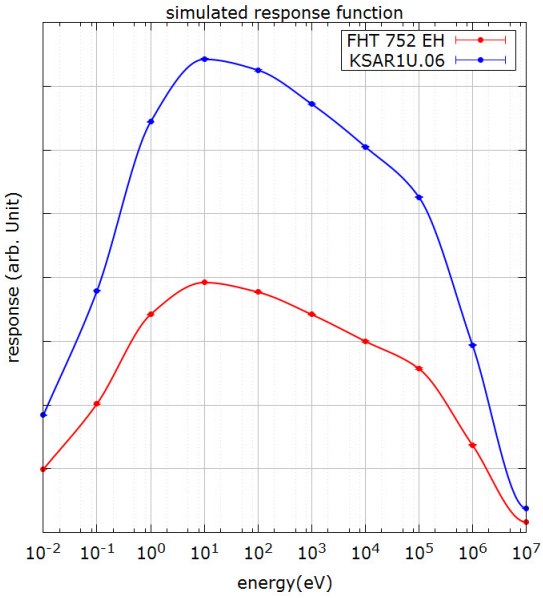

Figure 8: Simulated response function of modeled KSAR1U.06 and FHT 752 EH; the points are connected for guiding the eye only.

Source Detector distance (m)	KSAR1U.06 (µSv/h per cps)	FHT 752 EH (µSv/h per cps)
under 1	0.070	0.40
1 to 3	0.060	0.30
3 to 12	0.040	0.15
12 to 28	0.025	0.10

Table 4: Condensed measurement signal to dose rate conversion factors for Cf-252 for the two handheld detectors in a concrete hall

6. Conclusion

A series of measurements to compare the response of handheld neutron detectors inside a building was carried out and a deviation from the $1/r^2$-law was observed. MCNP6 simulations of simplified models of the measurement devices and the building match the measurements qualitatively and provide explanations for the deviations from the $1/r^2$-law. The agreement of the MCNP6-calculations to the measurement results is satisfactory for the initial radiation protection and activity estimations in a deployment and allows for the future modelling of scenarios that are important to security and civil protection authorities.

7. Acknowlegements

We would like to thank RSICC and LANL for providing the MCNP6 package. We are grateful for the constructive discussions with Thermo and we would like to thank the BImA for allowing the measurements to be carried out in their building.

8. References

[1] Rosenstock W., Berky W., Chmel S., Friedrich H., Köble T., Risse M., Schumann O.; *Hand-held devices for the detection of clandestine nuclear material on-site;* IAEA Wien: Symposium on International Safeguards; 2010

[2] Cosack M., Lesiecki H.; *Dose Equivalent Survey Meters*; Radiation Protection Dosimetry, Volume 10, Issue 1-4; 1985; Pages 111–119

[3] Vega-Carrillo H.R., Manzanares-Acuña E., Hernández-Dávila,V.M., Gallego E., Lorente A., Donaire I.;*Water-extended polyester neutron shield for a 252Cf neutron source*; Radiation Protection Dosimetry, 126 (1-4); 2007; Pages 269-273

[4] Scallan L.M.; *EFFICIENCY MODELING FOR NEUTRON DETECTORS*; Thesis; Colorado State University; 2014

[5] Goorley, T., James M.; Booth T., Brown F., Bull J., Cox L.J., Durkee J., Elson J., Fensin M., Forster R.A., Hendricks J., Hughes H.G., Johns R., Kiedrowski B., Martz R., Mashnik S., McKinney G., Pelowitz D., Prael R., Sweezy J., Waters L., Wilcox T., Zukaitis T; *Initial MCNP6 Release Overview - MCNP6 version 1.0*; LA-UR-13-22934; Los Alamos National Laboratory; 2013

[6] McConn R.J., Gesh C.J., Pagh R.T., Rucker R.A., Williams R.G., *Compendium of Material Composition Data for Radiation Transport Modeling*; PNNL-15870 Rev. 1; Pacific Northwest National Laboratory ; 2011

[7] *Neutron reference radiation for calibrating neutron measuring devices used for radiation protection purposes and for determining their response as a function of neutron energy;* International Organization for Standardization Standard ISO/DIS 8529, Geneva; 1989

[8] Aza E., Caresana M., Cassell C., Colombo V., Damjanovic S., Gilardoni S., Manessi G.P., Pangallo M., Perrin D., Silari M.; *Instrument intercomparison in the stray neutron field around the Proton Synchrotron*, CERN-RP-2013-054-REPORTS-TN-V.2; CERN, Geneva; 2013

[9] Peurrung A.J., Stromsworld D.C., Hansen R.R., Reeder P.L., Barnett D.S.; *Long-Range Neutron Detection*; PNNL-13044, Pacific Northwest National Laboratory; 1999

[10] Piotrowski T., Mazgaj M., Żak A., Skubalski J., *Importance of Atomic Composition and Moisture Content of Cement based Composites in Neutron Radiation Shielding*; Procedia Engineering, Volume 108; 2015; Pages 616-623

Using MCNP to Reduce the Background Sensitivity of a Non-Destructive Assay Passive Neutron Coincidence Counting Chamber

Vittoria Baldioli, Paul Mullarkey, Ali Coghill, Natalie Bain, Avril Cormack, Richard Gunn, Douglas Paton

Dounreay Site Restoration Ltd, Dounreay, Thurso, Caithness, Scotland
E-mail: vittoria.baldioli@dounreay.com, paul.mullarkey@dounreay.com

Abstract

A Passive Neutron Coincident Counter has been designed and operates successfully to assay waste materials at Dounreay. Due to size constraints and operating plant limitations i.e. access door size and small room deployment, the system incorporated only 2cm external Polythene shielding before the thermal neutron Cadmium filter. The purpose of the external polythene shielding is to thermalize external sources of epi-thermal and fast neutrons which are then absorbed by a 2mm layer of Cadmium. Hence the intention is to reduce the background neutron count rate to a minimum as far as possible in order to 1) improve the measurement stability (systematic errors arising from variations in the background) and 2) reduce as far as practicable the PNCC "Accidentals" count-rate thus improving random statistical errors associated with the measurement.

During the routine (best practice) trending of daily control chart measurements it was noticed that the Passive neutron Totals count-rate varied between 300cps and 800cps. At the same time the co-incident reals neutron count rate was an order of magnitude lower and of little value in spotting adverse detector trends. Additionally, the close proximity of operators in-front of and near the instrument during measurements was observed. A suite of MCNP models of the PNCC instrument in its operating environment were benchmarked and Totals neutron count-rates were calculated with a simulated operator in the room and with additional floor mounted slabs of Polythene shielding.

The benchmarked MCNP models matched the instrument neutron Totals within 8%. The MCNP background neutron rate with an operator present / not present closely matched the control chart count-rates. After additional Polythene shielding surrounded the instrument the observed reduction in the Totals neutron count-rate closely matched the MCNP modelled neutron count-rate. The modelling also highlighted the effect on measurements of an operator being in the vicinity of the instrument during a measurement and so the instrument operating instruction was changed to exclude operators from the vicinity during measurements. Finally, it was recognised at the end of the exercise that the above works from MCNP allowed a very simple qualitative yet favourable ray-traced assessment computation of dose-rates 12µSv/hr which lies within the health physics measured range of 3µSv/hr up to 16µSv/hr.

Keywords: MCNP; Non Destructive Assay; Passive Neutron

1. Introduction

The background sensitivity of a Non-Destructive Assay Passive Neutron Co-incidence Counting (PNCC) system employed on the Dounreay site for the assay of waste materials was investigated, with the ultimate aim to improve the measurement stability and reduce the statistical errors associated with the system.

The system investigated [1] consists of a counting chamber constructed from a cylindrical slab of high density polyethylene moderator, into which the detectors are fixed. These comprise six sets of five ^{3}He tubes surrounded by a 2mm thermal neutron

Cadmium filter, which provides maximised chamber efficiency by absorbing external surplus thermal neutrons.
An external polythene shield is also incorporated with the system, the purpose of these slabs being to thermalize the external sources of epi-thermal and fast neutrons, so that they can be absorbed by the aforementioned Cadmium liner.
Because of the size constraints of the locale in which the system is deployed, the polythene shielding had a thickness of 2cm only, well below the 6cm recommended for effective shielding by the literature. [2]

Because a low and stable background is important for neutron counting to achieve suitably low detection limits, a detailed study of the background was performed in order to assess normal variation and evaluate any additional variation caused by everyday work activities. Repeat measurements were taken over a number of days during normal working shifts, whilst normal work activities were being carried out. The data collected was used to quantify the normal variation in background and set up background fail settings for the system. A passive neutron totals count-rate variation of between 300cps and 800cps was observed during the trending of daily control chart measurements. It was strongly suspected that the high rate was attributable to sources of neutron radiation in the locale and the variation was likely due to transient moderators e.g. personnel in the vicinity of the instrument who act as effective neutron moderators.

The issue was thus two-fold: a high rate would introduce a systematic bias in the measurement error, whilst a varying background would generally introduce an undesirable transient effect. This study was therefore performed to obtain a practical solution to avoid the high background fluctuation, as well as permanently reduce the new totals rate, also given the constraint that the NDA system is located in close proximity to these sources of neutrons and cannot be relocated. Therefore, a shielding solution was required.

An investigation using MCNP [3] was thus initiated to look at what could be achieved 1) to reduce the variation seen in uncorrelated total neutrons and 2) how the net totals could be reduced to a level at, or better than, comparable PNCC instruments elsewhere.
MCNP was employed in the present study because of its suitability to examine theoretical changes in the system's design without the need to resort to potentially expensive and unpractical hardware modifications.

2. Methodology

Any MCNP study of this type follows 3 basic procedures. 1) Define the problem, specify the requirements and required outcome of the investigation; the "Modelling Specification". 2) Specify the models, usually a master base model, and then scenarios and benchmark. 3) Analyse the results and make recommendations.

The specification states unambiguously which materials are used, tallies required, the geometry and any major assumptions and limitations.
In this way, a complete model of the system is generated, and the required outcomes are agreed by all up-front. The ESARDA Good Practice Guide for the use of Modelling Codes in Non Destructive Assay of Nuclear Material [4] is a very useful reference.

2.1. System Model Benchmarking

Firstly, a model of the Passive Neutron Coincidence Counter was required.
The aim of this step of the work was to produce a referenced known 'benchmarked' MCNP model for the PNCC system, which could then be extended in scope to explore new performance prediction studies.
Once this model was set-up, a ^{252}Cf source was modelled within the system, in order to obtain modelled data that directly replicated the existing empirical daily measurements results. The difference in agreement between empirical and theoretical data was found to be 8.5%, and an error less than 0.2% and a stable Figure of Merit were achieved with a computational time of 16 minutes.
The good agreement between theoretical and empirical data, and the low errors obtained provided confident proof of the inherent validity of the benchmarked MCNP model, which could thus be used as a tool in the instrument performance study.

2.2. Models Suite

2.2.1. Geometry

In order to replicate the real-life set-up, the benchmarked model of the counting chamber

was modelled within a room. The nearby source of neutron radiation was rendered with a neutron cloud in a locale next door.

To examine the changes in the system's response due to the addition of moderating shields of different thicknesses, a suite of MCNP models was set-up, by modelling various thicknesses of moderating polythene slabs placed between the counting system and the next-door neutron cloud. Polythene thicknesses ranging between 0cm and 10cm were tested, in 1cm increments.

As mentioned, the effect of the presence of operators in the vicinity on the system response was also investigated. To this end, a phantom moderating shielding person was also included in the model, assuming approximately 80Kg of water (H_2O) at a full density of 1 gcm^{-3}. This provided a worst case but reasonable assumption, as water is around 80% of body mass by volume. A ltwr card was included in the models, in order to ensure the correct thermal neutron treatment at room temperature.

The geometry set up can be seen in figure 1, which shows MCNP x-y plane and x-z plane representation of the geometry to be converted into surfaces and cells, along with a 3D rendering of the consequently constructed model.

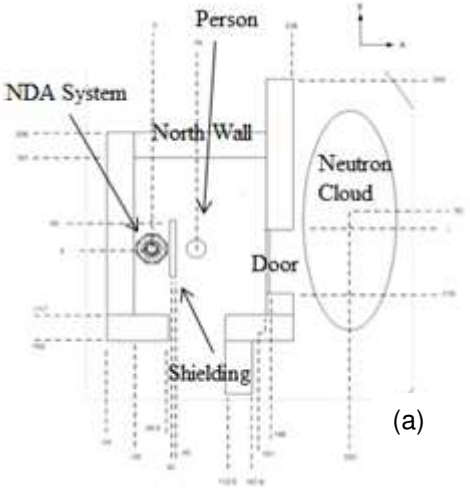

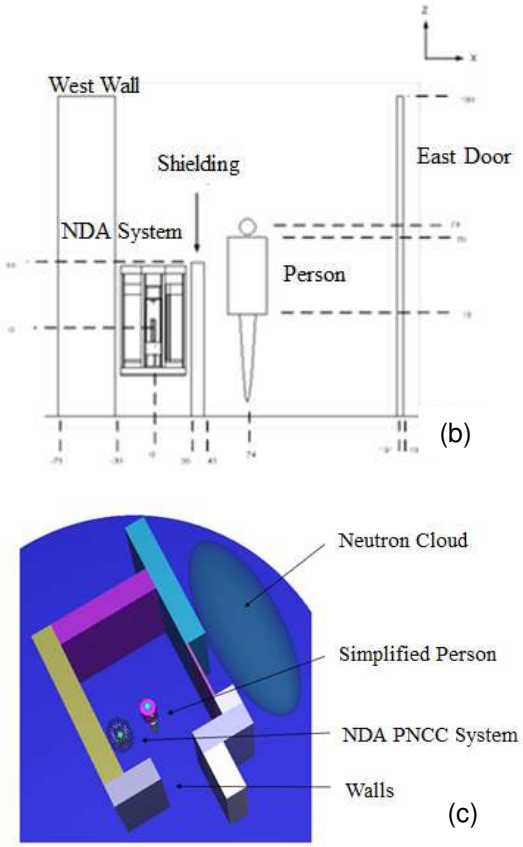

Figure 1: 2D x-y (a) and x-z (b) plane representation of the geometry universe. 3D rendering of geometry set-up (c), showing the counting chamber, the moderator shielding slab, and the phantom person, as well as the neutron cloud next-door. (Centre of chamber at x,y,z=0).

2.2.2 Source

It was recognised the high totals rate might be caused by various materials at discrete locations in the next-door room, each with their own specific neutron emissions, as well as individual emission spectra. However, it was reasoned that, as the neutrons pass through the wall and into the assay room, the differences in their spectra are smoothed out, and their origin species becomes less important.

Because of the above, and since ^{252}Cf is a spontaneous fission source often substituted for plutonium to calibrate passive neutron coincidence counting instruments, the neutron source was assumed to be, and modelled as, 100% ^{252}Cf. Moreover, reference empirical measurements already existed for ^{252}Cf in the measurement chamber.

The source term was thus set-up in the model as a constrained cylindrical source within an ellipse; in order to achieve a convergence to a stable result within a reasonable computational

time, the source was biased to emit particles in the negative x-direction, i.e. towards the system. This is represented in figure 2 below, showing a 2D rendering of the source of neutrons, with tracks for the first 250 particles. Obvious from the representation is the significant scattering taking place in the concrete walls compared to through the door.

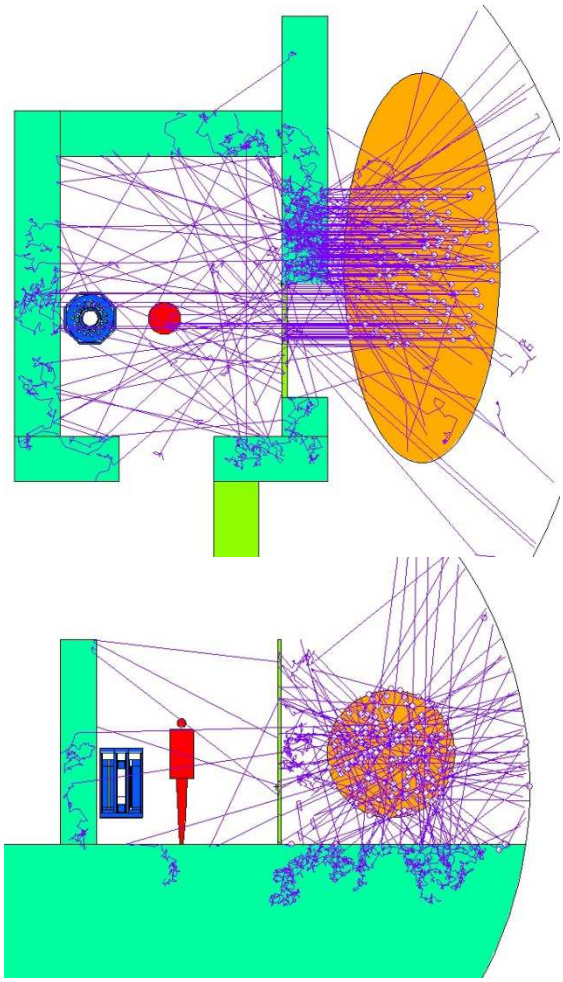

Figure 2: 2D x-y and x-z plane representation of tracks from the first 250 particles in the geometry universe, including scattering and random walks.

3. Results and Discussion

A series of MCNP models were run, and the effect on the instrument response for polythene shielding thicknesses of 0cm to 10cm was investigated, both in the presence and absence of a potential person standing next to the system.

The modelled MCNP F4 tallies resulted in a neutron chamber efficiency, which was scaled to give an effective neutron totals count rate in the chamber. These values are graphically represented as a function of polythene shielding thickness in figure 3 below, both with and without the presence of a moderating person standing next to the system, with the blue and the red polynomial respectively.

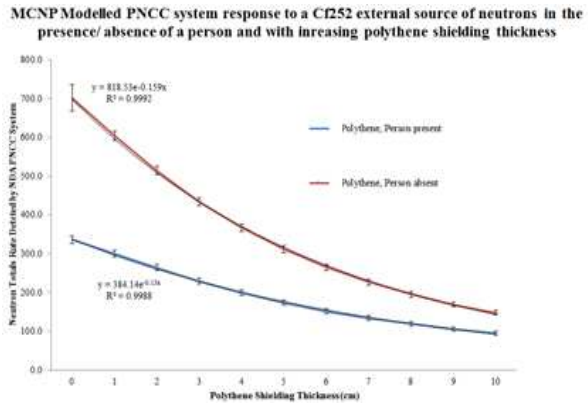

Figure 3: Theoretical neutron totals rate as modelled with MCNP as a function of shielding thickness, with and without the presence of a moderating person.

The first significant aspect of the modelled figures is the results relating to 0cm of extra polythene shielding, i.e. the original real life scenario. The theoretical neutron totals rates as modelled with MCNP were calculated to be ~336cps and ~702cps for with and without a person present, respectively. This is in extremely good agreement with the observed empirical fluctuations between 300 and 800cps, clearly indicating that a person in the vicinity of the instrument does provide a significant amount of background variation.

The other significant aspect of the results is the direct correlation between increasing shielding thickness and reduction of neutron background totals rate. Thus, additional polythene has a significant and obvious effect on the background.
Since any reduction in the background reduces the chances of an unrevealed fault remaining concealed, it is clearly advantageous to maximise the opportunity to detect any faults and thus potentially avoid erroneous reporting of materials. This can be achieved by employing slabs of shielding polythene between the counting system and an external source of neutrons. From the literature, (4) an extra 4cm of polythene shielding would be ideal for the system. This was also demonstrated in the present work, taking into account the theoretical results shown in figure 3, as well as the physical constraints of the system location.

All MCNP models passed all statistical tests, and a stable Figure of Merit and a maximum error of 0.52% on the F4 tally was achieved.

In order to scale the MCNP results to convert to a count rate figure, the neutron cloud was assumed to have an effective activity of 2MBq as it transported through the wall. This was deemed appropriate as Health Physics measurements in the assay room revealed dose rate measurements ranging between 3 and 16 μSv/h. Crudely correcting for the neutron cloud distance and the wall, and knowing the free space dose equivalent of a 1 MBq ^{252}Cf source at 1m, it was possible to perform a rudimental ray-traced assessment computation of dose rates of ~12μSv/h, which lie at the upper end of the Health Physics measurements.
This good agreement provided further reassurance that the modelling work produced a fair representation of the real life scenario investigated.

4. Conclusion

A model of a Passive Neutron Coincidence Counter was constructed and benchmarked with MCNP.
The system was modelled to replicate the real life situation at its physical location, which involved the presence of a nearby source of neutrons, and the system original shielding situation, i.e. only 2cm of polythene in place. The study was performed in order to investigate how to reduce the high fluctuation in neutron totals rates observed from daily background measurements, and generally reduce the background. The ultimate aim was thus to improve the measurement stability of the system and reduce the chance of erroneous material reporting, or of a system fault remaining undetected.

Because the fluctuation observed in the background was suspected to be due to human proximity with the system, the effect of a person standing in front of the system was investigated, as well as the effect that slabs of polythene of various thicknesses would have on the instrument response, if placed between the system and the external neutron source.
The models passed all statistical checks, and the theoretical results for the neutron Totals rates matched the empirically observed values within 8%. Moreover, a stable Figure of Merit and a maximum error of 0.52% on the F4 tally was achieved.

The MCNP calculated background neutron rates with or without the presence of a phantom person closely matched the empirically observed rates in the same conditions.
Moreover, the general modelled trend proved a direct correlation between increasing shielding thickness and reduction in background rates.

From the above results, because it was desirable to keep background rates both stable and low, it was possible to provide two recommendations. Firstly, the instrument operating instruction was changed to exclude human presence in the vicinity of the system during assays. Furthermore, an additional 4cm of polythene was incorporated as shielding to the system, which is in line with current practices and values quoted in the literature.

Finally, the present work also allowed a rudimental but favourable ray-trace assessment computation of dose rates of ~12μSv/h within the assay room, which is in good agreement with the Health Physics measured dose rates of 3μSv/h - 16μSv/h.

5. Acknowledgments

The authors would like to thank the plant operators who daily operate the NDA system and who also *moderated* our background study. Our appreciation also extends to all of our colleagues who offered support and expertise throughout the project.

6. References

[1] Burke K.; *Detail Design Report for the DSRL Packet Monitor (NDA62/63).* Antech; 2016.

[2] Reilly D. et al; *Passive Nondestructive Assay of Nuclear Materials;* LA-UR-90-732. Los Alamos National Laboratory; 1991.

[3] Goorley T. et al; MCNP6.1. Los Alamos National Laboratory; 2013.

[4] Chard P. et al; *A Good Practice Guide for the use of Modelling Codes in Non Destructive Assay of Nuclear Material;* ESARDA Bulletin 42. European Commission Joint Research Centre (EC-JRC).

Advanced Experimental Fuel Counter (AEFC) Model Results Compared to Measurements of Irradiated IRT Assemblies

Alexis Trahan[1], Holly Trellue[1], James Tutt[1], Karen Miller[1], Sapar Baytelesov[2], Fakhrulla Kungurov[2], Jalil Yusupov[2], and Umar Salikhbaev[2]

[1] Los Alamos National Laboratory, Los Alamos, New Mexico, USA
[2] Institute of Nuclear Physics, Tashkent, Uzbekistan

Abstract

Detection of neutrons from both active and passive measurements of irradiated nuclear fuel gives valuable insight into how much fissile material is present. The Advanced Experimental Fuel Counter (AEFC) instrument was used to measure irradiated IRT (In-Reactor Thimble) fuel assemblies from the WWR-SM research reactor at the Institute of Nuclear Physics (INP) in Tashkent, Uzbekistan. Spontaneous fission and (α, n) neutrons originate from the fuel itself and propagate through multiplication to detectors located on the outside of the assembly to give passive counts, which are proportional to burnup. Active neutron measurements with a ^{252}Cf source are further helpful in estimating fissile content. We have performed irradiation simulations for a representative model of an IRT-4M assembly using the Monte Carlo transport/burnup codes MCNP/*Monteburns* to determine the isotopic composition within the fuel and the code SOURCES to determine passive neutron source terms. These source terms are then propagated through a MCNP model of the AEFC instrument to the neutron detectors. Results of simulated and measured singles and doubles count rates are comparable and presented in this paper. Significant changes to the simulated results were observed with different initial fuel mass and density and the presence/absence of a control rod during irradiation, and a sensitivity study of the effects of these changes is also included.

1. Introduction

The Advanced Experimental Fuel Counter (AEFC) instrument was developed at Los Alamos National Laboratory (LANL) for underwater nondestructive assay (NDA) of spent nuclear fuel assemblies [1]. Simulations of fuel irradiation and neutron transport from the cooled spent fuel to detectors in the AEFC instrument were also performed. Six ^{3}He tubes are used to perform neutron coincidence counting in the AEFC both in passive measurements (fuel alone) and active measurements (fuel + ^{252}Cf interrogating source). An ion chamber (IC) is also used to measure gamma emissions from the fuel. The goal of measurements with the AEFC is to determine fuel parameters such as residual fissile mass of research reactor spent fuel.

In 2014, the AEFC was deployed on a field trial to measure irradiated IRT (In-Reactor Thimble) fuel assemblies from the WWR-SM research reactor at the Institute of Nuclear Physics (INP) in Tashkent, Uzbekistan. A range of fuel assemblies with varying burnup (and therefore fissile mass) and cooling times were measured using the AEFC, and fissile mass determination was demonstrated as discussed in Miller et al. [2]. This dataset serves as the foundation on which to build a library of spent IRT assemblies that could be used to develop a model-predict-measure-compare (MPMC) approach. This method entails modeling a variety of assemblies in order to predict the detector responses, then measuring real assemblies and comparing to the predictions to characterize the measured assemblies. The ultimate goal

would be to use the MPMC approach with the AEFC to verify IRT assemblies in the future. Representative irradiated IRT assemblies were created through simulations with the linkage code *Monteburns* between the Monte Carlo N-Particle transport code MCNP and the isotope generation and depletion code CINDER90 to recreate the conditions of the measured fuel in Tashkent [3] [4]. Spontaneous fission and (α, n) neutron source terms from the simulated assemblies were then inserted into a validated model of the AEFC instrument to predict detected neutron rates for comparison with experimental data.

2. AEFC Instrument

The AEFC instrument contains six boron-lined ^{3}He tubes embedded in high density polyethylene (HDPE) on one side of a fuel measurement funnel. The ^{252}Cf interrogation source, when used for active measurements, is located on the opposite side of the funnel forcing interrogating neutrons to travel through the fuel assembly to reach the detection region. The efficiency of a ^{252}Cf source in air in the interrogation slot is approximately 2.2%. The tungsten-collimated IC is located above the HDPE sheath and therefore measures a slightly higher axial region of the fuel than the ^{3}He tubes. Figure 1 shows diagrams of the AEFC instrument for reference. More detail on the geometry including dimensions, operating parameters, and mechanical design can be found in [5].

The ^{3}He detectors in the AEFC measure the total rate of neutron detections (singles rate) and the rate of time-correlated neutron detections (doubles rate). The doubles rate is used widely in NDA techniques as a signature of fission [6]. The IC performs gross gamma-ray counting. The IC signal is connected to a current-to-pulse converter (CPC) which produces transistor-transistor logic (TTL) pulses proportionally to the rate of gamma-ray detection in the IC. The TTL pulses from the IC are fed into a shift register (JSR-15) along with the ^{3}He tube signals so that a single data acquisition and analysis unit can be used for both detector types. Because the AEFC is an underwater measurement system, all signal and high and low voltage cables run from the instrument to the data acquisition unit on dry land through Tygon tubing.

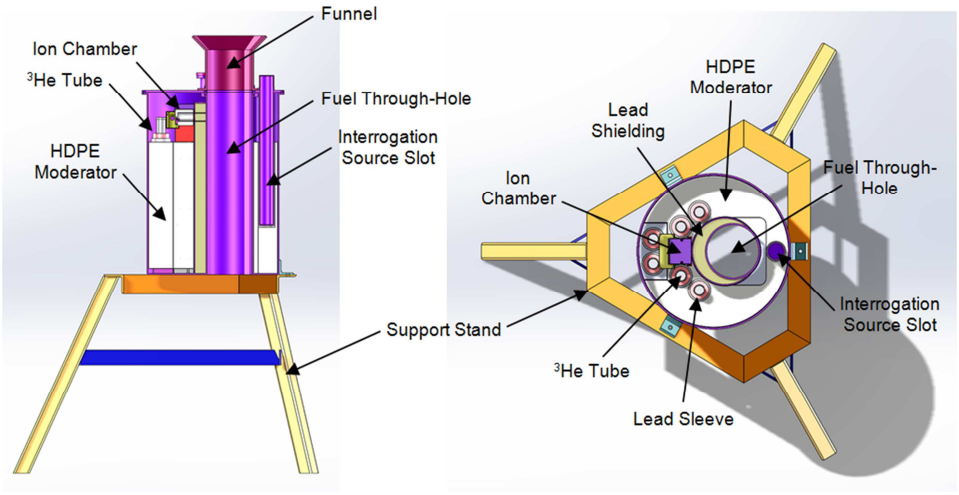

Figure 1. Cross-sectional and top-down view of the AEFC instrument from *[2]*.

3. Spent Fuel Parameters

A subset of the assemblies measured in the 2014 field trial are used for the simulation comparison. The purpose of comparing with the simulated assemblies is to try to identify logical trends in the AEFC instrument response to fuel parameters and ultimately, to use the variety of simulated assemblies to create a MPMC approach for the AEFC to characterize spent fuel. Therefore, assemblies chosen for

comparison displayed the most logical and physical trends in the measured response for practical comparison to simulation. The spent IRT fuel assemblies used in this work are all 19.75%-enriched UO_2-Al fuel with a total length of 882 mm and an active length of 600 mm [2]. The assemblies used all have six concentric square fuel plates and a declared burnup between 55-62%, where burnup is defined as the percent of ^{235}U depleted during irradiation in the core. The assemblies were discharged between 2-12 years prior to the field trial.

4. Modeling Methodology

We performed irradiation calculations with the code *Monteburns* to determine the isotopic composition of fuel in a variety of IRT-4M assemblies as a function of burnup [7] [8]. *Monteburns* links the Monte Carlo transport code MCNP to the isotope generation and depletion code CINDER90 or ORIGEN-S to perform system-dependent transmutation calculations [3] [4] [9]. One of the challenges in comparing results from the simulations to the experiments was not knowing the detailed reactor operating conditions during each irradiation. An infinitely-reflected IRT assembly MCNP model with six tubes and 19.75% enriched uranium (UO_2-Al) alloy fuel was created as shown in Figure 2. Calculations were performed using two different starting masses of uranium in the assembly, two different powers for the assembly itself, and various control rod insertion amounts. Table 1 contains some of the irradiation times and burnups resulting from some calculated time steps; the actual simulations used time steps of 20 days, but results every 60 days are reported here for simplicity.

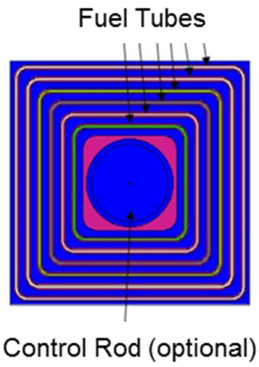

Figure 2. Infinitely-reflected fuel assembly model in MCNP

Irradiation time (days)	Burnup (MWd/MTU)	% U-235 burned
0	0	0.00
0.5	112.54	0.09
3	788.25	0.52
23	5291.91	3.40
63	14294.02	9.05
123	27805.48	17.23
183	41313.05	25.22
243	54823.20	33.03
303	68335.01	40.46
363	81843.85	47.67
423	95353.69	54.60
483	108861.84	61.20

Table 1. Irradiation Times and Burnups in IRT Simulations

Following the irradiation calculations, neutron source terms were created from the resulting isotopic compositions using the code SOURCES4C by formatting them into MCNP source particle definitions

(SDEF cards) for each fuel region for both spontaneous fission and (α, n) reactions individually [10] [11]. The number of total neutrons emitted from the assembly for the different cases with a burnup of ~60% of initial ^{235}U fissioned and two years of cooling after discharge is given in Table 2. As can be seen from the table, there is a large variation in the neutron source term when irradiation simulations were performed under different conditions. When the control rod was inserted, the resulting calculated passive neutron source term in the middle axial region was too low compared to measurements, but when it was removed, the neutron source term was too high. Thus, partial insertion of the control rod produced comparable results with experimental data in the axial center of the assembly.

Geometry	Init. ^{235}U Mass (g)	Fuel Density (g/cc)	Power (MW)	CR Insertion (cm)	Neutron Emission Rate (n/s)
square/ assembly	264.63	3.38	0.6	none/ water	5.11E+04
rounded/ assembly	263.25	3.5	0.3	none/ void	5.16E+04
rounded/ assembly	263.25	3.5	0.3	4 of 58 cm	4.02E+04
rounded/ assembly	263.25	3.5	0.3	19 of 58 cm	2.8E+04

Table 2. Neutron source emissions for different cases in parametric study.

5. Results

MCNP was used to create a high fidelity model of the AEFC. Comparison of measured and modeled neutron singles and doubles detection efficiencies for a source in the active interrogation source slot and in the center of the fuel funnel were used to validate the model. In the field trial work, each assembly was measured in three positions: upper, middle, and lower, which represented regions of the assembly within the range of the ^{3}He detectors. For our comparison, we use the middle active and passive measurements of each assembly. The MCNP models of the IRT fuel assemblies are therefore centered axially (with respect to the center of the ^{3}He tubes) and radially in the fuel funnel in the simulated AEFC instrument. Active interrogation neutrons thermalize in the water inside the fuel funnel and induce fission in the fissile isotopes in the fuel proportionately to the mass of fissile material. Because the declared burnup is a measure of depleted ^{235}U mass, the residual fissile mass should, in theory, be straightforward to accurately simulate. This was the case in our work; as long as the correct amount of fissile material was in the simulated spent fuel assemblies, the agreement with experimental active interrogation results was good as shown in Figure 3. One sigma error bars are shown on the experimental data, and the simulated results have uncertainties too low to see on these plots. The experimental results have been corrected for dead time and an efficiency loss due to lower operating HV [2]. The singles and doubles rates agree with a Root Mean Squared (RMS) error of 7.3% and 11.0%, respectively.

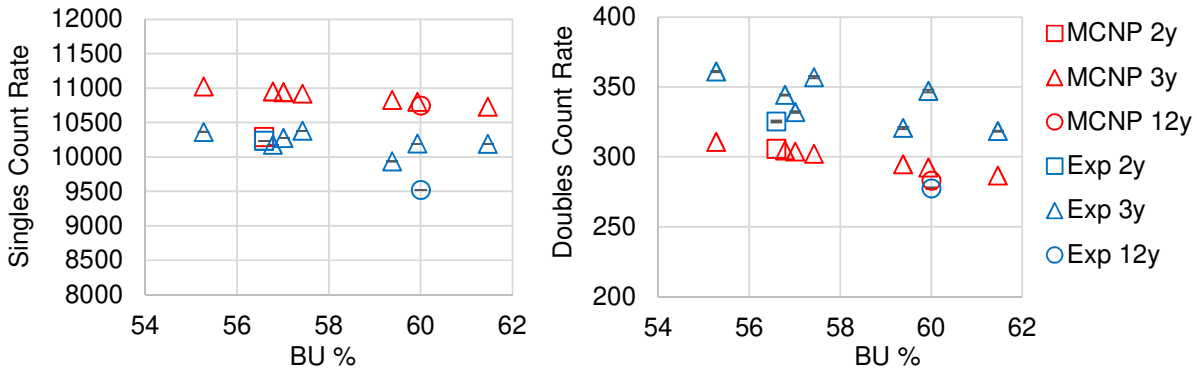

Figure 3. Comparison of simulated and experimental singles and doubles rates from the AEFC active interrogation measurements of spent IRT fuel assemblies.

The passive neutron singles and doubles rates from spent fuel are considerably more difficult to accurately simulate. There are known nuclear data issues that make it difficult to determine the correct amount of ^{244}Cm, ^{240}Pu, and other higher actinides in simulated spent fuel assemblies. As ^{244}Cm and other spontaneous fission nuclides provide the primary neutron source in passive measurements, any error in ^{244}Cm mass in the assemblies will result in an error in the simulated AEFC-measured singles and doubles rates. The mass of ^{244}Cm and ^{240}Pu produced is also highly dependent on parameters such as fuel density, control rod insertion, and reactor power. These parameters were varied in the parametric study described in Section 4 to determine the conditions that produced singles and doubles count rates most similar to those measured. The other source of passive neutrons from IRT spent fuel is (α, n) reactions, which are simulated separately from the spontaneous fission sources and the results are added for the composite passive neutron signal. Figure 4 shows the comparison of the singles and doubles rates from simulation and experiment, which agree with an RMS error of 22.0% and 11.9%, respectively.

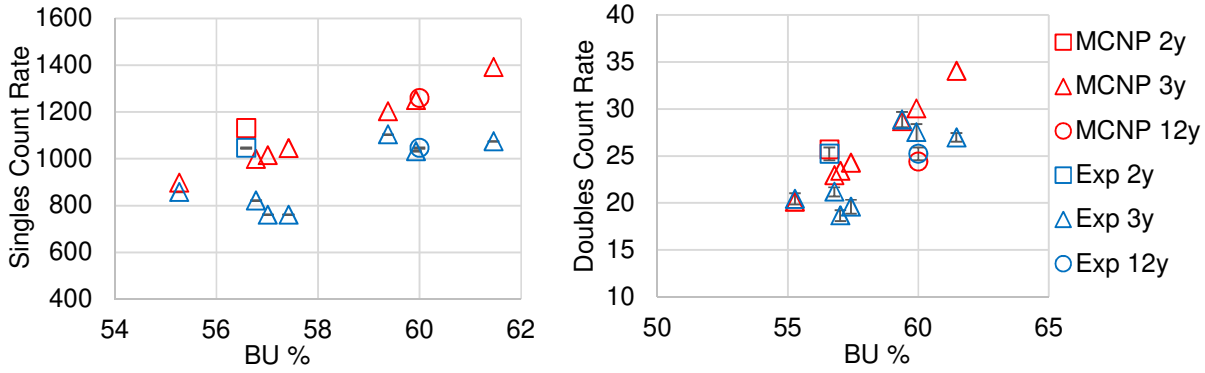

Figure 4. Comparison of simulated and experimental singles (upper) and doubles (lower) rates from the AEFC passive measurements of spent IRT fuel assemblies.

The simulated active singles are consistently too high while the simulated active doubles are consistently low, with the exception of the 12 year case. This could be partially due to an inaccurate ^{252}Cf source strength, as we know there is 5-10% uncertainty associated with that value. The passive singles and doubles are both slightly too high in simulation, which could be due to a control rod not inserted far enough during the simulated burning process.

6. Conclusions and Future Work

The work presented in this paper shows that simulated neutron detector counts for IRT spent nuclear fuel assemblies can be successfully validated to measured results from the AEFC instrument. A simulated library of spent IRT fuel assemblies was created by comparing to experimental results from the AEFC instrument. The ultimate goal of the library of assemblies is to obtain an accurate model of the detector response to assemblies with varying physical and operational parameters. The detector responses can then be used in a MPMC approach to characterize or verify fuel assemblies in the field. This would represent a significant advance over the current state-of-practice wherein quantitative verification is performed after the measurement campaign is completed. The singles and doubles rates from active interrogation agreed between experiment and simulation with RMS errors of 7.3% and 11.0% respectively. The singles and doubles rates from passive interrogation agreed between experiment and simulation with RMS errors of 22.0% and 11.9% respectively. Future work should include a comparison of the upper and lower fuel region measurements and development of the model-predict-measure-compare (MPMC) approach for future fuel characterization efforts. Additionally, full core IRT reactor irradiation calculations could be performed and to enable more accurate estimations of spent fuel compositions with

more detailed information on the operating parameters and enrichments of all assemblies burned during the cycle(s) of interest.

7. Acknowledgements

The authors would like to thank the staff at the INP in Uzbekistan for their hospitality in accommodating these measurements and providing us the unique opportunity test the AEFC at their reactor. We would also like to thank the additional LANL staff members who have contributed to this work: Howard Menlove, Johnna Marlow, Martyn Swinhoe, and Carlos Rael. LA-UR-18-23150

References

[1] M. T. Swinhoe, H. O. Menlove, J. B. Marlow, C. D. Rael and A. P. Belian, "A Portable Spent Fuel Counter for Research Reactor Fuel," in *Institute of Nuclear Materials Management*, Nashville, TN, 2006.

[2] K. A. Miller, H. O. Menlove, C. D. Rael, S. Baytelesov, F. Kungurov, J. Yusupov, U. Salikhbaev, M. Mayorov, U. Yazuv, B. Reid, C. Gesh, J. Marlow and L. Szytel, "Preliminary Results of the 2014 Field Trial of the Advanced Experimental Fuel Counter (AEFC) for Verification of Research Reactor Spent Fuel at the Institute of Nuclear Physics (INP)," in *ESARDA Symposium Proceedings*, Manchester, UK, 2015.

[3] H. R. Trellue and D. I. Poston, "User's Manual, Version 2.0 for MONTEBURNS, Version 5B," Los Alamos National Laboratory, Los Alamos, NM, 1999.

[4] T. Goorley, J. M. Booth and e. al., "Initial MCNP6 Release Overview: MNCP6 version 1.0," *Nuclear Technology,* vol. 164, pp. 3-12, 2012.

[5] H. O. Menlove, M. T. Swinhoe, J. B. Marlow and C. D. Rael, "Advanced Experimental Fuel Counter (AEFC) Calibration and Operation Manual," Los Alamos National Laboratory, Los Alamos, NM, 2008.

[6] D. Reilly, N. Ensslin, H. Smith and S. Kreiner, Passive Nondestructive Assay of Nuclear Materials, Washington DC: U.S. Nuclear Regulatory Agency, Office of Nuclear Regulatory Research, 1991.

[7] A. Rakhamanov, J. R. Deen, N. A. Hanan and J. E. Matos, "A Neutronic Feasibility Study for LEU Conversion of the WWR-SM Research Reactor in Uzbekistan," in *International Meeting on Reduced Enrichment for Research and Test Reactors*, Sao Paulo, Brazil, 1998.

[8] E. P. Ryazantsev, P. M. Egorenkov, V. A. Nassonov, A. V. Taliev, A. D. Gerstle, A. A. Karpukhin, V. M. Chernyshov, B. S. Yuldashev, T. B. Ashrapov and A. A. Dosimbaev, "Testing of the IRT-4M Type FA with LEU UO2-Al Fuel in WWR-CM Reactor," in *International Meeting on Reduced Enrichment for Research and Test Reactors*, Las Vegas, NV, 2000.

[9] *Scale: A Comprehensive Modeling and Simulation Suite for Nuclear Safety Analysis and Design,* Oak Ridge, Tennessee: Available from Radiation Safety Information Computational Center at Oak Ridge

National Laboratory as CCC-785, 2011.

[10] R. A. Weldon, M. L. Fensin and H. R. Trellue, "Total Neutron Emission Generation and Characterization for a Next Generation Safeguards Initiative Spent Fuel Library," *Progress in Nuclear Energy,* vol. 80, pp. 45-73, 2015.

[11] W. B. Wilson, R. T. Perry, E. F. Shores, W. S. Charlton, T. A. Parish, G. P. Estes, T. H. Brown, E. D. Arthur, M. Bozoian, T. R. England, D. G. Madland and J. E. Stewart, "SOURCES4C: A Code for Calculating (alpha, n), Spontaneous Fission, and Delayed Neutron Sources and Spectra," Los Alamos National Laboratory, Los Alamos, NM, 2002.

MCNP simulations of prototype DDSI detector

Li Caldeira Balkeståhl, Zsolt Elter, Sophie Grape, Carl Hellesen

Uppsala University

Abstract:

I will present simulation studies of the Differential Die-Away Self-Interrogation detector (DDSI) developed at Los Alamos National Laboratory for nuclear safeguards purposes. The response of the DDSI instrument to spent nuclear fuel is simulated with MCNP6 using F8 capture tallies, and the early die-away time is calculated by an exponential fit to the Rossi-alpha distribution of the true neutron coincidences.

This study is done for a fuel library of 980 simulated PWR 17x17 spent fuel assemblies. Serpent2 is used for the burn-up calculations to define the spontaneous fission source used for the MCNP6 neutron transport calculations. The investigated fuels have initial enrichment (IE) 2-5%, burn-up (BU) of 15-50 GWd/tU, cooling time (CT) of 5-70 y and standard operational history.

The die-away time is modelled as a function of BU and CT for different IEs. Sensitivity studies, regarding for example irradiation power density and operational history, are discussed.

Keywords: MCNP; DDSI; detector response; spent nuclear fuel; neutron detection

1. Introduction

Non-destructive assay (NDA) of spent nuclear fuel is used in safeguards for the verification of operator declarations. In this verification procedure, the consistency between the declared spent fuel parameters burn-up (BU), initial enrichment (IE) and cooling time (CT) and measured signatures is investigated.

NDA techniques for spent nuclear fuel measure the radiation coming from the fuel, either in passive measurements where the spent fuel is the only source, or in active measurements where an interrogation source is used to induce a response from the fuel. Commonly available instruments for nuclear safeguards verification measure either gamma radiation, neutron radiation, both, or Cherenkov light emitted from spent fuel.

Traditionally, the signatures from different measurement techniques are analysed separately, and in gamma techniques usually only a few isotope ratios are used. Multivariate analysis (MVA) techniques, on the other hand, allow for the inclusion of many signatures simultaneously. Currently, the safeguards group at Uppsala University is developing an MVA approach for spent fuel characterisation. This paper is part of that development by investigating a passive neutron signature, to be included in the MVA. This is a work in progress, and this paper mainly presents the simulation methods used together with a limited sensitivity analysis.

1.1 Multivariate analysis for spent nuclear fuel characterisation

Passive gamma spectra from spent nuclear fuel measurements with high purity germanium detectors (HPGe) provide information about many fission products present in the fuel. The high resolution of HPGe-detectors allows for a good separation of full-energy peaks, and the approach studied at Uppsala University takes advantage of this by including several peaks from several fission products. In the first paper [1], it was shown that principal component analysis (PCA) in conjunction with partial least squares regression (PLS) on isotope concentrations could be used to determine BU, IE and CT, for fuels with cooling times less than 20 years.

Subsequent studies have followed: studies of how well different MVA of isotope concentrations can be used to discriminate between UOX and MOX fuels [2], and to determine BU, IE (or initial fissile content for MOX), CT and Pu content of spent fuel [3]; and investigations of partial defect detection on the level of 30% based MVA of gamma-ray intensities from simulated HPGe spectra [4].

The results are promising, but for cooling times longer than 20 years, when the short-lived fission products have decayed, fewer isotopes and lower gamma-ray intensities remain to be measured with passive gamma techniques. To further develop this MVA methodology, we will investigate and include also passive neutron techniques. As a first step in this direction, the Differential Die-away Self-Interrogation (DDSI) prototype instrument, a passive neutron detection technique, has been modelled. This particular detector has been selected because it has been used to measure spent fuel in Sweden. The same set of fuels have also been measured with a HPGe-detector. Having the same fuel measured with different techniques is a prerequisite to be able to apply the MVA methodology developed on simulated data to experimental data.

1.2 Differential Die-away Self-Interrogation (DDSI) instrument

The DDSI prototype instrument has been developed in Los Alamos National Laboratory as part of the Next generation safeguards initiative – spent fuel project [5]. It has been extensively simulated and studied in [6], tested in fresh fuel measurements [7] and a spent fuel measurement campaign has recently been performed.

The DDSI detector consists of 56 ^{3}He tubes distributed in 4 detector pods, as shown in figure 1. The ^{3}He tubes detect thermal neutrons slowed down in the surrounding polyethylene, while cadmium lining of the detector pods prevents neutrons that thermalized in the fuel assembly and water from reaching the detectors. A lead shield around the fuel assembly is used to keep the count rate at a manageable level.

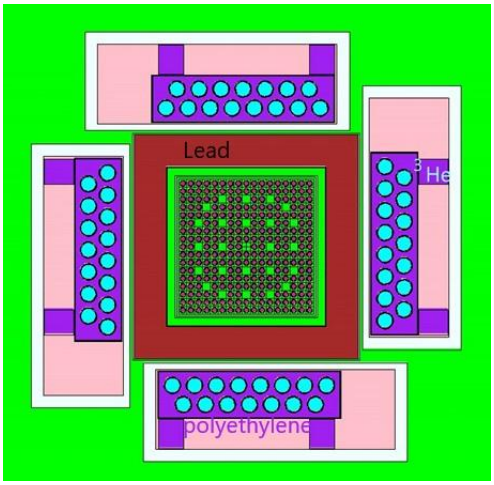

Figure 1: Schematic of the DDSI detector from MCNP. The ^{3}He tubes are shown in blue, the surrounding polyethylene in purple, the steel enclosure of the detector pods in white, the lead in brown and the water in green. The rods of the 17x17 PWR fuel assembly can be seen in the centre of the figure.

The detector operates in list-mode, and the main idea is to analyse time correlation of detected neutrons as a way to determine fissile content. This is achieved by constructing a Rossi-alpha distribution from the neutron list mode data, which describes the time differences between all detected neutrons. An example Rossi-alpha distribution is shown in figure 2, together with the exponential fits performed. The exponential die-away of detected neutron coincidences has two components: one fast component and one slow component. The fast component describes the time difference between detected neutrons from the same spontaneous fission or from subsequent induced fast fissions. The slow component describes the time difference between detected neutrons from induced thermal fission events. The DDSI instrument also has an inherent die-away time, determined by its geometry

and design, and this die-away time is longer than the fast component and considerably shorter than the slow component. This means that the fast component in fact becomes governed by the die-away time of the detector. Both components can be seen in figure 2, where they were obtained by fitting a sum of exponentials to the simulated Rossi-alpha distribution. Also shown in the same figure is the exponential fit in the range 4-52 µs. The decay constant of this fit, the so-called early die-away time, has been shown in [8] to be proportional to the leakage multiplication of the specific assembly. This early die-away time is dependent on the specific geometry of the instrument, and also varies with varying fuel parameters.

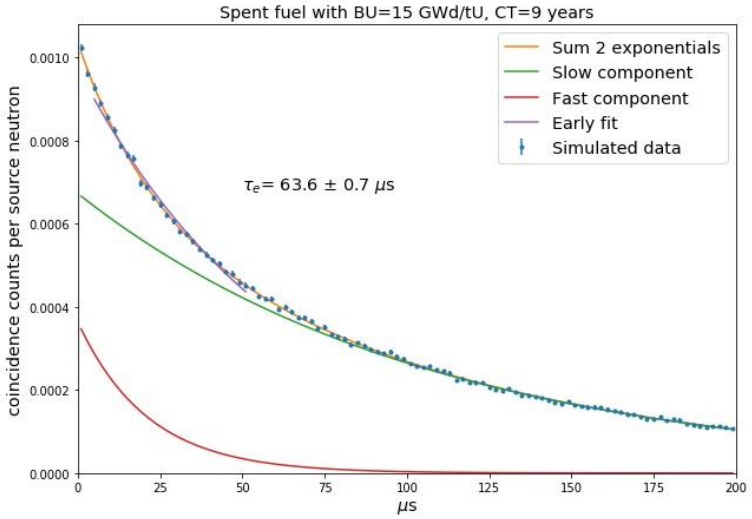

Figure 2: Rossi-alpha distribution from simulated DDSI data (blue points) for a PWR 17x17 spent nuclear fuel with BU=15 GWd/tU and CT=9 y. The two components (red and green) of the fit of a sum of two exponentials (orange) are shown. The exponential fit between 4 and 52 µs (purple) gives the early die-away time τ_e.

2. Simulation methods

The simulations of the DDSI response are done in two steps. First, Serpent2 [9] is used to simulate the nuclear fuel burnup and provide the fuel's isotope concentrations. In the second step, MCNP6 [10] is used to simulate the neutron transport and detection in the DDSI instrument, with a spontaneous fission source given by the isotopic concentration as simulated by Serpent2.

2.1. Serpent2 burnup simulation

The burnup and radioactive decay of the PWR fuel is simulated with Serpent2. In total, 980 fuel assemblies are simulated with the following fuel parameters: initial enrichment from 2-5 %, in steps of 0.5%; burn-up uniformly sampled between 15 and 50 GWd/tU and cooling time uniformly sampled between 5 and 70 years.

The PWR rods are modelled as cylinders with a radius of 4.1 mm filled with UOX, surrounded by 0.1 mm void and 0.4 mm thick zirconium cladding. The rods are arranged in an infinite 2D-lattice with 1.26 cm pitch, with water filling the rest of the geometry. Serpent2 is run in criticality source mode with operational history defined in one year cycles of irradiation at constant power density (corresponding to 10 GWd/tU) followed by 30 days down-time in between cycles, and the length of the last cycle adjusted to get the desired burn-up. The radioactive decay of the isotopes in the fuel is then calculated for the desired cooling time. The resulting isotope concentration in the UOX material is used as input in the following MCNP6 simulation.

2.2. MCNP6 neutron transport simulation

MCNP6 is used to simulate the transport of neutrons from the PWR fuel to the DDSI instrument and their detection in the ^{3}He tubes. The spent fuel assembly is a 17x17 assembly, with 1.26 cm pitch and

rods with 4.1 mm radius UOX, surrounded by 0.1 mm ^{4}He and 0.4 mm of zirconium cladding. The material composition of the fuel is taken from the output of the Serpent2 simulation. The source is distributed over all the rods as a spontaneous fission source, but restricted to a 145 cm axial height centred around the DDSI detector (for variance reduction by geometric truncation).

The fuel assembly is surrounded by water and by the DDSI instrument (as seen in figure 1), centred vertically, having ^{3}He detectors with 40 cm active length. Following the findings of [6], several F8 coincidence capture tallies, with different pre-delay, are used to produce the Rossi-alpha distribution from 0 to 200 µs with 2 µs bins. The early-die away time is then calculated from a fit to this distribution (see section 1.2).

3. Sensitivity studies

In order to decide on a time-efficient and accurate simulation, a few sensitivity studies comparing different options have been performed and are presented here. The goal of the simulations is to have a reliable die-away time determination to use in the MVA methodology, and the work so far has focused on the Rossi-alpha distribution and the die-away time.

3.1. Geometry

The active part of the ^{3}He-detectors is only 40 cm in height, while a fuel assembly is almost 4 meters long. Simulating source neutrons from the whole length of the fuel assembly would result in many histories where no events reach the detectors, thus wasting computing power. To decide on a reasonable axial height to simulate, simulations have been performed with the source distribution restricted to 5 cm axial slices of the fuel assembly, starting at the middle point of the detector and moving upward. The number of detected singles and doubles events were recorded, and the cumulative percentage of these was used to select a vertical height corresponding to more than 95% detected events in both cases. Figure 3 shows the cumulative percentage of singles and doubles events detected in this simulation, together with the 95% and 98% levels. For the 95% level, it is enough to have a source reaching 72.5 cm from the centre of the detector(i.e. with a total axial height of 145 cm).

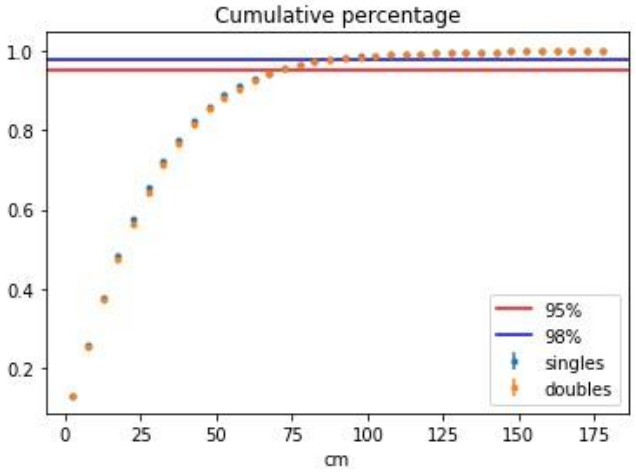

Figure 3: The cumulative percentage of singles and doubles detected in slices of 5 cm source length.

The whole length of 365 cm of the fuel assembly is modelled, but the source is restricted as mentioned above. The simulated universe consists of a sphere of water with 2 m radius surrounding the DDSI detector and fuel.

3.2. MCNP TOTNU card

By default, MCNP6 samples both prompt and delayed fission neutrons. In this simulation, where the time is only tracked for each history and no time dependency of the source is used, delayed neutrons should not play a role in the determination of the die-away time. In order to investigate this, four different fuels with 3.5% IE, low and high BU and low and high CT (within the range given above) were simulated with the TOTNU card turned off (this turns off the delayed neutrons). A comparison of results between this and the default simulation (including both prompt and delayed neutrons), showed that the resulting early die-away time differed with only up to 3% (the statistical error in τ_e is less than 2%). A Kolmogorov-Smirnov two-sample test of the two Rossi-alpha distributions resulted in a very small test statistic (≤ 0.04), indicating that the distributions come from the same parent distribution. The conclusion is therefore that delayed neutrons do not play a role in the early die-away time determination, and the default selection of the TOTNU card turned on can be kept.

3.3. LLNL fission model

Different fission models can be used to describe the fission process in simulations. The LLNL fission model implemented in MCNP was found in [6] to give a better agreement between simulations and fresh fuel measurements of the singles and doubles rates of the DDSI instrument, although the discrepancy between experiment and simulation did not fully disappear. The discrepancy concerns the total doubles and singles rates, not the early die-away time, and as such might not play a role for the implementation into the MVA methodology.

In order to study the impact of the fission model, both the LLNL fission model and the default MCNP6 fission model were used. However, the use of the LLNL fission model in MCNP6 prevented the use of parallel computing, and thus greatly increased the time needed for the simulation. The same four simulated fuels as in section 3.2 were simulated using the LLNL model and compared to the default model (MCNP6 default). As in 3.2, the early die-away time differs slightly with up to 3%, and the Kolmogorov-Smirnov two-sample test of the Rossi-alpha distributions results in a very small test statistic (≤ 0.06). The conclusion is therefore, that the LLNL model does not make a significant difference for the determination of the early die-away time, and it is sufficient to keep the default fission model in MCNP6.

4. Conclusions

As part of the development of a MVA technique for characterisation of spent nuclear fuel, we have simulated the response of the prototype DDSI detector developed in Los Alamos National Laboratory. The sensitivity tests performed so far have not shown any significant differences between default options in MCNP and other alternatives.

Figure 4 shows the resulting early die-away time for the library of 980 simulated spent fuel assemblies. The next steps in this project are to model the early die-away time as function of the fuel parameters and use this as input to the MVA methodology.

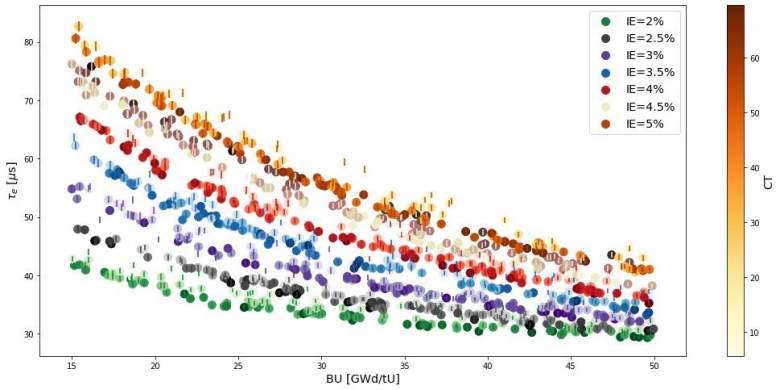

Figure 4: Early die-away time as a function of BU. Different IE are shown as different colors, and the CT is shown as the shading of the data points.

5. Acknowledgements

This work was funded by the Swedish Radiation Safety Authority (SSM) under agreement SSM2016-661-1. The authors would also like to acknowledge Holly Trellue at LANL for enabling the collaboration between LANL and UU and for assisting with the project. We would also like to express our gratitude to Alexis Trahan at LANL for providing the DDSI instrument model and information on the DDSI in general.

6. References

[1] Hellesen, C. et al., *Nuclear spent fuel parameter determination using multivariate analysis of fission product gamma spectra; Annals of Nuclear Energy,* Vol. 110, 2017, p 886-895.

[2] Åberg Lindell, M. et al., *Discrimination of irradiated MOX fuel from UOX fuel by multivariate statistical analysis of simulated activities of gamma-emitting isotopes; Nuclear Instruments and Methods in Physics Research, A,* Vol. 885, 2018, p 67-78.

[3] Åberg Lindell, M. et al., *Determination of irradiated nuclear fuel characteristics by nonlinear multivariate regression of simulated gamma-ray Emissions; Accepted for publication in Nuclear Instruments and Methods in Physics Research, A,* 2018

[4] Elter, Zs. et al., *Partial defect identification in PWR spent fuel using Passive Gamma Spectroscopy; Accepted for presentation at the PHYSOR 2018 conference,* April 22-26, Cancun, Mexico.

[5] Humphrey, M.A., Tobin, S.T., and Veal, K.D., *The Next Generation Safeguards Initiative's Spent Fuel Nondestructive Assay Project; Journal of Nuclear Material Management*, Vol. 40, 2012, p 6-11

[6] Trahan, A.C*., Utilization of the Differential Die-Away Self-Interrogation Technique for Characterization and Verification of Spent Nuclear Fuel*, PhD thesis, 2016

[7] Trahan, A. C. et al., *Fresh Fuel Measurements with the Differential Die-Away Self-Interrogation Instrument; IEEE Transactions on Nuclear Science*, Vol. 64, No.7, 2017, p 1664-1669

[8] A. C. Kaplan et al., *Determination of Spent Nuclear Fuel Assembly Multiplication with the Differential Die-Away Self-Interrogation Instrument, Nuclear Instruments and Methods A*, Vol. 575, 2014, p 20-27

[9] Leppänen, J., et al., *The Serpent Monte Carlo code: Status, development and applications in 2013; Ann. Nucl. Energy*, Vol. 82, 2015, p 142-150

[10] Goorley, T. et al., *Initial MCNP6 Release Overview; Nuclear Technology,* Vol. 180, 2012, p 298-315

Characterisation of spent nuclear fuel by theoretical calculations and non-destructive analysis

P. Schillebeeckx[1], G. Alaerts[1], A. Borella[2], L. Fiorito[2,3], K. Govers[2], J. Paepen[1], Y. Parthoens[2], B. Pedersen[4], A. Stankovskiy[2], G. Van den Eynde[2], M. Verwerft[2], R. Wynants[1], G. Žerovnik[1]

[1]EC - JRC G.2, Retieseweg 111, B - 2440 Geel, Belgium
[2]SCK•CEN, Boeretang, B - 2400 Mol, Belgium
[3]OECD - NEA, Quai Alphonse Le Gallo 46 , F – 92100 Boulogne-Billancourt, France
[4]EC - JRC G.II.7, Via Enrico Fermi 2749, I - 21027 Ispra, Italy

Abstract:

The characterisation of spent nuclear fuel assemblies in view of transport, intermediate storage and final disposal is discussed. The observables of interest that need to be determined are the decay heat, and neutron and γ-ray emission rates and spectra together with the inventory of specific nuclides that are important for criticality safety analysis and for the verification of the fuel history. All these observables cannot be determined during routine operation. Hence, the characterisation will be based on calculations combined with results of Non-Destructive Analysis (NDA). In this work the input parameters affecting most the results of theoretical calculations are identified. In addition, an NDA system to determine the neutron emission rate of a spent nuclear fuel sample is presented. Results of such measurements can be used to validate the results of theoretical calculations. This system will also be used to demonstrate that spent nuclear fuel samples can be characterised by NDA in a conventional controlled area outside a hot cell environment.

Keywords: spent nuclear fuel; decay heat; burnup credit; NDA; uncertainty; neutron emission; burnup

1. Introduction

The characterisation of Spent Nuclear Fuel (SNF) is important for a safe, secure, ecological and economical route over all stages of nuclear waste disposal: handling, transport, intermediate storage and geological disposal. The observables of interest are the decay heat, neutron and γ-ray emission rates and spectra and reactivity. To avoid too conservative loading schemes, the inventory of strong neutron absorbing nuclides is also required. In addition, the amount of specific nuclides is important to verify the fuel history such as the burnup, initial enrichment and cooling time.

Some of the observables can be determined by Non-Destructive Analysis (NDA) [1][2]: e.g. decay heat [3]-[6] and neutron rate [7][8] and γ-ray emission spectra [9]-[11]. However, a measurement of the decay heat of an assembly lasts at least one day [6]. This is too long for routine operations. In addition, to determine the inventory of specific nuclides for a criticality safety assessment and verification of the fuel history theoretical calculations are required. Therefore, a full characterisation of a SNF assembly will rely on the combination of theoretical calculations with results of NDA measurements. Evidently, the theoretical calculations need to be validated and realistic confidence limits have to be determined. Both the validation and estimation of confidence limits require high quality experimental data and a good understanding of the physical phenomena at play.

In this work, the quantities of importance to determine the observables of interest by theoretical calculations are identified. Uncertainties based on the present status of the nuclear data are given. In addition, a NDA system to determine the neutron emission rate of a SNF sample in a conventional controlled area is presented.

2. Computational methods

To calculate the nuclide inventory of SNF a neutron transport code coupled with a nuclide production and depletion code is required. Neutron transport calculations can be performed deterministically by solving the Boltzmann transport equation directly or stochastically by Monte Carlo simulations. They return the spatial and energy distribution of the neutron fluence rate. These distributions are needed to obtain energy averaged neutron induced interaction rates, which are in their turn used to calculate the interaction rates in the nuclide production and depletion step. The time dependence of the nuclide concentration is obtained by solving the Bateman equations, considering the complex influence of nuclear reactions and decay chains on the individual nuclide concentration. The simplest approach to solve this equation is the matrix exponential method. This method is based on a Taylor series expansion and is implemented in the ORIGEN-S module of the SCALE code system [12]. Modern codes, such as e.g. ALEPH2 [13] or SERPENT [14], use more advanced methods to solve the Bateman equations. They significantly reduce computing time to reach convergence. After the end of the fuel irradiation, i.e. during the cooling time period, the nuclide inventory is governed by the decay processes. This involves decay data, which are compiled in decay data libraries, e.g. Ref. [15]. They have mostly relatively low uncertainties compared to other nuclear data involved in the calculations.

The calculations rely on nuclear data (i.e. cross sections for neutron induced interactions, fission product (FP) yields, neutron and γ-ray emission probabilities and spectra, decay data), fuel fabrication data and reactor operation and irradiation conditions. The fuel design, fuel composition, reactor operation and irradiation conditions and cooling time will be referred to as fuel history. This involves quantities such as the Initial Enrichment (IE), Void Fraction (VF), BurnUp (BU) and Cooling Time (CT). Evidently, the quality and confidence limits of the theoretical calculations strongly depend on the quality of the Nuclear Data (ND) and the documentation of the Fuel History (FH). In this contribution results of such calculations by means of the SERPENT code [14] are reported.

3. SNF observables or source terms

The main SNF observables or source terms of interest, i.e. the decay heat, neutron and γ-ray emission rates and spectra, and the nuclide inventory required for a criticality safety analysis and to verify the fuel history, are studied. The nuclides contributing to the observables of interest are identified and estimates of confidence limits due to nuclear data uncertainties are given. The study is based on a simple model using the SERPENT code [14] considering a UO_2 fuel pellet that is irradiated at a constant thermal power of 250 W. The total mass of the UO_2 pellet is 5 g with an initial enrichment of 4.8 wt%. A burnup of 50 MWd/kgHM is reached after 1000 d of irradiation. The irradiation conditions are representative for an irradiated PWR fuel pin.

3.1. Decay heat

The decay heat of SNF originates from the decay of radionuclides present in the fuel. The decay heat rate or power P as a function of cooling time t, i.e. time difference with the end of the irradiation, can be expressed as:

$$P(t) = \sum_j p_j \, N_j(t) \, , \quad (1)$$

where p_j is the decay heat rate per nucleus for nuclide j (or specific power of nuclide j) and N_j is the total number of nuclei of nuclide j present in the SNF. The heat rate per nucleus p_j is:

$$p_j = E_{r,j} \lambda_j \, , \quad (2)$$

with λ_j the decay constant and $E_{r,j}$ the energy per decay that can be recovered as heat. This energy is also referred to as the recoverable energy per decay.

The decay of a radionuclide due to the emission of a charged particle, such as an α- or β-particle, usually leaves the daughter nucleus in an excited state. This mostly results in the emission of γ-rays. It is usually assumed that the energy of the γ-rays involved in the decay process is fully transferred into heat. Hence, in case of α-decay the energy $E_{r,j}$ is the total disintegration energy. However, in case of

β-decay a fraction of the disintegration energy is transferred into neutrino or anti-neutrino energy. This energy will not be converted into heat and the energy dissipated into heat is determined by the energy distribution of the emitted γ-rays and electrons. In practice, not all the kinetic energy of the emitted electrons or γ-rays is transferred into measured heat. Some of this energy might be lost due to γ-rays that escape from the measurement system or due to electrons producing Bremsstrahlung escaping partly from the system [16]. The fraction that is lost depends on the γ-ray or Bremsstrahlung energy and the material composition of the environment.

The total decay heat rate together with the individual contribution of α- and β-particles and γ-rays is shown as a function of cooling time in Figure 1. The relative contributions of the main radionuclides are plotted in Figure 2. These figures reveal that for cooling times between 1 a and 10 a the decay heat is primarily due to β-decay of relatively short-lived fission product decay chains, mainly the decay of ^{144}Ce/^{144}Pr, ^{106}Ru/^{106}Rh and ^{134}Cs. For cooling times between 5 a and 10 a there is also a contribution from the decay of ^{90}Sr/^{90}Y and ^{137}Cs/^{137m}Ba. The decay of these nuclides produces the largest contribution for cooling times between 10 a and 50 a. In this time period α-decay of ^{238}Pu, ^{241}Am and ^{244}Cm also contributes to the decay heat. With increasing cooling time the contribution due to the decay of ^{241}Am becomes the dominant one. For cooling times longer than 100 a the decay heat is primarily produced by α-decay due to the presence of ^{238,239,240}Pu and mainly ^{241}Am.

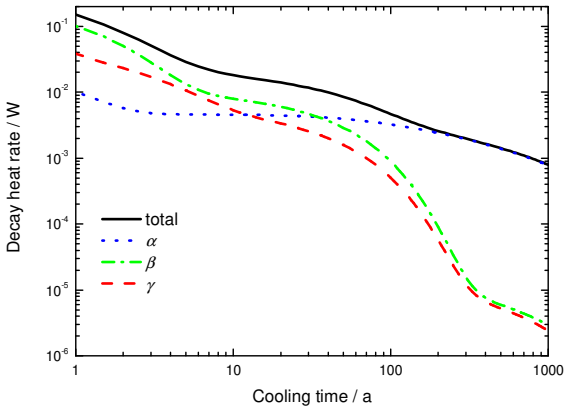

Figure 1: Decay heat rate as a function of cooling time for a SNF sample resulting from the irradiation of 1 cm^3 of fresh UO_2 fuel with a burnup of 50 MWd/kgHM. Contributions due to the emission of γ-rays and α- and β-particles are also plotted.

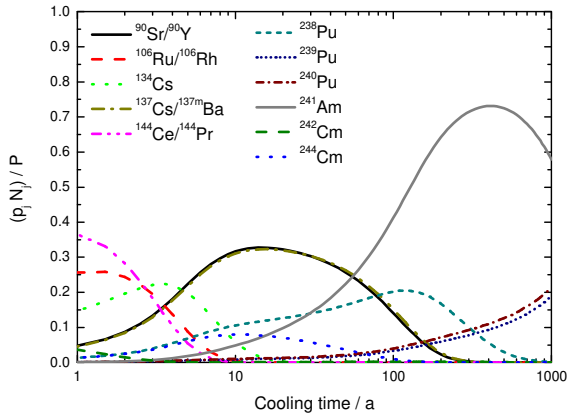

Figure 2: Relative contribution of radionuclides to the total decay heat of a SNF sample as a function of cooling time. The SNF originates from the irradiation of fresh UO_2 fuel with a burnup of 50 MWd/kgHM.

The uncertainty of the decay heat rate is due to the uncertainties of the decay constants, the recoverable energies per decay, and the number of nuclei of the contributing nuclide. The decay constants λ_j for nuclides with half-lives longer than 1 a are mostly well known. For the above mentioned nuclides the uncertainty of the decay constants is the largest for ^{106}Ru, i.e. about 0.6 % [15]. The uncertainty of the recoverable heat in case of α-decay is the largest for ^{241}Am, i.e. about 0.4% [17]. No recommended values including uncertainties can be found in the literature (e.g. Refs. [18][19][20][21]) for the recoverable heat for nuclides of interest decaying by β-decay. From the decay data recommended in Ref. [15] an average recoverable heat of 1129.4 (14) keV is calculated for the decay of ^{90}Sr/^{90}Y. This value deviates by 1.6 % from the value 1147 (9) measured by Ramthum [22] using a calorimeter. The value of Ramthum [22] is the only direct measured value that is reported in the literature. This indicates that the recoverable heat derived from decay data might be biased and the corresponding uncertainties underestimated.

An estimation of the uncertainty of the number of nuclei requires a detailed sensitivity analysis. The complexity of the analysis depends on the contributing radionuclides. For a cooling time of about 10 a, the decay heat is fully dominated by the decay of ^{90}Sr and ^{137}Cs. These nuclides are primarily produced through neutron induced fission. Hence, the uncertainty of the number of nuclei is due to the one of the fission cross section and the cumulative fission product yields. In case of a fuel assembly irradiated in a thermal system the combined uncertainty due to the cross section and fission yield is about 2.5% and 1.8% for ^{90}Sr and ^{137}Cs, respectively [18].

3.2. Neutron emission

Neutron emission by SNF is predominantly due to spontaneous fission of heavy nuclides and (α,n) reactions due to the presence of oxygen. Hence, the total neutron emission rate S_n is the sum of a contribution due to spontaneous fission (sf) and (α,n) reactions:

$$S_n(t) = \sum_j (s_{sf,j} + s_{\alpha,j})\, N_j(t)\ . \quad (3)$$

The specific neutron emission rate per nucleus due to spontaneous fission and (α,n) reactions following the decay of nuclide j are denoted by $s_{sf,j}$ and $s_{\alpha,j}$, respectively. The specific emission rate due to spontaneous fission is:

$$s_{sf,j} = < \nu >_j \lambda_{sf,j}\ , \quad (4)$$

where $<\nu>_j$ is the total number of neutrons emitted per spontaneous fission and $\lambda_{sf,j}$ is the decay constant for spontaneous fission of the nuclide j. The production of neutrons by (α,n) reactions is mostly treated under the realistic assumption of an infinitely thick target, i.e. the thickness is sufficient to stop α-particles and prevent them from escaping. The specific neutron emission rate due to α-decay of the nuclide j becomes:

$$s_{\alpha,j} = \lambda_{\alpha,j} \sum_{l,k} n(E_{\alpha,k}) Y_l(E_{\alpha,k})\ , \quad (5)$$

where $\lambda_{\alpha,j}$ is the decay constant for α-decay of the nuclide j, $n(E_{\alpha k})$ the probability that an α-particle is emitted with an energy $E_{\alpha,k}$ by the nuclide j and $Y_l(E_{\alpha,k})$ is the neutron yield for an α-particle with an energy $E_{\alpha,k}$ due to the interaction with the target material l. The neutron yield $Y_l(E_\alpha)$ is the total number of neutrons produced per incident α-particle with energy E_α interacting with a target material. This neutron yield Y_l can be calculated by:

$$Y_l(E_{\alpha,k}) = n_l \int_0^{E_{\alpha,k}} \frac{\sigma_l(\alpha,n)}{\frac{dE}{dx}} dE_\alpha\ , \quad (6)$$

where n_l is the number density of target material l, $\sigma_l(\alpha, n)$ is the neutron production cross section for an α-particle interacting with a target nucleus l and dE/dx is the linear stopping power of the target material.

The total neutron emission rate as a function of cooling time together with the contribution from spontaneous fission and (α,n) reactions is shown in Figure 3. For cooling times shorter than 100 a, the neutron emission is dominated by spontaneous fission neutrons. For cooling times longer than 100 a, the contribution from neutrons produced by (α,n) reactions becomes non negligible.

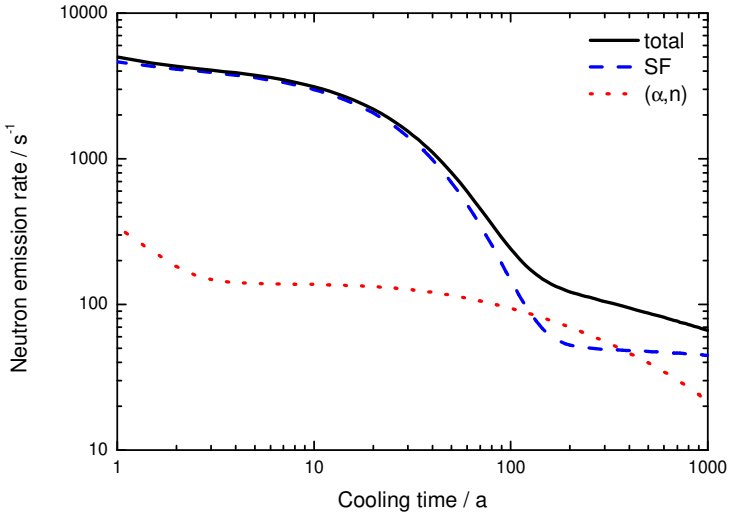

Figure 3: Neutron emission rate, together with the contribution due to spontaneous fission (sf) and (α,n) reactions, as a function of cooling time for SNF originating from 1 cm^3 of fresh UO_2 fuel with a burnup of 50 MWd/kgHM.

Figure 4 and Figure 5 show the relative contributions of specific nuclides to the neutron emission originating from spontaneous fission and (α,n) reactions, respectively. Due to the relatively short half-life of ^{242}Cm ($T_{1/2}$ = 162.86 (8) d), its contribution to the neutron emission is only important for short cooling times. For cooling times between 1 a and 30 a, the largest contribution is due to the emission of fission neutrons by ^{244}Cm, with a relatively small contribution from (α,n) reactions due to the decay of ^{238}Pu, ^{242}Cm and ^{241}Am. For cooling times longer than 100 a the neutron emission is mainly due to spontaneous fission of ^{240,242}Pu and ^{246}Cm and (α,n) reactions due to the decay of ^{241}Am.

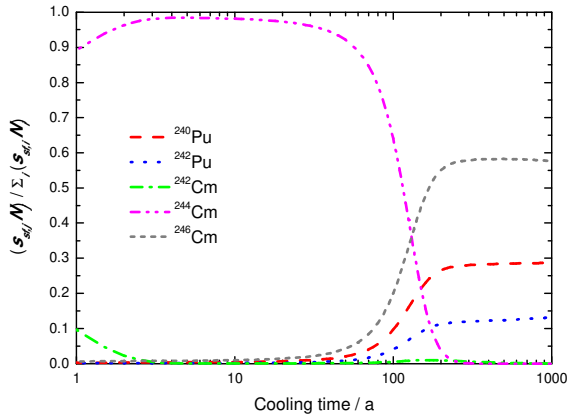

Figure 4: Relative contribution of ^{240,242}Pu and ^{242,244,246}Cm to the total SF neutron emission rate as a function of cooling time. The results are shown for SNF originating from UO_2 fuel with a burnup of 50 MWd/kgHM.

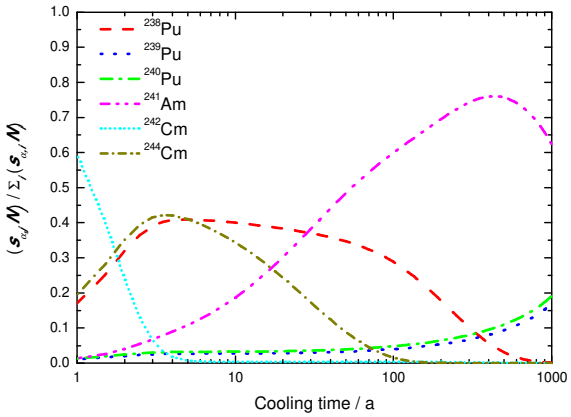

Figure 5: Relative contribution of ^{238,239,240}Pu, ^{241}Am and ^{242,244}Cm to the total neutron emission by (α,n) reactions as a function of cooling time. The results are shown for SNF originating from UO_2 fuel with a burnup of 50 MWd/kgHM.

The uncertainty of the total neutron emission rate is due to the uncertainties of the specific emission rates and the number of nuclei of the contributing nuclides. For most of the actinides, the decay constants and total neutron emission probabilities for spontaneous fission have uncertainties less than 1.5% and 0.5%, respectively [15][18]. The main component in the uncertainty of the neutron emission due to spontaneous fission is the uncertainty of the number of nuclei of the actinides. Thick target yields for (α,n) reactions in nuclear material have recently been reviewed by Simakov and van den Berg [23]. They recommended thick target yields with an uncertainty of 8.1% and 8.6% for UO_2 and PuO_2 target materials, respectively. This uncertainty originates from the one of the (α,n) reaction cross section.

The contribution due to ^{244}Cm(sf) fully dominates the neutron emission for cooling times between 3 a and 20 a. The uncertainty of the specific neutron emission rate $s_{sf,j}$ is about 0.85%. The production of ^{244}Cm is due to successive (n,γ) reactions and β-decay. A sensitivity analysis for a thermal system with UO_2 fuel shows that the uncertainty of the total number of ^{244}Cm nuclei due to the uncertainty of the (n,γ) reactions cross sections is about 3.2In case of a system with a fast neutron spectrum the uncertainty due to the uncertainty of the (n,γ) reaction cross sections becomes 10% [23].

3.3. Gamma-ray emission

Spent nuclear fuel contains a number of γ-ray emitting radionuclides with different decay constants and γ-ray emission spectra. Therefore, the γ-ray spectrum will strongly depend on the cooling time. The γ-ray emission spectrum can be derived from:

$$S_\gamma(E_\gamma, t) = \sum_{j,k} n(E_{\gamma,k})\,\delta(E_\gamma - E_{\gamma,k})\,\lambda_j N_j(t) \quad , \quad (7)$$

where $n(E_{\gamma,k})$ is the probability for the emission of a γ-ray with energy $E_{\gamma,k}$ by radionuclide j and $\delta(x)$ is the Dirac delta function. The energy dependence of the γ-ray emission is important since the penetrability of an emitted γ-ray strongly depends on its energy. The γ-ray emission energy rate, denoted by $\varphi_{q\gamma}(E)$, is defined as:

$$\varphi_{q\gamma}(E_\gamma, t) = S_\gamma(E_\gamma)E_\gamma \, . \quad (8)$$

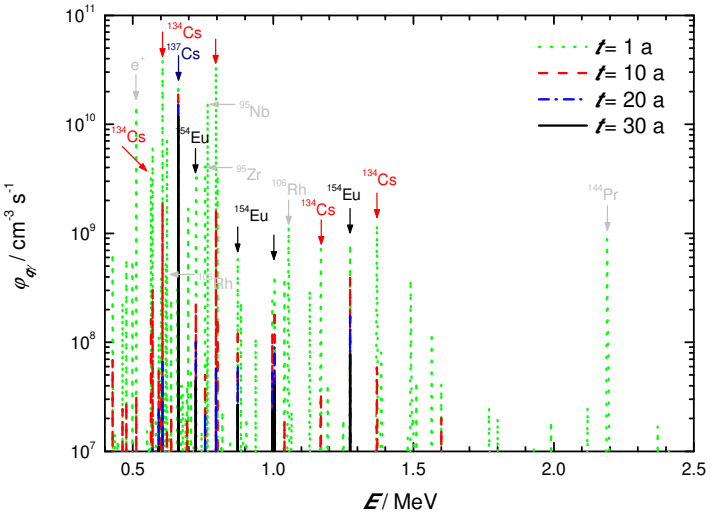

Figure 6: Energy dependence of the γ- ray emission rate energy $\boldsymbol{\varphi_{q\gamma}(E)}$ by a 1 cm^3 SNF sample originating from the irradiation of fresh UO_2 fuel with a burnup of 50 MWd/kgHM.

Figure 6 shows the energy dependence of the γ-ray emission energy rate $\varphi_{q\gamma}(E)$ for SNF originating from fresh UO_2 fuel. Only the contribution of γ-rays with an energy E_γ > 400 keV is presented. For cooling times shorter than 10 a, the γ-ray spectrum is dominated by γ-rays originating from the decay of relatively short-lived fission products, i.e. the decay of ^{95}Zr, ^{95}Nb, ^{106}Ru/^{106}Rh and ^{144}Ce/^{144}Pr. There is also a contribution of 511 keV γ-rays due to electron-positron annihilation following β^+ decays. For cooling times between 10 a and 30 a, the most prominent γ-rays result from the decay of ^{134}Cs, ^{137}Cs/^{137m}Ba and ^{154}Eu. For larger cooling times, i.e. between 30 a and 200 a, the 661 keV γ-ray due to the ^{137}Cs/^{137m}Ba decay dominates the spectrum. For cooling times longer than 400 a there is practically only a contribution of low energy γ-rays due to the decay of ^{241}Am. These γ-rays will be absorbed by the fuel and will not contribute to the dose rate.

The decay constants and γ-ray emission probabilities and energies of interest are reported in nuclear decay libraries, e.g. Ref. [15]. The main contribution to the uncertainty of the calculated γ-ray spectrum is due to the uncertainty of the number of nuclei N_j. For example, the uncertainty of the intensity of the 661 keV γ-ray due to the decay of ^{137}Cs/^{137m}Ba is about 0.27% and 0.25% due to the decay constant and emission probability, respectively [15]. Considering the discussion in Section 3.1, one can conclude that this uncertainty can be neglected compared to uncertainty of the total number of ^{137}Cs nuclei that are produced during reactor operation.

3.4 Reactivity

A safe transport, storage and disposal of SNF requires a (sub)-criticality safety analysis. To avoid unnecessarily over-engineered and expensive transport and storage casks, the loading scheme needs to account for the reduction in nuclear reactivity of the SNF [25]. This reduction is due to the net reduction of fissile nuclides and the production of non-fissile, strong absorbing actinides and fission products. The concept of accounting for the presence of these nuclides in a (sub)-criticality analysis is referred to as BurnUp Credit (BUC). Hence, criticality safety assessments for SNF management considering BUC require a nuclide inventory estimation and nuclear reactivity calculations involving far more nuclides than would be considered in a conservative approach based on the inventory of the fresh fuel. Nuclides strongly affecting the BUC of a SNF assembly are: ^{95}Mo, ^{99}Tc, ^{101}Ru, ^{103}Rh, ^{109}Ag, ^{133}Cs, ^{147,149,150,151,152}Sm, ^{235,236,238}U, ^{239,240,241}Pu [25]. Also the inventory of ^{155,157}Gd is important for BUC, when they are present as burnable poisons in the fresh fuel.

3.5 Fuel history

BurnUp (BU) of SNF is used as a measure for the total energy that is produced by nuclear fuel during reactor operation. Evidently, it is directly related to the total number of neutron induced fission reactions that occurred. An ideal BU indicator is a parameter that is directly proportional to the time integrated thermal power and is not sensitive to other irradiation conditions or fuel history parameters

such as fuel composition and cooling time. The total number of ^{148}Nd nuclei produced during irradiation is often used as a BU indicator [26]. It is produced by neutron induced fission or by decay of very short lived fission products ($T_{1/2}$ < 2 min), such that its production rate is proportional to the total fission rate. In addition, it is stable, has a relatively low cross section for neutron absorption and for a given incident neutron energy its cumulative yield does not depend strongly on the target nucleus. Hence, its removal during irradiation is negligible and its concentration is independent of cooling time. The ^{148}Nd concentration depends on the type of fuel, i.e. UO_2 or MOX, and type of reactor, i.e. fuel-to-moderator ratio that affects the neutron energy distribution. However, it is not sensitive to changes of fuel composition during neutron irradiation or to small variations in the fresh fuel composition. Other nuclides that are commonly used as BU indicators are the ratio of the number of nuclei, e.g. ^{134}Cs/^{137}Cs [27], ^{143}Nd/^{144}Nd and ^{145}Nd/^{146}Nd, and the total number of ^{139}La [26] and ^{244}Cm [27] nuclei that are produced. The ^{134}Cs/^{137}Cs ratio can also be used to verify the cooling time.

A global thermal power measurement in a PWR, based on a thermal balance on the secondary side, can be measured with an accuracy of about 2%. A measurement of local power variations is more complex. Some reactor designs enable insertion of dosimeters at different positions in the core to assess the spatial power distribution during operation. Alternatively, the local thermal reactor power can be estimated from concentrations of so-called power indicators that are present in SNF. The concentration of an ideal power indicator reaches equilibrium very quickly, i.e. within hours or days. Under these conditions, its equilibrium concentration is a function of the power and is not sensitive to other operation parameters, such as fuel composition and burnup. A relatively good candidate for a power indicator is ^{149}Sm. It is predominantly produced by decay of the short-lived ^{149}Pm ($T_{1/2}$ = 53.08 (5) h), which is produced by a sequence of decays of very short-lived FP, i.e. ^{149}Pr ($T_{1/2}$ = 2.26 (7) min) and ^{149}Nd ($T_{1/2}$ = 1.728 (1) h). The production rate of ^{149}Pm is proportional to the total fission rate and the ^{149}Pr cumulative yield.

3.6 Nuclides of importance

The discussion in the previous sections reveals that a specific source terms $S_y(t)$ as a function of cooling time can be expressed as:

$$S_y(t) = \sum_j f_y(ND_j) \left(N_{0,j} + g\left(N_{0,pc}, \lambda_{pc}, t\right)\right) e^{-\lambda_j t} , \quad (9)$$

where λ_j is the decay constant of nuclide j, $N_{0,j}$ is the total number of nuclei of nuclide j at the end of the irradiation, and $f_y(ND_j)$ is a function of nuclear data ND_j., which represents e.g. the specific recoverable heat per decay or specific neutron emission per decay of nuclide *j*. The function $g\left(N_{0,pc}, \lambda_{pc}, t\right)$ accounts for a possible build-up of nuclide j due to the decay of precursors.

The structure of Eq. 9 shows that three terms need to be considered to estimate the confidence limits of the calculated observables: the decay constants λ_j, the number of nuclei at the end of irradiation N_{0j} and the functions $f_y(ND_j)$. The decay constants λ_j and λ_{pc} that are required and are recommended in nuclear data libraries have relatively low uncertainties [15]. The functions $f_y(ND_j)$ depend only on nuclear data that are specific for each nuclide contributing to the observable. These are: decay data, specific neutron emission data and recoverable energies. Unfortunately, dedicated libraries such as Ref. [18][19][20][21] do not include recommended values for all of them. On the other hand a calculation of the total number of nuclei at the end of the irradiation, $N_{0,j}$ and $N_{0,pc}$, requires as input nuclear data and information about the fuel history. A detailed sensitivity analysis is needed to assess the impact of them. The impact of the initial enrichment and burnup on the inventory of some nuclides is illustrated in Figure 7. It plots the relative sensitivity of the number of nuclei to the initial enrichment and burnup. The relative sensitivity of the number of nuclei to a fuel history parameter *x* is obtained from a calculation of the partial derivative with respect to the parameter:

$$\frac{\delta N/_{\delta x}}{N/_x} = \frac{\delta N/_N}{\delta x/_x} . \quad (10)$$

The results in Figure 7 reveal that a variation of 1% of the initial enrichment and burnup changes the number of nuclei for e.g. ^{244}Cm by 2% and 4%, respectively.

The main nuclides that contribute to the observables discussed in the section 3 are reported in Table 1. The table indicates for which observable(s) the nuclide is important and which specific nuclear data ND_j are required: decay constants, recoverable energy, specific neutron emission rates and/or γ-ray emission probabilities. The nuclear data required to produce the nuclide inventory are not specified. A detailed sensitivity analysis is needed to identify them. In case the nuclide is only important for BUC it is not included in the table. These nuclides are specified in Section 3.4.

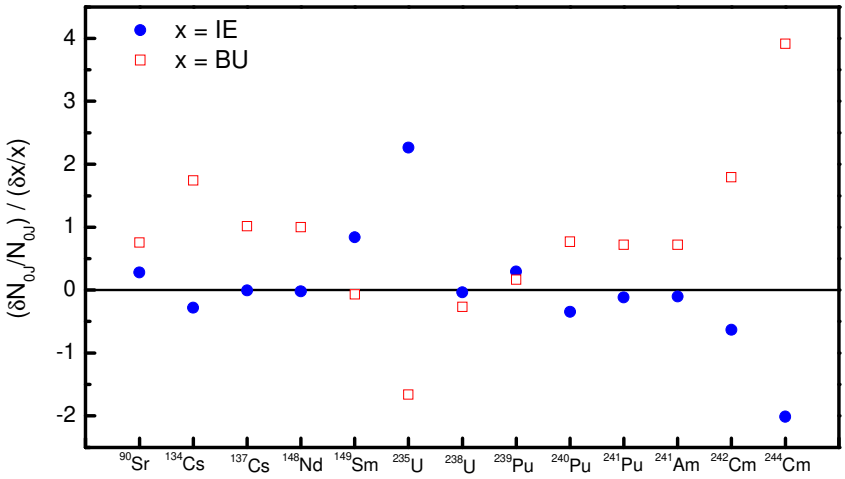

Figure 7: The relative sensitivity of the number of nuclei to variations in the initial enrichment (IE) and burnup (BU) for some nuclides that are important to SNF observables discussed in Section 3.

Nuclide(s)	$T_{1/2}$	P	S_n	S_γ	FH	BUC	ND
^{90}Sr/^{90}Y	28.80 (7) a	×					λ_β, E_r
^{106}Ru/^{106}Rh	371.5 (21) d / 30.1 (3) s	×		×			λ_β, E_r
^{134}Cs	2.0644 (14) a	×		×	x		$\lambda_\beta, E_r, n(E_\gamma)$
^{137}Cs/^{137m}Ba	30.05 (8) a / 2.552 (1) min	×		×	x		$\lambda_\beta, E_r, n(E_\gamma)$
^{144}Ce/^{144}Pr	284.89 (6) d / 17.29 (4) min	×		×			$\lambda_\beta, E_r, n(E_\gamma)$
^{148}Nd	stable				×		
^{149}Sm	stable				x	×	
^{154}Eu	8.601 (4) a			×	x		$\lambda_\beta, n(E_\gamma)$
^{238}Pu	87.74 (3) a	×	×	x			$\lambda_\alpha, E_r, \lambda_{sf}, s_{sf}, s_\alpha$
^{239}Pu	24100 (11) a	×				×	$\lambda_\alpha, E_r, s_\alpha$
^{240}Pu	6561 (7) a	×	×			×	$\lambda_\alpha, E_r, \lambda_{sf}, s_{sf}, s_\alpha$
*^{241}Pu**	*14.33 (4) a*	×				×	λ_β, E_r
^{241}Am	432.6 (6) a	×	×			×	$\lambda_\beta, E_r, s_\alpha$
^{242}Cm	162.86 (8) d	×	×				$\lambda_\alpha, E_r, \lambda_{sf}, s_{sf}, s_\alpha$
^{244}Cm	18.11 (3) a	×	×		x		$\lambda_\alpha, E_r, \lambda_{sf}, s_{sf}, s_\alpha$
^{246}Cm	4723 (27) a		×				λ_{sf}, s_{sf}

Table 1: List of nuclides important for the characterisation of SNF. Cooling times between 1 a and 1000 a were considered. The table includes the half-life ($T_{1/2}$), the observable of interest and the nuclear data $\boldsymbol{ND_j}$ that are required to calculate the observable following the structure of Eq. 9. The nuclear data are: fission product yields decay constants (λ_α, λ_β, λ_{sf}), recoverable energy (E_r), specific neutron emission rates (s_{sf} and s_α) and γ-ray emission probabilities ($n(E_\gamma)$). Nuclides which are only important for BUC are not included in the list.
Decay data are taken from: http://www.lnhb.fr/nuclear-data/nuclear-data-table/

**The inventory of ^{241}Pu is mainly important for the formation of ^{241}Am.*

4. Measurement of the neutron emission by a SNF pellet

The discussion in Section 3 reveals the importance of theoretical calculations for the characterisation of SNF assemblies. They are required to determine the inventory of nuclides specified in Table 1. At present such theoretical calculations are primarily validated by results of radiochemical analysis, which are time consuming and costly. Therefore, JRC Geel and SCK•CEN started a collaborative effort to characterise a SNF sample by NDA. The final objective is to characterise a SNF sample taken from a fuel pin with a fully documented and well-known fuel history for its γ-ray emission spectrum, neutron emission rate and nuclide vector. The nuclide vector will be determined by Neutron Resonance Transmission Analysis (NRTA) at the GELINA facility of the JRC Geel. The main principles of this method are described in Ref. [28].

Most of the facilities dealing with the characterisation of SNF have dedicated installations to prepare the sample for radiochemical analysis and to measure its γ-ray emission spectrum. However, they are mostly not equipped to determine the neutron emission rate and nuclide vector by NDA. The main difficulty, in particular for NRTA, is that such measurements cannot be performed in a hot cell facility. The first phase of the collaboration project has two objectives:

- determine the neutron output of a SNF sample by NDA with an uncertainty of less than 2%,
- demonstrate that NDA on a SNF sample can be carried out in a conventional controlled area outside a hot cell.

To realise these objectives we make use of the special hot cell facilities of the SCK•CEN and a neutron counter that is in use at the JRC Geel. The neutron counter is a counter of the AWCC type (see e.g. Ref. [29]) that is used for nuclear safeguards applications. The counter consists of two concentric rings of ^{3}He proportional counters embedded in poly-ethylene. The inner and outer ring contain each 21 ^{3}He detectors.

To measure the neutron output of a SNF sample in a conventional controlled area, outside a hot cell, special procedures are needed to avoid any contamination and excess dose rate. This requires a licensed transport container that reduces the external dose rate and does not have a strong impact on the measurement performance of the detection device. These conditions are fulfilled by the GT-75 transport container of the SCK•CEN. It is licensed to transfer a radioactive sample from a hot cell to a controlled area and it fits into the neutron well counter available at the JRC Geel. Additional containers made from aluminium and DENAL® (a tungsten-nickel-iron-cobalt alloy) are inserted in the GT-75 container to reduce the contamination risks and to limit radiation dose to a minimum.

4.1 Results of MC-simulations

To verify the final dose rate and characteristics of the detection system a series of Monte Carlo simulations were carried out using MCNP5 [30]. The dose rate estimates at the external surface of the device with 3 SNF pellets loaded in the transport container are reported in Table 2. According to the Belgian legislation, no special authorization is required when the dose rate in contact is below 20 μSv/h. Under these conditions, only an additional marker/barrier has to be placed to prevent that staff can approach the containment. The data in Table 2 reveal that this condition is fulfilled for a SNF sample with a cooling time longer than 20 a.

Configuration	Dose rate, D / (μSv/h)			
	3 a	10 a	20 a	30 a
GT-75 container	786	156	70	40
GT-75 + Al and DENAL		40	17	9

Table 2: Dose rate at the external surface of the neutron counter with a SNF sample placed in the GT-75 container and with the additional aluminium and DENAL® container inserted in the GT-75 container.

The impact of the transfer container on the detection efficiency has been verified by calculating the detection efficiency of the AWCC detector placing a point source in the centre of the cavity with and without the GT-75 container. The results of these calculations for different neutron sources are summarised in Table 3. The results show that the presence of the container has a limited impact on the detection efficiency for fission neutrons.

Neutron source	Detection efficiency		Ratio
	without GT-75	with GT-75	
AmLi(α,n)	0.362	0.344	0.950
PuO_2(α,n)	0.294	0.315	1.070
AmBe(α,n)	0.246	0.303	1.230
^{240}Pu(sf)	0.321	0.330	1.028
^{252}Cf(sf)	0.310	0.315	1.016

Table 3: Detection efficiency of the detection device for different neutron sources. The detection efficiency is given for a configuration with and without GT-75 container in the device. The results are obtained from Monte Carlo simulations using MCNP5 [30].

For a final analysis the detection efficiency will be derived from measurements using a calibrated ^{252}Cf source. The energy spectra for neutrons produced by spontaneous fission of ^{252}Cf and ^{244}Cm are slightly different. Results of Monte Carlo simulations indicate that the detection efficiency for neutrons due to ^{244}Cm(sf) is by only a factor 1.006 higher compared to the one for neutrons due to ^{252}Cf(sf).

4.2 Experimental validation of the MC-simulations

Evidently the results of the MC simulations need to be validated by experimental data. A first validation campaign was performed at JRC Geel using a calibrated AmBe(α,n) neutron source. The source was certified for its neutron emission rate by measurements in a manganese bath. The results of the calibration measurements are summarised in Table 4. The measured detection efficiency proved to be about 15% lower compared to the simulated one. The experimental ratio between the detection efficiency with and without container is in very good agreement with the calculated one. Also the ratio of the detection efficiency of the inner and outer ring and the moderation time are well reproduced by the theoretical calculations. Hence, there is a relatively good agreement between experimental and calculated detector characteristics, except for the absolute detection efficiency.

	MCNP	Exp.
Detection efficiency without GT-75 container	0.246	0.209 (2)
Ratio between detection efficiency inner/outer ring	1.41	1.39 (2)
Ratio between detection efficiency with and without GT-75 container	1.23	1.27 (1)
Moderation time	53.0 μs	54.3 (2) μs

Table 4: Comparison of the experimental and calculated detection efficiency for different configurations of the detection device. The calculated and measured moderation time are also given. The quoted uncertainties are only due to counting statistics. The uncertainties due to the Monte Carlo statistics can be neglected.

Previous experience in modelling similar detection devices, see e.g. Looman et al. [31], suggests that the relative difference between experimental and calculated detection efficiency is mostly less than 5%. Therefore, the 15% relative difference observed for the detector studied in this work is not acceptable. Unfortunately, the present detector was constructed before 1990 and documentation to verify the design parameters could not be retrieved. The present geometry in the MCNP input file is based on the specifications of a similar commercial device [29]. To verify the reason for the difference between calculated and measured detection efficiency, the impact of the source position, polyethylene density of the device, detector performance, electronics, HV settings and stability was verified. None of these effects, even combined, could explain the difference of 15%. Therefore, we suspect that the supposed total ^{3}He volume based on 400 kPa is overestimated. Considering the calculated detection efficiency as a function of pressure shown in Figure 8, the experimental efficiency of 0.209 (2) for an AmBe(α,n) neutron source would correspond with a ^{3}He pressure of about 250 kPa.

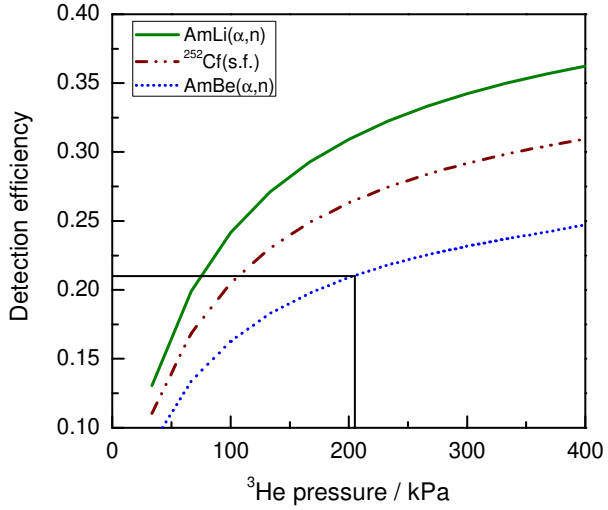

Figure 8: Detection efficiency as a function of the ^{3}He pressure for different neutron sources: AmLi(α,n), AmBe(α,n) and ^{252}Cf(sf). The results are obtained by Monte Carlo simulations. The black line indicates the pressure that would correspond with a 0.205 detection efficiency for AmBe(α,n).

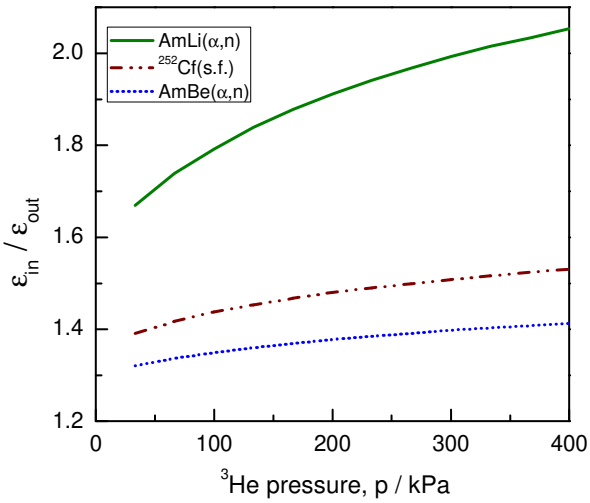

Figure 9: Ratio of the detection efficiency of the inner and outer detector ring ($\varepsilon_{in}/\varepsilon_{out}$) as a function of the ^{3}He pressure for different neutron sources: AmLi(α,n), AmBe(α,n) and ^{252}Cf(sf). The results are obtained by Monte Carlo simulations.

To verify the performance of the detection device, in particular the ^{3}He pressure, additional measurements with calibrated AmLi(α,n), AmBe(α,n) and ^{252}Cf(sf) sources will be carried out at JRC Ispra. The pressure of the detector can also be determined by using the ratio between the counts in the inner ring and the counts in the outer ring. This is shown in Figure 9, which plots this ratio as a function of ^{3}He pressure for a AmLi(α,n), AmBe(α,n) and ^{252}Cf(sf) source based on results of MC simulations. The results in Figure 9 suggest that the pressure can be derived from the ratio obtained with an AmLi source without knowing the intensity of the source.

5. Summary and outlook

The characterisation of SNF in view of transport, intermediate storage and final disposal of SNF was discussed. The main observables of interest that have to be determined are the decay heat and neutron and γ-ray emission rate and spectra. In addition, the inventory of fissile nuclides and fission products with large absorption cross sections are required for criticality safety assessments and the inventory of other specific fission products, such as ^{148}Nd and ^{149}Sm, can be used as burnup and power indicators.

The quantities of importance to determine the observables of interest by theoretical calculations were discussed. A list of nuclides that are required to estimate the observables by theoretical calculations was identified. Uncertainties of the observables based on the present status of the nuclear data were estimated. For a cooling time between 10 a and 100 a the most important contributors to

- the decay heat are: ^{90}Sr/^{90}Y, ^{137}Cs/^{137m}Ba, ^{238}Pu, ^{241}Am and ^{244}Cm;
- the γ-ray emission rate are: ^{134}Cs, ^{137m}Ba and ^{154}Eu; and
- the neutron emission rate are: ^{238}Pu, ^{241}Am and ^{244}Cm.

Based on this list a more detailed sensitivity analysis will be carried out to define realistic confidence limits for the observables that are derived from theoretical calculations.

An NDA system to determine the neutron emission rate of a SNF sample was presented. The performance of the system was assessed by Monte Carlo simulations and verified by results of measurements using a AmBe(α,n) neutron source. Additional measurements using calibrated AmLi(α,n), AmBe(α,n) and ^{252}Cf(sf) sources will be carried out at JRC Ispra. The system will be used to determine the neutron output of a SNF sample with a well-known fuel history at the SCK•CEN.

6. References

[1] Hsue S.T., Crane T.W., Talbert W.L. and Lee J.C.; *Nondestructive Assay Methods for Irradiated Nuclear Fuels*, Los Alamos Report, LA-6923, 1978

[2] Tarvainen M., Lévai F., Valentine T.E., Abhold M. and Moran B., *NDA Techniques for spent fuel verification and radiation monitoring*; STUK-YTO-TR 133, 1997

[3] Debertin K. and Ramthun H., Burn-up determination of irradiated fuels by means of their heat output, Atomkernenergie (ATKE) 21 (1973) 119 - 122

[4] Jaboulay J.C. and Bourganel S., *Analysis of MERCI Decay Heat Measurement for PWR UO2 Fuel Rod*; Nuclear Technology 177 (2012) 73 - 82

[5] Maeda S., Sekine T. and Aoyama T., *Measurement and analysis of decay heat of fast reactor spent MOX fuel*; Annals of Nuclear Energy 31 (2004) 1119 - 1133

[6] Sturek F. and Agrenius L., *Measurements of decay heat in spent nuclear fuel at the Swedish interim storage facility*, CLAB; Svensk Kärnbräslehantering AB, R – 05 – 62, December 2006

[7] Menlove H.O., Menlove S.H. and Tobin S.J., *Fissile and fertile nuclear material measurements using a new differential die-away self-interrogation technique*; Nuclear Instruments and Methods A 602 (2009) 588 - 593

[8] Henzl V., Croft S., Richard J., Swinhoe M.T. and Tobin S.J., Determination of the plutonium content in spent fuel assembky by passive and active interrogation using a differential die-away instrument; Nuclear Instruments and Methods A 8712 (2013) 83 - 92

[9] Willman C., Håkansson, Osifo O., Bäcklin, A. and Svärd S.J., *Nondestructive assay of spent nuclear fuel with gamma-ray spectroscopy*; Annals of Nuclear Energy 33 (2006) 427 - 438

[10] Koleška M., Viererbl L., Marek M., Ernest J., Šunka M. and Vinš M., *Determination of IRT-2M fuel burnup by gamma spectroscopy*; Applied Radiation and Isototpes, 107 (2016) 92 - 97

[11] Favalli A. Vo D., Grogan B., Jansson P., Liljenfeldt H., Mozin V., Schwalbach P., Sjöland A., Tobin S.J., Trellue H. and Vaccaro S., *Determining initial enrichment, burnup, and cooling time of pressurized-water-reactor spent fuel assemblies by analysing passive gamma spectra measured at the Clab interim-fuel storage facility in Sweden*; Nuclear Instruments and Methods A 820 (2016) 102 - 111

[12] Oak Ridge National Laboratory (ORNL), *Scale: A Comprehensive Modelling and Simulation Suite for Nuclear Safety Analysis and Design, Version 6.1*; Report ORNL/TM-2005/39, Available from Radiation Safety Information Computational Center at Oak Ridge National Laboratory as CCC-785 (2011).

[13] Stankovskiy A., Van den Eynde G. and Fiorito L., *ALEPH v2.6, A Monte Carlo Burn-up Code;* User's Manual, Restricted Contract Report SCK•CEN-R-5598, revision 2.6.3 (2015).

[14] Leppänen J. *Serpent – a Continuous-energy Monte Carlo Reactor Physics Burnup Calculation Code*; User's Manual, VTT Technical Research Centre of Finland (2015).

[15] http://www.lnhb.fr/nuclear-data/nuclear-data-table/

[16] Ramthun H., Das calorimeter als messgerät für die aktivität radioaktiver stoffe; Thermochimica Acta, 40 (1980) 145 - 155

[17] American National Standards Institute, *Pluitonium-Bearing Solids Calibration Techniques for Calorimetric Assay*; ANSI N15.22-1975 and revision

[18] Kocherov N., Lammer M. and Schwerer O., *Handbook of nuclear data for safeguards*; Report INDC(NDS)-0376, IAEA, 1997

[19] Nichols A.L., *Nuclear Data Requirements for Decay Heat Calculations*; Workshop on Nuclear Data and Nuclear Reactors: Physics, Design and Safety, Trieste, 25 February – 28 March 2002, p. 67-195.

[20] Nichols A.L., Aldama D.L. and Verpelli M., *Handbook for nuclear data for safeguards: database extensions*, August 2008; Report INDC(NDS)-0534, IAEA, 2008

[21] Chadwick M.B. et al., *ENDF/B-VII.1 Nuclear Data for Science and Technology: Cross Sections, Covariances, Fission Product Yields and Decay Data*, Nuclear Data Sheets 112 (2011) 2887 - 2996

[22] Ramthun H., *Microcalorimetric determination of the mean β-energy of* ^{90}Sr + ^{90}Y; Standardization of radionuclides, IAEA Vienna, 1967; p. 589 - 599

[23] Simakov S. and van den Berg Q.Y., *Update of the α-n Yields for Reactor Fuel Materials for the Interest of Nuclear Safeguards*; Nuclear Data Sheets 139 (2017) 190 - 203.

[24] Borella A., Calleja A. and Fiorito L., *Sensitivity studies on the production of Cm isotopes in spent fuel for safeguards applications;* M&C 2017 - International Conference on Mathematics &

Computational Methods Applied to Nuclear Science & Engineering, Jeju, Korea, April 16-20, 2017

[25] Chesterman A.S., Clapham M.J. and Gardner N., *Radiometric characterisation supports, burnup credit, safeguards and radionuclide inventory determination for spent fuel transport, storage and disposal*; Report IAEA-SM-253/35. In: Book of Extended Synopses, International Symposium on. Storage of Spent Fuel from Power Reactors, Vienna, Austria, 1998

[26] Ilas G. and Gauld I.C., *Analysis of Experimental Data for High-Burnup PWR Spent Fuel Isotopic Validation— Vandellós II Reactor*; Report NUREG/CR-7013 ORNL/TM-2009/321, Oak Ridge National Laboratory, 2011

[27] Chesterman A.S., Simpson A. and Clapham M., *Burnup Credit Measurements for Cask Loading Compliance – A Review of Techniques and Calibration Philosophies*; In: Proc. Int. Conf. WM2011, paper No. 11194, Phoenix, USA (2011).

[28] Schillebeeckx P., Becker B., Harada H. and Kopecky S., *Neutron Resonance Spectroscopy for the Characterisation of Materials and Objects*; JRC Science and Policy Reports, Report EUR 26848 EN, 2014

[29] http://www.canberra.com/products/waste_safeguard_systems/pdf/JCC-51-SS-C36907.pdf

[30] X-5 Monte Carlo Team, *MCNP™–A General Monte Carlo N-Particle Transport Code, Version 5*; Los Alamos National Laboratory, LA-UR-03-1987, 2004

[31] Looman M., Peerani P. and Schillebeeckx P., *An overview of NDA Instruments Modelled with the MCNP PTA Code at the JRC Ispra*; Proceedings of the 23rd ESARDA Symposium on Safeguards & Nuclear Material Management, Bruges, Belgium, 8-10 May2001

Preliminary Insights from the Assessment of Nuclear Data Needs for Nonproliferation

Timothy Ault[1#], Catherine Romano[2$], Fredrik Tovesson[1#], Donald Hornback[1], Christopher Pickett[1#], Christopher Ramos[1]

[1] US National Nuclear Security Administration, Office of Defense Nuclear Nonproliferation Research & Development
[2] Oak Ridge National Laboratory
[#] Contractor for US National Nuclear Security Administration
[$] Corresponding Author, Email: romanoce@ornl.gov

Abstract:

Many nuclear nonproliferation applications, particularly those which entail the numerical modeling of nuclear reactions and decay, rely on the quality of underlying nuclear data such as cross sections, gamma spectra, fission yields and multiplicity, branching ratios, and half-lives. The US National Nuclear Security Administration's Office of Defense Nuclear Nonproliferation Research and Development and Oak Ridge National Laboratory co-organized the Nuclear Data Roadmapping and Enhancement Workshop (NDREW) in January 2018 in order to develop a strategy for the prioritization of nuclear data gaps in several nonproliferation fields. The workshop consisted of 12 breakout group discussion sections addressing a variety of nuclear data types as well as affiliated topics including uncertainty/covariance, benchmarks, and facilities. This paper describes key preliminary insights from this workshop coupled with additional findings from the analysis of prior efforts related to nuclear data needs.

Keywords: nuclear data; workshop; prioritization; National Nuclear Security Administration

1. Introduction and Background

Often times, the users of numerical modeling tools trust that the libraries containing nuclear data, whether retrieved from a practitioners' guide that uses data from unknown or undocumented sources such as the Passive Nondestructive Assay (PANDA) manual [1] or an internationally established library like the Evaluated Nuclear Data Files (ENDF) [2], are comprised entirely of well-known, experimentally-determined parameters. In reality, the uncertainties in nuclear data values (if quantified at all) often drive the overall uncertainty of essential computations in fields such as nondestructive assay and active interrogation. Unfortunately, it can be difficult for users to pinpoint which parameters most substantially impact their calculations. Even when needs have been identified, the collection and implementation of new data can be costly and time consuming, and interdependencies between nuclear data sets can introduce unanticipated complications. Some nuclear data-dependent communities have adopted strategies for addressing and managing their nuclear data needs, while others do not yet have a clear prioritization and implementation strategy. In general, the nuclear nonproliferation community of data users has not been as engaged as some other nuclear communities in this regard.

The United States National Nuclear Security Administration's (NNSA's) Office of Defense Nuclear Nonproliferation (DNN) Research and Development (DNN R&D) oversees a spectrum of efforts to "detect, identify, and characterize: 1) foreign nuclear weapons programs, 2) illicit diversion of special nuclear materials, and 3) global nuclear detonations." [3]. These efforts entail the application, development, and adaptation of a variety of techniques, methods, models, and technologies which require a comprehensive understanding of pertinent nuclear reactions and properties. Examples of the key parameters associated with these reactions and properties include cross sections, branching ratios, half-lives, gamma decay

energies, neutron-gamma correlations, and many others. These parameters frequently have a major impact on the overall uncertainty of a measurement or simulation, and in some cases they can even be the dominant contributor to uncertainty. Therefore, the nonproliferation community has a vested interest in improving nuclear data in a manner that augments the capabilities of their end-users.

Since 2000, DNN R&D has supported more than 25 laboratory-led projects in the area of nuclear data. These projects have spanned a range of interests in the office, having been funded by four different office portfolios: data science, forensics, near-field detection, and safeguards. At least 12 of the projects have involved the experimental measurement (either direct or indirect/surrogate) of neutron-induced or (α,n) reaction cross sections. A specific example is the recent improvement of the $^{19}F(\alpha,n)^{22}Na$ cross section, which led to a decrease in the neutron emission rate uncertainty for UF_6 from 50% to 13% [4]. Other projects have featured experimental work on other parameters, such as fission yields or decay data, or they have focused on non-experimental work such as nuclear data evaluations, reaction theory and associated computation, uncertainty quantification methods, data formatting, and experimental infrastructure (e.g., designing and building new equipment). While DNN R&D has achieved significant progress through these projects, the opportunity exists to better coordinate across portfolios and to structure nuclear data research and development in a systematic manner that effectively leverages office resources to resolve high-priority gaps. This paper discusses past and current efforts to achieve this goal and the conclusions that have been determined thus far.

2. Previous Efforts to Identify and Prioritize Data Needs for Nonproliferation

Since the 1970s, the world's leading nuclear organizations have produced dozens of documents dedicated to the discussion and identification of nuclear data needs. A significant portion of these have originated from the nuclear energy community, such as the NEA's 2014 report on needs for advanced reactor systems [5] and the International Atomic Energy Agency's (IAEA's) investigation of the impact of data on modern nuclear technology design [6]. Other fields that have furbished similar reports include isotope production (medical and otherwise), astrophysics, and defense programs. Only a handful of nuclear data needs documents have specifically addressed nonproliferation, and some of these have focused on improvements to a very narrow topic. For instance, Los Alamos National Laboratory (LANL) wrote a report on needs for emerging non-destructive assay techniques in the context of safeguards for the Global Nuclear Energy Partnership (GNEP) [7].

DNN R&D has also played a role in fostering discussions of nuclear data needs. These have included:

- A 2013-2014 survey, developed by LANL and Oak Ridge National Laboratory (ORNL) and supported by DNN R&D, to identify nuclear data deficiencies in nonproliferation. The survey captured results from more than 30 individuals at 14 universities and laboratories in the US and Japan. Responders agreed on the importance of some topics, while many other topics shared no overlapping interest. Most of the deficiencies were related to neutron physics in some manner, including the multiplicities of fissile material, fission yields, and cross sections for both neutron-induced and (α,n) reactions [8].
- A 2013-2014 ORNL investigation of the discrepancies between simulated and observed reactor fuel isotopics, especially for fission products. Many fission products were accurately predicted (within 5%), but others varied by 10-20% or even more in a few instances. By extension, these results suggest limitations in certain nonproliferation techniques related to safeguards and reactor monitoring [9].
- The "Nuclear Data Needs and Capabilities for Applications" (NDNCA) workshop that was held at Lawrence Berkeley National Laboratory (LBNL) in 2015, targeting not only nuclear security but also nuclear energy and medical isotopes. The workshop broadly covered many topics and applications, producing a long list of needs for several disciplines [10].
- The Nuclear Data Exchange Meeting (NDEM) in Washington, DC in 2016. In contrast to NDNCA, NDEM produced a specific resolution plan for prioritized cross-cutting nuclear data needs, complete with cost estimates and timelines. This proposal was not enacted or further developed, but it did inform both the scope of the solution, as well as the need for unified planning across government agencies moving forward [11; 12].

All of these efforts advanced the office's ability to understand its own nuclear data gaps and

helped to set the stage for new efforts, discussed below, to achieve specific actionable outcomes which can be prioritized and resolved.

3. The Nuclear Data Roadmapping and Enhancement Workshop (NDREW)

In light of the previous endeavors, the idea for NDREW was formulated in September 2017 after a series of discussions between DNN R&D and its laboratory partners. Much of the workshop's content coalesced during a November 2017 gathering of the Nuclear Data Working Group (NDWG) that was embedded into the Cross Section Evaluation Working Group (CSEWG) meeting at Brookhaven National Laboratory (BNL). There was also an important planning meeting at LANL in December 2017.

The workshop was conducted over three days from January 23-25, 2018 at the University of California Washington Center in Washington, DC. The first half-day of the workshop consisted of a series of presentations to introduce and frame the workshop's context and objectives, to allow program managers from other organizations to share their connection to the issues of nuclear data, and to share the perspectives of data "end-users" and curators. Most of the workshop, i.e. the remainder of Day 1, all of Day 2, and the first half of Day 3, divided attendees into topical breakout discussion sessions, the insights from which are discussed in Section 4 of this paper. The latter half of Day 3 summarized the key findings of the discussions sessions and covered a near-term funding opportunity spearheaded by DNN R&D and the US Department of Energy's Office of Nuclear Physics within the Office of Science [13].

Ultimately, 117 individuals attended NDREW. Of these, over half (56%) came from US national laboratories, while the remainder came from the US government, other governments, private industry, or academia. Overall, at least 40 different organizations were represented, including international representation from the European Commission's Joint Research Centre and the IAEA.

4. Preliminary Insights by Topical Area

Most of the meeting was comprised of 12 topical discussion sessions. These sessions were arranged such that three sessions took place in parallel for a half day each. Three of these sessions focused on fission, another three focused on neutron-induced reactions other than fission, two focused on other nuclear reactions, and four focused on miscellaneous supporting topics. The highlights of these sessions are not presented chronologically, but rather in a systematic order.

Fission I, Independent and Cumulative Yields: This session examined fission yield data and their present suitability for nonproliferation applications. Fission fragments represent the initial conditions that determine the emission of prompt and eventually beta -delayed neutron and gamma emissions, which constitute signatures of specific nuclear materials. Gamma-ray spectroscopy is used to determine the presence of a given fission fragment species and to infer its yield based on the intensity of specific gamma lines or double- and triple-coincidence gamma gates. For nuclear forensics, cumulative yields are used to characterize fuel and determine the neutron spectra that can be used to reconstruct and infer specific designs. For stockpile stewardship, cumulative yields are also needed to interpret historical data. For both applications, cumulative yields are needed as a function of incident neutron energy and isotope. The thrust of the discussion was on the evaluation of existing data, and to a lesser extent on theory and modeling needs. Evaluated nuclear data file (ENDF) formats currently do not permit the obvious storage of uncertainties for fission yield data, and resolving this issue was deemed to be a high priority. The group identified its top priorities as the evaluations of fission yield data for U-235, U-238, and Pu-239. The need to address these data in the short term was driven in part by the opportunity afforded by the anticipated IAEA Coordinated Research Project (CRP) on fission yield evaluations.

Fission II, Prompt Neutron and Gamma Ray Emissions from Fission: This session considered nuclear data for correlated prompt neutrons and gamma rays from fission. Prompt emissions from fission are pertinent to safeguards, emergency response, arms control, and other areas of interest for nonproliferation. For example, they are essential in the detection and characterization of special nuclear materials (U-235 and Pu-239). Many safeguards and emergency response instruments use these signatures, including neutron coincidence/multiplicity counters and gamma spectroscopy systems. These methods rely on angular distributions, multiplicity-dependent energy distributions, and other higher-order quantities for which data are currently deficient,

even for important isotopes. Participants identified priorities among both spontaneous fission data and neutron-induced fission data. Signatures of interest judged to be particularly important for these isotopes included: energy spectra for prompt neutrons and gamma rays, number distributions (multiplicities), correlations between the number of neutrons and the energy distribution of the neutrons, angular correlations of the neutrons, and correlations between neutron and gamma ray emissions. The group also emphasized the development of relevant physics and transport codes. Overall, the group recommended conducting new experiments at existing facilities, and improving models of fission emissions and validation using experimental data.

Fission III, Decay Data: This session discussed decay data, particularly in the context of fission yields, but also covering beta-spectra data related to reactor antineutrino studies. Branching ratios dictate the relationship between cumulative and independent fission yields. However, cumulative fission yields are measured separately, and maintained in an entirely separate format (ENDF), than branching ratios (which are in the Evaluated Nuclear Structure Data File, or ENSDF, format). The discussion emphasized branching ratios as the principal parameter of interest (or, in some cases, ratios of branching ratios); however, half-lives, gamma ray energies, decay heat energies, and the shape of the beta decay spectrum are also of interest. Ultimately, the session leader advocated for communicating decay data priorities for evaluation to the NNDC. The group also emphasized value in developing a new application programming interface (API) for ENSDF to enable new parsing, search, and uncertainty capabilities.

Actinide Cross Sections: This session addressed both experimentation and theory for neutron absorption cross sections in actinides. Several nonproliferation applications require an understanding of the complex web of actinide isotopes interconnected by multiple neutron captures. Relatively small uncertainties for individual cross sections can propagate into large uncertainties in overall accumulation and depletion rates, thereby restricting the utility of a particular method or measurement. A particular challenge is the difficulty of measuring nuclides that may be short lived and/or difficult to isolate, presenting gaps in many areas of the actinide web which are difficult to fill. Attendees also called for improved capabilities in structure-informed reaction modeling, particularly for (n,γ) and (n,2n) reactions, to better understand the properties of reactions where target material would be very difficult to procure or use. Overall, the group recommended developing a generalized data collection methodology and, as a demonstration case, applying it to a single isotope of high interest.

Neutron Capture and Associated Spectra: This session focused on gamma ray spectral nuclear data needs following (n, γ) reactions. The narrow focus on spectral data was selected in part to avoid overlap with the Actinide Cross Sections session which focused on the production/destruction aspects of neutron capture for forensics and quantifying fuel isotopic composition. Improvements to gamma spectral data would enable better modeling of both active and passive neutron interrogation parameters, which are instrumental for a variety of nonproliferation approaches. The group concluded that an initial focus should be dedicated to the evaluation of existing data before committing to new experimental measurements for this data type. Attendees also mentioned the need for benchmarks for gamma spectral data, although this topic was discussed in more detail in the "Development of Benchmark Exercises" session.

Inelastic Neutron Scattering and Associated Spectra: This session considered gamma-ray spectral nuclear data needs following inelastic neutron scattering ((n,n'γ)) reactions. These reactions are important for most of the same applications where (n, γ) reactions are important. At higher energies, (n,n'γ) becomes increasingly important relative to (n,γ), and the quality and quantity of the data decreases significantly. Attendees noted that there is some existing (n,n'γ) reaction data which has the potential to be converted to cross sections, and that this could be a useful near-term objective. As with neutron capture, new benchmarks are also needed for the validation of (n,n'γ) data. Beyond experimentation, attendees noted the need for improvements in reaction modeling.

(α,n) Reactions: This session covered (α,n) reactions and their passive neutron contributions which impact various nonproliferation applications. In some cases, (α,n) neutrons constitute the primary signal of interest, such as the measurement of outgoing neutrons in order to estimate the quantity and enrichment of uranium in its hexafluoride form. In other situations, (α,n) neutrons constitute a portion of the neutron background that need to be subtracted from total measurements to determine some parameter of interest. Most of the discussion emphasized reactions on fluorine

and oxygen. Reaction cross sections received the most attention, but outgoing neutron energy spectra were also considered important. Moving forward, the group recommended designing benchmark studies and collecting thick-target data for the high-priority isotopes, along with evaluating recently obtained data.

Gamma-Induced Reactions: This session addressed photonuclear reactions, such as photofission (γ, f) and photonuclear neutron release (γ, n), and their intersections with nonproliferation applications. Areas of interest include active gamma-based interrogation techniques such as nuclear resonance fluorescence (NRF), which involves the interrogation of cargo containers with gamma rays. Subcritical assembly experiments and forensics applications may also rely on high-quality photonuclear data to understand their contribution amidst neutron-induced reactions, etc. The discussion centered on needs related to the "big 3" isotopes (U-235, U-238, Pu-239). Neutron multiplicity was a high priority (including the breakdown of prompt and delayed neutrons), with gamma multiplicity, angular distributions, fission product yields, and cross sections also being of interest. For parameters related to active interrogation, the group's recommendations were less specific, with the discussion focusing more on the need for better beam and detector equipment than on particular isotopic needs.

Uncertainty, Sensitivity, & Covariance: This section discussed gaps and future needs in the areas of uncertainty, sensitivity, and covariance analysis. Uncertainty quantification and sensitivity analyses are critical techniques for providing confidence margins on measurements and simulations for all nuclear applications. In nonproliferation, topics of interest include: special nuclear material (SNM) detection, tracking, and deterrence; nuclear forensics; and materials analysis. Primary needs include: correlated treatment of various particles emitted from fission for uncertainty propagation in Monte Carlo simulation related to correlated detection; reactor burnup; decay and irradiation correlation studies; gaps in the key SNM isotope cross-section reactions; and decay chain studies. Furthermore, attendees desired a number of automated sensitivity and uncertainty quantification analysis "plug-and-play" tools for passive and active interrogation problems.

Data Processing & Transport Codes: This session examined data processing and transport code needs in terms of nuclear data. Radiation transport is the fundamental particle physics framework at the core of most nuclear applications from radiation detection and shielding to nuclear weapons and reactors. This framework underlies a suite of simulation models and codes typically employed for proliferation and special nuclear material detection, tracking, and deterrence. Primary needs include: correlated treatment of particles emitted from fission including neutron to other neutrons, neutrons to photons, and delayed emissions from decay of fission fragments; improved temperature resolution for neutron thermal scattering law data; more complete photofission libraries and delayed emission treatments for active gamma interrogation; and a tool to fill in data and cross section library gaps in ENDF. Furthermore, the user community desired more validation, verification, and benchmarking across several application spaces. Attendees emphasized the need for more complete ENDF libraries (perhaps employing theoretical models as needed) and correlated particle treatment across broad energy and material spaces.

Development of Benchmark Exercises: This session focused on the need for the nonproliferation community to validate its codes and data through the development of benchmarks. Attendees agreed that new benchmarks should consist of integral experiments, quasi-integral experiments, and validation experiments. This session introduced the notion of a Nonproliferation Benchmark and Validation Suite Repository (NBVSR) which would consist of a series of benchmarks specifically configured to support nonproliferation applications. The NBVSR would need to incorporate uncertainties, sensitivities, documentation, accessibility, peer review, and a data management plan. Such an effort would require a significant investment of human capital from both the nonproliferation and nuclear data communities. Several measurements were discussed as potential candidates for a benchmark study, although the group did not arrive at a consensus for prioritizing these candidates before the end of the meeting. One of the session's co-chairs, Rian Bahran of LANL, agreed to develop a paper that may further elucidate benchmarking opportunities for nonproliferation.

Targets, Facilities, and Detector Systems: This session addressed three largely distinct topics related to supporting capabilities for data improvements, allocating roughly equal time to each of the three topics. Targetry includes the production of necessary isotopes as well as the shaping of material to produce targets with geometries suitable for nuclear data

experiments. Facilities include necessary capabilities such as neutron sources, reactors, critical assemblies, and others. Detector systems are used in conjunction with facilities to obtain the parameters of interest from a given experiment. All of these capabilities must be maintained in order to augment existing nuclear data with new measurements. For targetry, attendees called for an examination of the existing system for obtaining isotope sources to reduce the time and cost required to obtain nuclear data targets. Top facility needs included a setup specifically dedicated to neutron scattering measurements along with work on the rabbit sample transfer system for the Device Assembly Facility (DAF). Top detector needs included systems for neutron scattering experiments, along with detection systems compatible for gamma-induced fission measurements.

5. Conclusions

This paper has described the relationship between nonproliferation and nuclear data along with the motivations and key outcomes of NDREW. Some progress was made in producing a specific prioritization of nuclear data needs for nonproliferation. There were a handful of gaps that received nearly universal support as important near-term goals, such as evaluations for fission yields for the "big three" isotopes (^{235}U, ^{238}U, ^{239}Pu), branching ratios associated with xenon production, and evaluations for recently collected (α,n) data. The group succeeded in providing more specific, nonproliferation-oriented needs than previous gatherings. Furthermore, attendees appreciated the opportunity for different communities, such as experimentalists, theorists, evaluators, data curators, end-users, and program managers, to interact with one another and establish a new dialogue. The workshop did not address some nuclear data topics, such as cross sections for inelastic neutron scattering and the properties of antineutrino reactions, due in part to their coverage in other venues.

In the near term, DNN R&D will focus on using the results from NDREW, coupled with the outcomes from other meetings and follow-up discussions with data end-users, to produce a strategic document which prioritizes nuclear data activities for the office over the next 5-10 years. While there are no plans to make this document public, it will be used to inform decision-making for the office in subsequent years. However, there are plans to post an abridged account of the workshop's important outcomes, along with much of its presentation content, on the National Nuclear Data Center website. Many attendees expressed the desire to continue the discussions initiated at NDREW, perhaps in the form of an annual workshop series. Specific implementation plans for this idea have not yet been finalized. However, a special "Nuclear Data for Nonproliferation" technical track has been organized as part of the upcoming Institute of Nuclear Materials Management (INMM) Annual Meeting from 22-26 July 2018 in Baltimore, USA. Consisting of 24 papers distributed among three sessions, this technical track represents an opportunity to further engage stakeholders outside of NNSA, including the international community.

The nearest-term allocation of nuclear data funding has already been planned, and a collaborative funding announcement issued by the Office of Nuclear Physics, backed by DNN R&D, has been issued [13]. The focus for this announcement consists of differential and integral measurements for fission yields, including the development of tools to evaluate fission yields. Future funding announcements will consider other nuclear data topics.

6. Acknowledgements

The authors would like to thank Rian Bahran (LANL) and Lee Bernstein (LBNL) for their extensive and valuable contributions during the planning and execution of NDREW. Other session leaders also provided their time and support, including: Teresa Bailey (Lawrence Livermore National Laboratory [LLNL]), Todd Bredeweg (LANL), Jason Burke (LLNL), Matt Devlin (LANL), Susan Hogle (ORNL), Libby McCutchan (BNL), Sara Pozzi (University of Michigan), Brian Quiter (LBNL), Brad Rearden (ORNL), Sean Stave (NNSA), and Patrick Talou (LANL). Donna Raziano and Susan Uhlhorn (both LLNL) were instrumental in providing logistical support for the workshop. Noel Nelson (NNSA), Christopher Chapman (ORNL), and Aaron Hurst (LBNL) served important roles as notetakers. Finally, the workshop would not have been a success without the support of its 117 engaged speakers and attendees.

7. References

[1] Reilly D, Enselin N., Smith H, and Kreiner S; *Passive Nondestructive Assay of Nuclear Materials ('PANDA Manual');* US Nuclear Regulatory Commission Report NUREG/CR-

5550; Los Alamos National Laboratory Report LA-UR-90-732; 1991

[2] Brown D et al; *ENDF/B-VIII.0: The 8th Major Release of the Nuclear Reaction Data Library with CIELO-project Cross Sections, New Standards and Thermal Scattering Data*; *Nuclear Data Sheets*; Vol. 148; pp. 1-142; 2018

[3] NNSA Nonproliferation Research and Development web page; https://nnsa.energy.gov/aboutus/ourprograms/nonproliferation/rd; Accessed Mar 2018

[4] Peters W et al; *A Kinematically Complete, Interdicsiplinary, And Co-Institutional Measurement of the $^{19}F(\alpha,n)$ Cross Section for Nuclear Safeguards Science*; Idaho National Laboratory Report INL/EXT-16-38791; 2016

[5] Organisation for Economic Co-Operation and Development (OECD) Nuclear Energy Agency; *Meeting Nuclear Data Needs for Advanced Reactor Systems*; Report NEA/NSC/WPEC/DOC(2014)446; 2014

[6] Forrest R; *Nuclear Science and Data Needs for Advanced Nuclear Systems*; *Energy Procedia*; Vol. 7; pp. 540-552; 2011

[7] Santi P. et al; *The Role of Nuclear Data in Advanced Safeguards*; GLOBAL 2007 Conference on Advanced Nuclear Fuel Cycles and Systems; Boise, ID, USA; 9-13 Sep 2007

[8] Bahran R et al; *A Survey of Nuclear Data Deficiencies Affecting Nuclear Non-Proliferation*; 2014 INMM Annual Meeting; Atlanta, GA, USA; 20-24 Jul 2014

[9] Francis M, Weber C, Pigni M, and Gauld I; *Reactor Fuel Isotopics and Code Validation for Nuclear Applications*; Oak Ridge National Laboratory Report ORNL/TM-2014/464; 2015

[10] Bernstein L et al; *Nuclear Data Needs and Capabilities for Applications*; White Paper; 2015

[11] Romano C; *Update on the Nuclear Data Working Group*; ANS Advances in Nuclear Nonproliferation Technology and Policy Topical; Santa Fe, NM, USA; 25-30 Sep 2016

[12] Romano C; *The Nuclear Data Working Group: Accomplishments and Future Plans*; Proceedings of the 58th Meeting of the Institute for Nuclear Materials Management; Indian Wells, CA, USA; 16-20 Jul 2017

[13] US Department of Energy Office of Science, Nuclear Physics; *Nuclear Data Interagency Working Group /Research Program*; DOE National Laboratory Announcement LAB 18-1903; Released March 2018

Numerical Method for High Count-Rate Dead-Time Correction in Neutron Multiplicity Counting using Multi-Channel List-Mode Recorders

Ludwig Holzleitner*

European Commission – Joint Research Center (JRC) – Karlsruhe – P.O. Box 2340 – 76125 Karlsruhe – Germany, Ludwig.Holzleitner@ec.europa.eu .

Daniela Henzlova, Martyn T. Swinhoe

NEN-1 – Safeguards Science and Technology Group – Los Alamos National Laboratory – Los Alamos – NM 87545 – USA

Abstract:

In the field of neutron multiplicity counting, modern list mode recorders provide increased possibilities for neutron data analysis. The most recent generation can give both exact timing information and channel information where and when an event had been recorded. A new method for dead-time correction presented here makes use of this information to calculate a second pulse train containing estimations of pulse losses at specific positions. Using this, the histograms of Reals plus Accidentals (R+A) and Accidentals (A) obtained by ordinary multiplicity counting are directly corrected using statistical methods. Since the calculation of these values is derived directly from the corrected histograms R+A and A, this dead-time correction method works in principle for any kind of multiplicity (Singles, Doubles, Triples, …). The system calibrates itself by calculating the probabilities of dead-time loss at the specific channels with actual measurement data using some basic properties of the Rossi-Alpha distribution. Although the method is described here from a neutron counting perspective, it is applicable to any kind of instrument with similar characteristics.

Keywords: nuclear safeguards, non destructive analysis, neutron measurements, neutron multiplicity counting, list mode counters, dead time correction

1. Introduction:

Neutron multiplicity counting is a technique used for non-destructively assaying the quantity of fissile material such as, e.g. uranium (U), plutonium (Pu), californium (Cf), etc. It is based upon the fact that neutrons from spontaneous or induced fission events are emitted substantially simultaneously. The probabilities of having a 0,1,2,3, etc. neutrons in a fission event (sometimes called the multiplicity distribution: Singles, Doubles, Triples, …) provides a signature of the material under examination. A neutron detector typically comprises a body of polyethylene having a cavity in the middle to accommodate a sample during measurement. Around the cavity, gas proportional counters, often ^{3}He tubes, are embedded in the polyethylene body. There is a high probability that a neutron emitted from the sample will collide with hydrogen in the polyethylene. Neutrons thus lose energy until thermal equilibrium with the material is reached. A fraction of these thermalised neutrons eventually hit an atom of the gas in one of the gas proportionality counters. If so, a charge is released and collected at

* Corresponding Author

the electrode of the tube. The gas proportional counters are connected to preamplifiers, which receive the electric pulses from the gas proportional counters, process them and output them as a pulse train for further processing. Until recently the pulse trains from the individual preamplifiers were collected and merged in a single pulse train, sent for analysis to an analysing electronics called multiplicity counter.

Due to various reasons a pulse is likely to be lost if it arrives close in time to another, leading pulse. This may happen within the ^{3}He tube itself, on the way from the tube to the preamplifier (pile-up) or within the preamplifier itself. The reaction within the ^{3}He tube $^{3}He+n \rightarrow p+^{3}H+765keV$ could lead to two pulses resulting from the two positively charged particles. Therefore the charge collection time of some preamplifiers is adjusted such as to cover the pulses from both particles from such a reaction, thus also resulting in dead-time loss. After the preamplifiers normally no loss due to dead-time takes place aside from pile-up when collecting the signals from individual preamplifiers. However, this can be overcome by using a FIFO-buffer called de-randomizer.

Since a short time so called list mode recorders were introduced which can record these pulses and store the times of pulse arrival in a computer-file. The most advanced generation can record the pulses simultaneously from all preamplifiers and give synchronized arrival times of pulses on all of its input-channels. This additional information can be used to obtain further information on the dead-time behaviour of the system and thus make an advanced attempt to correct the multiplicity distribution for dead-time loss using statistical comparison between the pulse arrival and arrival times on individual channels. Figure 1 shows a schematic setup of a neutron detector using a multi-channel list-mode recorder.

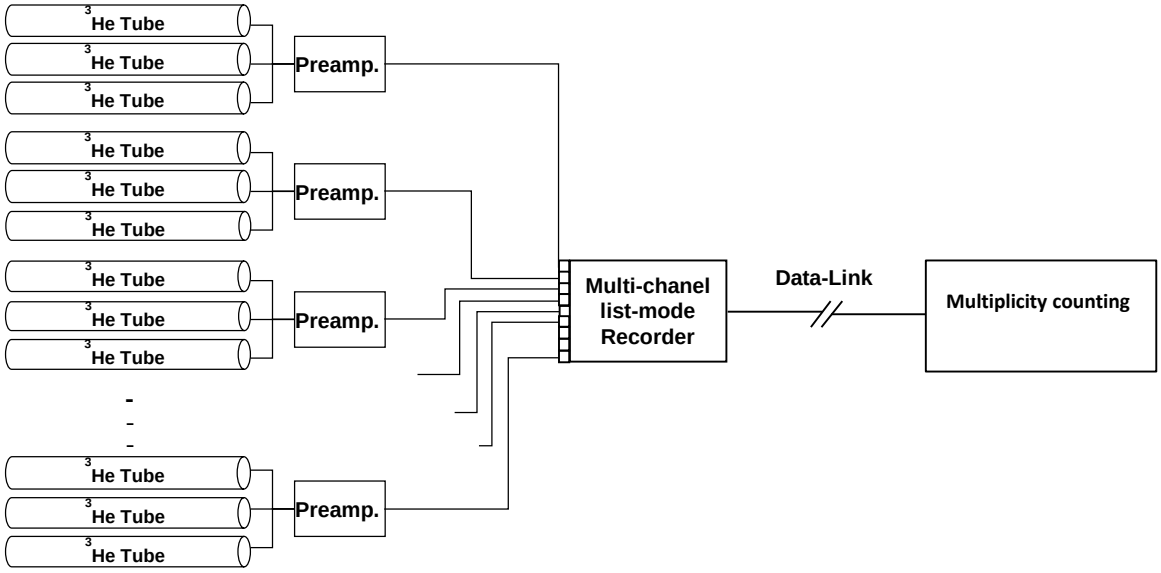

Figure 1: Schematic setup of neutron multiplicity counting using a multi-channel list-mode recorder.

2. Estimation of dead-time loss:

The idea for estimating the pulses lost on the individual channels is based on the idea, that a neutron emitted by the sample within the cavity is randomly captured by one of the ^{3}He tubes surrounding the sample. This is justified by the fact, that neutrons are moderated within the polyethylene in which the ^{3}He tubes are embedded and therefore may be reflected several times before capture. Although the chances of capture could differ from channel to channel, it is assumed there is no cross-correlation

from one neutron to another concerning its place of capture. However, regarding detectors with ^{3}He tubes arranged in several rings and wired ring-wise to preamplifiers, there could be certain preferences for neutrons to be captured on inner or outer rings depending on the energy. However, this case shall not be considered here, the calculations explained subsequently can easily be done ring by ring to overcome this difficulty.

Let's denote the overall global time of the detector by t, in contrast to the time at certain channels to be denoted by τ, sometimes as τ_i with an index i, indicating the number of the channel for that specific timeline. Whereas the global time is the same for the whole detector, the time for the individual channels runs individually indicating the time from a certain preceding event e.g. from a leading recorded pulse on a particular channel or from a trigger at a Rossi-Alpha distribution. The time along a pulse train is in principle continuous. All multiplicity counters as well as list mode recorders or other pulse train analysing electronics work with a certain clock speed (usually given in MHz), cutting this continuous time in a sequence of discrete time intervals of uniform duration (the duration determined by the clock speed), in the following called TICs. The analysing electronics can only recognize whether there is a pulse within such a time interval on a given channel or not, in case there are more pulses within the same TIC on the same channel, only one pulse is recognized. Therefore we will in the following consider time as a series of small time intervals, either bearing a pulse at a certain channel or not.

Pulses are denoted as $P_i(t)$ and considered as a 1 (if there was a pulse within a TIC) or 0 (in case not) on the global timeline t, where i indicates the channel where it was accounted. A "count" $C_i(t)$ is a pulse counted for in contrast to a "lost pulse" $L_i(t)$. Of course $P_i(t) = C_i(t) + L_i(t)$. The relative efficiencies of channels are denoted as e_i, where of course $\sum_i e_i = 1$. The relative efficiency e_i for channel i is defined as the constant e_i for which the following equation holds in average over an arbitrary time period $[t_1, t_2]$ (where $\approx$ indicates "statistical equality in the long run" or equality within statistical uncertainties):

$$\int_{t_1}^{t_2} P_i(t)\,dt \approx e_i \int_{t_1}^{t_2} \sum_j P_j(t)\,dt \qquad \text{eqn. 1}$$

Subtracting $e_i \int_{t_1}^{t_2} P_i(t)\,dt$ from both sides, dividing both sides by $1 - e_i$ and using $P_i(t) = C_i(t) + L_i(t)$ yields:

$$\int_{t_1}^{t_2} P_i(t)\,dt \approx \frac{e_i}{1-e_i} \int_{t_1}^{t_2} \sum_{j\neq i} P_j(t)\,dt = \frac{e_i}{1-e_i} \int_{t_1}^{t_2} \sum_{j\neq i} \big(C_j(t) + L_j(t)\big)\,dt \qquad \text{eqn. 2}$$

The probability function $p_i(\tau_i)$ for losing a pulse at channel i has as timeline τ_i, the time from the last recorded pulse on that channel. This means in this model we assume non-updating dead-time: A lost pulse has no impact on the dead-time behaviour on that channel. The values of $p_i(\tau_i)$ range from 0 (a pulse at this channel and time is for sure recorded) to 1 (a pulse at this channel and time is for sure lost). Figure 2 shows a possible behaviour of such a dead-time probability function $p_i(\tau_i)$ and the corresponding behaviour of the pulse train $P_i(t)$ on channel *i*, the black parts indicating the observed pulses $C_i(t)$, the white ones the lost ones $L_i(t)$. Therefore we have in average over an arbitrary time period $[t_1, t_2]$ the following equation, where τ_i indicates the time difference from the last count on channel i to time t according to which the probability function $p_i(\tau_i)$ behaves. Therefore we have $L_i(t) \approx p_i(\tau_i) P_i(t)$ or eqn. 3:

$$\frac{L_i(t)}{p_i(\tau_i)} \approx P_i(t) \qquad \text{eqn. 3}$$

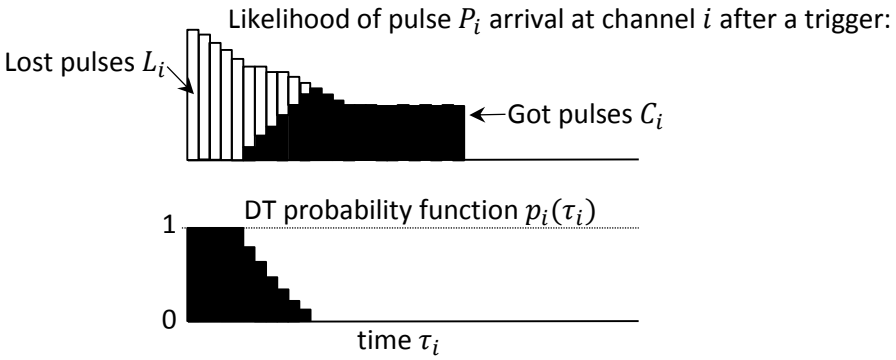

Figure 2: Dead time probability function determines the loss of pulses after a leading pulse.

Using eqn. 2 and eqn. 3 together we get:

$$\int_{t_1}^{t_2} \frac{L_i(t)}{p_i(\tau_i)}\,dt \approx \frac{e_i}{1-e_i} \int_{t_1}^{t_2} \sum_{j\neq i} \big(C_j(t) + L_j(t)\big)\,dt \qquad \text{eqn. 4}$$

By reducing the interval $[t_1, t_2]$ to one TIC, the minimum time period our electronic can resolve, and multiplying both sides with $p_i(\tau_i)$ we get that in the long run the following equation holds in average:

$$L_i(t) \approx p_i(\tau_i) \frac{e_i}{1-e_i} \sum_{j\neq i} \big(C_j(t) + L_j(t)\big) \qquad \text{eqn. 5}$$

Up to now we considered just channel i. However, we have such an equation for each channel of our list mode electronics. Furthermore, by bringing all lost pulses to the left hand side and the counts to the right hand side we get the following system of equations while denoting the maximum number of channels as k:

$$\left(L_i(t) - p_i(\tau_i) \frac{e_i}{1-e_i} \sum_{j\neq i} L_j(t) \approx p_i(\tau_i) \frac{e_i}{1-e_i} \sum_{j\neq i} C_j(t) \right)_{i=1,\ldots,k} \qquad \text{eqn. 6}$$

It remains to replace the unknown lost pulses $L_i(t)$ by our estimations $l_i(t)$, the average estimated pulses lost at that position which we want to calculate. This results in the following matrix equation:

$$\begin{bmatrix} 1 & -\frac{p_1(\tau_1)e_1}{1-e_1} & \cdots & -\frac{p_1(\tau_1)e_1}{1-e_1} \\ -\frac{p_2(\tau_2)e_2}{1-e_2} & 1 & & -\frac{p_2(\tau_2)e_2}{1-e_2} \\ \vdots & & \ddots & \vdots \\ -\frac{p_k(\tau_k)e_k}{1-e_k} & -\frac{p_k(\tau_k)e_k}{1-e_k} & \cdots & 1 \end{bmatrix} \begin{bmatrix} l_1(t) \\ l_2(t) \\ \vdots \\ l_k(t) \end{bmatrix} = \begin{bmatrix} \frac{p_1(\tau_1)e_1}{1-e_1} \sum_{j\neq 1} C_j(t) \\ \frac{p_2(\tau_2)e_2}{1-e_2} \sum_{j\neq 2} C_j(t) \\ \vdots \\ \frac{p_k(\tau_k)e_k}{1-e_k} \sum_{j\neq k} C_j(t) \end{bmatrix} \qquad \text{eqn. 7}$$

Solving this matrix equation for $\left(l_i(t)\right)_{i=1,\dots,k}$ yields the desired estimation of lost pulses[1]. Doing so repeatedly for every t from our timeline and for every meaningful (means non-zero) right hand side we obtain a second, estimated pulse train containing the estimated average number of pulses lost at this position and time. However, one must be careful with the interpretation of these values: They do not represent the likelihood of a pulse being on that position; they represent the average number of pulses, which are – in the long run – lost in similar situations at this position, its reference being the recorded counts $C_j(t)$ on the other channels. One could also refer to them as the average number of cases where a corresponding accounted pulse $C_j(t)$ could be found on channel i as $L_i(t)$ if it were not seen on the other channel j due to slightly different reflection in the moderator. This difference can also be seen in the fact that the $l_i(t)$ may occasionally become larger than 1!

3. Determining the dead-time behaviour $p_i(\tau_i)$ – calibrating the system:

So far we assumed that we know the probabilities $p_i(\tau_i)$, according to which pulses are lost after a leading pulse. However, in general these probability functions are not known in advance, but must be estimated as well. This can be done using the measurement data directly, so no prior measurement using a calibration source is needed. It should be pointed out that the best way is to do it for each measured source individually, since the energies of the emitted neutrons influence the relative efficiencies or other detector characteristics essential for the correction method described above.

Concerning the relative channel-efficiencies e_i one simply may count how many counts were registered at each channel. These registered counts are reduced by dead-time, the reduction being higher as higher the count-rate at a channel. Nevertheless it provides with a sufficient good estimation of the relative channel-efficiencies as long as the count-rates at the individual channels do not differ by orders of magnitude.

Concerning the dead-time probability functions $\mathrm{p_i}(\tau_\mathrm{i})$ we take advantage of the Rossi-Alpha distribution: The Rossi-Alpha distribution is the distribution in time of events that follow after an arbitrary starting event. The Rossi-Alpha distribution (of Type I or Orndorff-type, see [1] for details) is obtained by fixing an arbitrary pulse from the pulse train as the starting pulse and recording each subsequent pulse in a bin corresponding to the time-distance from the starting pulse to the subsequent pulse (up to a predetermined maximum distance). Then, the next pulse of the pulse train is fixed as the starting pulse and the process is iterated. Each bin of the distribution thus indicates the count of pulses occurring at a particular distance from a starting pulse. The early part of a Rossi-Alpha distribution shows the behaviour of pulses close to a leading pulse. Hence the dead-time effect can especially be noticed there. Since we want to estimate exactly this effect, using a Rossi-Alpha distribution is a natural choice.

Now we use the observation of eqn. 2 with $P_i(t) = C_i(t) + L_i(t)$: Provided a non-dead-timed pulse train, the fraction of pulses received and lost on one channel follows statistically the equation:

[1] There exists a possibility that during $0 < p_i(\tau_i) < 1$ a pulse occurs on that channel i. This pulse then produces another timeline τ_i on channel i with another probability function $p_i(\tau_i)$ starting afresh. This could lead to 2 entries from the same channel i in eqn. 7. The treatment of these double entries in eqn. 7 is complicated and exceeds the scope of this paper. It shall be subject for discussion in another publication. Ignoring it may, depending on the exact from of $p_i(\tau_i)$, lead to a slight underestimation of the total lost pulses (of a few %).

$$C_i(t) + L_i(t) \approx \frac{e_i}{1 - e_i} \sum_{j \neq i} \left(C_j(t) + L_j(t) \right) \qquad \text{eqn. 8}$$

Since the Rossi-Alpha distribution is just the superposition of many short time-lines following a leading pulse, eqn. 8 shall especially hold for it. Moreover, if we calculated the lost pulses $\mathrm{l_i(t)}$ correctly, they shall also follow this rule (where $L_i(t)$ are replaced by the calculated $l_i(t)$):

$$C_i(t) + l_i(t) \approx \frac{e_i}{1 - e_i} \sum_{j \neq i} \left(C_j(t) + l_j(t) \right) \qquad \text{eqn. 9}$$

The idea is to use this eqn. 9 and apply it to a Rossi-Alpha distribution with accounted pulses $C_i(t)$ and estimated lost pulses $l_i(t)$. For this we must first build such a Rossi-Alpha distribution, however we trigger only with pulses $C_i(t)$ actually recorded. Discriminate between the parts of the Rossi-Alpha distribution arising from pulses recorded $C_i(t)$ and pulses $l_i(t)$ calculated. Also discriminate between pulses on channel i and pulses on another channel, see Figure 3.

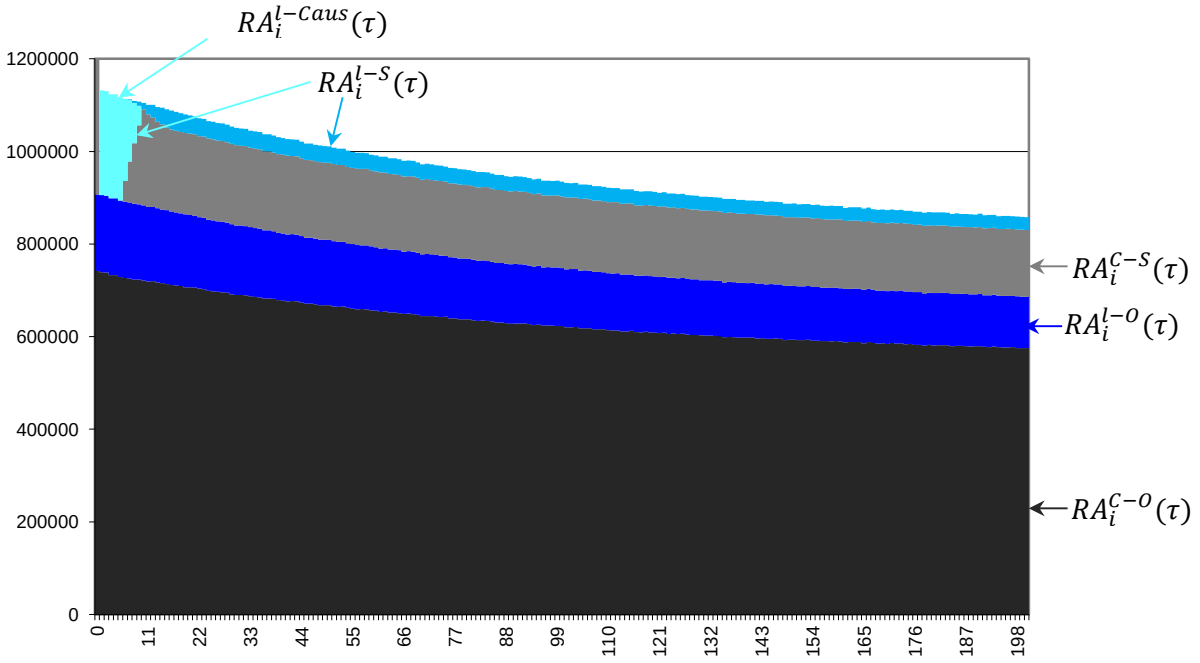

Figure 3: Rossi-Alpha distribution from a simulation with its parts: $RA_i^{C-S}(\tau)$ [■], $RA_i^{C-O}(\tau)$ [■], $RA_i^{l-O}(\tau)$ [■] and $RA_i^{l-S}(\tau)$ [■ + ■]. $RA_i^{l-S}(\tau)$ consists of 2 parts, $RA_i^{l-Caus}(\tau)$ [■], which can be obtained during solving eqn. 7, and the rest. Black/grey parts are observed; blue parts are lost due to dead-time and must be reconstructed from solutions of eqn. 7.

Denote as:

- $RA_i^{C-S}(\tau)$ the Rossi-Alpha triggered on channel i where only accounted pulses $C_i(t)$ from channel i are recorded.
- $RA_i^{C-O}(\tau)$ the Rossi-Alpha triggered on channel i where only accounted pulses $C_{j \neq i}(t)$ other than from channel i are recorded.
- $RA_i^{l-S}(\tau)$ the Rossi-Alpha triggered on channel i where only estimated lost pulses $l_i(t)$ from channel i are recorded.

- $RA_i^{l-O}(\tau)$ the Rossi-Alpha triggered on channel i where only estimated lost pulses $l_{j\neq i}(t)$ other than from channel i are recorded.
    - $RA_i^{l-Caus}(\tau)$ is a part of $RA_i^{l-O}(\tau)$. It is obtained when building a Rossi-Alpha distribution from the $l_i(t)$ using the corresponding τ_i as time information instead of *t*. This must to be done during solving eqn. 7 and building the estimated train of lost pulses and consists of the pulses which loss had been caused by the trigger of the Rossi-Alpha!

If the probabilities $p_i(\tau_i)$ were accurate, the following equation should hold:

$$\frac{e_i}{1-e_i}\left(RA_i^{C-O}(\tau)+RA_i^{l-O}(\tau)\right)-\left(RA_i^{C-S}(\tau)+RA_i^{l-S}(\tau)\right)\approx 0 \qquad \text{eqn. 10}$$

We use this to iterate for the dead-time probability functions $p_i(\tau_i)$:

1. Start with an initial guess of the dead-time probability functions, e.g. $p_i(\tau_i)=0$. Take a part of the pulse stream and build the Rossi-Alpha distributions $RA_i^{C-S}(\tau)$, $RA_i^{C-O}(\tau)$ from it as described before.
2. Estimate lost pulses by repeatedly solving eqn. 7 for every t from our timeline and every meaningful (non-zero) right hand side. Thus obtain a second, estimated pulse train $l_i(t)$.
    - At the same time, for each channel i, build up a small Rossi-Alpha distribution $RA_i^{l-Caus}(\tau)$ from the $l_i(t)$ using τ_i for time. It is a part of $RA_i^{l-S}(\tau)$, consisting only of estimated lost pulses showing the time-distance to the trigger having ***caused*** its loss.
3. After that do the following for each channel i:
    - Build Rossi-Alpha distributions $RA_i^{l-S}(\tau)$ and $RA_i^{l-O}(\tau)$ as described before.
    - Calculate the new guess for the dead-time probability functions $p_i^{new}(\tau_i)$ as:

$$p_i^{new}(\tau_i)=\frac{\frac{e_i}{1-e_i}\left(RA_i^{C-O}(\tau)+RA_i^{l-O}(\tau)\right)-\left(RA_i^{C-S}(\tau)+RA_i^{l-S}(\tau)-RA_i^{l-Caus}(\tau)\right)}{RA_i^{C-S}(\tau)+RA_i^{l-Caus}(\tau)} \qquad \text{eqn. 11}$$

4. Stopping criterion: If the dead-time probability functions $p_i(\tau_i)$ estimated lost pulses were accurate, the difference of this new guess $p_i^{new}(\tau_i)$ to the previous one should be very small. If sufficiently small, stop and take the $p_i^{new}(\tau_i)$ as dead-time probability functions, else take the $p_i^{new}(\tau_i)$ as dead-time probability functions and proceed with step 2. Of course we could also check whether eqn. 10 holds sufficiently well and use this as stopping criterion.

It had been found that this iteration process converges and in general reaches a sufficiently good result within less than 10 iteration steps.

4. Correcting the multiplicity distribution:

During multiplicity counting one collects a multiplicity histogram $(m_0, m_1, m_2, \dots)$ in the following way: One triggers at time t_0 and sums up all pulses received during a time period $[t_0+\tau_1, t_0+\tau_2]$, with some fixed offsets τ_1 and τ_2 from t_0 (of course $\tau_1<\tau_2$). This means for a given t_0 one calculates $M=\sum_{t_0+\tau_2}^{t_0+\tau_1}\sum_i C_i(t)$ and increases m_M by the number of triggers $\sum_i C_i(t_0)$ within the histogram $(m_0, m_1, m_2, \dots)$. In the end the numbers $(m_0, m_1, m_2, \dots)$ tell you how often there had been 0,1,2, … pulses accounted for within such a gate triggered by a pulse. τ_1 is called delay or pre-delay, the difference $\tau_2-\tau_1$ is called gate-with.

This histogram is affected by pulse loss due to dead-time in 2 ways: First, if a pulse is lost it cannot trigger a gate and the entry in the histogram $(m_0, m_1, m_2, \dots)$ is lost. Second, the number of pulses $M = \sum_{t_0+\tau_2}^{t_0+\tau_1} \sum_i C_i(t)$ is calculated wrongfully due to missing pulses within the gate period $[t_0 + \tau_1, t_0 + \tau_2]$, so the wrong m_M may be increased in the histogram $(m_0, m_1, m_2, \dots)$.

For correcting the multiplicity distribution we have first to perform a few theoretical considerations: Assume we have g gates with multiplicity M and p pulses lost in total within all of these gates. This means in average there were $x = p/g$ pulses missing in each gate, giving an average chance of p/Mg that a pulse got lost. As long as the measurement conditions stay the same, this number is theoretically constant. Since neutrons collide within the moderator of the detector and are reflected sufficiently often we can assume that the channels, where the neutrons are detected are independent from event to event. Therefore also the probability whether there had been a loss due to dead-time caused by a leading neutron is independent from each other. Mathematically such success/failure experiments are described by the Binomial distribution with the expectation p/g. However, as there are infinitely many gates (we can measure only finitely many of them) we need to let $g \to \infty$. Of course then also the total number of lost pulses increases, but the expectation p/g stays the same due to unchanged measurement conditions. It is well known (see [1], pp. 27) that the Binomial distribution tends to the Poisson distribution $P_{p/g}$ with parameter p/g if the expectation converges to a number different from both 0 and ∞. Therefore our distribution in question is the Poisson distribution $P_{p/g}$. The way how we calculated the missing pulses according to eqn. 7 was, that we took those pulses we got as reference and assumed they could be accounted on another channel *i*, where they were likely to be lost in the dead-time shadow of its leading pulse, its likelihood determined by $p_k(\tau_k)e_k/(1 - e_k)$. We justified assume they could as well be accounted at the missing position if they were reflected a bit different within the moderator. But then there were not at the position where we actually found them. Therefore we apply the Poisson distribution to gates with multiplicity $M - 1$.

However, that this model cannot be entirely correct is easily seen on the fact that it allows in principle, although with a very small probability, all pulses to be lost in a gate. But at least some pulses must remain there, at least those which have causes the others to be lost due to dead-time causes by them. This clearly demonstrates that this model does not entirely fit to the situation, but for the moment it is all we have. Also the assumption to correct the gates with multiplicity $M - 1$ is sloppy and not strictly justified. Therefore we use this as a first attempt and will try to improve it in a later stage. It is evident that the re-assignment of lost pulses to the gates to reconstruct the initial multiplicities is more sophisticated than described here and needs further, closer analysis.

The correction works now as follows: We apply multiplicity counting involving both pulse trains $(C_1(t), C_2(t), \cdots, C_k(t))$ and $(l_1(t), l_2(t), \cdots, l_k(t))$ in the following way, resulting in 4 histograms $(m_0, m_1, m_2, \dots)$, $(\overline{m_0}, \overline{m_1}, \overline{m_2}, \dots)$, $(n_0, n_1, n_2, \dots)$, and $(\overline{n_0}, \overline{n_1}, \overline{n_2}, \dots)$, see Figure 4 for an example:

1. Trigger on the dead-timed pulse train $(C_i(t))_{i=1,\cdots,k}$ and count the pulses $C_i(t)$ in the gate of the dead-timed pulse train as described before: Calculate $M = \sum_{t_0+\tau_2}^{t_0+\tau_1} \sum_i C_i(t)$ and increase m_M by $\sum_i C_i(t_0)$. This yields the normal dead-time affected multiplicity histogram $(m_0, m_1, m_2, \dots)$.
   1.1. Trigger on the dead-timed pulse train $(C_i(t))_{i=1,\cdots,k}$ and count the pulses $l_i(t)$ in the gate of the estimated lost pulse train: Calculate $x = \sum_{t_0+\tau_2}^{t_0+\tau_1} \sum_i l_i(t)$ and increase $\overline{m_M}$ by $x \sum_i C_i(t_0)$. This yields a histogram $(\overline{m_0}, \overline{m_1}, \overline{m_2}, \dots)$ containing the estimated sum of lost pulses in gates with the (dead-timed affected) multiplicity $M - 1$. This statistics indicates how the former multiplicity histogram $(m_0, m_1, m_2, \dots)$ needs to be updated later.
2. Trigger on the estimated lost pulse train $(l_i(t))_{i=1,\cdots,k}$ and count the pulses $C_i(t)$ in the gate of the dead-timed pulse train: Since there is always an observed pulse at the same time as an estimated lost pulse we may use $M = \sum_{t_0+\tau_2}^{t_0+\tau_1} \sum_i C_i(t)$ from step 1 before. We increase n_M by the sum of triggers on the estimated pulse train $\sum_i l_i(t_0)$. This yields a dead-timed multiplicity histogram

$(n_0, n_1, n_2, \dots)$ for lost triggers/gates which could simply be added to the original, dead-timed histogram.

2.1. Trigger on the on the estimated lost pulse train $(l_i(t))_{i=1,\cdots,k}$ and count the pulses $l_i(t)$ in the gate of the estimated lost pulse train: Again one can use the result $x = \sum_{t_0+\tau_2}^{t_0+\tau_1} \sum_i l_i(t)$ from step 1.1 before. Weight this with the sum of estimated lost triggers $\sum_i l_i(t_0)$, means calculate $x \sum_i l_i(t_0)$. Then increase $\overline{n_M}$ by $x \sum_i l_i(t_0)$. This yields a histogram $(\overline{n_0}, \overline{n_1}, \overline{n_2}, \dots)$ containing the average number of lost pulses in lost gates with a certain (dead-timed affected) multiplicity $M-1$. This statistics indicates how the former multiplicity histogram $(n_0, n_1, n_2, \dots)$ has to be updated for lost pulses inside its gates, before adding it to the original, dead-timed histogram.

3. Then the correction works as follows: Create a new histogram $(m_0^{new}, m_1^{new}, m_2^{new}, \dots)$ and redistribute the entries of the histograms $(m_0, m_1, m_2, \dots)$ and $(n_0, n_1, n_2, \dots)$ to it for all i=0,1,2,3,… as follows:

$$m_{i+j}^{new} = m_{i+j}^{new} + m_i Pois_{[\overline{m_{i+1}}/m_{i+1}]}(j) \quad \text{for j=0,1,2,…} \qquad \text{eqn. 12}$$

$$m_{i+j}^{new} = m_{i+j}^{new} + n_i Pois_{[\overline{n_{i+1}}/n_{i+1}]}(j) \quad \text{for j=0,1,2,…} \qquad \text{eqn. 13}$$

The multiplicity histogram $(m_0^{new}, m_1^{new}, m_2^{new}, \dots)$ calculated as described above is now corrected for dead-time loss. Using this procedure on the histograms for the "R+A gate" (where τ_1 is small) and the "A gate" (where τ_1 is large but using the same difference $\tau_2 - \tau_1$) and then from these such improved multiplicity histograms calculating the Singles, Doubles, Triples leads to improved results on these values. Concerning the way how these Singles, Doubles, Triples are derived from the multiplicity histograms the reader is referred to [3].

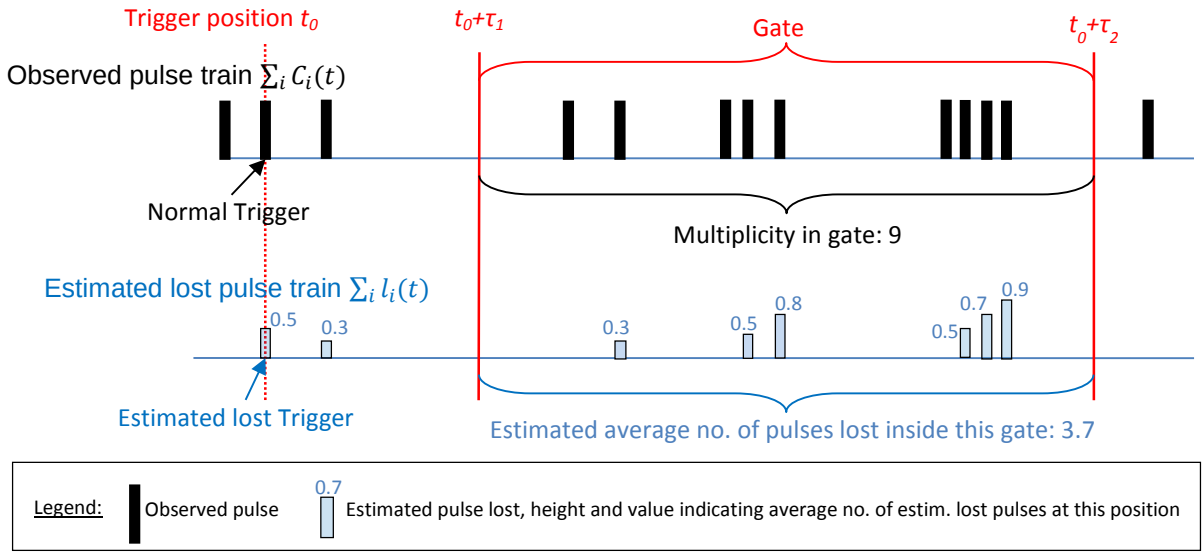

Figure 4: Example of multiplicity histogram collection where the sum of observed $\sum_i \mathbf{C_i(t)}$ pulses and estimated lost pulses $\sum_i \mathbf{l_i(t)}$ is plotted. Here $\mathbf{M} = \sum_{t_0+\tau_2}^{t_0+\tau_1} \sum_i \mathbf{C_i}(\mathbf{t}) = \mathbf{9}$ and $\sum_i \mathbf{C_i}(\mathbf{t_0}) = \mathbf{1}$ so $\mathbf{m_9}$ shall be increased by 1; $\mathbf{x} = \sum_{t_0+\tau_2}^{t_0+\tau_1} \sum_i \mathbf{l_i}(\mathbf{t}) = \mathbf{3.7}$ so $\overline{\mathbf{m_9}}$ shall be increased by 3.7; Since $\sum_i \mathbf{l_i}(\mathbf{t_0}) = \mathbf{0.5}$, $\mathbf{n_9}$ shall be increased by 0.5 and $\overline{\mathbf{n_9}}$ by 0.5*3.7=1.85.

5. Some results from simulations:

In order to test the theory explained above, a simulation was performed: As minimum time-slot (TIC) 100ns were used, the simulation was run for about 10 sec, corresponding to 100 Mega-TICs. During this simulation a Poisson-process was simulated, each event producing 10 neutrons. About 10 million neutrons were produced in these 10 seconds, corresponding to a rate of 1 million per second. These neutrons were delayed in time with an exponential distributed die-away of 10 microseconds and then randomly distributed to 5 channels. This simulated pulse stream unaffected by dead-time was stored for later comparison.

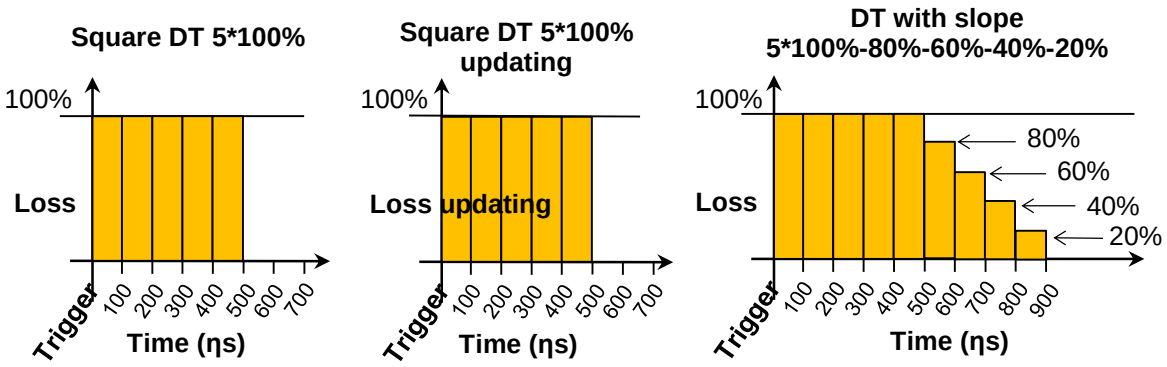

Figure 5: Dead-time patterns applied: Square dead-time (left), square updating dead-time (middle), where the dead-time pattern seen is starts anew also for lost pulses, and dead-time with slope

Then several dead-time patterns were applied to this simulated pulse stream (see Figure 5):

1) Square DT 5*100%: All pulses arriving on the same channel one to 5 TICs after a leading pulse were deleted.
2) Square DT 5*100% updating: All pulses arriving on the same channel one to 5 TICs after a leading pulse were deleted. Additionally the dead-time pattern is updating, means also a deleted pulse restarts the dead-time pattern afresh.
3) Slope DT: All pulses arriving on the same channel one to 5 TICs after a leading pulse were deleted. Pulses on TIC 6 after a leading pulse on the same channel were deleted with 80% probability, on TIC 7 with 60%, on TIC 8 with 40% and on TIC 9 with 20% probability. Pulses arriving at TIC 10 or later on the same channel were left unchanged. This way a smooth transition from zero count-rate to the full count-rate was achieved.

Since we are using a simulation we know exactly how many pulses were deleted and can compare it to the reconstructed ones. Figure 6 shows a comparison using a Rossi-Alpha distribution of the 3 dead-time patterns, triggered on observed pulses only: The calculated pulses of estimated lost pulses (in red) and the original deleted pulses (in green). As one can see the reconstruction works extremely well for the square dead-time pattern and for the slope. For the updating square dead-time pattern there is a slight underestimation in lost pulses, which is not surprising since our model assumes non-updating dead-time. The loss for the square dead-time was 12.04% (true) versus 12.05% (estimated), for the updating square dead-time 13,12% (true) versus 12.98% (estimated) and for the slope dead-time pattern as 15.9% (true) versus 15.9% (estimated). Hence the underestimation in the updating case is 1.07% from the amount of originally deleted pulses.

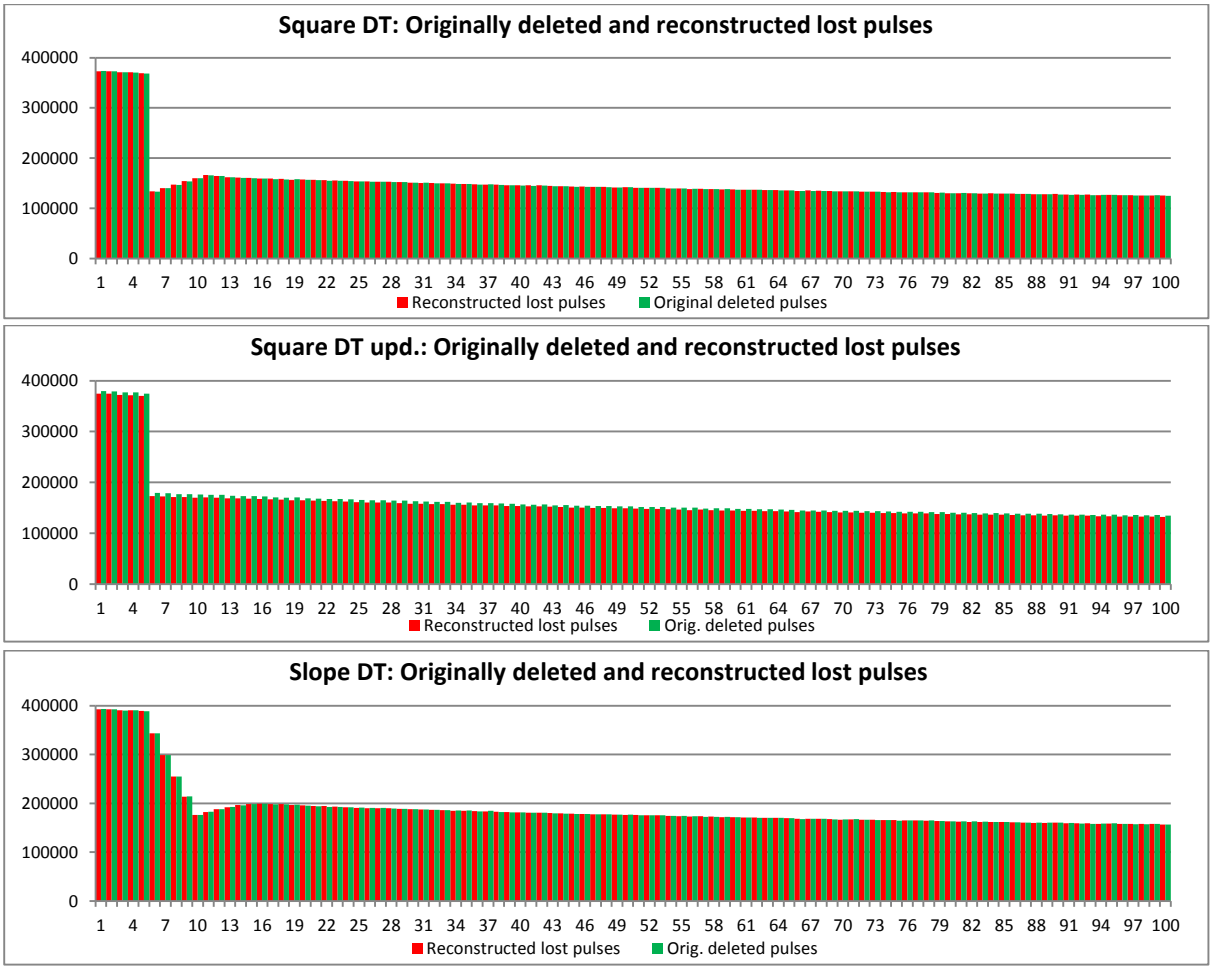

Figure 6: Rossi-Alpha parts of deleted / reconstructed lost pulses for the 3 dead-time patterns: Original deleted pulses are in green, the reconstructed are in red.

In Figure 7 one can see the effects the different dead-time patterns have on a Rossi-Alpha distribution. The parts one can observe are marked in black [■] (observed on other channels than the trigger channel) and grey [■] (observed on the same channel than the trigger channel). The blue parts mark these parts of the Rossi-Alpha distribution, which were reconstructed as described before: The dark blue part [■] is reconstructed and occurring on other channels than the Rossi-Alpha trigger, the light and medium blue parts are reconstructed as well [■ + ■] and occur on the same channel than the Rossi-Alpha trigger. The light blue part [■] was estimated according to eqn. 7 as having been caused to be lost by the trigger. The original Rossi-Alpha without dead-time loss is displayed on top-left, dead-timed with the square dead-time pattern on top-right, updating square dead-time pattern on bottom-left and slope dead-time pattern bottom-right. The different height of these Rossi-Alpha distributions arise from the fact, that triggering was done on observed pulses only and the dead-time patterns give raise to different dead-time losses: The loss for the square dead-time was estimated as 12.05% (true loss 12.04%), for the updating square dead-time pattern as 12.98% (true loss 13,12%) and for the slope dead-time pattern as 15.9% (true loss 15.9%). Because the estimation method described here is based on the assumption of non-updating dead-time it is clear that for the updating dead-time pattern the estimation is less precise. However, a recent study [5] indicates that dead-time using ^{3}He counters may follow a non-updating (paralyzable) dead-time model rather than an updating one. One should note the different forms of the light and medium blue part [■ + ■] and the grey parts [■] of these distributions (which all occur on the same channel as the trigger): Whereas at the square dead-time pattern the caused part [■] is also squared, the observed grey part on the same channel

has a small peak at its start at TIC 6 while later the dead-timed pulses not caused by the trigger start building up. In contrast, for the updating dead-time pattern the grey part shows no peak at all, but the caused part [■] is having its updating part past TIC 6. At the slope dead-time pattern the 3 parts overlap during the period where the dead-time probability is between 1 and 0!

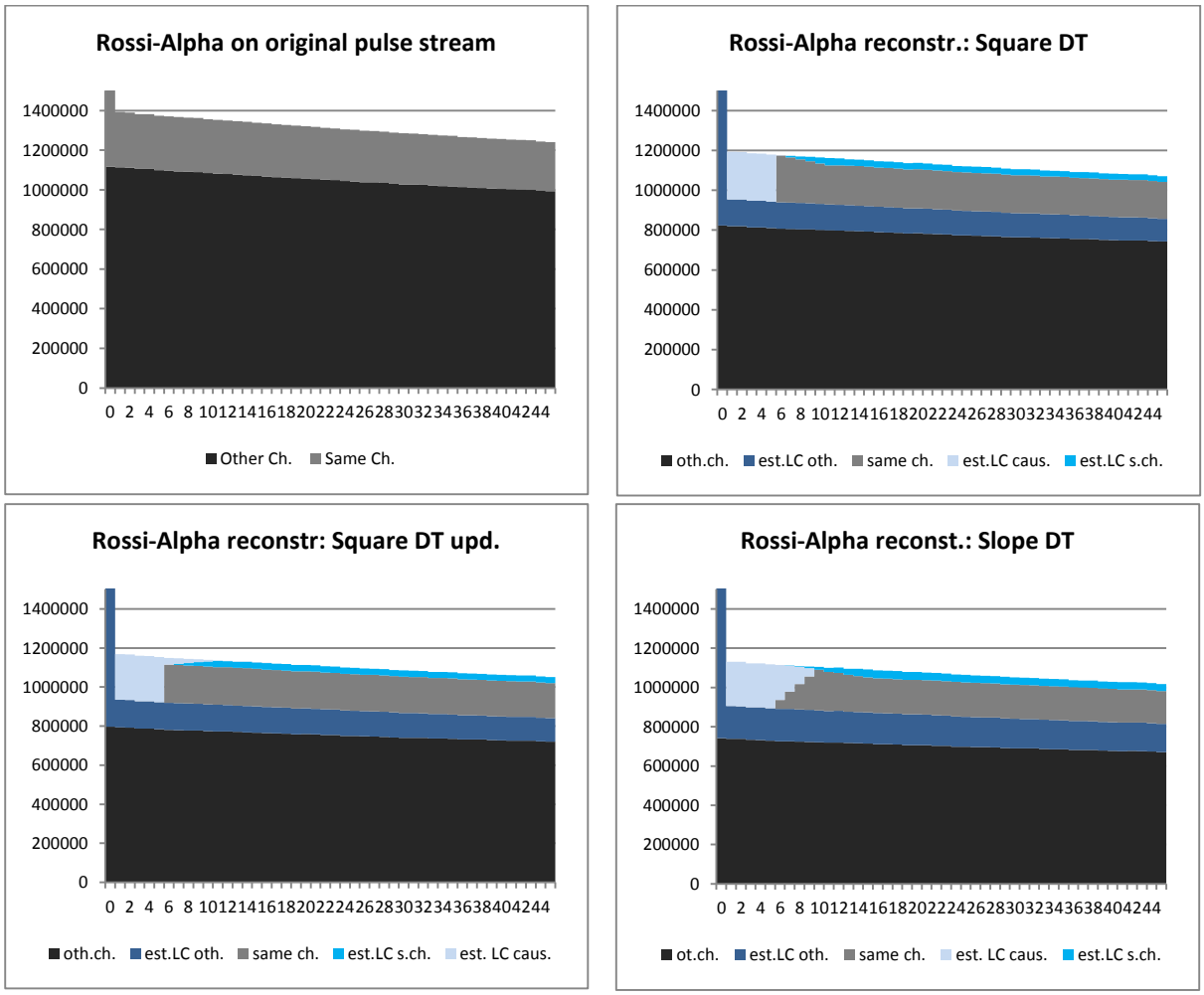

Figure 7: Early parts of Rossi-Alpha and reconstructions from different dead-time patterns: Original without dead-time (top-left), square dead-time (top-right), square dead-time updating (bottom-left) and slope dead-time (bottom-right). The different height with respect to the original is due to the fact that lost pulses are not used as triggers.

Figure 8 shows the multiplicity histograms of the pulse trains when affected by the different dead-time patterns: Dark and light green [■ + ■] show the original R+A and A histograms, red/orange [■ + ■] the dead-timed R+A and A histograms and dark/light blue [■ + ■] the corrected R+A and A histograms. The dead-timed are higher, but pushed to the left side of the scale, indicating the pulse loss within the gates. The original, green curves and the respective corrected blue ones match relatively well. However, at the bottom-right a multiplicity histogram from a random pulse distribution (no multiple emission of neutrons) with the same count-rate, using the same square dead-time pattern as top-left is displayed: As one can see the blue and green curves show considerable difference. This indicates that the re-assignment of lost pulses to gates still needs closer analysis and improvement. The reason why random pulse trains are worse in reconstructing the multiplicity histograms is not yet known. However, the overall estimation of lost pulses worked very well, the dark and light curves match perfectly indicating that there are no multiplicities at all.

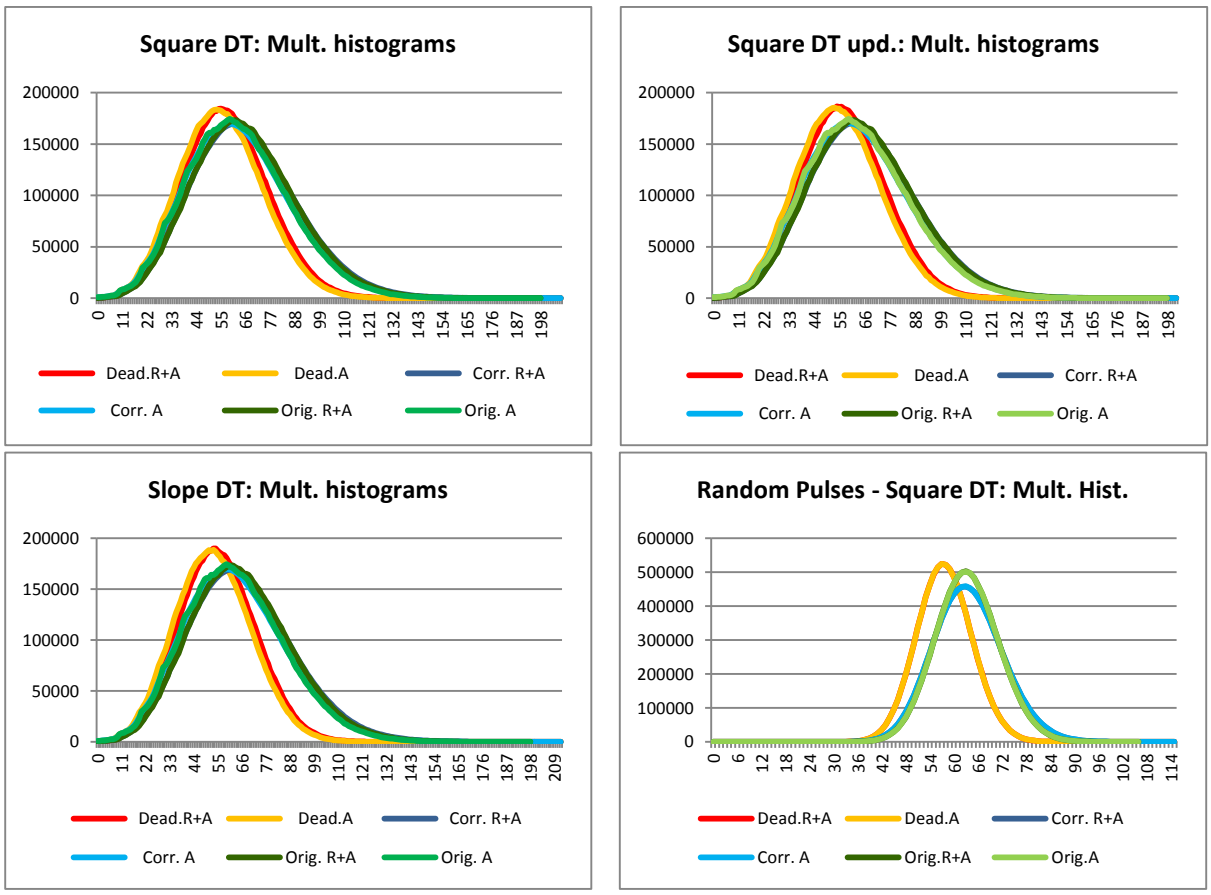

Figure 8: Multiplicity Histograms for the original pulse train, the dead-time affected using different dead-time patterns and its corrections: Dark/light green is the original R+A and A multiplicity histogram, red/orange the dead-timed R+A and A histogram and dark/light blue the corrected R+A and A histogram. Bottom-right: Multiplicity histogram form random pulse distribution

In Figure 9 and Table 1 the results of Singles, Doubles and Triples rates are displayed, for the original pulse train as well as for the dead-timed using the different dead-time patterns and for its corrections. Because during the simulation artificially multiple emissions of 10 neutrons per fission were used, the Doubles and Triples in this graph are artificial high with respect to Singles. As one can see, the correction of Singles and Doubles works very well, the correction for Triples is less precise and varies case by case. In general the Triples are, due to the high simulated count-rate, extremely affected by dead-time loss: In the case of dead-time with slope, which is the case with the highest dead-time loss, the dead-time affected pulse train gives even negative Triples. Negative Triples as seen in this case are a result of high dead-time loss and were found also by theoretical considerations, see [4]. These simulations just confirm the results of that paper. Nevertheless the Triples could be corrected back to a reasonable value.

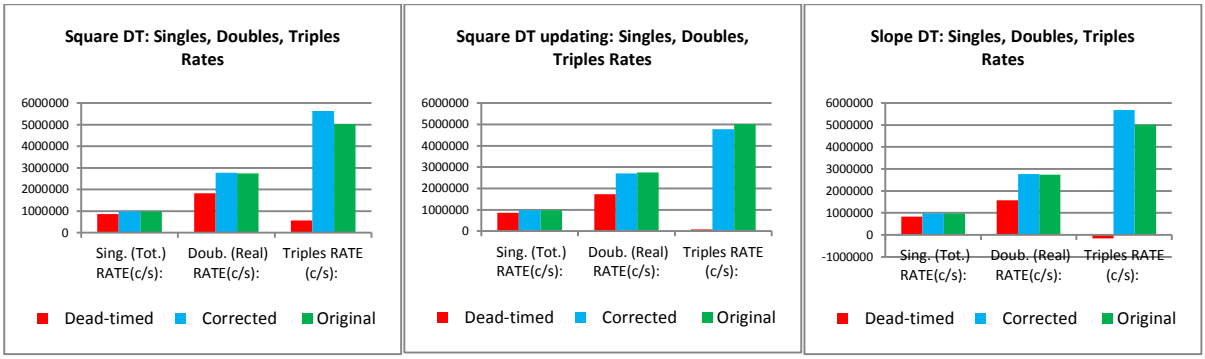

Figure 9: Original, dead-timed and corrected Singles, Doubles and Triples rates for different dead-time patterns: Square dead-time (left), Square updating dead-time (middle), Slope dead-time (right).

Mult.:	Original	Square dead-time		Square dead-time updating		Slope dead time	
		Dead-timed	Corrected	Dead-timed	Corrected	Dead-timed	Corrected
Singles	984751.51	866217.28	984938.36	855546.46	983184.01	828199.3	984728.26
Doubles	2743153.44	1823359.71	2764907.43	1728863.44	2704281.66	1580435.96	2765900.66
Triples	5016977	564682.86	5635323.26	76023.85	4766877.48	-164463.81	5681821.51

Table 1: Original, dead-timed and corrected Singles, Doubles and Triples rates for the different dead-time patterns

The processing of this 10 seconds simulated data of a count-rate of 10 Mpulses/sec (about 100 Mpulses in total) took about 30 seconds pure computing time after calibration on a commercial i7 INTEL processor using one core only. Further speedup using multiple cores is possible. A major bottleneck in this process is still the data transfer from the hard disk, however using fast SSDs can speed up this process as well.

6. Conclusion:

A new method for dead-time correction using a comparison of the signals of different preamplifiers has been developed. It was designed for high and very high count-rates and can calibrate itself directly from measurement data, provided the count-rate is sufficiently high. The estimation of lost pulses and the calibration had been demonstrated to work very well, the results of correction of Singles, Doubles and Triples works reasonably good. However, some improvement of the statistical method of re-assignment of lost pulses to gates is still desirable. The method has several advantages over traditional dead-time correction methods: It was designed and works for high and very high count rates; it does not need any calibration prior to measurement, but can use the measurement data for calibration directly, provided that the pulse train is dense enough; it works for any gate-with, delay, pre-delay and even fast accidentals, in principle it works also for higher moments like Quadruples. However due to the higher statistical uncertainty of these higher moments, which increase over proportional with count-rate, it needs to be investigated in how far it would be applicable; the computing time is reasonable. Last but not least this method has potential for further development, e.g. for estimating double pulsing using a similar comparison technique between channels.

7. Acknowledgements:

This work was done within the framework of the EURATOM – US/DOE agreement. The Authors want to thank all persons who contributed with their useful discussions and comments to this topic, special thanks to Darius Ancius, Paolo Peerani, Bent Pedersen and Peter Schwalbach.

8. References:

[1] Babala D.: *On the Theory of Rossi-Alpha Experiment in Reactor Noise Studies*, Nuclear Science and Engineering 26, pp. 418-424 (1966).

[2] Kersting G. and Wakolbinger A.: *Elementare Stochastik*, Birkhäuser, Basel, 2008.

[3] Ensslin N., Harker W. C., Krick M. S., Langner D. G., Pickrell M. M. and Stewart J. E.: *Application Guide to Multiplicity Counting*, LA-13422-M 1998.

[4] Hauk D. K., Croft S., Evans L. G., Favalli A., Santi P. A.: *Study of a theoretical model for the measured gate moments resulting from correlated detection events and an extending dead time*, Nuclear Instr. Methods, A719, pp. 57-69 (2013).

[5] Ianakiev K., Iliev M., Swinhoe M., Petersen B., Varasano G., Bugucarska T., Holzleitner L., De Baere P., Vaccaro S., Couland M.: *Field trial of KM200 Electronics in the JRC PUNITA Facility*, ESRRDA, 2017, Düsseldorf, Germany, 2017.

Non-destructive Assay in the Role of Consistency Checking

Tom Burr[1], Claude Norman[1], Chris Orton[2], Sergey Zykov[2]

[1]Safeguards Information Management, International Atomic Energy Agency
[2]Non-destructive Assay Servies

Abstract

In the context of inspector verification of operator declarations of item masses, Zykov [1] proposed to compare predicted observables to measured observables in difficult assay situations. Zykov [1] made the point that "inversion" of measurements to infer item mass may not always be needed (for example, in gross defect measurements), and that inversion amplifies the effects of errors. Non-destructive assay (NDA) measurements made on items selected to be measured by the inspector would be used "as is" to check for consistency with the operator declarations, rather than "inverted" to infer nuclear material mass. Declared item properties such as mass and container properties would be used to predict the NDA detector responses. A pass/fail criterion based on NDA counts would be applied to each item selected for verification.
This paper shows quantitatively in a generic calibration context that the "forward model only approach," i.e. comparing predicted to measured observables, has larger detection probability (DP) than the "invert to infer mass approach," because it avoids noise amplification associated with inverting from NDA counts to mass. The International Atomic Energy Agency's (IAEA's) DP depends on both the selection probability (at least one defective item occurs in the inspector's random sample) and the measurement identification probability (a truly defective item is inferred to be defective on the basis of measurement activities) as a function of the item nuclear material loss. The functional relation between identification probability and item nuclear material mass loss can be obtained for either the "forward model only" or the "inverted" approach. However, the "forward model only approach" does not provide a mass estimate, only a pass/fail criterion associated with a consistency check; therefore, the IAEA's relative operator-inspector difference statistic (ROID) could not be computed, although an alternative test (a nonparametric "sign" test) for trend could be computed. In addition to the generic calibration context, the Cherenkov viewing device is used as a conceptual illustration.

Keywords: calibration; consistency check; detection probability; forward model; inverse model

1. Introduction

1.1 Inspector verification measurements

Operator declarations are verified on a sampling basis by inspectors who measure sampled items during inspections that occur once or a few times per year. The relative operator-inspector differences

$$d = ROID = (O - I)/O\,, \qquad (1)$$

where O is the operator declared mass value and *I* is the mass value measured and/or inferred by the inspector, are compared to alarm thresholds to monitor for possible data falsification by the operator. The alarm thresholds are estimated by applying a type of analysis of variance, using several years of prior paired (*O*,*I*) data as illustrated in Figure 1. Figure 1 plots $n = 5$ ROID values in each of $g = 4$ groups, with the mean ROID value indicated in each group with a horizontal line. The groups are inspection periods, which are ordered by time. An effective measurement error model must account for variation within and between groups, where a group is an inspection period. A multiplicative error model used for the inspector (*I*) (and similarly for the operator *O*) is

$$I_{kj} = \mu_{kj}(1 + S_{Ik} + R_{Ikj})\,, \qquad (2)$$

where I_{kj} is the inspector's measured value of item *j,* with true value μ_{kj} R_{Ikj} is the random error of item *j* from group *k,*and $S_{Ik} \sim N(0, \delta_{SI}^2)$ is a short-term systematic error in group *k* [2-4], which is randomly generated once per inspection period. Regarding notation, the ~ symbol means independently and identically distributed, and $N(0, \delta_{RI}^2)$ denotes the normal distribution with mean 0 and variance δ_{RI}^2 , where δ_{RI} is the relative standard deviation of the inspector's random errors.

1.2 Zero-defect sampling plans

For inspector verification measurements of operator declared nuclear material masses, the IAEA uses zero-defect sampling, which means that the only acceptable (passing) sample is one for which no defects are found. A defective item is one for which the operator's declared nuclear material mass has been falsified. Therefore, the non-detection probability is the probability that no defects are found in a sample of size *n* when one or more true defective items are in the population of size *N*.

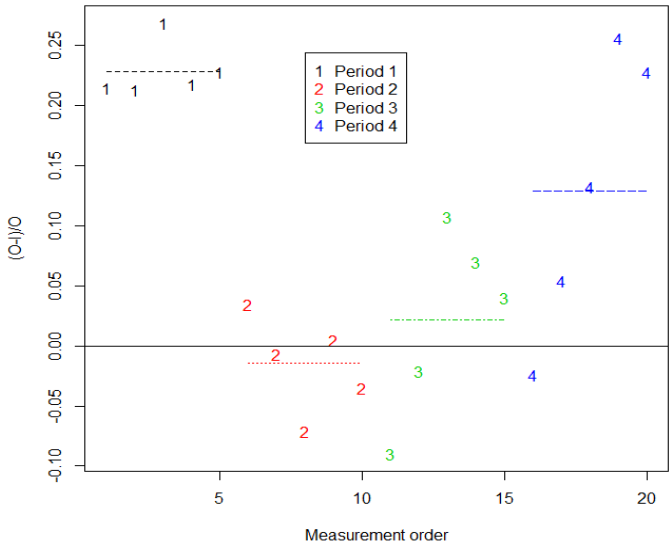

Figure 1. Example with *n* = 5 $OID = (O - I) / O$ values in each of *g*=4 inspection periods.

For one-item-at-a-time testing, the non-detection probability is given by

$$\text{Prob(discover 0 defects in sample of size } n) = \sum_{i=Max(0,n+r-N)}^{Min(n,r)} A_i \times B_i \qquad (3),$$

where the term A_i is the probability that the selected sample contains *i* truly defective items, which is given by the hypergeometric distribution with parameters on *i*, *n*, *N*, *r,* where *i* is the number of defects in the sample, *n* is the sample size, *N* is the population size, and *r* is the number of defective items in the population. More specifically, $A_i = \dfrac{\binom{r}{i}\binom{N-r}{n-i}}{\binom{N}{n}}$ is the probability of choosing *i* defective items from *r* defective items in a population of size *N* in a sample of size *n*, which is the well-known hypergeometric distribution. The term B_i (the non-identification probability) is the probability that none of the *i* truly defective items is identified as defective based on the individual tests. The value of B_i depends on the metrology, the defect size (defined as the amount by which the declared item nuclear material mass differs from its best accountancy value), and the alarm threshold. Assuming a multiplicative error model for the inspector measurement (and similarly for the operator), and assuming there is only one measurement method (extensions to more than one method, such as NDA and DA, are straightforward) implies that, for an alarm threshold of *k* = 3, for $d_j = (O_j - I_j) / O_j \approx (O_j - I_j) / \mu_j$, calculate $B_i = P(d_1 \le 3\delta_T, d_2 \le 3\delta_T, ..., d_i \le 3\delta_T)$, where

$\delta_T = \sqrt{\delta_R^2 + \delta_S^2}$, which is given by the multivariate normal cumulative distribution function (CDF) $B_i = \frac{1}{(2\pi)^{i/2} \mid \Sigma_i \mid^{1/2}} \int_{-\infty}^{3\delta} ... \int_{-\infty}^{3\delta} \exp\{\frac{-(\mathbf{z}-\boldsymbol{\lambda})^T \Sigma_i^{-1} (\mathbf{z}-\boldsymbol{\lambda})}{2}\} dz_1 dz_2 ... dz_i$, where each of the components of $\boldsymbol{\lambda}$ equal $1\,SQ/r$ (SQ is a significant quantity; for example, 1 SQ = 8 kg for Pu, and *r* was defined above as the number of defective items in the population) [3]. The term Σ_i in the B_i calculation involved in the multivariate normal integral is a square matrix with *i* rows and columns with values $(\delta_R^2 + \delta_S^2)$ on the diagonal and values δ_S^2 on the off-diagonals. The relative standard deviations (RSD) δ_R and δ_S are defined in the context of Eq. (2), and $\delta_R = \sqrt{\delta_{RO}^2 + \delta_{RI}^2}, \delta_S = \sqrt{\delta_{SO}^2 + \delta_{SI}^2}$. The requested sample size is based on the minimum detection probability (maximum non-detection probability) over a range of possible *r* values (*r* is the true number of defective items in the population of size *N*), assuming each defective item has the same defect size.

2. Alternatives to the multivariate normal CDF

The normal CDF is used to calculate the identification probability B_i in Eq. (3) when one assumes that $d_j = (O_j - I_j)/O_j \approx (O_j - I_j)/\mu_j$ has approximately a normal distribution [3]. Equation (3) allows for B_i to be a user-defined probability density function, such as the normal density, or any other specified density that is suggested by measurement evaluations .The identification probability, B_i, can be based on forward modelling, or on inverse modelling.

Figure 4 plots the identification probability versus the mean shift (loss of nuclear material) for forward modelling (regression) in Fig.2a and for inverse modelling (calibration) in Fig. 2b. Least squares regression can be applied to the forward model model

$$Y = \beta_0 + \beta_1 x_T + R_Y \qquad (4),$$

in a generic context, where *Y* is the random detector response and x_T is the assumed known (without error; see below) true value of the predictor (the nuclear material mass). In regression applications, one main goal is to estimate *Y* at a future known x_T value. If the variance of R_Y , $\sigma_{R_y}^2$, is constant as x_T changes (that is, is independent of x_T and therefore also of $y_T = \beta_0 + \beta_1 x_T$), then ordinary least squares (OLS) estimates $\hat{\beta}_0$ and $\hat{\beta}_1$ minimize the residual sum of squares, $RSS(\tilde{\beta}_0, \tilde{\beta}_1) = \sum_{i=1}^{n} (y_i - (\tilde{\beta}_0 + \tilde{\beta}_1 x_i))^2$. If $\sigma_{R_y}^2$, is not constant as x_T changes then weighted least squares (WLS) $RSS(\tilde{\beta}_0, \tilde{\beta}_1) = \sum_{i=1}^{n} (y_i - (\tilde{\beta}_0 + \tilde{\beta}_1 x_i))^2 / \sigma_{R_{Y_i}}^2$ can be used instead of OLS. The OLS estimates $\hat{\beta}_0$ and $\hat{\beta}_1$ are random variables conditioned on the values of x_T in the training (calibration) data; the estimates $\hat{\beta}_0$ and $\hat{\beta}_1$ vary across hypothetical or real calibrations due to variation in the realized values of the random values R_Y. Note that the term “training” is in this context the same as “calibration,” but more broadly, “training” can involve model selection and model parameter estimation. The term “testing” involves performance on data that were not used in training.

Eq. (4) can be used in either of two ways in calibration to infer the corresponding *x* value using future *Y* values. References [2,4] and references therein show that of the two ways, reverse calibration using $X = \alpha_0 + \alpha_1 Y + R_X$ tends to have lower root mean squared error than inverse calibration using (4) followed by $\hat{x} = (Y - \hat{\beta}_0)/\hat{\beta}_1$. Both reverse and inverse calibration involve ratios of random variables, for which analytical approximations have been shown to be inaccurate [2,4], and so should be analysed by simulation for better accuracy. Typically, the error RSD in the “known” true values x_T is relatively small, 0.1% or less, while the RSD in *Y* can be considerably larger, 1%, 5%, or even 10%.

The identification probability of reverse calibration can be compared to that of forward modelling only. Figure 2 plots the errors in fitting Eq. (1) using 5 standards spaced equally from 1 to 2 to calibrate. Readers familiar with OLS regression will recognize that the error magnitudes are smallest near the center of the calibration data and largest at both ends. The 0.025 and 0.975 quantiles are indicated at test values of 1, 1.25, 1.5, 1.75, and 2 kg. Notice that a mean shift from 1.75 to 1.5 will not have large identification probability. Similarly to Figure 2, Figure 3 shows that for a test value 2.0 kg, a mean shift of 0.44 kg to 1.56 kg has 0.95 identification probability, with a false alarm rate 0.05.
Note from Figure 4 that the identification probability for any mean shift is larger for forward modelling than for inverse calibration; therefore, the DP is also larger for forward modelling.

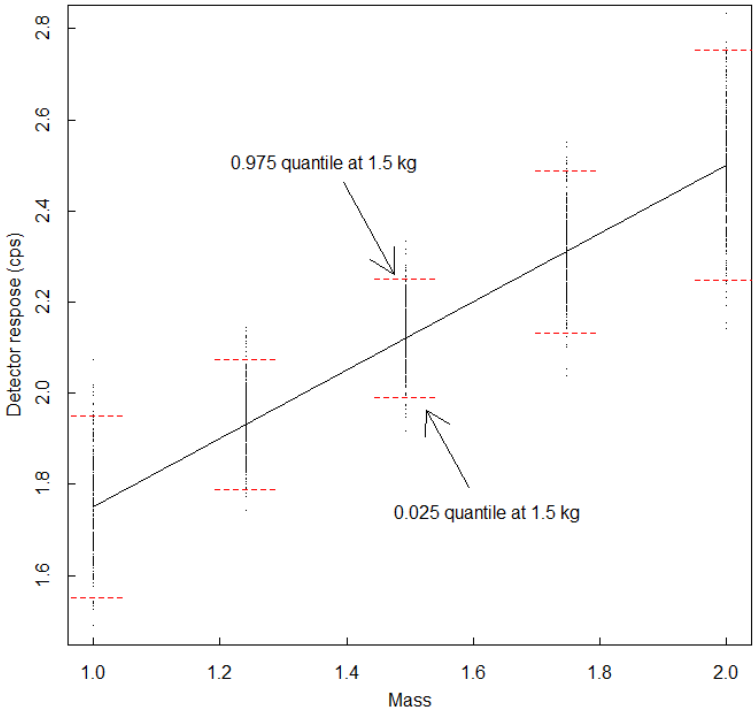

Figure 2. True detector response (solid line with intercept 1 and slope 0.75) and intervals that contain 95% of the predicted values at a mass of 1, 1.25, 1.5, 1.75, and 2 kg.

For a population of N = 100 items and a sample of n = 5 items, Figure 5 plots the DP versus the mean shift (defect size) for forward modelling and inverse calibration, using the identification probability versus mean shift as in Figure 4 in Eq. (3), and also using step-function approximations to the identification probability (the step function is conservatively set to 0 if the identification probability less than 0.95 and to 1 if 0.95 or larger). Figures 2-5 all used RSDs in X and Y of $\delta_{RX} = 0.001$ and $\delta_{RY} = 0.07$, respectively. and $\beta_0 = 1, \beta_1 = 0.75$ in Eq. (4).

3. Example of Forward Modelling in a Partial Defect Test using the DCVD

Figure 6 plots observed and modelled/predicted detector responses in the digital Cherenkov viewing device (DCVD) for monitoring spent fuel assemblies to detect partial defects (e.g. missing pins) [5-7]. Figure 6 is an example of the best-expected performance of data consistency checking in the DCVD for a partial defect measurement, assumed to have identification probability equal to 0 if the mean shift is less than 50%, and equal to 1 if the mean shift is 50% or more (missing pins in spent fuel assemblies). Note that even in this nice-performance example of the DCVD, while there are no outliers, too many measured assemblies fall above the predicted line toward the low end of the data range. The smallest mean shift that can be detected,with false alarm probability 0.05 and detection probability 0.95, is obtained by solving for the largest value of the response y satisfying

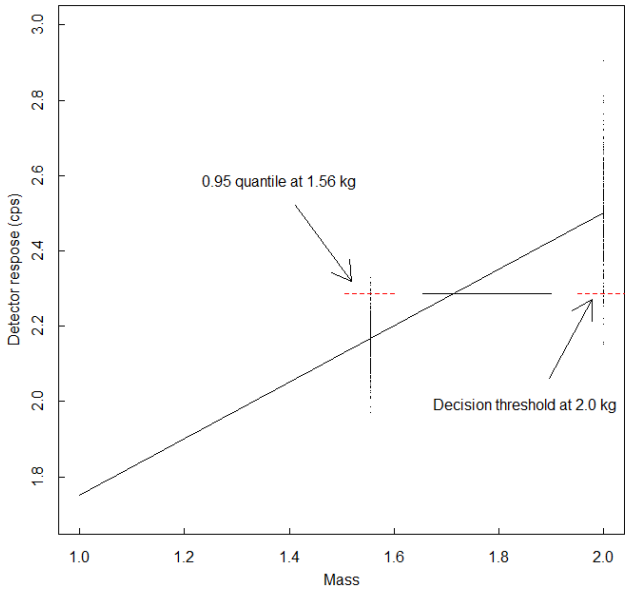

Figure 3. Illustration of identification probability for a mass shift of 0.44 kg using forward regression.

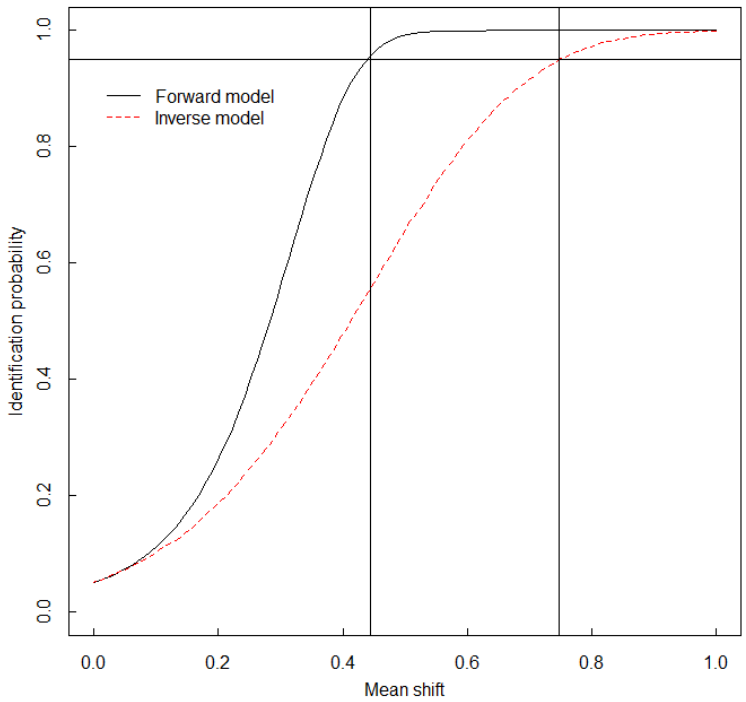

Figure 4. Identification probability versus mass mean shift for the forward and inverse models.

$y(1+\delta) \le y_{Test}(1-\delta)$. For example, again using $\beta_0 = 1, \beta_1 = 0.75$, thecorresponding largest value of *x* satisfies $x = \{(\beta_0 + \beta_1 x_{Test})(1-\delta)/(1+\delta) - \beta_0\}/\beta_1 = \{1 + .75x_{Test})(.7/1.3) - 1\}/.75$.

It should be noted that this portion of the DCVD analysis for partial defect analysis is a relative comparison of similar assemblies organized into their respective light pattern groups. Each predicted value is compared to the corresponding measured value and a least squares fit to the (predicted, measured) pairs through the origin is obtained. The slope of the fit is then used as a correction factor to adjust values to the same scale for comparison. Because the fit is forced through zero, it adds to the many assemblies above the predicted line at the low end of the scale. No attempt is made to back-calculate the value of burn up or enrichment from the DCVD measurement. The comparison is

therefore an example of a forward model, which is only one part of a larger analysis to determine whether a partial defect has occurred. Smaller defects are noted, and every residual = (measurement-predicted)/predicted greater than 30% is scrutinized.

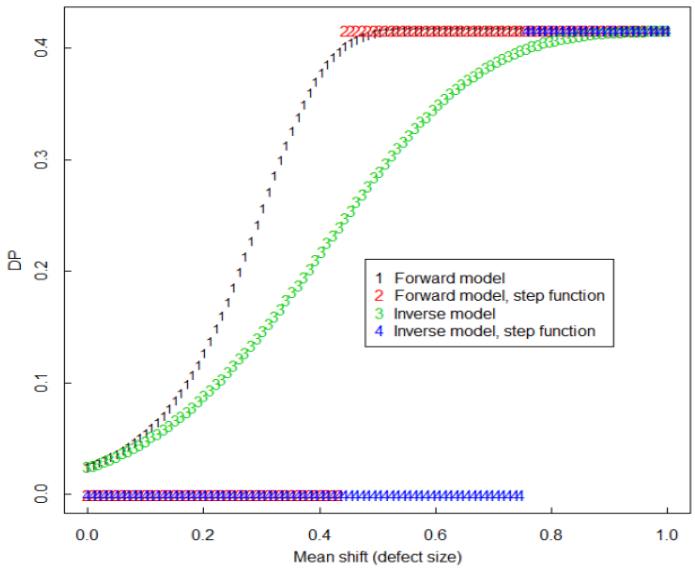

Figure 5. Detection probability versus mass mean shift (defect size as a fraction of 1 = 100% of the item mass) for the same example that is used in Figures 2-4.

4. Discussion and Summary

Using a generic calibration context it was shown that the "forward model only approach" has larger detection probability (DP) than the "invert to infer mass approach," because it avoids noise amplification associated with inverting from NDA counts to mass. The DP in Eq. (3) depends on both the selection probability (at least one defective item occurs in the inspector's random sample) and the measurement identification probability (a truly defective item is inferred to be defective). The estimated relation between the identification probability and item nuclear material mass loss can be used in sampling calculations using either the "forward model only" or the "inverted" approach. The ROID $d = (O - I)/O$ in Eq. (1) monitors individual paired differences in estimated nuclear material mass between operator and inspector, and the difference statistic $D = m\sum_{j=1}^{n}(O_j - I_j)$, where m is a factor used to extrapolate from the sample to the population, is used to check for trends. It should be mentioned that the "forward model only approach" does not provide a mass estimate, only a pass/fail criterion associated with a consistency check; therefore, the traditional ROIDs and the overall D could not be computed. However, the pass/fail criterion can be used for the verifications of each item, and an alternative overall test (a nonparametric "sign" test) for trend could still be computed.

In addition to the generic calibration context, the DCVD was used as a conceptual illustration of the forward model approach. There is no current way in the forward model for the DCVD to separate error components into systematic and random; therefore, all *n* verification measurements would be assumed to be independent. Reference [8] also describes the forward model option, using both fresh and spent fuel verification activities as examples. Regardless of whether one uses forward or inverse modelling, a forward model is required, because inverse modelling requires a forward model that links item properties to observables. Therefore, improvements to forward models are of course always beneficial, and the benefits can be quantified as described in Sections 2 and 3.

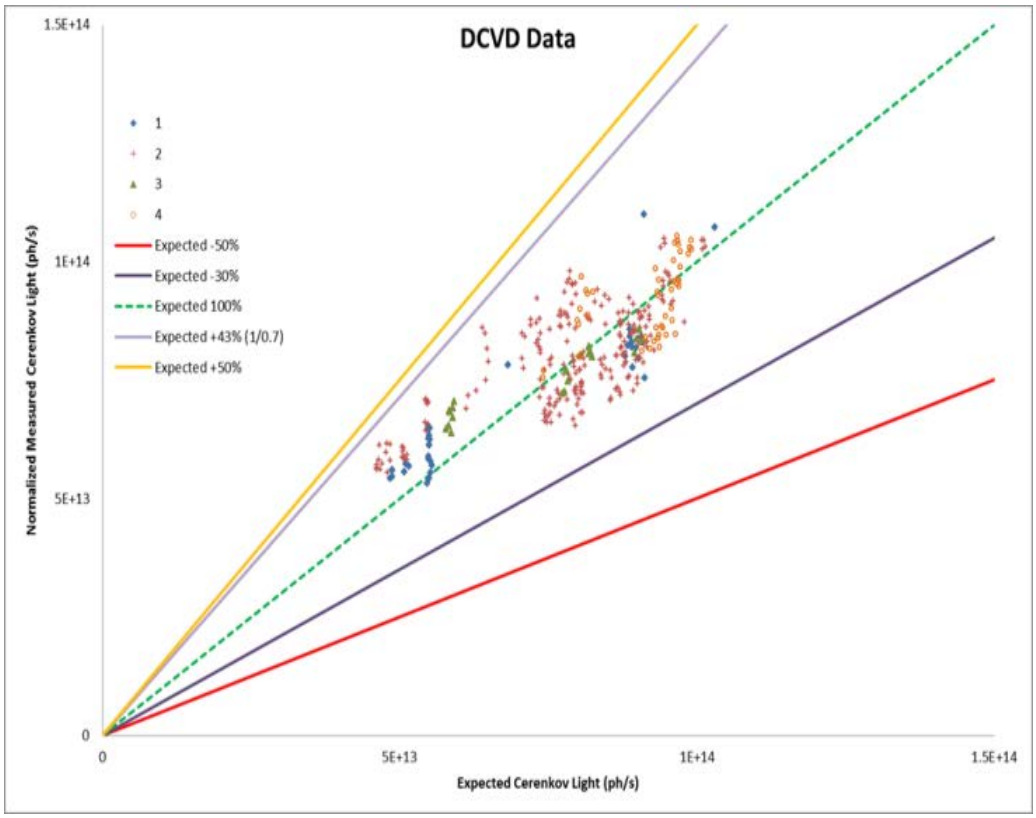

Figure 6. CVD partial defect forward model approach.

References

[1] Zykov, S. Technical challenges and technological gaps in IAEA safeguards, Proceedings of the Institute of Nuclear Materials Management, 2015.

[2] Burr, T.,Croft, S., Krieger, T., Martin, K., Norman, C. Walsh, S., Uncertainty Quantification for Radiation Measurements: Bottom-Up Error Variance Estimation Using Calibration Information, Applied Radiation and Isotopes, 108,49-57, 2015.

[3] Burr, T., Krieger, T., Norman, C., Zhao, K, The Impact of Metrology Study Sample Size on Verification Sample Size Calculations in IAEA Safeguards, European Journal Nuclear Science and Technology, 2, 36, 2016a.

[4] Burr, T., Croft, S., Jarman. K., Nicholson, A., Norman, C., Walsh, S., Improved Uncertainty Quantification in NonDestructive Assay for Nonproliferation, Chemometrics, 159, 164-173, 2016b.

[5] Branger, E., Grape, S., Jaconsson, S., Jansson, P., Sunden, E., Comparison of prediction models for Cherenkov light emissions from nuclear fuel assemblies, Journal of Instrumentation, doi:10.1088/1748-0221/12/06/P060072017.

[6] Chen, J., et al., Partial defect detection in LWR spent fuel using a Digital Cerenkov Viewing Device, Proceedings 50th annual meeting of Institute of Nuclear Materials Management, 2009.

[7] Orton CR, D Parise, S Lackner, S Jung, D Belemsaga, L Turtos Carbonell, F Muelhauser, G Bernasconi, A Lebrun. 2017. The International Atomic Energy Agency's Experience Verifying Spent Fuel Using the Digital Cerenkov Viewing Device. Proceedings of the Institute of Nuclear Materials Management 58th Annual Meeting, Indian Wells, CA, 16-20 July 2017.

[8] Vaccaro, S., Gauld, I., Vescovi, M., Tagziria, H., Smejkal, A., Schwalbach, P. The forward-problem approach in safeguards verification: directly comparing simulated and measured observables, ESARDA bulletin 54, 70-75 2017.

GETTING IN TOUCH WITH THE EU

In person

All over the European Union there are hundreds of Europe Direct information centres. You can find the address of the centre nearest you at: https://europa.eu/european-union/contact_en

On the phone or by email

Europe Direct is a service that answers your questions about the European Union. You can contact this service:

- by freephone: 00 800 6 7 8 9 10 11 (certain operators may charge for these calls),

- at the following standard number: +32 22999696, or

- by electronic mail via: https://europa.eu/european-union/contact_en

FINDING INFORMATION ABOUT THE EU

Online

Information about the European Union in all the official languages of the EU is available on the Europa website at: https://europa.eu/european-union/index_en

EU publications
You can download or order free and priced EU publications from EU Bookshop at: https://publications.europa.eu/en/publications. Multiple copies of free publications may be obtained by contacting Europe Direct or your local information centre (see https://europa.eu/european-union/contact_en).

KJ-07-18-105-EN-N

The European Commission's science and knowledge service
Joint Research Centre

JRC Mission
As the science and knowledge service of the European Commission, the Joint Research Centre's mission is to support EU policies with independent evidence throughout the whole policy cycle.

EU Science Hub
ec.europa.eu/jrc

@EU_ScienceHub
EU Science Hub - Joint Research Centre
Joint Research Centre
EU Science Hub

Publications Office

doi:10.2760/055930
ISBN 978-92-79-98443-3